Transport in Nanoscale Systems

by

Dmitry S. Novikov

Submitted to the Department of Physics
in partial fulfillment of the requirements for the degree of

Doctor of Philosophy

at the

MASSACHUSETTS INSTITUTE OF TECHNOLOGY

September 2003

Author .....
Department of Physics
May 14, 2003

Certified by .....
Leonid S. Levitov
Professor of Physics
Thesis Supervisor

Accepted by .....
Thomas J. Greytak
Chairman, Department Committee on Graduate Students

Transport in Nanoscale Systems

by

Dmitry S. Novikov

Submitted to the Department of Physics
on May 14, 2003, in partial fulfillment of the
requirements for the degree of
Doctor of Philosophy

Abstract

In part I of the Thesis charge ordering and transport in arrays of coated semiconductor nanocrystals (quantum dot arrays) are studied.

Charge ordering in dot arrays is considered by mapping the electrons on the dots onto the frustrated spin model on the triangular lattice. A number of phases is identified for this system. Phase diagram is studied by means of the height field order parameter. Novel correlated fluid phase is identified, in which transport of classical charges exhibits correlated behavior. Freezing transitions into commensurate ground state configurations are found to be of the first order.

A novel model of transport in disordered systems is proposed to account for experimentally observed current transients in dot arrays at high bias. This transport model yields a non-stationary response in a stationary system. The model proposes a particular power law noise spectrum that is found to be consistent with experiments.

In Part II of the Thesis novel effects in Carbon nanotubes are predicted. These effects can be manifest in transport measurements.

First, it is shown that a strong electric field applied perpendicularly to the tube axis can fracture the Fermi surface of metallic nanotubes and significantly reduce excitation gap in semiconducting nanotubes. The depolarization problem is linked to the chiral anomaly of 1+1 dimensional Dirac fermions.

Second, coupling between a surface acoustic wave and nanotube electrons is proposed as a means to realize an adiabatic charge pump. Incompressible states are identified in the single particle picture, and the corresponding minigaps are found. Conditions for pumping experiment are identified.

Third, electron properties of a nanotube in a periodic potential are considered. It is shown that when the electron density is commensurate with the potential period, incompressible electron states exist. Electron interactions are treated in the Luttinger liquid framework, and excitation gaps corresponding to incompressible states are found using the phase soliton approach.

Thesis Supervisor: Leonid S. Levitov
Title: Professor of Physics

Acknowledgments

This work would not have been possible without the advice, support and encouragement of many people that I am happy to mention here.

First, I would like to thank my research advisor, Professor Leonid Levitov, for his guidance and constant support. Leonid's exceptional creativity, exemplary taste and outlook in Physics, as well as his unforgiving sense of humor has made our work a true adventure. Leonid has always been extremely helpful and super-available for any questions or comments, as well as provided me with opportunities for very useful scientific visits.

Second, I would like to thank my colleagues and collaborators.

Part I of my Thesis has been inspired and heavily based on the collaboration with the groups of Professors Marc Kastner (MIT Physics) and Moungi Bawendi (MIT Chemistry). I would like to thank Marc and Moungi, as well as their graduate students Nicole Morgan and Mirna Jarosz, for numerous discussions that gave me a taste of experimental challenges they face. Marija Drndic has been both a great colleague and a wonderful person to chat with. Certain numerical results of Chapter 2 have been obtained together with Boris Kozinsky during sleepless nights in Athena clusters at MIT. The rest of the numerics from that Chapter has been performed at the Cavendish Laboratory in Cambridge, England.

A set of results from Part II of my Thesis have been obtained together with Dr. Ben Simons and Dr. Valery Talyanskii from the Cavendish Laboratory. I am happy to thank them for the collaboration.

Prof. Patrick Lee's great set of lectures in many-body physics provided me with inspiration. I am also thankful to Patrick for the financial support for 1.5 months during the summer of 2000.

I have enjoyed numerous discussions about both physics and life with my friends and colleagues Michael Fogler, Ilya Gruzberg, Andrey Shytov, Lesik Motrunich, Evan Reed and Jung-Tsung Shen.

Last but not least, I am delighted to thank here those to whom I am grateful for

keeping me sane and happy during these years. My special thanks go to Veronika for her enormous support and encouragement through her love and cheerfullness. My scientific advisor in college, and later a colleague and a friend Valerij Kiselev has always been the one who could equally well understand the challenges in science and in life. Finally, my greatest thanks and devotion go to my parents who have always had more faith in me than I have had in myself.

Contents

List of Figures

List of Tables

Part I

Transport in Nanoparticle Arrays

Chapter 1

Review of Experiment and Theory

I would like to describe a field,
in which little has been done,
but in which an enormous amount
can be done in principle.
R. P. Feynman,
"There is plenty of room at the bottom"

Our understanding about the microscopic world has been moving forward by studying systems that nature created. This progress has gradually led to discovery of chemical elements, then to the structure of atom, nucleus, and nucleons. In a recent decade or so, a new way to study microscopic systems emerged. Recent progress in the nanoscale fabrication opened up a possibility to *design* matter by designing the elementary building blocks rather than just use what nature has to offer. These so-called "artificial atoms" [3], or *quantum dots*, can consist of a handful of real atoms of a metal or a semiconductor and be tuned and controlled to have desired properties.

The aim of the present Part of the Thesis is to study in detail a particular system made entirely of such artificial building blocks. This system, which is a closely packed array ("solid") of nearly identical coated semiconductor nanocrystals put together by self-assembly, can be considered the simplest of its kind. Despite their seeming simplicity, quantum dot arrays appear to be rich systems that exhibit a variety of physical phenomena.

An important feature of dot arrays is their *tunable properties*. The composition, size, and coating of individual quantum dots can be adjusted, which makes it possible to create novel nanoscale systems with a control of the Hamiltonian by the system's design. Advancements in colloidal chemistry has allowed one to produce such quantum dots in large quantities. It has led to a possibility to create novel solids composed of a macroscopically large number of semiconducting nanocrystals. These materials possess a great potential both for basic research and applications [4].

In this Part of my Thesis I will focus on *charge ordering* and *transport* in quasi-two-dimensional quantum dot arrays (QDAs) [5, 6, 7]. An example of such an array is shown in a TEM image, Fig. 1-1. The outline of the present Part is as follows.

First, in the present Chapter, I will describe basic properties and synthesis of the QDAs, as well as review experiments on dot arrays. In reviewing the experiments I will mostly focus on transport phenomena, as transport is a natural and powerful probe for nanoscale systems. Moreover, as I will show in this Chapter, transport measurements done so far yield a rather unexpected outcome. In the present Chapter I will also review appropriate theoretical models of transport, namely hopping conductivity and dispersive transport.

Charge ordering in dot arrays will be studied theoretically [1] in Chapter 2. There we will see that an interplay between the long range Coulomb interaction and the triangular geometry of an ideal two dimensional array (Fig. 1-1) can lead to a rich phase diagram even though the system is essentially *classical* at realistic temperatures. I will show that electrons on the array can exhibit *collective behavior*, and will study phase transitions that correspond to freezing into commensurate configurations. It will also be shown that transport measured at a low bias can serve as a probe of charge ordering in the ground state, with singularities of conductivity corresponding to ordering phase transitions.

Transport in QDAs will be analyzed in detail in Chapter 3. The novel transport model [2] that I will present in that Chapter accounts for anomalous transport in QDAs measured at a high bias. It will be shown how a non-ohmic, non-stationary current can arise in a *stationary* system. This transport model will be based on a

stationary Lévy process.

1.1 QDA properties, synthesis and transport

In the present Section I will first briefly describe existing artificial nanoscale systems, such as epitaxially grown quantum dot arrays, as well as Josephson junction arrays. I will contrast them with the novel colloidal quantum dot arrays that are the focus of the present Part of the Thesis. I will then briefly touch upon the synthesis of individual dots and their self-assembly on a substrate. Next I will describe the results of transport measurements on the dot arrays. These experiments show that, in response to a voltage step, a remarkable power law decay of current over five decades of time is observed. This effect has not been understood, and the purpose of the Chapter 3 of the present Thesis is to propose a phenomenological model for its explanation.

Dot arrays currently used for transport measurements are rather disordered (Fig. 1-2). In Section 1.2 I will review existing theoretical models of transport in disordered systems and show that they fail to explain the observed transport effects.

1.1.1 QDAs versus other artificial systems

First quantum dot arrays have been made by applying *epitaxial techniques* [8]. Such arrays (either regular or irregular) are made of InAs or Ge islands embedded into the semiconductor substrate. The dot size in a typical array can be tuned in the 10-100 nm range with the rms size distribution of 10-20%. Progress in fabrication stimulated a number of experimental [9, 10, 11, 12] and theoretical [13] works on the electronic ordering and transport in these arrays. Infrared [9] and capacitance [10] spectroscopy, as well as conductivity measurements [11] show the quantized nature of charging of the dots. Recently interesting effects have been observed due to interactions of the two dimensional electrons with dot arrays [12]. A common feature of the epitaxially grown dot arrays is a relatively small role of electron interactions on the dots. Indeed, the interdot Coulomb interaction in such systems is an order of magnitude weaker than the dot charging energy and the offset charge potential fluctuations.

Another class of artificial sytems characterized by the control of the Hamiltonian during the system design are the *Josephson arrays*. There have been extensive theoretical [14] and experimental [15] studies of phase transitions and collective phenomena in Josephson arrays. In both dot arrays and Josephson arrays experimental techniques available for probing magnetic flux or charge ordering, such as electric transport measurements and scanning probes, are more diverse and flexible than those conventionally used to study magnetic or structural ordering in solids. However, Josephson arrays at present are rather difficult to produce and to control, and, besides, they require liquid Helium temperatures to operate.

In the present Thesis we will focus on a different system that has been fabricated recently [5, 6, 7]. This system is based on nanocrystallite semiconductor quantum dots that are synthesized by the means of colloidal chemistry. The individual nanocrystals (typically made of CdSe or CdTe) can be made with high reproducibility, of diameters $\sim 1.5 - 15$ nm tunable during synthesis, with a narrow size distribution (down to 5% rms). One should keep in mind that a 5% deviation in size at such a small scale corresponds to a thickness of a single atomic layer.

These semiconductor quantum dots can be forced to assemble into ordered three-dimensional closely packed colloidal crystals [6], with the structure of stacked two-dimensional triangular lattices. Due to higher flexibility and structural control, these systems are expected to be good for studying effects inaccessible in the more traditional epitaxially grown self-assembled quantum dot arrays described above. In particular, the high charging energy of nanocrystallite dots comparable to or larger than room temperature, and the triangular lattice geometry of the dot arrays [6, 7], Fig. 1-1, are very interesting from the point of view of exploring novel kinds of both charge ordering and transport [1, 16, 17, 18, 19, 20].

The physics of colloidal quantum dot arrays becomes even more complex if one considers randomness in interdot couplings and the offset charge, time fluctuations of the above leading to the $1/f$ noise, effects of the environment, aging, and so forth.

In the present Section I will first briefly touch upon the synthesis and selection procedures for the quantum dots as well as their self-assembly into arrays. After that

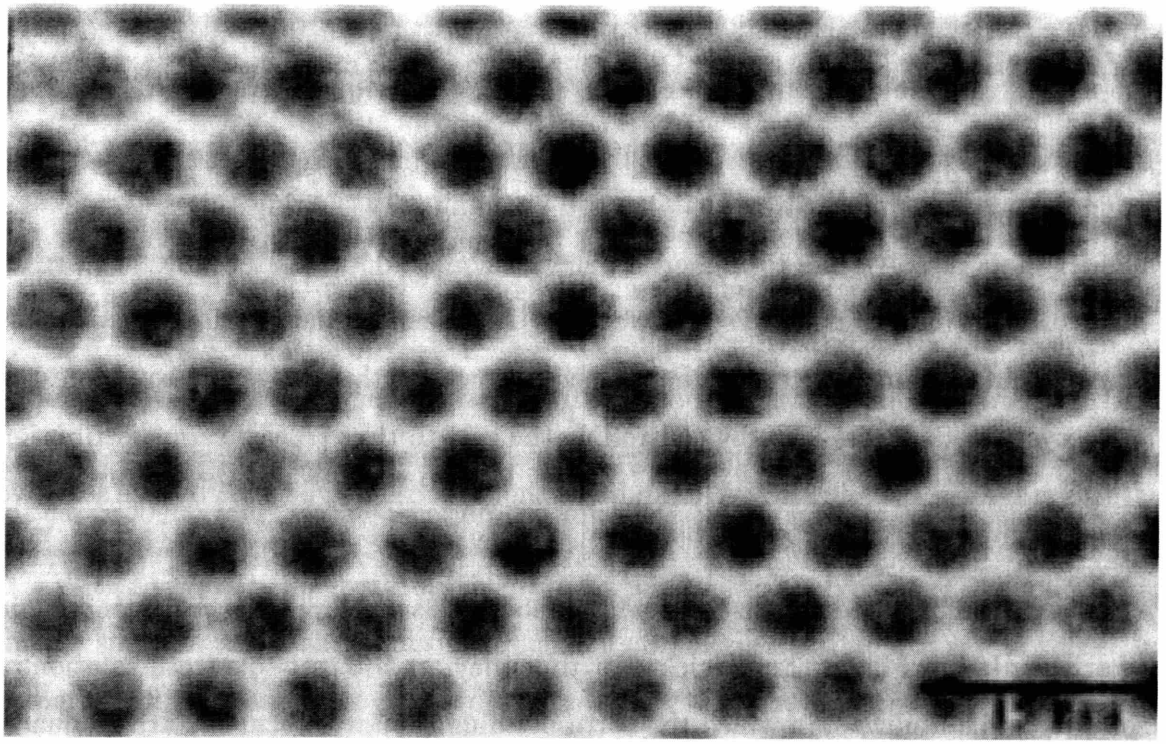

Figure 1-1: TEM image of a quantum dot array. Courtesy Bawendi group, MIT Chemistry Department

I will present a review of transport measurements on CdSe arrays.

1.1.2 Synthesis of nanocrysal arrays

Recent progress in colloidal chemistry has allowed one to produce semiconducting nanocrystals in macroscopic quantities, to select them according to their size with an accuracy up to 5% rms, as well as to make two- and three-dimensional synthetic materials [5, 6, 7]. Below I briefly outline the main stages of the nanocrystal array synthesis following the works of C.B. Murray, C.R. Kagan, D.J. Norris and M.G. Bawendi, as described in Refs. [5, 6, 7].

Monodisperse semiconducting nanocrystals are prepared by an injection of metal-organic precursors into a flask containing a hot ($\sim 150 - 350\,\mathrm{C}$) coordinating solvent, as described in Ref. [7]. This process is based on the framework for production of monodisperse colloids laid by La Mer and Dinegar [21]. According to the latter, precursor concentration has to be just above the nucleation threshold so that only a small

fraction of reagents participates in the nucleation stage. In this case, as shown by Reiss [22], the size distribution of colloids during a subsequent slow growth stage in an undersaturated solution becomes more narrow. Further growth of semiconducting nanocrystals is dominated by the Ostwald ripening [23]. During this stage smaller nanocrystals dissolve due to higher surface tension, and the material is being redeposited on the larger nanocrystals. For the II-VI semiconducting nanocrystals this stage lasts for minutes or even hours. Such a slow growth enables one to obtain the nanocrystals of a desired size by controlling the growth time [7]. The size distribution at this stage can be below 15%. It can be further reduced down to 5% by size selective procedures [7].

After being isolated and size-selected, nanocrystals are capped by either inorganic or organic layer of about 1 nm thick. For that they are brought to a fresh solution of solvents and stabilizers, in which the corresponding capping precursors are gradually added at a certain temperature [7]. Capping prevents nanocrystals from a direct electrical contact with each other.

Finally, capped nanocrystals form two- or three-dimensional arrays when deposited on a substrate from a solvent. As the solvent evaporates, nanocrystals rearrange themselves and self-assemble into regular structures like the one shown in Fig. 1-1, as described in Refs. [6, 7].

1.1.3 Transport in nanocrystal arrays

There has been a number of transport measurements on the colloidal CdE dot arrays, with E=S, Se, or Te. One class of experiments [19, 20, 24] have been devoted to the "vertical transport" geometry, in which a film (typically $\sim$ 200 nm thick) of nanocrystals is sandwiched between metallic source and drain. The results of these experiments are somewhat contradictory. On the one hand, a steady state current that is a power law of the applied voltage is observed [20, 24]. On the other hand, Ginger and Greenham [19] observe a slow *decay* in time of a dc current under a constant applied bias.

In the present Thesis I will focus on the results of the transport measurements

performed on the quasi-two-dimensional CdSe quantum dot arrays [17, 18] in the *field effect transistor geometry*, as schematically shown in Fig. 1-2. In such a setup a dc current is measured between a negative source and a grounded drain, with a gate voltage controlling electron density on the array. Measurements are done in the cryostat at 77 K.

In experiments [17, 18] a film of nanocrystals about 200 nm thick is deposited on oxidized, degenerately doped Si wafers with oxide thickness $\approx$ 200 nm (see Fig. 1-2). Gold electrodes, fabricated on the surface before deposition of nanocrystals, consist of bars 800 μm long with separation of 2 μm.

With a typical nanocrystal size of 5 nm (including the capping layer), the dot array in the space between electrodes is about 400 dots across and 40 dot layers thick. In experiments [17, 18] dot arrays possess a local closely-packed order. However, the arrays are imperfect on a larger scale, having practically no long range order, as illustrated by the TEM image in Fig. 1-2.

Prior to electrical measurements samples are typically annealed at 300 C in vacuum inside of the cryostat. Annealing reduces the distance between the nanocrystals and enhances electron tunneling [17, 18].

For QDAs made of coated CdSe dots the zero bias conductance has been found to be immeasurably small [17, 18]. Therefore electron transport in dot arrays has been studied using strong applied fields of the order of 100 V between source and drain. This *large bias regime* corresponds to the voltage of several hundred meV between the neighboring dots, which is of the order of the dot charging energy (about 200 meV) and the interdot Coulomb energy (about 50 meV) [17, 18].

Below we summarize the results of Refs. [17, 18]. When a negative voltage step is applied to the source at time $t = 0$, with the drain grounded, the following are observed:

(i) A *power law decay* of the current

$$I = I_0 \, t^{-\alpha} \, , \quad 0 < \alpha < 1 \tag{1.1}$$

is always found. The law (1.1) has been verified to hold for up to five decades in time, from hundreds of milliseconds to tens of hours (Fig. 1-3).

(ii) This is a true current from source to drain, rather than a displacement current, since the net charge corresponding to (1.1) diverges with time. Already for observation times $\sim 10^3$ s, the transported charge is orders of magnitude greater than that capacitively accumulated on the array, as shown in Fig. 1-3.

(iii) The exponent α is *non-universal.* It depends on temperature, dot size, capping layer, bias voltage and gate oxide thickness.

(iv) The system has a *Memory effect*: Suppose the bias is off for $t_1 < t < t_2$. The current measured as a function of a *shifted time* $\tilde{t} = t - t_2$ is of the form (1.1) with an amplitude $\tilde{I}_0 < I_0$. This is illustrated in Fig. 1-3, in which the transient for long times is recorded after that for the shorter time, giving rise to a smaller amplitude. The amplitude $\tilde{I}_0$ is restored, $\tilde{I}_0 \to I_0$, by increasing the *off* interval $t_2 - t_1$, by annealing at elevated temperature, or by applying a reverse bias or bandgap light between t_1 and t_2.

To explain the current decay (1.1) it has been suggested that this time-dependent current is the result of the time dependence of the state of the system, either because trapping of electrons slows further charge injection from the contact [19] or because of Coulomb glass behavior of the electrons distributed over the nanocrystals [17].

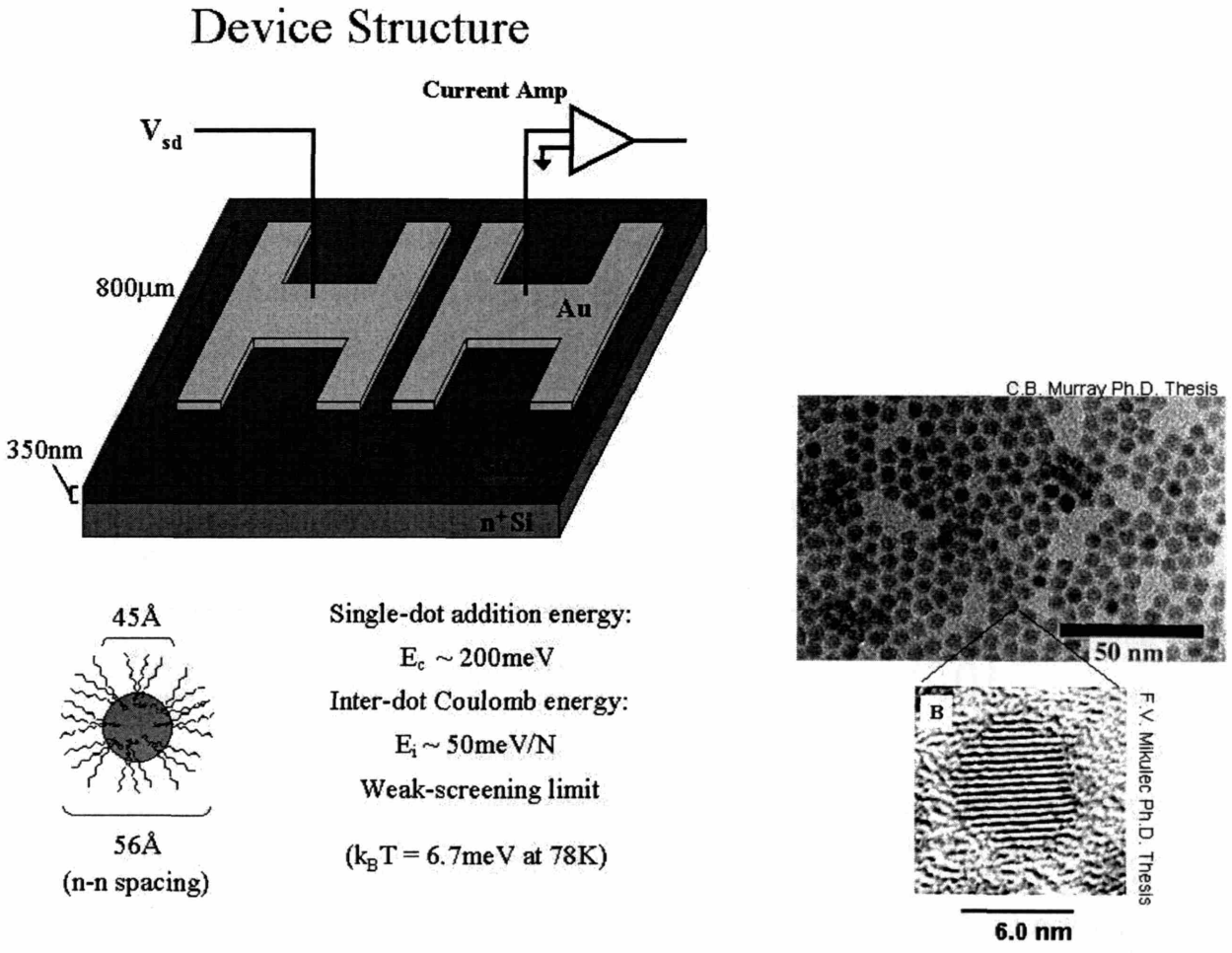

Figure 1-2: Experimental setup used for transport measurement in the films of QDAs. Reproduced with permission, courtesy N.Y. Morgan, Ref. [18]

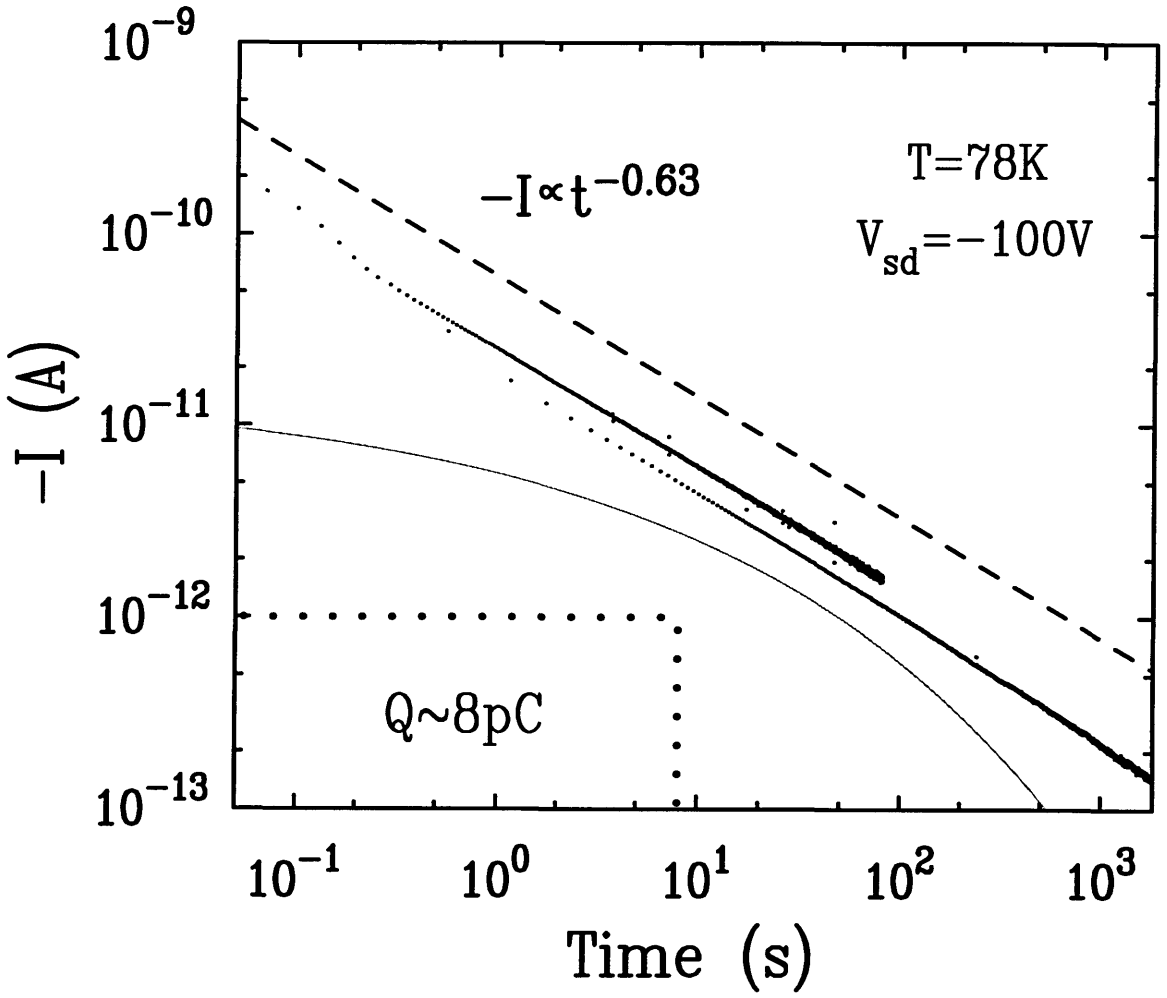

Figure 1-3: Typical current transient observed in [17, 18], with the estimated exponent $\alpha = 0.63$. The lower transient illustrates the memory effect: same exponent α but a lower amplitude I_0. The area in the lower left corner corresponds to the upper bound on the charge capacitively accumulated on the array. A stretched exponential (fine solid line) provides a very poor fit for the current.

1.2 Theoretical models of transport in disordered systems

In the previous Section transport measurements on the quantum dot arrays have been reviewed. We have seen that dot arrays are extremely resistive, with the ohmic conductivity being inobservably small. Also, in experiments [17, 18] both a non-universal power law decay in current and memory effects are observed.

Let us consider possible mechanisms of transport in dot arrays and the reasons of their very large resistance under experimental conditions [17, 18].

We can safely assume that at Nitrogen temperatures, transport in this system occurs by electron hops between the neighboring dots via quantum mechanical tunneling through potential barriers introduced by the capping layers. Energetics of the system suggests that this hopping is incoherent, and is assisted by some sort of relaxation mechanism, e.g. phonons.

An inobservably small ohmic conductivity under such conditions can be due to strong interdot potential barriers, as well as due to a possible phonon bottleneck for energy relaxation.

The effect of disorder in QDAs can play a significant role. Let us name several types of disorder that are present in dot arrays. First of all, the triangular lattice symmetry on the large scale is broken, as it is evident from Fig. 1-2. Second, there most probably is a strong randomness in the tunneling hopping amplitudes between the neighboring dots, since the barrier amplitude and thickness enter the tunneling amplitude in the exponential. Third, an offset charge can also contribute to the disorder.

Disordered electronic systems are characterized by unusual transport phenomena. Some of these, such as variable range *hopping conductivity* [25], are time independent, whether or not they involve electron-electron interactions [26]. However, when the many-body ground state is determined predominantly by electron-electron interactions, such as in the Coulomb glass, relaxation to the ground state can be slow; memory effects in conductivity have been attributed to this relaxation [27]. Another

situation in which the time dependence of the state of the sytem leads to time dependent transport is when the charge carriers distribute themselves among localized states as time progresses. This leads to a power-law time decay of the current after excitation with a light pulse, for example, and is called *dispersive transport* [28, 29, 30, 31].

In the present Section I will review standard theoretical models of transport in disordered systems, namely *hopping conductivity* (Sec. 1.2.1) and *dispersive transport* (Sec. 1.2.2).

1.2.1 Hopping conductivity

Hopping conductivity is a standard transport mechanism in doped semiconductors [25, 26]. In such systems electron wave functions are localized on donors that are randomly placed in a bulk semiconductor. Such localized electron states are assumed to be hydrogen-like. In the case of a small donor concentration, this assumption yields an exponentially small overlap between states on different impurity sites.

The Coulomb energy dominates ground state properties of a doped semiconductor, since in the absence of free carriers the Coulomb interaction is unscreened. In the ground state the configuration of electrons on the donors is determined by minimizing the sample's Coulomb energy.

Now let us ask, What happens if a small bias is applied across a sample. In this case, due to interactions with phonons, electrons can incoherently tunnel, or *hop*, on the unoccupied impurity sites. By calculating the hopping rates using the Golden Rule, one arrives at the random resistor network of Miller and Abrahams [32]. According to the latter, a sample can be represented by a set of resistors R_{ij} between the nodes $i, j, ...$ that correspond to the impurity sites. The resistances between these nodes are given by

$$R_{ij} = R_{ij}^0 \, e^{\xi_{ij}} \ . \tag{1.2}$$

The pre-exponential factor R_{ij}^0 in Eq. (1.2) is a slowly varying function of the distance

$\mathbf{r}_{ij}$ between the donor sites, and

$$\xi_{ij} = \frac{2r_{ij}}{r_0} + \frac{\epsilon_{ij}}{kT} \ . \tag{1.3}$$

In Eq. (1.3) r_0 is the scale on which the wave function of a localized state decays exponentially, and

$$\epsilon_{ij} = \tfrac{1}{2} \left(|\epsilon_i - \epsilon_j| + |\epsilon_i - \mu| + |\epsilon_j - \mu| \right) \ . \tag{1.4}$$

Here ϵ_i is the time-averaged electronic level energy of site i in the field of all other impurities and electrons, and μ is the chemical potential.

The resistance of the Miller-Abrahams network (1.2) can be estimated in the following cases.

• *High temperature regime*: In this case one discards the second term in Eq. (1.3) and calculates the resistance of the random network of bonds using the *percolation theory* (a review of which is given e.g. in Chapter 5 of the book [26]). According to the latter, the resistance of the strongly inhomogeneous sample is dominated by that of the *infinite cluster* penetrating through the sample,

$$R = R_0 e^{\xi_c} \ , \tag{1.5}$$

where ξ_c is related to the percolation threshold in a given spatial dimensionality.

• *Variable range hopping regime*: In this case the temperature T is so low that typical resistances between neighboring sites can become larger than those between certain remote sites whose energies happen to lie very close to the Fermi level. Hopping in this limit happens in a narrow band near the Fermi energy, provided that the density of states $\nu(\mu) \neq 0$, and, as shown by N.F. Mott in 1968, the sample resistance has a universal temperature dependence (Mott's Law) [25]:

$$R(T) \sim e^{(T_0/T)^{1/4}} \ . \tag{1.6}$$

Here

$$k_B T_0 \propto \frac{1}{\nu(\mu) r_0^3} \,. \tag{1.7}$$

• *Coulomb gap regime*: At yet lower temperatures the Coulomb correlations in the variable range hopping regime yield a vanishing density of states at a Fermi level [26], which in three dimensions

$$\nu \propto (\epsilon - \mu)^2 \,, \tag{1.8}$$

and in two dimensions

$$\nu \propto |\epsilon - \mu| \,. \tag{1.9}$$

This, according to Efros and Shklovskii [26], yields the steeper temperature dependence in the exponential:

$$R(T) \sim e^{(T_1/T)^{1/2}} \,. \tag{1.10}$$

Here

$$k_B T_1 \propto \frac{e^2}{\varepsilon r_0} \,, \tag{1.11}$$

where e is the electron charge and ε is the dielectric constant of the sample.

In all of the considered cases, hopping conductivity picture corresponds to an *ohmic* transport, with a self-averaging resistivity of the sample. Therefore this mechanism cannot describe an essentially *non-ohmic* transport observed in Refs. [17, 18].

1.2.2 Dispersive transport

Dispersive transport has been first observed in photocurrent measurements [33, 34] in amorphous materials (As_2Se_3, *a*-Se and others). In a typical experiment, a film of an amorphous material is sandwiched between the semi-transparent source and drain contacts that are held at a constant bias. A short light pulse photoexcites pairs of charged carriers on one surface of the film, and the source-drain voltage pulls charge carriers to the other side of the film resulting in a current $j_c(x,t)$, where $0 < x < L$,

with L being the film thickness. The resulting photocurrent

$$I(t) = \frac{1}{L}\int_0^L dx\, j_c(x,t) \tag{1.12}$$

is measured. It has been observed [33, 34] that the current (1.12) in this case *decays* as a power law of time,

$$I(t) \propto t^{-\alpha_1} \ . \tag{1.13}$$

The dispersive behavior (1.13) is in contrast to the normal (Markoffian) diffusion picture, in which $j_c(x,t)$ is the Gaussian packet of charge density that moves with a constant velocity. In this case the photocurrent (1.12) should be constant at $t \ll t_L$ and zero at $t \gg t_L$, where t_L is the *transit time* across the sample. Switching of the photocurrent from a constant to a zero value occurs around $t = t_L$ on the time scale that is determined by the variance of the Gaussian packet $j_c(x,t)$.

A phenomenological explanation of the transient photocurrent (1.13) has been proposed by Scher and Montroll [28] and others [29]. In these works it is assumed that (i) the diffusion of carriers in amorphous films can be described in the single particle picture, i.e. carriers do not interact with each other; (ii) such diffusion is modelled by a *continuous time random walk* on the one dimensional lattice. The key assumption of the models [28, 29] is that the time distribution of the hops between the neighboring sites has a *power law tail*

$$\phi(\tau) \sim \frac{a}{\tau^{1+\mu}} \ , \quad 0 < \mu < 1 \ . \tag{1.14}$$

The distribution (1.14) is an example of the *Lévy walk* [35]. Continuous time random walks of the Lévy form are thoroughly reviewed in the recent article by Bouchaud and Georges [36]. Below we show that in the dispersive transport model described above the current (1.12) has an asymptotic behavior (1.13).

We start from a slightly more general problem, introducing the notation that we will need later in Chapter 3. Consider a random walker at the origin at time $t = 0$ that makes hops to the right, $x \to x + l$, with a probability w, and to the left, $x \to x - l$,

with a probability $\bar{w} = 1 - w$. We assume that these hops happen at random times t_n, with the distribution of times between successive hops given by Eq. (1.14). In this case the probability distribution function $\mathcal{P}(x,t)$ of the random walker obeys the following *master equation*:

$$\mathcal{P}(x,t) = \int_0^t dt'\, \phi(t-t') \left\{ w\mathcal{P}(x-l,t') + \bar{w}\mathcal{P}(x+l,t') \right\} + \delta_{x,0} \left[\theta(t) - \int_0^t \phi(t')dt' \right] . \tag{1.15}$$

Here the first term in Eq. (1.15) governs the probability for a walker to be at a site x due to incoming hops from the site $x-l$ and outgoing hops to the site $x+l$, whereas the second term defines the initial condition, $x = 0$ during the time interval before the first hop has been made. Fourier transforming Eq. (1.15) we obtain

$$\mathcal{P}_{k,\omega} = \frac{i}{\omega + i0} \cdot \frac{1 - \phi(\omega)}{1 - \psi(k)\phi(\omega)} . \tag{1.16}$$

Here

$$\phi(\omega) = \int_0^\infty dt\, \phi(t) e^{i\omega t} = 1 - \frac{(-i\omega)^\mu}{A_\mu} , \tag{1.17}$$

where

$$A_\mu = \frac{\mu}{a\Gamma(1-\mu)} , \tag{1.18}$$

and

$$\psi(k) = we^{-ikl} + \bar{w}e^{ikl} \tag{1.19}$$

is the characteristic function for a single hop.

Eq. (1.16) is an expression for the *anomalous diffusion* propagator. It can be easily generalized both to the case of a continuous medium and multiple dimensions. Now let us focus on the specific case considered by Scher and Montroll [28].

In the works [28, 29] it is assumed that at $t = 0$ all carriers are located at $x = 0$ (corresponding to photoexciting a layer much thinner than the film's thickness L), and the hops are *unidirectional*, $w = 1$, since the pulling voltage across the sample is large. In this case

$$\psi(k) = e^{-ikl} . \tag{1.20}$$

The probability distribution function $\mathcal{P}(x,t)$ given by the inverse Fourier transform of $\mathcal{P}_{k,\omega}$ is determined by the pole of the expression (1.16),

$$k \sim \omega^{\mu} \ . \tag{1.21}$$

We are interested in how the position $\bar{x}$ of an "average carrier" of the packet propagates with time. For that one could use an estimate

$$\bar{x} \sim t^{\mu} \ , \tag{1.22}$$

that follows from Eq. (1.21). The current (1.12) is proportional to the *velocity* of the average carrier [28],

$$I(t) \propto \frac{d\bar{x}}{dt} \sim t^{-(1-\mu)} \ . \tag{1.23}$$

Therefore we obtain the power law (1.13) for the photocurrent with the exponent

$$\alpha_1 = 1 - \mu \ . \tag{1.24}$$

In the work [28] it has been also derived that the dispersive transport regime switches at the *transit time* $t = t_L$, when the average carrier hits the other end of the film:

$$\bar{x}(t_L) = L \ . \tag{1.25}$$

In this case the boundary condition at $x = L$ results in a steeper power law,

$$I(t) \propto t^{-\alpha_2} \ , \tag{1.26}$$

where

$$\alpha_2 = 1 + \mu \ . \tag{1.27}$$

The prediction of the Scher-Montroll model

$$\alpha_1 + \alpha_2 \equiv 2 \tag{1.28}$$

has been validated in a variety of amorphous materials [33, 34, 37]. The class of stochastic processes governed by the propagator (1.16) with the long tail in the hopping distribution (1.14) is called *anomalous diffusion.*

Let us now discuss the microscopic origin of the power law tail in the distribution (1.14). Continuous time random walks with power law distributions (1.14) generally arise when the system's dynamics is determined by a broad distribution of time scales. In the case of dispersive transport, these are the *trap escape times* in amorphous solids.

Consider a simple trap model [29, 30], in which the escape time depends on energy ϵ via an activation exponential,

$$\tau = \tau_0 \, e^{\beta\epsilon} \; . \tag{1.29}$$

In such a system, the density of states of a form

$$\nu(\epsilon) = \nu_0 e^{-b\epsilon} \tag{1.30}$$

yields the hopping time distribution of the form (1.14) with

$$\mu = \frac{b}{\beta} \tag{1.31}$$

and

$$a = \frac{\nu_0 \, \tau_0^{\mu}}{\beta} \; . \tag{1.32}$$

The latter model appears to be generally valid for amorphous materials, and it has been used to determine their spectral properties from transport measurements [29, 37].

Finally, let us discuss the dispersive transport mechanism in the context of the power law current decay (3.1) observed in the CdSe quantum dot arrays [17, 18].

Naively, one could notice a strong analogy between the power law decay of the photocurrent in amorphous solids, and current in the QDAs. However, such analogy is superficial, since the experimental conditions for these two classes of phenomena are in fact very different. In the photocurrent measurements, the amount of photoexcited charge is *finite.* Therefore the current decays with time as the carriers are absorbed by the drain electrode. In the QDA transport measurement setup used in [17, 18], charge

carriers (holes) are *constantly injected* from the source. When such a permanent supply of carriers is used in conductivity measurements in amorphous solids, the resultant current in fact *grows* with time [38, 39] when a constant bias is applied. This is explained by gradually *filling in* of the traps and smoothing the trapping potential for the carriers, effectively reducing the sample "resistance" with time.

To conclude this subsection, we have reviewed the dispersive transport model of Scher and Montroll and showed that it does not provide a satisfactory explanation for the transport measurements [17, 18] in the quantum dot arrays.

1.2.3 Disscussion

As we have demonstrated above, conventional transport scenarios in disordered systems fail to explain the transport measurements reviewed in Sec. 1.1.3. The hopping conductivity picture yields an ohmic sample resistance, whereas the dispersive transport yields a power law decay in current under very different assumptions.

In the present thesis in Chapter 3 below we propose a *novel non-ohmic transport model* [2] that bears a certain similarity to the dispersive transport picture reviewed above. In particular, our model is also based on the Lévy statistics. In contrast to the Scher-Montroll mechanism, our model does not rely on time-varying sample properties (such as filling in of the traps in amorphous solids). In Chapter 3 we show that it is possible that the system can remain *truly stationary*, but nonetheless exhibit a transient response. Our model leads to a specific prediction about the *noise spectrum* of the system. In Chapter 3 we present measurements on CdSe QDAs that give results consistent with our predictions.

Meanwhile, in the following Chapter 2 we will focus on the charge ordering in the ground state of a perfect triangular array of dots.

Chapter 2

Ground State

...we can see how the whole
becomes not only more than
but very different
from the sum of its parts
P. W. Anderson,
"More is Different"

In the present Chapter we study charge ordering and equilibrium hopping dynamics of electrons in a nanoparticle array [1]. Our major finding will be a *collective behavior* of essentially *classical electrons* in a large system due to an interplay between the geometric frustration of the array and Coulomb interactions.

For simplicity, in this Chapter we view the nanocrystal array as a regular two dimensional triangular lattice, where sites correspond to individual dots, like the ones shown in Fig. 1-1. The assumption we make by idealizing the lattice is valid at least locally, since the dot arrays maintain a local orientational order. In general, for a large enough sample, the long range orientational order is broken. Our assumption can be justified by noting that due to large tunneling barriers between the dots, electron hopping dynamics in the real system is dominated by charges hopping onto the neighboring sites. In this case it is the local coordination (the number of nearest neighbors) that matters most, and it is preserved in the real system.

Another major assumption that we make through the entire Chapter is that we

are not allowing multiple occupancy for a lattice site. Since the Coulomb energy of adding a second electron to the dot is much larger than both the interaction energy between charges on neighboring dots and the temperature, this assumption is also justified.

Below we study charge ordering on a triangular lattice by making a connection to earlier studied frustrated spin problems. A novelty of our system is in its long range Coulomb interaction between electrons on the dots, in contrast to a typically short range exchange interaction between spins in spin models. We show that a number of phases arises due to an interplay between frustration in a triangular array geometry and the long-range character of the interaction.

In particular, we identify a novel *correlated fluid phase* that exists in a range of densities and at not too low temperatures. Ordering in this phase is described in terms of a height field variable and unbound dislocations that are the topological defects of the height field.

We demonstrate a relation between the dynamical response (zero bias conductivity) and ordering in the charged system. At low temperature the system freezes into a commensurate, or *solid* phase. We explicitly study this freezing for a set of simplest densities. We show that at the densities $n = 1/3,\ 2/3$ and $n = 1/2$, freezing occurs via a first order phase transition.

The outline of the present Chapter is as follows.

In Section 2.1 we introduce the main means of studying ordering and dynamics, namely the Monte-Carlo model of charges hopping on the neighboring sites of a triangular lattice. We construct the spin-charge mapping, write the Hamiltonian and introduce the Boltzmann hopping dynamics for the system, as well as define a zero bias conductivity.

In Section 2.2 we draw the phase diagram for the system as well as describe its charge ordering in various phases. To describe charge ordering we introduce the height field order parameter. It is shown that a description in terms of the height field is valid when the temperature is of the order of or below the nearest neighbor interactions. We discuss the topological defects of the height field that are present

in the system at intermediate temperature. Fluctuations of the height variable are studied by means of a phenomenological continual model. The effective rigidity of the height surface is calculated from the stochastic dynamics. Rigidity is found to be smaller than its upper bound derived from the phenomenological model by means of scaling arguments. This rules out a possibility of the Berezinskii – Kosterlitz – Thouless defect binding phase transition in the correlated fluid phase. In this section we also relate equilibrium height field fluctuations to the charge dynamics. The corrections to conductivity and compressibility of the charge system are found to be local everywhere in the correlated fluid phase.

Finally, in Section 2.3 we study freezing into commensurate states at charge densities $n = 1/3, 2/3$ and $n = 1/2$. We employ both the symmetry arguments and the stochastic dynamics to determine the order of the freezing phase transitions. For the type B dynamics the derivative of the transport coefficient with respect to temperature has the same singularity as the heat capacitance, $(T - T_c)^{-\alpha}$ [42]. Hence we expect the conductivity to behave similarly to the average energy near the freezing phase transition. Such similarity is discussed in the end of Section 2.3.

2.1 Monte-Carlo model of charge dynamics

The aim of the present Section is to introduce a hopping dynamics of charges on the two dimensional triangular lattice. We model the system as a set of classical charges that incoherently hop on the neighboring sites according to the Boltzmann dynamics.

In Section 2.1.1 we make a connection between the charge problem and a classical Ising problem with long range antiferromagnetic interactions. We also outline novel experimental and theoretical issues of the charge ordering problem compared to the spin problems.

In Section 2.1.2 a model Hamiltonian is introduced for the system of electrons on the quantum dot array. After that we describe the stochastic dynamics and provide a mapping between the charge and spin problems.

Charge ordering at different temperatures is studied in Section 2.1.3 using the dependence of density on temperature at a fixed gate voltage (cooling curves).

Finally, in Section 2.1.4 we consider the zero bias dc conductivity as a function of temperature and electron density. The calculated conductivity agrees with the classical limit of the fluctuation - dissipation theorem. We use conductivity to characterize different domains in the phase diagram and to identify transitions between them.

2.1.1 Charge and Spin Problems

Theoretical analysis of the charge problem can benefit from making connection to the better studied Ising spin problems. In the situation when charging energy enforces single or zero occupancy of all dots, one can interpret occupied dots as an 'up spin' and unoccupied dots as a 'down spin.' This provides a mapping between the problem of charge ordering on a triangular lattice of quantum dots and spin ordering on a triangular lattice. Since the like charges repel, the corresponding spin interaction is of an antiferromagnetic kind. The charge density plays a role of a spin density, and the gate voltage corresponds to external magnetic field, as summarized in Table 2.1. Besides, one can map the offset charge disorder (random potentials on the dots) onto the random magnetic field in the spin problem.

There are, however, both theoretical and experimental aspects of the charge - spin mapping that make the two problems not entirely equivalent. First, charge conservation in the problem of electrons hopping on a dot array implies the total spin conservation in the corresponding spin problem. This leads to an additional constraint, namely forbidding single spin flips. Microscopically, spin conservation requires the Kawasaki (or type B) dynamics [40] as opposed to the nonconserving Glauber (or type A) dynamics [41]. This makes no difference with regard to the thermodynamic state at equilibrium, since the system with the conserved total spin is statistically equivalent to the grand canonical ensemble. However, order parameter conservation manifests itself both in a slower dynamics [42] and in collective transport properties of the correlated fluid phase discussed below.

Another important difference between the charge and spin problems is the form of interaction. Majority of spin systems are described in terms of nearest neighbor exchange couplings. In particular, the relevant spin problem for us here is the triangular Ising antiferromagnet ($\triangle$IAFM), which was exactly solved in zero field [43]. It was found that there is no ordering phase transition in this case at any finite temperature. In the charge problem presented here the long range Coulomb interaction makes the phase diagram more rich. We find phase transitions at finite temperature for certain charge filling densities.

Let us also summarize novel *experimental* issues of the charge ordering problem compared to spin problems:

• Transport measurements in a charge system is a novel means of studying both equilibrium and nonequilibrium properties. Spin systems are usually studied by

Table 2.1: Charge-spin mapping

Charge model	Spin model
$q = 1$	$s = \uparrow$
$q = 0$	$s = \downarrow$
V_{ij}	J_{ij}, AF sign
V_{gate}	H_{ext}

means of thermodynamic measurements. In the present Chapter we utilize and numerically confirm the similarity [42] in critical behavior of the conductivity and of the average energy. In Section 2.3 below we use both dynamic and thermodynamic quantities to investigate the phase diagram.

• As shown in Chapter 1, the quantum dot array is potentially a more complex system if one considers a variety of other factors that we have left behind in the present Chapter, namely randomness in interdot couplings and the offset charge, time fluctuations of the above leading to the $1/f$ noise, effects of the environment, and so forth.

2.1.2 The model

The Hamiltonian $\mathcal{H}_{\rm el}$ of the electrons on the quantum dots describes the Coulomb interaction between charges q_i on the dots and coupling to the background disorder potential $\phi(\mathbf{r})$ and to the gate potential $V_{\rm g}$:

$$\mathcal{H}_{\rm el} = \frac{1}{2}\sum_{i,j} V(\mathbf{r}_{ij}) q_i q_j + \sum_{\mathbf{r}_i} (V_{\rm g} + \phi(\mathbf{r}_i)) q_i \ . \tag{2.1}$$

The position vectors $\mathbf{r}_i$ run over a triangular lattice with the lattice constant a, and $\mathbf{r}_{ij} = \mathbf{r}_i - \mathbf{r}_j$. The interaction V accounts for screening by the gate:

$$V(\mathbf{r}_{ij} \neq 0) = \left(\frac{q_i q_j}{\epsilon |\mathbf{r}_{ij}|} - \frac{q_i q_j}{\epsilon \sqrt{(\mathbf{r}_{ij})^2 + d^2}} \right) e^{-\gamma |\mathbf{r}_{ij}|} \ . \tag{2.2}$$

Here ϵ is the dielectric constant of the substrate, and $d/2$ is the distance to the gate plate. The single dot charging energy $\frac{1}{2}V(0) = e^2/2C$ is assumed to be high enough to inhibit multiple occupancy, i.e. $q_i = 0, 1$.

The exponential factor in (2.2) is introduced for convenience, to control convergence of the sum in (2.1). Below we use $\gamma^{-1} = 2d$. In the case of spatially varying ϵ the interactions can be more complicated. If the array of dots is placed over a semiconductor substrate, one has to replace ϵ by $(\epsilon + 1)/2$ in the Eq. (2.2).

In a real system electron tunneling occurs mainly between neighboring dots. The

tunneling is incoherent, i.e. assisted by some energy relaxation mechanism, such as phonons. Since the tunneling coupling of the dots is weak we focus on charge states and ignore effects of electron spin, such as exchange, spin ordering, etc.

Our approach in the present Chapter is based on the stochastic Monte-Carlo (MC) dynamics. The states undergoing the MC dynamics are charge configurations with $q_i = 0, 1$ on a $N \times N$ patch of a triangular array. Periodic boundary conditions are imposed by the Hamiltonian (2.1) using the $N \times N$ charge configurations extended periodically in the entire plane. Periodicity in the MC dynamics is respected by allowing charges to hop across the boundary, so that the charges disappearing on one side of the patch reappear on the opposite side.

Charge conservation gives additional constraint, $\sum q_i = \text{const}$. The presence of such a conservational constraint slows down the dynamics yet it is irrelevant for the statistical equilibrium properties. Thus when studying ordering we extensively use the nonconserving A dynamics, where the natural parameter to control is the gate voltage $V_{\rm g}$, whereas the charge conserving B dynamics is used to investigate conductivity at fixed charge filling density,

$$n = \frac{1}{N^2} \sum_{i=1}^{N^2} q_i \ . \tag{2.3}$$

The classical Boltzmann ($k_B \equiv 1$) stochastic dynamics is defined differently for the A and B cases. In the A case, the occupancy of a randomly selected site i is changed or preserved with the probabilities W_i and $\overline{W}_i$ respectively:

$$\mathbf{A}: \qquad W_i/\overline{W}_i = e^{-2\Phi_i/T_{\rm el}} \ , \quad W_i + \overline{W}_i = 1 \ . \tag{2.4}$$

This happens during a single MC "time" step. Here

$$\Phi_i = \sum_{r_j \neq r_i} V(\mathbf{r}_{ij}) q_j + V_{\rm g} + \phi(\mathbf{r}_i) \ , \tag{2.5}$$

and $T_{\rm el}$ is the temperature in the charge model.

In the B case, we first randomly select the site i. At each MC "time" step, we attempt to exchange the occupancies q_i and $q_{i'}$ of a site i and of a randomly chosen

site i' neighboring to i. MC trials continue until $q_j \neq q_i$ for a particular $j = i'$. Then the occupancies of the sites i and j exchange with probability $W_{i\to j}$, and remain unchanged with probability $W_{i\to i}$:

$$\mathbf{B}: \; W_{i\to j}/W_{i\to i} = e^{(\Phi_i - \Phi_j)/T_{\rm el}} \; , \quad W_{i\to j} + W_{i\to i} = 1 \; . \tag{2.6}$$

The model (2.1,2.2,2.4,2.6) possesses an electron-hole symmetry. To make it manifest, it is convenient to introduce a "spin" variable (in accord with charge-spin mapping described above in Sec. 2.1.1),

$$s_i = 2q_i - 1 = \pm 1 \; , \tag{2.7}$$

and to replace (2.1) by an equivalent spin Hamiltonian

$$\mathcal{H}_{\rm s} = \frac{1}{2}\sum_{i,j} V(\mathbf{r}_{ij}) s_i s_j + \sum_{\mathbf{r}_i} (\mu + 2\phi(\mathbf{r}_i)) s_i \; . \tag{2.8}$$

Eqs. (2.7) and (2.8) map the charge system with charges q_i onto the spin system with long range interactions (2.2). The sign of the coupling (2.2) is positive, which coincides with the sign of the antiferromagnetic nearest neighbor coupling. To preserve the form of interaction in (2.8), we rescale the temperature, defining the "spin" temperature

$$T = 4\, T_{\rm el} \; , \tag{2.9}$$

and introduce the chemical potential

$$\mu = 2V_{\rm g} + V_{\mathbf{k}=0} \; , \tag{2.10}$$

representing external field for spins s_i. Here $V_{\mathbf{k}}$ the Fourier transform of the interaction (2.2). In terms of spin variables the charge density (2.3) is given by

$$n = \frac{1}{2}\left(1 + \frac{1}{N^2}\sum s_i\right) \; . \tag{2.11}$$

In our discussions below, unless explicitly stated, we consider a system without disorder, $\phi(\mathbf{r}) = 0$. The distance to the gate which controls the range of the interaction (2.2) is chosen to be $0 \leq d/2 \leq 5a$, whereas the limit $d \ll a$ corresponds to the $\triangle$IAFM problem [43, 44, 45] with nearest neighbor interaction. The temperature T is measured in units of the nearest neighbor coupling $V(a)$. To reach an equilibrium at low temperatures, we take the usual precautions by running the MC dynamics first at some high temperature, and then gradually decreasing the temperature to the desired value.

2.1.3 Ordering at fixed gate voltage

Using the type A dynamics algorithm described above, we study $T \to 0$ ordering at fixed chemical potential μ. Cooling curves show the temperature dependence of electron density $n(T)$ for $d = 2a$ (Fig. 2-1), and for the $\triangle$IAFM problem realized at $d \ll a$ (Fig. 2-2). Due to electron-hole symmetry $n \leftrightarrow 1 - n$, it is enough to consider only the region $0 \leq n \leq 1/2$. There is a qualitative similarity between the two plots, both in the character of cooling curves (slowly varying at large T, followed by a strong fluctuations region before finally converging to the zero temperature density), and in the cooling features for the densities $n = 0$ and $n = 1/3, 2/3$.

However, the long range interacting case shows some additional features. The most obvious one is that values of n at $T \to 0$ form an infinite set, n being a continuous function of V_g. Contrarily, for the $\triangle$IAFM case $n(V_g)$ discontinuously jumps between its four allowed values, $n(T \to 0) = \{0,\ 1/3,\ 2/3,\ 1\}$. The latter correspond to the incompressible states (plateaus in $n(V_g)$).

Features that are typical in the long range case and are absent in the $\triangle$IAFM also include ordering at other simple fractions, such as $n = 1/2$, which is an attractor for the family of curves at small μ (curves are shown for the values of $\mu = 0.05,\ 0.1,\ 0.2,\ 0.3$). Ordering into $n = 1/2$ incompressible phase is weaker than into $n = 1/3$ and $n = 2/3$, since it is controlled by the next-to-nearest neighbor interactions. Ordering at simple fraction phases like $n = 1/4$, though not pronounced in cooling curves, manifests itself in the conductivity features discussed below. All

such orderings correspond to certain types of freezing phase transitions which we study in Section 2.3 for the cases of $n = 1/3,\ 2/3$, and $n = 1/2$. We also notice that in the system with long-range interactions freezing occurs into a number of intermediate densities, and in general depends on the cooling history, especially near incompressible densities.

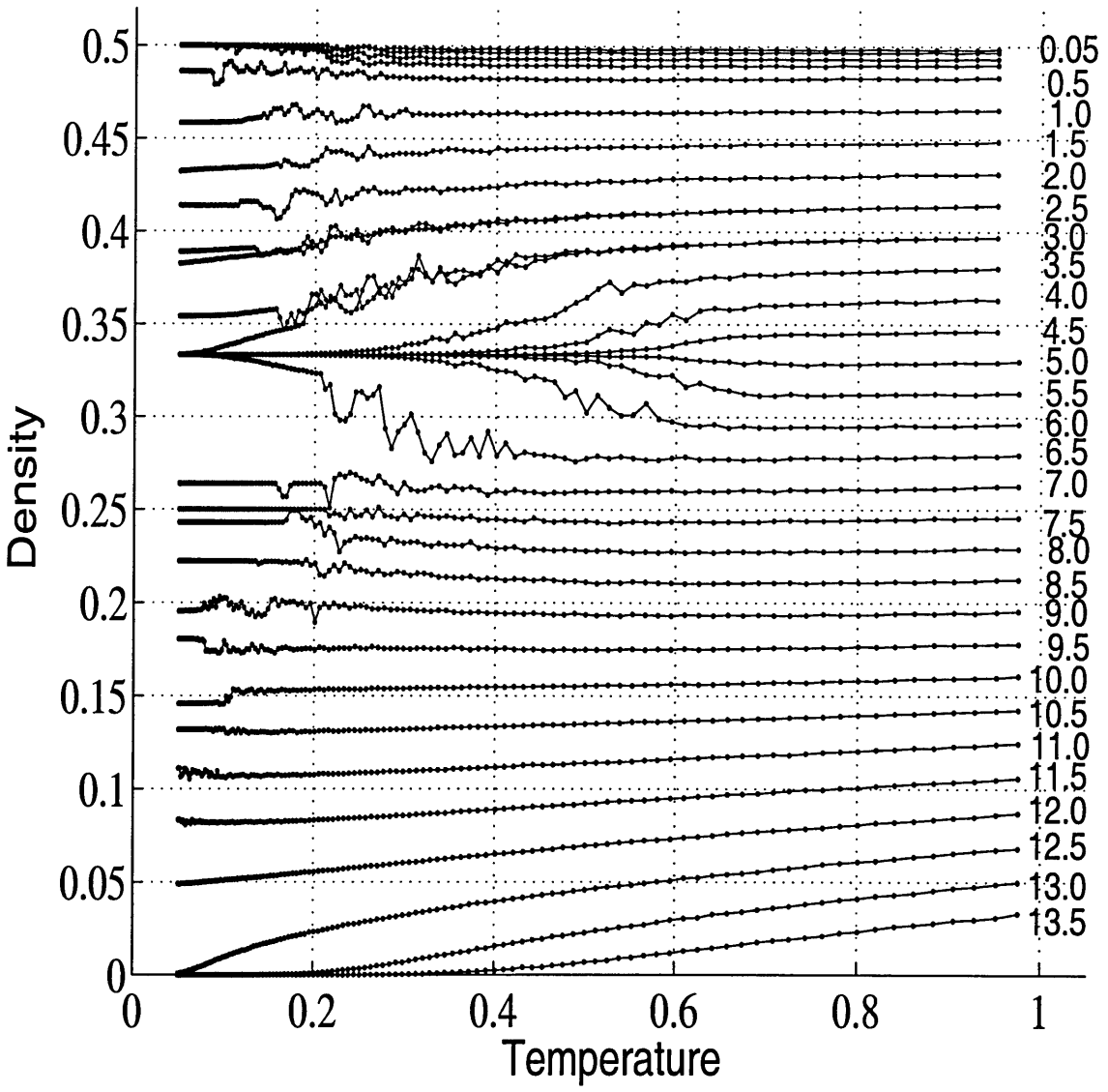

Figure 2-1: Cooling curves for $d = 2a$. Due to the electron - hole symmetry, only the density domain $0 \leq n \leq 1/2$ is shown. The values of μ are given to the right of the curves. Not shown are values of $\mu = 0.1, 0.2, 0.3$ for the curves converging to the density $n = 1/2$

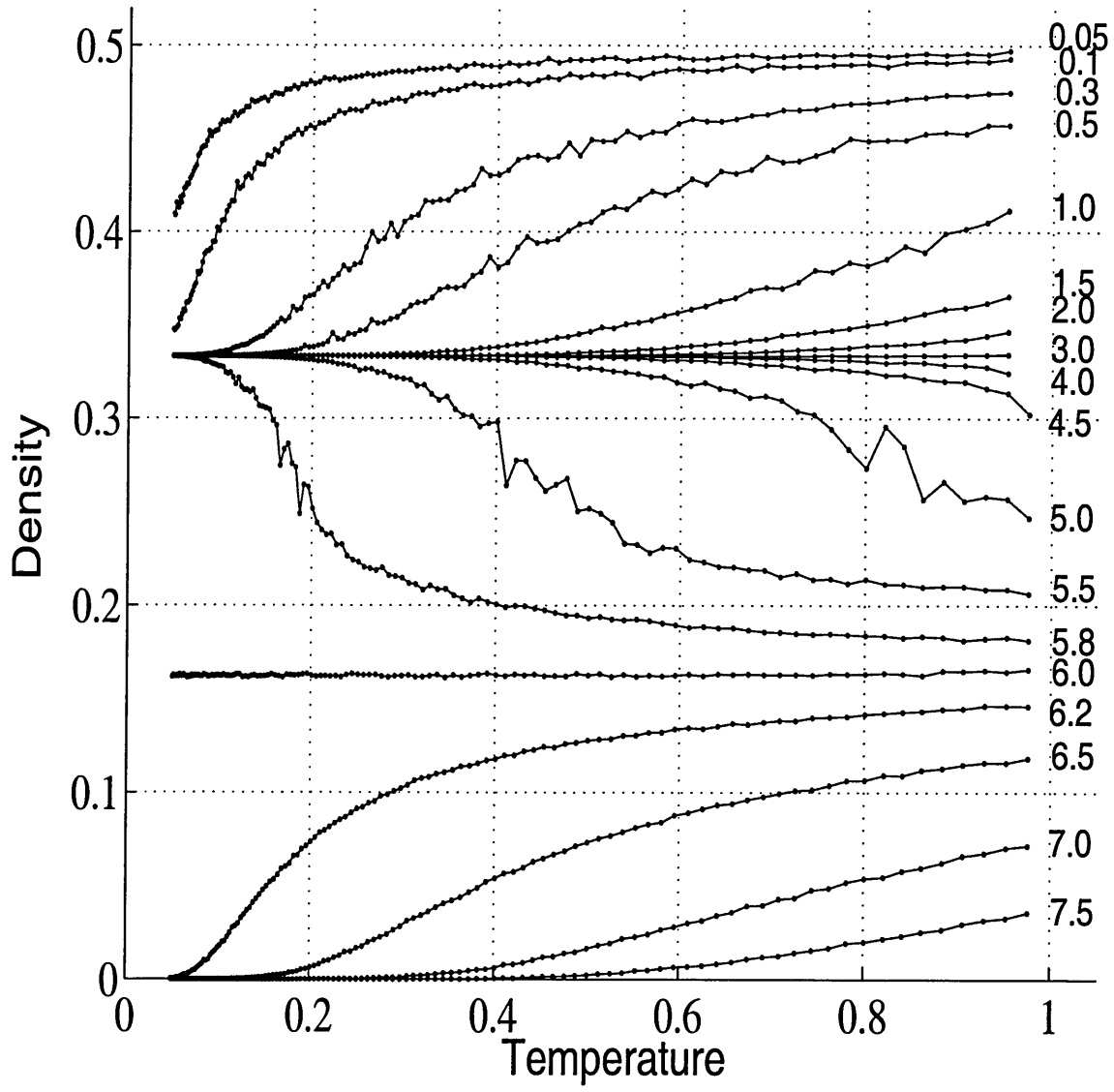

Figure 2-2: Cooling curves for $d \ll 1$ (pure $\triangle$IAFM case). The values of μ are given to the right of the curves

2.1.4 Conductivity

We focus on the conductivity of the charge system because of the two reasons. First, this quantity is experimentally accessible in the dot arrays [16, 17]. As we have mentioned in Chapter 1, currently dot arrays are extremely resistive and the zero bias conductivity is unmeasurably large. One could expect, however, to have novel dot coatings that could reduce interdot tunneling barriers and make the conductivity at low bias possible to measure. Secondly, as we shall see below, zero bias dc conductivity as a function of density and temperature distinguishes between different phases of the system.

In the present Chapter we consider electron hopping conductivity in presence of a small external electric field. Electron hops in a real system are realized by inelastic tunneling assisted by some energy relaxation mechanism, such as phonons. The latter adds a (non-universal) power law temperature dependence to the total conductivity

$$\sigma_{\text{total}} = \sigma(T)\, T^{\alpha} \,. \tag{2.12}$$

In this Chapter we assume for simplicity that the energy relaxation mechanism is such that $\alpha = 0$. A generalization of this model to arbitrary α presents no problem.

The conductivity temperature dependence $\sigma(T)$ for several densities is shown in Fig. 2-3. The MC simulation is made on a 18×18 patch using the conserving dynamics (type B). The external electric field $\mathbf{E}$ is applied along the patch side. The field is chosen to be large enough to induce current exceeding the equilibrium current fluctuations, and yet sufficiently small to ensure the linear response

$$\mathbf{j} = \sigma \mathbf{E} \,. \tag{2.13}$$

The linearity holds if the external field is much smaller than both temperature and the next-to-nearest neighbor interaction strength. In our numerics we use the field

values E such that

$$Ea \sim (1-5) \cdot 10^{-2} V(a) \ll \min\{V(\sqrt{3}a), T\} \ . \tag{2.14}$$

The conductivity σ is obtained from (2.13). During stochastic dynamics of type B described in subsection 2.1.2, the potential difference between the adjacent sites is calculated as

$$\Phi_j - \Phi_i = (s_j - s_i)\ \mathbf{Ea} \ . \tag{2.15}$$

Here the charge carried during a single hop is $s_j - s_i = \delta s = \pm 2$ since electrons and holes in our model carry the "charges" $s_i = \pm 1$, and $\mathbf{a}$ is a vector along the direction of the hop, $|\mathbf{a}| = a$. In the present Chapter we employ the field $\mathbf{E}$ along the height of the elementary lattice triangle, so that $|\mathbf{Ea}| = Ea\cos\frac{\pi}{6}$. The current density is calculated as

$$j = |\delta s|\ a\cos\frac{\pi}{6} \cdot \frac{\mathcal{N}_+ - \mathcal{N}_-}{\mathcal{N}} \ , \tag{2.16}$$

where $\mathcal{N}_\pm$ is the number of hops along (against) the direction of $\mathbf{E}$, and $\mathcal{N}$ is the total number of MC trials at each temperature step.

As seen from Fig. 2-3, there are three temperature regions for the conductivity σ. These regions correspond to different phases of the system that are described in the following Section and depicted there in Fig. 2-6.

The high temperature *disordered* phase conducts via spatially and timely uncorrelated hops of individual electrons. Conductivity in this phase can be evaluated analytically, see Eq. (2.18) below.

At $T \to 0$ the system freezes into its ground state configuration, and the conductivity vanishes (*solid* phase). Both the ground state configuration and the freezing temperature T_n depend on the density n. Near rational n the ground state is commensurate. At temperatures below freezing, $T < T_n$, conductivity is zero. The behavior of $\sigma(T)$ near freezing temperature is singular (Fig. 2-3). Singularities near rational n are also present in the conductivity dependence on the density, $\sigma(n)$. They are indicated by arrows in Fig. 2-4.

Finally, for any density $1/3 \leq n \leq 2/3$ there is an intermediate temperature region, where the conductivity is finite and has a collective character (*correlated fluid* phase). Below in Section 2.2 we study the correlated fluid properties using the height field order parameter approach.

An independent consistency check for the validity of our MC dynamics can be provided by the fluctuation-dissipation theorem. This theorem [46] relates current fluctuations with conductivity:

$$\int dt \, \langle j_\mu(t) j_\nu(0) \rangle = 2\sigma_{\mu\nu} T \; . \tag{2.17}$$

We find that our simulations are in accord with (2.17) in all temperature regions. In the correlated phase we explicitly evaluate the integral in the right hand side of (2.17) by numerically averaging in τ and t the product $j_\mu(t+\tau) j_\nu(t)$, and compare the result with the conductivity obtained directly from Eqs. (2.13,2.16) to make sure that the system is indeed at equilibrium.

At large temperature $T \gg V(a)$, one can evaluate the left hand side of (2.17) explicitly and find the universal high temperature asymptotic behavior of the conductivity,

$$\sigma = a^2 \, \frac{n(1-n)}{T} \; . \tag{2.18}$$

To obtain (2.18) we note that for a high enough temperature the current is delta-correlated in time,

$$\langle j_\mu(t) j_\nu(0) \rangle = \left\langle j^2 \right\rangle \, \delta_{\mu\nu} \, \delta(t) \; . \tag{2.19}$$

The amplitude

$$\left\langle j^2 \right\rangle = \frac{4}{6} \cdot 2n(1-n) \cdot (\delta s)^2 \cdot \left(a \cos \frac{\pi}{6} \right)^2 \cdot w \tag{2.20}$$

does not depend on temperature since the hops are equally probable, $W_{i \to j} = W_{i \to i} \equiv w = 1/2$ at $T \gg V(a)$. Since the field $\mathbf{E}$ is aligned along the height of the elementary lattice triangle, only four out of possible six bond directions contribute to conductivity. Each bond is selected with a probability $2n(1-n)$ of choosing the electron and the adjacent hole. The conductivity tensor is isotropic, $\sigma_{\mu\nu} = \sigma \, \delta_{\mu\nu}$. One can

explicitly check this by doing a similar high temperature calculation with the field $\mathbf{E}$ along any other direction. Fig. 2-3 shows that the results of our MC dynamics are consistent with the universal conductivity behavior (2.18), where we set $a = 1$.

The change in conductivity character while cooling down from the disordered into the correlated and solid phases can also be seen in Fig. 2-4. Here we plot the product $\sigma \cdot T$ as a function of the electron density n for several temperatures. We show the results only for the interval $0 \leq n \leq 1/2$ utilizing the electron-hole symmetry. The screening length was taken to be $d = 2a$. The high temperature curve is clearly consistent with the $n(1-n)$ dependence (2.18). The low temperature curves show that conductivity vanishes at a number of densities that are simple fractions $(n = 1/4, 1/3, 1/2)$. This indicates freezing of the system into a commensurate state at these values of n. The commensurate state at $n = 1/3$ is shown in Fig. 2-5 (A). Below in Section 2.3 we consider the freezing phase transitions at $n = 1/3,\ 2/3$ and $n = 1/2$.

At densities near these simple fractions, the system conducts via hops of excess electrons or holes moving in the frozen crystalline background. Such a situation is shown in Fig. 2-5 (B), for the case of $n = 1/3+\epsilon$. Since the conductivity is proportional to the excess charge density, $\sigma(n)$ in Fig. 2-4 has cusps near incompressible densities (simple fractions $n = 1/4,\ 1/3,\ 1/2$).

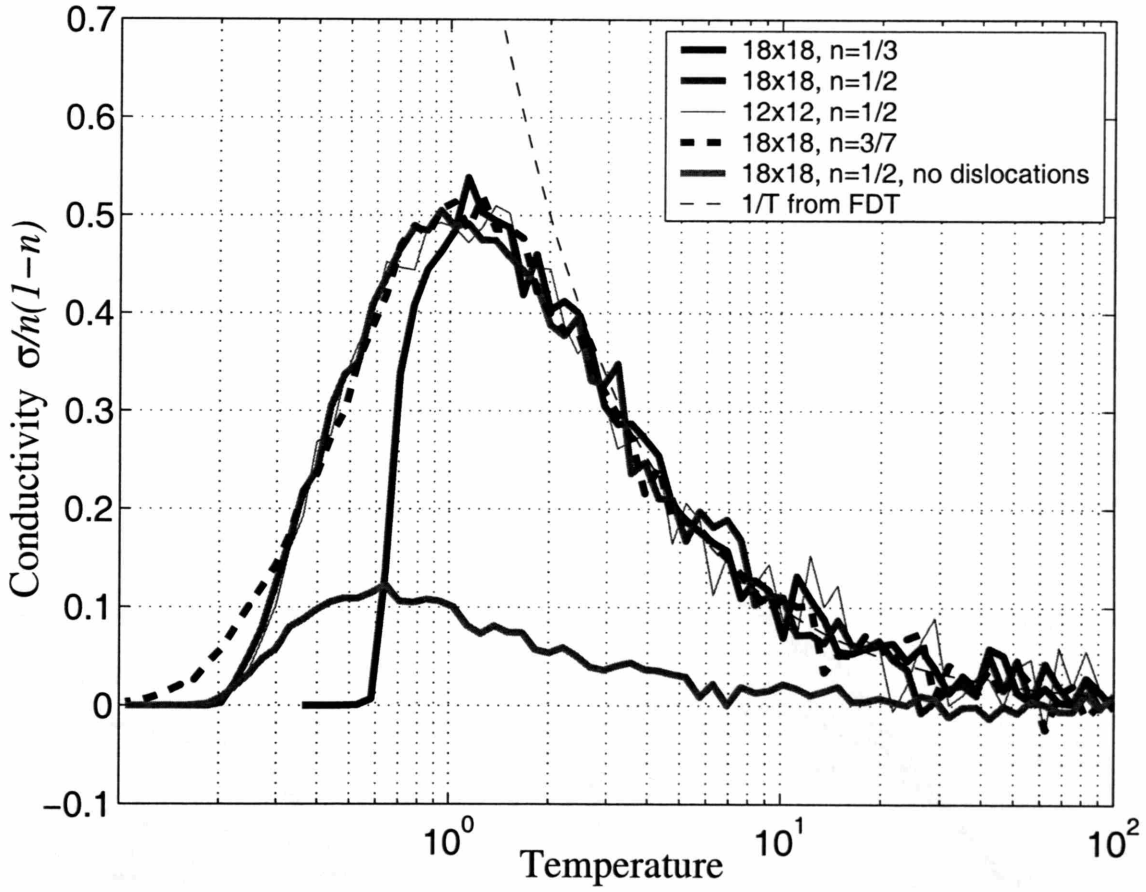

Figure 2-3: Temperature dependence of the zero bias dc conductivity $\sigma(T)$. Shown are the curves $\sigma/n(1-n)$ for $n = 1/3$, $n = 1/2$, and for a typical intermediate density (taken here $n = 3/7$), calculated for the $N = 18$ patch with the screening length $d = 2a$. Dashed line indicates the asymptotic large temperature behavior (2.18). Dotted line corresponding to $N = 12$ patch for the density $n = 1/2$ shows that finite size effects are negligible. The correlated conductivity part for $n = 1/2$ (lower curve), for which the hops that create dislocation pairs are forbidden (Section 2.2), is a small fraction of the total conductivity at large T, and becomes important at $T \sim V(\sqrt{3}a)$.

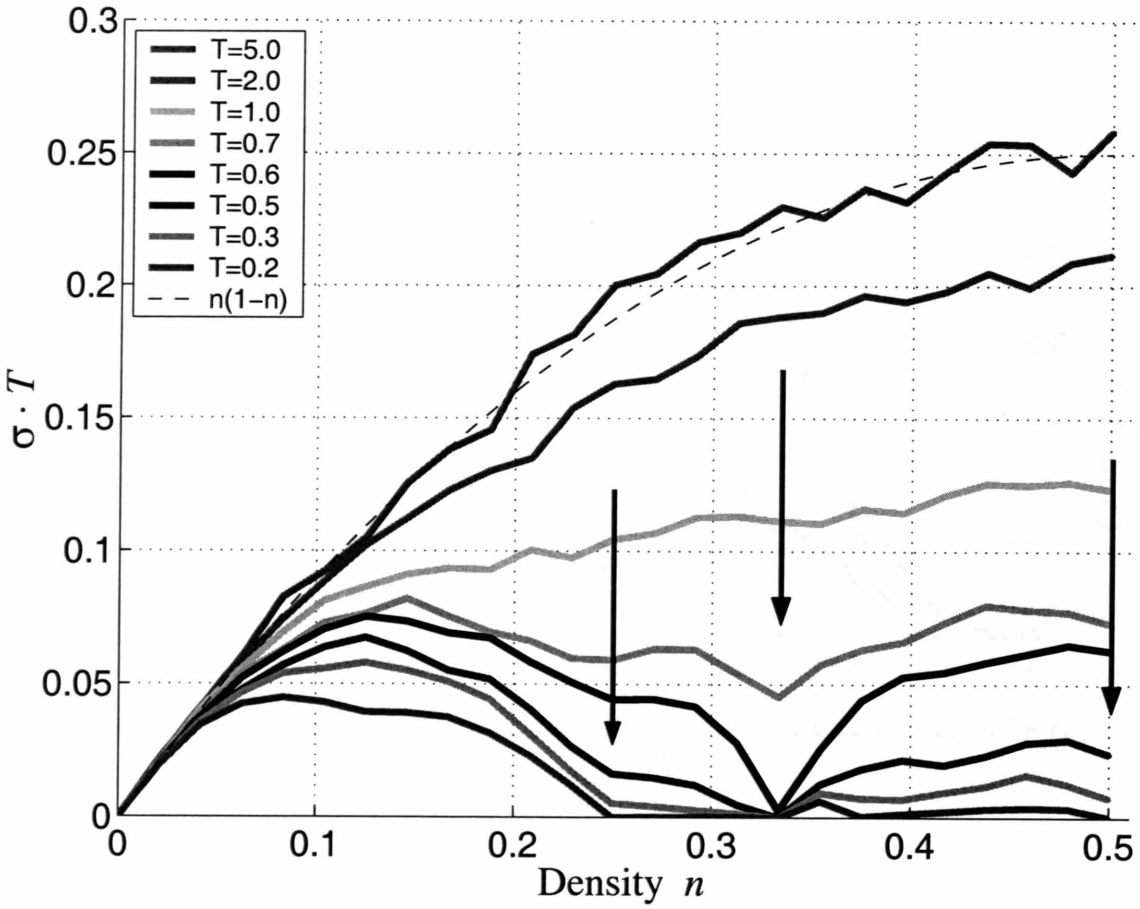

Figure 2-4: The product σT versus electron density for several temperatures. Temperature values are given in the units of $V(a)$. Arrows mark the features corresponding to the freezing phase transitions at $n = 1/4,\ 1/3,\ 1/2$. Dashed line indicates the high temperature limit $n(1-n)$, Eq. (2.18).

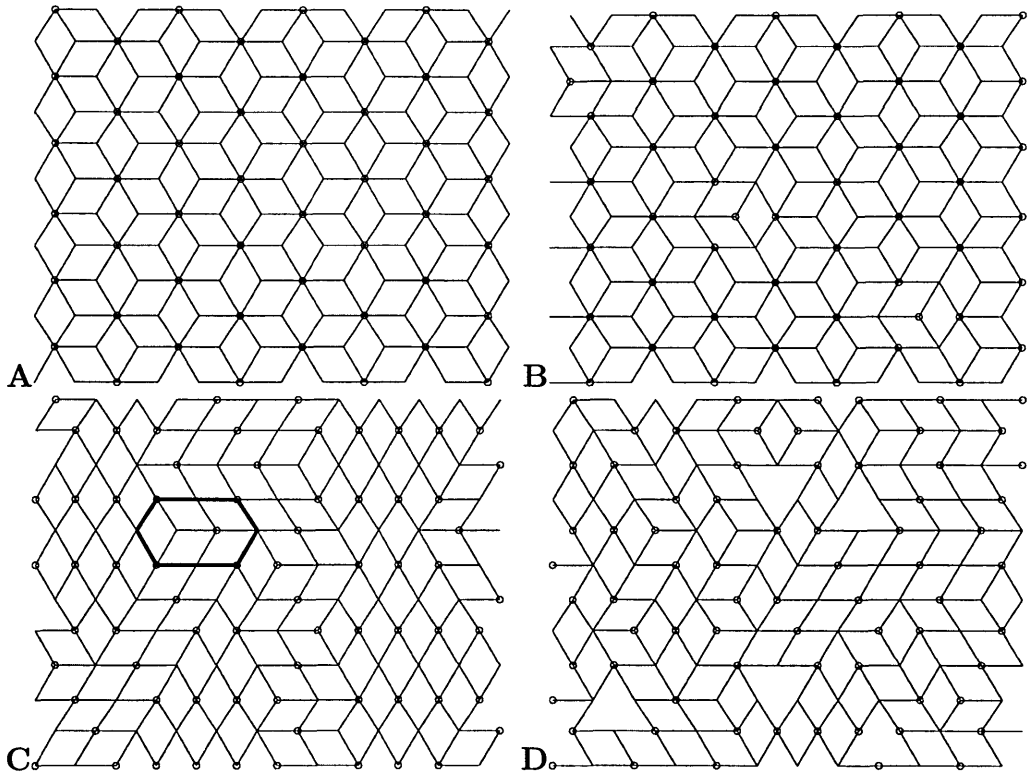

Figure 2-5: **A:** Commensurate charge configuration at $n = 1/3$. Electrons are shown as circles on the sites of the triangular array. Pairing of the triangles is revealed by erasing all frustrated bonds connecting sites with equal occupancy (see Sec. 2.2.1 for explanation). **B:** Typical Monte Carlo charge configuration for $n = 1/3+\epsilon$. There are three excess charges in the system ($\epsilon = 3/144$) hopping over the honeycomb network of unoccupied sites in the commensurate $\sqrt{3} \times \sqrt{3}$ state. The excess carriers, dilute at $\epsilon \ll 1$, are moving nearly independently on the background of the frozen $\sqrt{3} \times \sqrt{3}$ state. **C:** Typical charge configuration obtained in a Monte Carlo simulation for the filling fraction $n = 1/2$ in the correlated fluid phase. Two elementary cubic cells corresponding to a free charge are shown in bold. **D:** Typical charge configuration for the filling fraction $n = 1/2$. In this case, the temperature is higher and there are several topological defects ("triangles") present in the system. Following a loop around oppositely directed dislocations gives zero Burgers vector.

2.2 Phase Diagram

In the present Section we discuss the central result of this Chapter, namely the system's phase diagram (Fig. 2-6). This Figure shows the phase diagram of the system in the μ, T plane. Due to the particle-hole equivalence it is symmetric with respect to $\mu \leftrightarrow -\mu$. For a generic value of the chemical potential we find three distinct temperature phases: the disordered state at high temperature, the correlated fluid phase at intermediate temperatures, and the commensurate (solid) phases at low T. In Fig. 2-6 we show only the most pronounced solid phase regions, corresponding to principal fractions $n = 1/3,\ 2/3$, and $n = 1/2$. As $T \to 0$ we expect in Fig. 2-6 tiny domains of incompressible phases for any electron density n given by a simple fraction.

Phase diagram of the system is studied by means of a useful geometric construction that is called the height field. It is introduced in Sec. 2.2.1 below.

After outlining the parameter range (called correlated fluid) where the height field description is adequate, we study equilibrum properties and dynamics of the height variable in the rest of the present Section. In particular, we employ scaling arguments confirmed by the Monte-Carlo calculations to prove that unbound topological defects are always present in the correlated phase.

2.2.1 The height variable

To describe various ordering types we employ the height field order parameter originally introduced in the context of the $\triangle$IAFM problem [44, 45]. The ground state of the $\triangle$IAFM model (i.e. the model (2.1, 2.2) with the nearest neighbor interactions $d \ll a$), can be obtained by minimizing energy on each elementary triangular lattice plaquette. Given only two kinds of charges, it is impossible to avoid the frustrated bonds between the like charges. In any optimal configuration of charges the number of frustrated bonds has to be as small as possible. This is achieved by pairing the elementary triangles in such a way that they share frustrated bonds, as illustrated in Fig. 2-7. Erasing all such bonds from the picture one obtains a covering of the

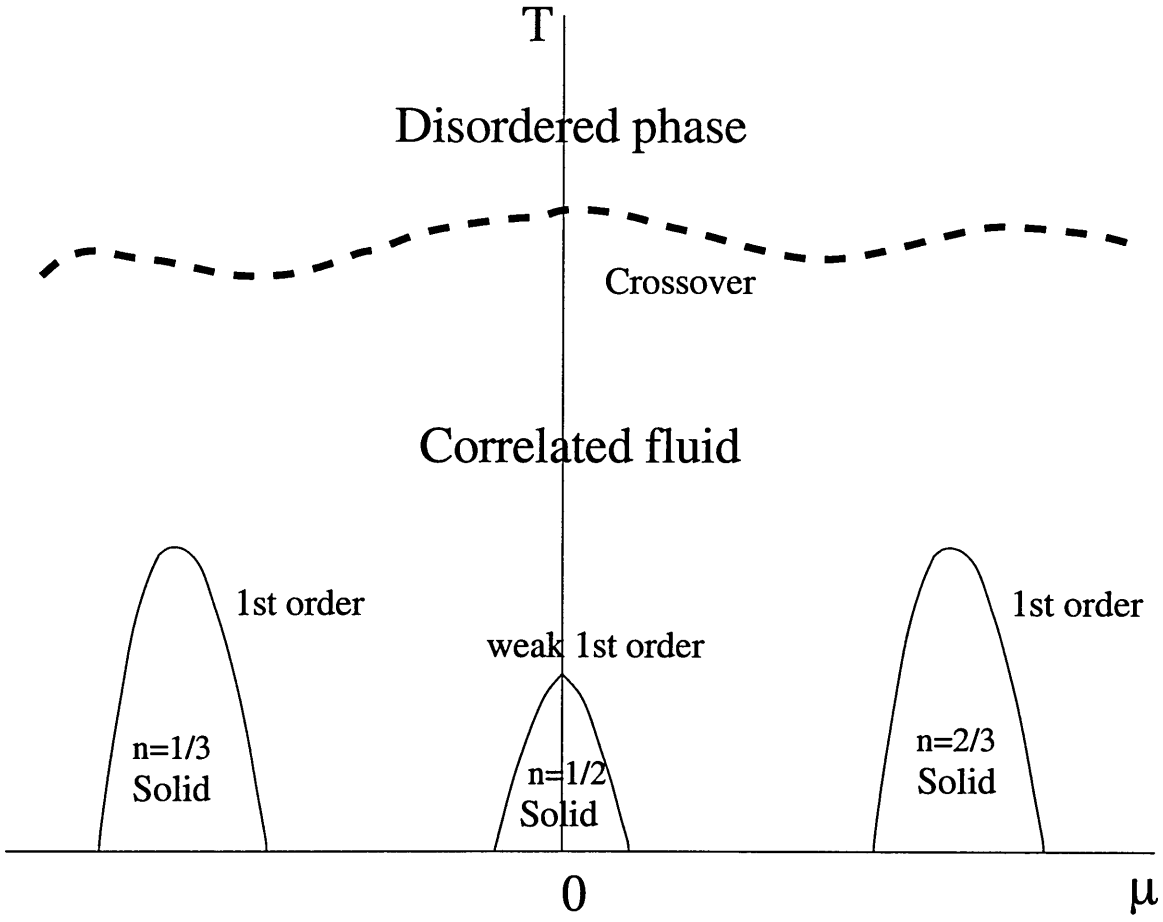

Figure 2-6: Phase diagram on the (μ, T) plane for a generic value of the interaction range d (drawn not to scale)

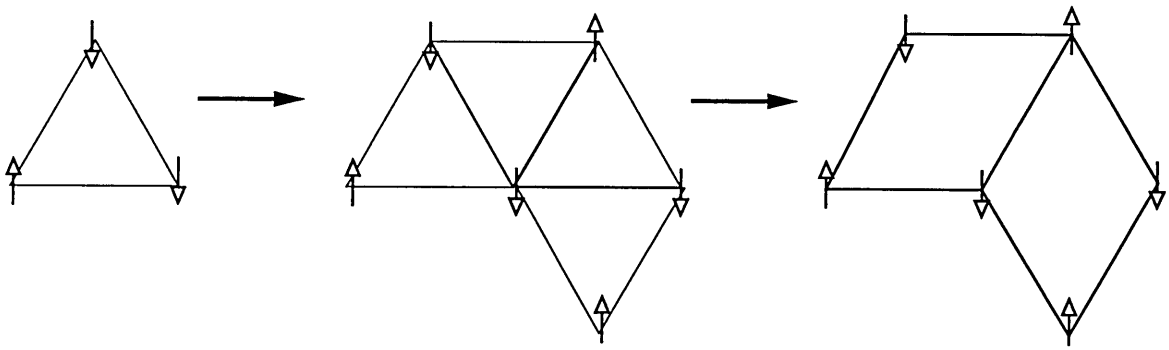

Figure 2-7: Covering of a frustrated lattice by diamonds for a spin problem. A triangular lattice is frustrated since each elementary triangle has at least one bond that connects like spins. In the ground state triangles share frustrated bonds. Erasing these bonds from the picture, we obtain a covering of a 2D plane by diamonds

$2D$ lattice by diamonds [44, 45], as shown in Fig. 2-5 (A – C). One can view such a covering as a projection along the (111) axis of a $2D$ surface in a cubic crystal. After this procedure each site $\mathbf{r}_i$ of the $2D$ lattice acquires the scalar number $h(\mathbf{r}_i)$, which is the height of the auxiliary surface in a $3D$ cubic crystal. The field values h are multiples of the distance between the cubic crystal planes

$$b = \frac{\ell}{3} = \frac{a}{\sqrt{2}} \,. \tag{2.21}$$

Here ℓ is the main diagonal of the unit cell in the cubic crystal. The mapping of the charged $2D$ system onto the height surface can only be realized if

$$1/3 \leq n \leq 2/3 \,, \tag{2.22}$$

with charge density n defined in Eq. (2.3), since for other densities the covering of the triangular lattice by diamonds described above does not exist. We are considering only the density range (2.22) in the present Chapter.

The height field h is defined globally and uniquely (modulo an overall sign) for any of the degenerate ground states of the ΔIAFM model. For $T > 0$, however, the height is defined only locally due to the presence of screw dislocations. Positions of

the dislocations are seen as large triangles in Fig. 2-5 (D). After going around any single triangle, one obtains a mismatch [47] in h equal to

$$b_{\triangle} = 2\ell = 6b \,, \tag{2.23}$$

which defines the Burgers vector of the dislocation. The dislocations of the height field are topological defects. They originate and disappear only in pairs.

Electron hopping dynamics can change the total number of dislocations. Each pair of triangles costs an energy of two frustrated bonds. Therefore at sufficiently low temperatures the probability of creating a pair of dislocations in the MC dynamics is exponentially suppressed. One can also expect that, even if the interaction is not of the nearest neighbor kind, the qualitative picture remains similar: the probability of creating a dislocation pair is exponentially small in $V(a)/T$. Electron hops that do not produce or destroy dislocations cost no energy in the $\triangle$IAFM model. In the problem with a long range interaction such hops generally cost finite energy which is determined by the strength of the next-nearest neighbor interaction.

Let us return to the phase diagram in Fig. 2-6. At $T \gg V(a)$ the height field does not exist due to the abundance of topological defects. In this high temperature state hopping of different electrons is completely uncorrelated. This regime is marked *disordered phase* in Fig. 2-6.

As the temperature lowers, the fugacity of a single defect scales as $e^{-V(a)/T}$, and the number of defects becomes exponentially small. In this case the height field is defined locally in the entire plane apart from rare defects. The conductivity is primarily due to "free charges" that hop without creating defect pairs. Hops of the free charges correspond to adding or removing two elementary cubic cells of the fictitious $3D$ crystal surface, as shown in Fig. 2-5 (C).

It is important that for electron densities $1/3 \leq n \leq 2/3$ considered here, there is a temperature interval in which the height order parameter is well defined, and simultaneously the fraction n_f of free charges is large. During MC simulations we accumulate a histogram for n_f and find that this is a nonconserved quantity with a

broad Gaussian distribution. The mean $\overline{n_f}$ is of the order of $10 - 50\%$ of the total electron density n for temperatures $V(\sqrt{3}a) \ll T \ll V(a)$.

Conservational constraints and a rough potential landscape yield a sophisticated dynamics for electrons at intermediate temperatures. However, the Ohmic conductivity remains finite (Fig. 2-3) since it is the free charges that provide the means for conductivity in the correlated phase. For the free charges the height field fluctuations provide an effective nonconserving (type A) dynamics (*correlated fluid* phase in Fig. 2-6).

To study a role of disorder on the dynamics is a challenging problem. For a relatively small disorder we find that the qualitative features of the dynamics do not change. We considered the zero bias dc conductivity in presence of the random potentials on sites, $\phi(\mathbf{r}_i)$ in the Hamiltonian (2.8). The random potentials distributed homogeneously in the interval $-\phi_0 \leq \phi(\mathbf{r}_i) \leq \phi_0$, with $\phi_0 \sim V(\sqrt{3}a)$ yield conductivity fluctuations that are larger than those in the clean system. However, the qualitative features of the conductivity temperature dependence are the same. In particular, the zero bias conductivity remains finite in the correlated fluid phase in the presence of disorder. We attribute the robustness of conductivity against the small random potential variations to the nonconserving dynamics of free charges.

The correlated nature of transport in the fluid phase can be revealed by modifying the MC dynamics to inhibit the MC moves that create new dislocation pairs. Altering the dynamics in such a way drastically changes the conductivity, as shown in Fig. 2-3. Now even at high temperature the dislocations are absent, since creating the new ones is explicitly forbidden. The height variable is then globally defined. In this case the only conductivity mechanism is the correlated motion of free charges. At high temperature such "correlated conductivity" is a tiny fraction of the total conductivity. However, at small T the relative contribution of the correlated conductivity increases. At $T \sim V(\sqrt{3}a)$ nearly all the conductivity in the real system is due to the correlated hops of the free charges. This is manifest in Fig. 2-3, where at high temperature the "correlated conductivity" curve for $n = 1/2$ is much lower than the regular conductivity for this density, and at $T \sim V(\sqrt{3}a)$ these curves coincide.

At lower temperature the correlated fluid freezes into the $T = 0$ ground state. The equilibrium charge ordering can be mapped [44, 45] onto the classical roughening transition [48]. Such transition in principle can be either of a finite order or continuous [49, 50, 51].

We study the charge system at equilibrium and discuss the corresponding freezing scenario in Section 2.3. In the present Section we consider equilibrium properties and dynamics of the correlated fluid phase.

2.2.2 Gaussian Fluctuations and the Rigidity

As it has been shown by Blöte and coworkers [44, 45], the height field fluctuations for the $\triangle$IAFM model at $T \to 0$ can be described by the Gaussian partition function

$$Z_0 = \int \mathcal{D}h(\mathbf{r})\, e^{-\frac{\kappa}{2}\int d^2\mathbf{r}\,(\nabla h)^2} \,. \tag{2.24}$$

The quantity κ is a stiffness, or *rigidity* of the height surface, which has been found [45] from the exact solution of the $\triangle$IAFM model [52] to be

$$\kappa_{\triangle\mathrm{IAFM}} = \frac{\pi}{9b^2} \,. \tag{2.25}$$

Below we adopt a usual convention to incorporate temperature into the effective rigidity and other parameters. Therefore temperature does not explicitly appear in the statistical sum, Eq. (2.24). The height surface fluctuations at equilibrium were studied numerically [53, 54] in the case of the nearest neighbor interactions, confirming the result (2.25) for the $\triangle$IAFM .

One expects that in the case of a long range interaction (2.2) and not too low temperature, qualitative features of the height surface fluctuations would remain similar to those of the $\triangle$IAFM case. Below we phenomenologically describe the correlated fluid phase by the partition function (2.24) with the effective rigidity κ which is a function of the density and temperature. As the temperature decreases, other terms in the in the effective free energy can become relevant. This issue is addressed in

subsections 2.2.3 and 2.2.4.

We numerically observe that the height field fluctuations in the correlated phase are Gaussian for a generic form of interaction, Eq. (2.2). To study height fluctuations and rigidity we employ an algorithm (see below) to assign height values $h(\mathbf{r}_i)$ to all points of a two dimensional lattice.

Assigning the height to each lattice point is a well defined procedure at $T = 0$. At finite temperature, the height is defined only locally due to the presence of dislocations. As we will see below, the dislocations are always present in the correlated phase, since there is no dislocation binding phase transition. Therefore, strictly speaking, the height field (and hence its effective rigidity) can be globally defined only at $T = 0$. This difficulty can be circumvented since in the correlated phase the number of dislocations is exponentially small. We expect that by defining the height locally with a small number of dislocations present we do not obtain large errors while measuring the rigidity κ.

Without dislocations any algorithm that assigns height to lattice sites gives the same height field values (modulo constant and overall sign). In the presence of dislocations one can only define the height field locally, by moving from one site to another. Different prescriptions can in principle lead to different height definitions for some fraction of the sites. Below we describe a particular algorithm of assigning the height field values to the $2D$ lattice sites used in the present Chapter.

To calculate the height $h(\mathbf{r}_m)$ for every point $\mathbf{r}_m = (x_m,\ y_m)$ of the $2D$ triangular array we first assign the auxiliary $3D$ coordinates

$$\mathbf{R}(\mathbf{r}_m) = \sum_s R_s(\mathbf{r}_m)\, \mathbf{e}_s \tag{2.26}$$

to each $\mathbf{r}_m$. Here the unit vectors $\mathbf{e}_s,\ s = 1, 2, 3$, are the basis vectors of the auxiliary $3D$ cubic lattice.

We work with an $N \times N$ rhombic patch of the $2D$ triangular array, using the coordinate system aligned with the array. The sites are labeled by integer coordinates $(i, j),\ i, j = 0, ..., N-1$. We place the origin in the upper left corner of the patch.

The first component, i, is the site number counted along the horizontal axis (upper edge of the patch). Numbers i increase as we go from left to right. The second component, j, is the site number along the axis which makes the angle $\pi/3$ with the first one. Numbers j increase as we go from the origin down and to the right, with $j = N - 1$ defining the lower edge of the patch. The conventional Cartesian coordinates $\mathbf{r}_m = (x_m,\ y_m)$ of the site $(i_m,\ j_m)$ are given by

$$x_m = i_m\, a + j_m \frac{a}{2}\ , \quad y_m = -j_m\, a \frac{\sqrt{3}}{2}\ . \tag{2.27}$$

To obtain the $3D$ coordinates for a particular charge configuration, we start from the upper row ($j = 0$) and move along the rows from left to right. The $3D$ coordinates $\mathbf{R}(i_{m'},\ j_{m'})$ are assigned to the sites $\{\mathbf{r}_{m'}\}$ connected with the current one $(i_m,\ j_m)$ by the following rules. Define $\mathbf{R}(i = 0,\ j = 0) \equiv \mathbf{0}$. Then, a bond $(i,j) - (i+1,j)$ yields $\delta_+ R_1(i+1,j)$, a bond $(i,j) - (i,j+1)$ yields $\delta_- R_2(i,j+1)$, and a bond $(i,j) - (i-1,j+1)$ yields $\delta_+ R_3(i-1,j+1)$. Here $\delta_\pm$ means increase (decrease) of the corresponding component of $\mathbf{R}$ with respect to its value at (i,j) by the amount b given in Eq. (2.21).

Once the positions $\mathbf{R}(\mathbf{r}_m)$ in the auxiliary cubic crystal are defined, the height at each site $\mathbf{r}_m$ is obtained as

$$h(\mathbf{r}_m) = \sum_{s=1}^{3} R_s(\mathbf{r}_m)\ . \tag{2.28}$$

In order to study fluctuations of the height surface in the correlated fluid phase at fixed temperature, we accumulate the histograms $\mathcal{P}[h(\mathbf{r}_i)]$ of height values for a number of points $\{\mathbf{r}_i\}$ in the $N \times N$ patch. Were the distribution $\mathcal{P}[h(\mathbf{r}_i)]$ Gaussian, the dependence $\log \mathcal{P}[h(\mathbf{r}_i)]$ versus $h(\mathbf{r}_i)|h(\mathbf{r}_i)|$ would have been piecewise linear and symmetric. By plotting $\log \mathcal{P}[h(\mathbf{r}_i)]$ versus $h(\mathbf{r}_i)|h(\mathbf{r}_i)|$ we confirm that the fluctuations of the height variable in the correlated fluid phase are Gaussian when the fluid is far from freezing.

As the temperature approaches $V(\sqrt{3}a)$, dependence $\log \mathcal{P}[h(\mathbf{r}_i)]$ versus $h(\mathbf{r}_i)|h(\mathbf{r}_i)|$ deviates from symmetric piecewise linear, which indicates that non quadratic terms in the free energy of the system become relevant. Such terms can yield a freezing

transition of a finite order (Section 2.3). In the present Section we consider another kind of a phase transition in the correlated fluid, namely that of topological defects binding [49]. Such a phase transition between the disordered and correlated fluid state would realize the $2D$ melting scenario proposed in [50]. It will become clear below that this scenario does not take place in the present model, as indicated by a crossover line in the phase diagram, Fig. 2-6.

2.2.3 Phenomenological Free Energy

In the correlated state, electrons on the sites of the array are described in terms of the height variable $h(\mathbf{r})$ and charge density $n(\mathbf{r})$. Microscopically the state of the system is defined uniquely by specifying either the height variable or the charge density. However, as we will see below, at large length scales height field and density decouple in the correlated fluid phase. Therefore we describe the system by a partition function of the form

$$Z_{\rm corr} = \int \mathcal{D}h(\mathbf{r}) \mathcal{D}n(\mathbf{r})\; e^{-\mathcal{F}[h,\; n]}\;. \tag{2.29}$$

Here the free energy

$$\mathcal{F}[h,\; n] = \mathcal{F}_h + \mathcal{F}_n + \mathcal{F}_{\rm int} \tag{2.30}$$

is a sum of the contributions of the height field, charge density, and the term $\mathcal{F}_{\rm int}$ describing their interaction. The temperature T is incorporated into $\mathcal{F}$ in accord to our convention.

We write the phenomenological free energy $\mathcal{F}_h$ associated with the height field in the following form:

$$\mathcal{F}_h = \int d^2\mathbf{r} \left(\frac{\kappa}{2} (\nabla_{\mathbf{r}} h)^2 \;+\; g \cos \frac{2\pi h}{b} \;+\; f\, V_{\rm g} \cos \frac{\pi h}{b} \right)\;. \tag{2.31}$$

Here the first term describes the Gaussian dynamics of the height surface with κ being its rigidity. The second term assigns higher statistical weight to the field configurations that pass through the points of the $3D$ cubic lattice. The period b in height is given by Eq. (2.21). The last term in (2.31) describes the coupling to the

gate voltage. Since positive and negative charges occupy two different sublattices of the $3D$ lattice, the gate voltage term has a period of $2b$ [55]. One can conjecture already at this point that the coupling f becomes more relevant than g as the system is driven into its low temperature solid phase. We will see below that this is indeed the case, and that the second term in (2.31) being less relevant does not significantly affect the dynamic and thermodynamic properties of the system.

Consider now the charge density $n_{\mathbf{r}}$. Electrons interact with each other and with an external electrostatic potential $\Phi^{\text{ext}}(\mathbf{r})$, which gives

$$\mathcal{F}_n = \frac{1}{2}\int d^2\mathbf{r}\, d^2\mathbf{r}'\, n_{\mathbf{r}} U_{\mathbf{r}-\mathbf{r}'} n_{\mathbf{r}'} + \int d^2\mathbf{r}\, n_{\mathbf{r}} \Phi^{\text{ext}}(\mathbf{r}) \; . \tag{2.32}$$

Here we use the interaction $U_{\mathbf{r}-\mathbf{r}'}$ of the form (2.2).

Finally, we need to account for the interaction between the height variable and the density. Such interaction distinguishes between positive and negative charges and therefore should be periodic in $2b$ for the same reason as for the last term in Eq. (2.31). Phenomenologically we write the interaction part $\mathcal{F}_{\text{int}}$ as

$$\mathcal{F}_{\text{int}} = \lambda \int d^2\mathbf{r}\; n_{\mathbf{r}}\; \cos\frac{\pi h_{\mathbf{r}}}{b} \tag{2.33}$$

with λ being an appropriate coupling. Below we perform a scaling analysis of the problem (2.30) at one loop.

2.2.4 Renormalization and Scaling

The nonlinear terms in Eqs. (2.31, 2.33) acquire nontrivial scaling dimensions due to the fluctuations of the height surface. At one loop, from the standard renormalization group procedure for the sine-Gordon model [56], the scaling dimensions of the couplings f, λ and g are correspondingly

$$X_f = X_\lambda = \frac{2\kappa^*}{\kappa} \; , \tag{2.34}$$

$$X_g = \frac{8\kappa^*}{\kappa} \; , \tag{2.35}$$

where we define

$$\kappa^* \equiv \frac{\pi}{8b^2} \ . \tag{2.36}$$

Comparing the above scaling dimensions with the scaling of the gradient term, we obtain that the gate voltage interaction becomes relevant when $X_f < 2$, or

$$\kappa > \kappa_f = \kappa^* \ . \tag{2.37}$$

The g-term becomes relevant at a larger rigidity:

$$\kappa > \kappa_g = 4\kappa^* \ . \tag{2.38}$$

The coupling λ between the density and height fields is relevant when the scaling dimension of the gradient term is larger than the sum of scaling dimensions of λ and n. The field n is not renormalized since its free energy is quadratic. From (2.32), the scaling dimension $X_n = 3/2$. Hence the height-density interaction is relevant when

$$\kappa > \kappa_\lambda = 4\kappa^* \ . \tag{2.39}$$

The nonlinear terms in (2.31) do not renormalize the rigidity κ at one loop. However, rigidity may obtain a one loop correction $\delta\kappa$ due to the interaction with the density, Eq. (2.33). Below we consider such a possibility.

Since the free energy $\mathcal{F}_n$ is Gaussian, we integrate out the field $n_{\mathbf{r}}$ in (2.29) and obtain an effective free energy for the height field:

$$\tilde{\mathcal{F}}_h = \mathcal{F}_h - \frac{\lambda^2}{2} \sum_{\mathbf{k}} \left(\cos \frac{\pi h}{b} \right)_{-\mathbf{k}} \frac{1}{U_{\mathbf{k}}} \left(\cos \frac{\pi h}{b} \right)_{\mathbf{k}} \ . \tag{2.40}$$

Consider the case of the screened Coulomb interaction of the form (2.2),

$$U_{\mathbf{k}} = \frac{2\pi}{k} \left(1 - e^{-kd} \right) \ . \tag{2.41}$$

At length scales larger than the screening length, $kd \ll 1$,

$$\frac{1}{U_{\mathbf{k}}} \approx \frac{1}{2\pi}\,(A + Bk) \tag{2.42}$$

with $A = 1/d$, $B = 1/2$. For the unscreened Coulomb interaction, $(U_{\mathbf{k}})^{-1}$ has the same form (2.42) with $A = 0$, $B = 1$. The local term $A/2\pi$ corrects the coupling constant g and does not contribute to the rigidity. The correction to rigidity $\delta\kappa$ arises from the nonlocal part of (2.40) with $U_{\mathbf{k}}^{-1} \to Bk/2\pi$. Expanding $\cos \pi h/b = \left(e^{i\pi h/b} + e^{-i\pi h/b}\right)/2$, we note that the terms $(e^{i\pi h/b})_{-\mathbf{k}}(e^{i\pi h/b})_{\mathbf{k}}$ + c.c. have a larger scaling dimension than the cross terms, $(e^{-i\pi h/b})_{-\mathbf{k}}(e^{i\pi h/b})_{\mathbf{k}}$ + c.c. . Neglecting the former and expanding the latter, we arrive at the following rigidity correction:

$$\delta\kappa = -J\kappa^* \,, \tag{2.43}$$

where we introduced a new dimensionless coupling

$$J \equiv 2B\,\frac{\lambda^2}{k} \,. \tag{2.44}$$

Note that the screening length d does not contribute to the rigidity correction. Screening of the Coulomb potential by the gate only changes the coefficient B in (2.44). The coupling J is renormalized via integrating out the fluctuations of the height field $h_{\mathbf{k}}$ at the scale $1/l_1 < k < 1/l_0$:

$$J_{l_1} = J_{l_0}\left(\frac{l_1}{l_0}\right)^{1-4\kappa^*/\kappa} \,. \tag{2.45}$$

Eq. (2.45) yields a natural result: The rigidity correction (2.43) due to the height-density interaction is relevant when the condition (2.39) holds, i.e. when the interaction term $\mathcal{F}_{\text{int}}$ is relevant.

As we have described in subsection 2.2.2, in the correlated phase far from freezing the fluctuations are Gaussian. This means that all the nonlinear terms considered above are irrelevant, and the rigidity κ is smaller than any of the fixed point rigidities

found above:

$$\kappa < \kappa_f < \kappa_g = \kappa_\lambda \ . \tag{2.46}$$

As the temperature lowers, the height surface becomes more rigid. The system could freeze into the smooth phase due to the last term in (2.31) when κ approaches κ_f from below [55]. Such a transition would be of an infinite order, i.e. with no singularities in any finite order derivative of the free energy. During the MC dynamics we observe the first order freezing phase transitions into incompressible states with $n = 1/2$ and $n = 1/3,\ 2/3$ (Section 2.3). Hence the rigidity in the correlated fluid phase is always less than κ_f, and jumps to the infinitely large value at the freezing transition.

The density and height fields effectively decouple, since the condition (2.46) yields that the coupling λ never becomes relevant in the correlated phase. This justifies our phenomenological approach of writing the free energy as a sum of the height and density contributions in Eq. (2.30).

With the MC code at hand, we check that $\kappa < \kappa_f$ in the correlated fluid. To calculate the rigidity we fit the height correlation function $\langle (h(\mathbf{r}) - h(\mathbf{0}))^2 \rangle$ to the one that follows from (2.24):

$$\left\langle (h(\mathbf{r}_i) - h(\mathbf{r}_j))^2 \right\rangle = \frac{1}{\pi\kappa} \ln \frac{|\mathbf{r}_{ij}|}{r_0} \ , \tag{2.47}$$

where r_0 is of the order of a lattice spacing. We tested our procedure by calculating the rigidity for the purely nearest neighbor interacting system ($d \ll a$) at $n = 1/2$. The MC dynamics gives the value $\kappa_{\triangle\text{IAFM}}$ (Eq. (2.25)) within several per cent accuracy. When the interaction is beyond the nearest neighbor, the calculated rigidity is always smaller than κ_f. In particular, when we turn on the long range interaction, the rigidity steeply drops from $\kappa_{\triangle\text{IAFM}}$ to a value several times smaller, consistently with $\kappa < \kappa_f < \kappa_{\triangle\text{IAFM}}$.

The absence of the phase transition between the correlated fluid and the high temperature disordered phase can be now explained using (2.46). Our argument is similar to the one given in Ref. [55]. The dislocation pairs unbinding [49] as a possible

$2D$ melting scenario [50] imposes a lower bound [55, 57] on the correlated fluid rigidity,

$$\kappa_{\rm KT} = \frac{8\pi}{b_\triangle^2} = \frac{2\pi}{9b^2} \ , \tag{2.48}$$

with the Burgers vector $b_\triangle$ of the dislocation given in (2.23). Since $\kappa < \kappa_f < \kappa_{\rm KT}$, the bound (2.48) is never reached. The dislocation pairs are present at any temperature in the correlated fluid phase with the exponentially small probability $\sim e^{-2V(a)/T}$. During the MC dynamics we often observe no dislocations at low temperature due to the finite system size.

Similar considerations also explain why the negative correction to the rigidity given by (2.43) is not important. The fixed point κ_λ beyond which the rigidity could flow to smaller values is never reached in the correlated fluid phase.

2.2.5 Dynamics

Above we showed that at equilibrium the coupling of the height and density fields is irrelevant. Below we discuss how the interplay between the h and n fields affects the system's dynamical properties. We obtain corrections to the conductivity and compressibility due to the height field fluctuations using the Langevin dynamics.

The type A Langevin dynamics for the height field is defined by

$$\partial_t h(\mathbf{r},t) = -\eta \frac{\delta \mathcal{F}}{\delta h} + \xi_{\mathbf{r},t} \ , \tag{2.49}$$

where ξ is the stochastic force,

$$\langle \xi_{\mathbf{r},t} \xi_{\mathbf{r}',t'} \rangle = \left\langle \xi^2 \right\rangle \delta(t-t') \, \delta(\mathbf{r}-\mathbf{r}') \ . \tag{2.50}$$

Its amplitude obeys the Einstein relationship

$$\left\langle \xi^2 \right\rangle = 2\eta T \ . \tag{2.51}$$

The type B Langevin dynamics for the charge density n is defined using the continuity

equation

$$\partial_t n + \nabla_{\mathbf{r}} \mathbf{j} = 0 \tag{2.52}$$

where the current $\mathbf{j}$ has a stochastic part $\mathbf{j}^L$:

$$\mathbf{j} = -\sigma \nabla_{\mathbf{r}} \frac{\delta \mathcal{F}}{\delta n} + \mathbf{j}^L \ , \tag{2.53}$$

$$\left\langle j_\mu^L(\mathbf{r},t) j_\nu^L(\mathbf{r}',t') \right\rangle = \left\langle (\mathbf{j}^L)^2 \right\rangle \delta_{\mu\nu}\, \delta(t-t')\, \delta(\mathbf{r}-\mathbf{r}') \ . \tag{2.54}$$

The conductivity σ is related to the stochastic current amplitude by the Nyquist formula

$$\left\langle (\mathbf{j}^L)^2 \right\rangle = 2\sigma T \ . \tag{2.55}$$

Eqs. (2.49, 2.53) and (2.31, 2.32, 2.33) yield

$$\partial_t h(\mathbf{r},t) = \eta \left(\kappa \nabla^2 h + \frac{2\pi g}{b} \sin \frac{2\pi h}{b} + \frac{\pi \lambda}{b}\, n \sin \frac{\pi h}{b} \right) + \xi(\mathbf{r},t) \ , \tag{2.56}$$

$$\partial_t n(\mathbf{r},\, t) = \sigma \nabla_{\mathbf{r}}^2 \left(\int d^2\mathbf{r}' V_{\mathbf{r}-\mathbf{r}'} n_{\mathbf{r}'} + \Phi_{\mathbf{r}}^{\mathrm{ext}} \right) - \nabla_{\mathbf{r}} \left(\mathbf{j}^h + \mathbf{j}^L \right) \ , \tag{2.57}$$

where we write the stochastic contribution to the current due to the height field fluctuations in the form

$$\mathbf{j}^h(\mathbf{r},\, t) = -\lambda \sigma \nabla_{\mathbf{r}} \cos \frac{\pi h_{\mathbf{r}}}{b} \ . \tag{2.58}$$

The height field fluctuations provide an additional contribution $\delta\sigma^h$ to the conductivity, which is determined by the classical limit of the fluctuation-dissipation theorem:

$$\left\langle j_\mu^h(-\omega,-\mathbf{k})\, j_\nu^h(\omega,\mathbf{k}) \right\rangle = 2\, \delta\sigma_{\mu\nu}^h(\omega,\mathbf{k})\, T \ . \tag{2.59}$$

The contribution to the conductivity that arises from the height field fluctuations is purely longitudinal:

$$\delta\sigma_{\mu\nu}^h(\omega,\mathbf{k}) = \frac{\lambda^2}{2T}\, \sigma^l(-\omega,-\mathbf{k})\, \sigma^l(\omega,\mathbf{k})\, k_\mu k_\nu\, \tilde{F}(\omega,\mathbf{k}) \ . \tag{2.60}$$

Here $\sigma^l(\omega,\mathbf{k})$ is the longitudinal part of the total conductivity σ, and $\tilde{F}(\omega,\mathbf{k})$ is a

Fourier transform of the correlator

$$F(\mathbf{r},t)=\left\langle \cos\frac{\pi h_{\mathbf{r},t}}{b}\cos\frac{\pi h_{\mathbf{0},0}}{b}\right\rangle_0=\frac{1}{2}\exp\left\{-\frac{\pi^2}{2b^2}\left\langle (h_{\mathbf{r},t}-h_{\mathbf{0},0})^2\right\rangle_0\right\}\ . \tag{2.61}$$

Averaging in (2.61) is done with respect to the noninteracting system, $\lambda=g=0$ in Eq. (2.56). The height field correlator in this case reads

$$\begin{aligned}\left\langle (h_{\mathbf{r},t}-h_{\mathbf{0},0})^2\right\rangle_0&=\sum_{\mathbf{k},\omega}\frac{\langle\xi^2\rangle}{(\eta\kappa k^2)^2+\omega^2}\left|1-e^{i\mathbf{kr}-i\omega t}\right|^2\\&=\frac{T}{\pi\kappa}\int_0^{1/a}dk\,\frac{1-e^{-\eta\kappa k^2|t|}\,J_0(kr)}{k}\ .\end{aligned} \tag{2.62}$$

Since at small $|t|$ and k^2

$$1-e^{-\eta\kappa k^2|t|}\,J_0(kr)\sim k^2\left(\frac{r^2}{4}+\eta\kappa|t|\right)\ , \tag{2.63}$$

for the correlator (2.62) we have

$$\left\langle (h_{\mathbf{r},t}-h_{\mathbf{0},0})^2\right\rangle_0=\frac{T}{2\pi\kappa}\ln\left(\frac{\mathbf{r}^2}{4a^2}+\frac{\eta\kappa|t|}{a^2}\right)\ . \tag{2.64}$$

Therefore Eq. (2.61) yields

$$F(\mathbf{r},t)=\frac{1}{2}\left(\frac{a^2}{\mathbf{r}^2/4+\eta\kappa|t|}\right)^{2\kappa^*/\kappa}\ . \tag{2.65}$$

Since $\kappa<\kappa^*$ in the correlated phase, the time correlations of the current $\mathbf{j}^h(\mathbf{r},t)$ have short memory and are local, i.e. one can approximate its correlator as $\left\langle j^h_\mu(\mathbf{r},t)\ j^h_\nu(\mathbf{0},0)\right\rangle\sim\delta_{\mu\nu}\,\delta(t)\,\delta(\mathbf{r})$. Hence one may treat $\mathbf{j}^h(\mathbf{r},t)$ as a Johnson - Nyquist noise, and the application of Eq. (2.59) is justified.

A correction to compressibility ν can be obtained directly from the statistical averaging with respect to the canonical distribution. Given that

$$\langle\Phi_{-\mathbf{k}}\,\Phi_{\mathbf{k}}\rangle=V_{\mathbf{k}}\ ,\quad\text{with}\quad\Phi=\frac{\delta\mathcal{F}}{\delta n}\ , \tag{2.66}$$

the correction to the density-density interaction can be obtained from (2.33),

$$\delta V_{\mathbf{k}} = \lambda^2 \int d^2\mathbf{r}\, e^{-i\mathbf{k}\mathbf{r}} \left\langle \cos\frac{\pi h_{\mathbf{r}}}{b} \cos\frac{\pi h_0}{b} \right\rangle_0 . \tag{2.67}$$

The latter correlator is given by Eq. (2.65) with $t = 0$. If

$$\kappa < 2\kappa^* , \tag{2.68}$$

the correlator in (2.67) is local, i.e. it can be approximated by the $2D$ delta function. Since (2.68) always holds in the correlated phase, Eq. (2.67) yields a finite compressibility

$$\nu = \frac{1}{\delta V_{\mathbf{k}=\mathbf{0}}} . \tag{2.69}$$

2.2.6 Conclusions

In the present Section we have outlined a phase diagram of the sysem, shown in Fig. 2-6. We considered in detail the charge system at intermediate temperatures $T \sim V(a)$. The correlated nature of charge dynamics allowed us to map the charge ordering problem on a triangular lattice onto the statistical mechanics of the height surface with nonlinear interactions. We have identified the *correlated fluid phase* of the charge ordering problem (Fig. 2-6) that corresponds to an almost freely fluctuating height surface. We have found the upper bound κ_f for the effective rigidity in the correlated phase. The value κ_f rules out the possibility for the Berezinskii - Kosterlitz - Thouless phase transition for the dislocations pairs binding. Contributions to the conductivity and compressibility of the charged system due to the correlated nature of charge dynamics appear to be local everywhere in the correlated fluid phase.

In the next Section we study freezing of the correlated fluid into the $T = 0$ commensurate states.

2.3 Freezing Phase Transitions

In the present Section we consider charge ordering of the system into the $T = 0$ ground state. We have already seen in Sec. 2.1.3 that ground state ordering is different for the systems with short range ("Ising") and long range interactions.

Indeed, an Ising system has only a finite set of commensurate ground state configurations, as outlined in Sec. 2.1.3. When such a system is gradually cooled down at a fixed chemical potential, its density n approaches either 0 or 1/3 (or their particle-hole symmetric counterparts 1 or 2/3). These densities are attractors for the cooling curves shown in Fig. 2-2. In this case the only nontrivial ground state is a commensurate $\sqrt{3} \times \sqrt{3}$ lattice shown in Fig. 2-5 (A), corresponding to the density $n = 1/3$ (or $n = 2/3$ via particle-hole symmetry).

The case of a charge system ineracting via a long range potential $V(r)$ (as in Eq. (2.2)) is less trivial. Indeed, cooling at a fixed chemical potential μ leads to the freezing into a particular ground state depending on the value of μ, as shown in Fig. 2-1. For a generic value of chemical potential a finite system freezes into a glassy, or disordered ground state. In principle, an infinite system with an ideally regular lattice should find its true ground state which is a commensurate charge configuration. In reality only configurations with simplest rational densities, such as $n = 1/2$ or $1/3$ are pronounced. This is illustrated in the phase diagram in Fig. 2-6.

Below we shall focus on the system with a long range interaction (2.2) in the density range $1/3 \leq n \leq 2/3$. We will study freezing of the correlated fluid present at $1/3 \leq n \leq 2/3$ into a commensurate, or solid phase. We will consider freezing into the two most pronounced commensurate states: at $n = 1/3,\ 2/3$, and at $n = 1/2$.

First, we use the symmetry considerations based on the Landau theory [46] to argue that both phase transitions at $n = 1/2$ and at $n = 1/3,\ 2/3$ are of the first order. After that we calculate the equilibrium energy distribution of the system in the vicinity of the transitions using the MC dynamics. The singularities in the moments of the energy distribution are used to characterize the freezing phase transitions. We also compare the critical behavior of the conductivity and of the average energy near

the freezing point.

Ground state ordering at $1/3 \leq n \leq 2/3$ can be characterized by a *tilt* $\mathbf{t}$ of the height surface. The $3D$ cubic crystal surface in Fig. 2-5 (A - C) is represented by the three kinds of diamonds (paired elementary triangles). Each diamond is normal to one of the unit basis vectors $\{\mathbf{e}_s,\ s = 1, 2, 3\}$ of the $3D$ crystal. We define the *normal vector* to the height surface,

$$\mathbf{m} = \mathcal{A}^{-1} \sum_{s=1}^{3} r_s \mathbf{e}_s \ , \quad \mathcal{A} = r_1 + r_2 + r_3 \ , \tag{2.70}$$

where r_s is the number of diamonds normal to the vector $\mathbf{e}_s$. The tilt $\mathbf{t}$ of the height surface is a projection of the vector $\mathbf{m}$ onto the $2D$ array,

$$\mathbf{t} = \mathbf{m} - (\hat{\mathbf{z}} \cdot \mathbf{m})\, \hat{\mathbf{z}} \ , \quad \hat{\mathbf{z}} = \frac{1}{\sqrt{3}} \left(\mathbf{e}_1 + \mathbf{e}_2 + \mathbf{e}_3\right) \ . \tag{2.71}$$

The average in (2.70) is performed locally over a domain with the number of diamonds $1 \ll \mathcal{A} \ll N^2$ for the $N \times N$ patch. In this case the vector $\mathbf{t}(\mathbf{r})$ is proportional to the local height gradient $\nabla_{\mathbf{r}} h(\mathbf{r})$. One can also define an *average tilt* of the patch with $\mathcal{A} = N^2$ in (2.70).

When the interactions are of the nearest neighbor ($d \ll a$), the height surface fluctuates freely at $T = 0$ since hops of free charges cost no energy (as discussed in subsection 2.2.1). The numbers r_s for the $N \times N$ patch fluctuate around their expected value of $N^2/3$, and the average tilt is $\mathbf{t} = \mathbf{0}$.

The long-range $V(\mathbf{r})$ lifts the exponential degeneracy of the ground state and yields ordering into commensurate phases. Average tilt $\mathbf{t}$ in each of the commensurate phases can take only a finite number of values allowed by the symmetry of the triangular lattice. The ground state has a finite entropy. Freezing temperature is determined by the strength of the next-nearest neighbor interactions.

Below we study the most pronounced ordering types when the interaction (2.2) is long-range. Due to electron-hole symmetry $n \leftrightarrow 1 - n$ it suffices to consider only the density interval $1/3 \leq n \leq 1/2$.

2.3.1 Freezing Transition at $n = 1/3,\ 2/3$

The ground state for $n = 1/3$ is a $\sqrt{3} \times \sqrt{3}$ configuration shown in Fig. 2-5 (A), with zero average tilt $\mathbf{t} = \mathbf{0}$. In this state, electrons can occupy one out of the three sublattices of the triangular lattice. To define an order parameter for the freezing transition at density $n = 1/3$, we introduce average electron densities n_i, $(i = 1, 2, 3)$ for each of the three sublattices, with their sum being the total density:

$$n_1 + n_2 + n_3 = n = \frac{1}{3} \,. \tag{2.72}$$

In the ground state one sublattice is fully occupied, and the other two are empty: $n_{i_1} = 1/3$, $n_{i_2} = n_{i_3} = 0$, which corresponds to a triple degeneracy. Above the transition temperature the occupation numbers n_i are equal: $n_i = 1/9$.

Consider the set $\{\delta n_i\}$,

$$\delta n_i = n_i - \frac{1}{9} \,, \tag{2.73}$$

$$\sum \delta n_i = 0 \,. \tag{2.74}$$

The symmetry of $\{\delta n_i\}$ in the high temperature phase is the permutations group S_3. The three dimensional representation of S_3 in the space of vectors $(\delta n_1\ \delta n_2\ \delta n_3)^T$ is reducible. Physically it follows from the charge conservation, Eq. (2.74), which yields that only two components of the set $\{\delta n_i\}$ are independent.

Under the linear transformation

$$\begin{pmatrix} \varphi_1 \\ \varphi_2 \\ \varphi_3 \end{pmatrix} = \begin{pmatrix} 0 & \frac{1}{\sqrt{2}} & -\frac{1}{\sqrt{2}} \\ -\sqrt{\frac{2}{3}} & \frac{1}{\sqrt{6}} & \frac{1}{\sqrt{6}} \\ \frac{1}{\sqrt{3}} & \frac{1}{\sqrt{3}} & \frac{1}{\sqrt{3}} \end{pmatrix} \begin{pmatrix} \delta n_1 \\ \delta n_2 \\ \delta n_3 \end{pmatrix} \tag{2.75}$$

the component φ_3, which is zero due to Eq. (2.74), decouples. The two dimensional representation of the group S_3 in the space of vectors $\varphi = (\varphi_1,\ \varphi_2)^T$ is irreducible. We choose the two dimensional vector φ as an order parameter of the phase transition at $n = 1/3$.

The free energy $\mathcal{F}_{1/3}$ in the vicinity of a transition is written in terms of the invariant polynomials of the symmetry group. According to the Hilbert theorem the invariant polynomials of S_3 can be represented as linear combinations of symmetric polynomials

$$\sigma_s = \sum_{i=1}^{3} (\delta n_i)^s, \quad s = 1, 2, 3... \ . \tag{2.76}$$

Using the transformation (2.75), we obtain the following invariants of φ: the quadratic

$$I^{(2)} = \varphi_1^2 + \varphi_2^2 \ , \tag{2.77}$$

the cubic

$$I^{(3)} = \varphi_2(\varphi_2^2 - 3\varphi_1^2) \ , \tag{2.78}$$

and the quartic invariant

$$I^{(4)} = (I^{(2)})^2 \ . \tag{2.79}$$

Hence the free energy near the freezing transition can be written as

$$\mathcal{F}_{1/3} = A_2 I^{(2)} + A_3 I^{(3)} + A_4 I^{(4)} \ . \tag{2.80}$$

The existence of the "symmetric cube" $I^{(3)}$ yields that the freezing phase transition at densities $n = 1/3,\ 2/3$ is of the first order.

2.3.2 Freezing Transition at $n = 1/2$

In the $n = 1/2$ ground state the height surface is flat, with an average tilt $\mathbf{t}$ introduced above having a maximum absolute value, $|\mathbf{t}| = \sqrt{2/3}$. In Fig. 2-5 (C) one can see a snapshot of the $n = 1/2$ state slightly above the freezing point. It has a domain structure with all the three possible domain types of maximum $|\mathbf{t}|$, as well as a small number of free charges present at the domain boundaries. In any flat domain of maximum $|\mathbf{t}|$ electrons occupy one out of the two sublattices. Three orientations of the tilt $\mathbf{t}$ and two possibilities for the sublattice occupancy at each value of $\mathbf{t}$ yield the total six fold degeneracy of the ground state at $n = 1/2$.

To characterize the ground state, we fix an elementary lattice triangle $\mathcal{T}$. The tilt $\mathbf{t}$ in the ground state can be aligned with either of the edges of $\mathcal{T}$. Let n_i be the electron density on the sublattice i that passes through the i-th edge of $\mathcal{T}$. Define $s_i = 2n_i - 1,\ i = 1,2,3$ to be the corresponding "spin" density. In the high temperature phase all $s_i = 0$. In the ground state, one of the spin densities is nonzero: $|s_j| = 1,\ s_i = 0,\ i \neq j$. We take the set $\{s_i\}$ as an order parameter for the freezing transition at $n = 1/2$.

The symmetry group P6mm of the lattice consists of the point group $\mathsf{C_{3v}}$ of the unit triangle $\mathcal{T}$, combined with translations $T_i,\ i = 1,2,3$ along the three directions (edges of $\mathcal{T}$). Below we study the three dimensional representation of the group P6mm [58] in the space of vectors $\{s_i\}$.

Consider first the point group operations of the unit triangle $\mathcal{T}$. There exist three inversions $\{\sigma_v^{(i)},\ i = 1,2,3\}$ in the vertical planes which pass through the heights of the triangle $\mathcal{T}$. Inversion $\sigma_v^{(i_1)}$ interchanges the components s_{i_2} and $s_{i_3},\ i_2, i_3 \neq i_1$. Two rotations $C_3^{\pm}$ by $\pm 2\pi/3$ around the center of $\mathcal{T}$ correspond to the cyclic permutations of the elements of $\{s_i\}$, $(C_3^+)^2 = C_3^-$. Neither of the $\mathsf{C_{3v}}$ point group operations changes sign of any s_i.

The signs of *any two* $s_{i_1},\ s_{i_2}$ are changed by applying the translation T_{i_3} along the edge $i_3 \neq i_1, i_2$ of the unit triangle. Three translations combined with the six point group operations of $\mathsf{C_{3v}}$ give the total 24 group elements of P6mm. The three dimensional representation of P6mm in the space of vectors $\{s_i\}$ is irreducible.

Similarly to the treatment in the previous subsection, to determine the order of the transition we consider invariant polynomials of the group P6mm. There is one quadratic invariant

$$I^{(2)} = s^2 \equiv s_1^2 + s_2^2 + s_3^2 \ , \tag{2.81}$$

one cubic invariant

$$I^{(3)} = s_1 s_2 s_3 \ , \tag{2.82}$$

and two quartic invariants

$$I_1^{(4)} = (s^2)^2 \ , \quad I_2^{(4)} = s_1^4 + s_2^4 + s_3^4 \ . \tag{2.83}$$

The phenomenological free energy up to the fourth order in s_i reads

$$\mathcal{F}_{1/2} = B_2 I^{(2)} + B_3 I^{(3)} + B_{41} I_1^{(4)} + B_{42} I_2^{(4)} \ . \tag{2.84}$$

We expect the first order phase transition at $n = 1/2$ due to the existence of the cubic invariant $I^{(3)}$ in the expansion (2.84).

2.3.3 Phase Transitions via the MC Dynamics

With the MC algorithm defined in Sec. 2.1, we study the charge system near the freezing phase transitions at densities $n = 1/3$ and $n = 1/2$ numerically. We focus on the equilibrium energy distribution $p(E)$, which is calculated from the MC dynamics (see below). We relate the moments of $p(E)$ to the thermodynamic quantities (average energy, heat capacity and its temperature derivative) in the vicinity of a phase transition. The plot of these quantities as functions of temperature provides information about the order of a freezing transition, and tells how close the system is to equilibrium during the MC dynamics.

We calculate the energy distribution $p(E)$ the following way. Let E be the energy of the system per one electron,

$$E = \frac{E_{\rm tot}}{nN^2} \ , \tag{2.85}$$

where the total energy $E_{\rm tot}$ is given by the first term of the "spin" Hamiltonian (2.8),

$$E_{\rm tot} = \frac{1}{2} \sum_{i \neq j} V(\mathbf{r}_i - \mathbf{r}_j)\, s_i s_j \ . \tag{2.86}$$

The energy distribution $p(E)$ is obtained as an energy histogram accumulated during the MC dynamics (Figs. 2-8, 2-9) for each value of temperature T. The functions

$p(E)$ in Figs. 2-8, 2-9 are normalized by the total number of the MC trials

$$\mathcal{N} = \sum_i p(E_i) \ . \tag{2.87}$$

We utilize the type B conserving dynamics in the case of $n = 1/3$, Fig. 2-8. As we shall see below, at density $n = 1/2$ the freezing transition features are less pronounced. The type A dynamics in the zero field ($\mu = 0$) is employed in this case (Fig. 2-9) to accumulate larger statistics by ensuring faster thermal equilibration.

If the system is at equilibrium, the energy distribution function $p(E)/\mathcal{N}$ calculated from the MC dynamics should coincide with the canonical distribution. Consider the first three moments of $p(E)$, defined as

$$M_1 = \langle E \rangle \ , \tag{2.88}$$

$$M_2 = \left\langle (E - \langle E \rangle)^2 \right\rangle \ , \tag{2.89}$$

$$M_3 = \left\langle (E - \langle E \rangle)^3 \right\rangle \ , \tag{2.90}$$

where the average with respect to $p(E)$ is calculated as

$$\langle f(E) \rangle = \frac{1}{\mathcal{N}} \sum f(E_i)\, p(E_i) \ . \tag{2.91}$$

If $p(E)/\mathcal{N}$ indeed coincides with the canonical distribution, its moments M_i are related to each other and to the observed thermodynamic quantities in a certain way that can be determined from the Gibbs partition function

$$Z = \sum e^{-E_i/T} \ . \tag{2.92}$$

Namely, in the case

$$\frac{p(E)}{\mathcal{N}} = \frac{e^{-E/T}}{Z} \ , \tag{2.93}$$

the average energy $\langle E \rangle$, the heat capacity C, and its logarithmic derivative $\partial C / \partial \ln T$

are given respectively by

$$\langle E \rangle = M_1, \tag{2.94}$$

$$C = \frac{\partial \langle E \rangle}{\partial T} = \frac{M_2}{T^2}, \tag{2.95}$$

$$\frac{\partial C}{\partial \ln T} = \frac{M_3 - 2TM_2}{T^3} . \tag{2.96}$$

It is important that Eqs. (2.94, 2.95, 2.96) yield relations

$$\frac{M_2}{T^2} = \frac{\partial M_1}{\partial T} , \tag{2.97}$$

$$\frac{M_3 - 2TM_2}{T^3} = T \frac{\partial}{\partial T} \left(\frac{M_2}{T^2} \right) \tag{2.98}$$

between the combinations of moments (2.88, 2.89, 2.90) only *at equilibrium.*

The way to characterize each freezing phase transition is the following. First, we determine how well the system is at equilibrium during the MC dynamics. We do this by plotting the right hand sides of Eqs. (2.94, 2.95, 2.96) as functions of temperature (Fig. 2-10) and checking that the relations (2.97, 2.98) are well satisfied. This yields that the set of normalized histograms $p(E)/\mathcal{N}$ calculated for the temperature region near the transition serves as a good approximation to the canonical distribution. This allows us to use Eqs. (2.94, 2.95, 2.96) to calculate the temperature behavior of the average energy $\langle E \rangle$ and its derivatives C, $T\partial C/\partial T$ at the transition. The order of a freezing phase transition is determined from the MC dynamics by examining the singularities in the temperature dependencies of the quantities $\langle E \rangle$, C and $T\partial C/\partial T$ in Fig. 2-10.

Consider freezing into the $n = 1/3$ ground state. The energy histogram $p(E)$ in Fig. 2-8 is a Gaussian above freezing. It widens significantly at the freezing temperature $T_{1/3}$ ($T_{1/3} = 0.63\, V(a)$ for the screening length $d = 2a$), and rapidly shrinks to a delta function for $T < T_{1/3}$. From Fig. 2-10 (left column of plots), one can see that the relations (2.97, 2.98) are well satisfied. We conclude that the system is ergodic and is at equilibrium during the MC dynamics. We observe a step in the average energy and a peak in the heat capacity, whose width is around 10% of the transition temper-

ature $T_{1/3}$. The finite width of the singularities is due to the finite system size, and it decreases when the size N increases. The quantities C and $\partial C/\partial \ln T$ calculated from the distribution $p(E)$ both have the same width. The features of the curves in Fig. 2-10 agree with the statement that the freezing transition at $n = 1/3,\ 2/3$ is of the first order in accord with the mean field arguments presented in subsection 2.3.1.

At density $n = 1/2$ the energy histogram $p(E)$ in Fig. 2-9 evolves similarly to that of the $n = 1/3$ case. At the transition the probability distribution $p(E)$ has two peaks, which points at the coexistence of the high- and low-temperature phases. The observed fluctuations in the successive moments of $p(E)$ (Fig. 2-10, right column) are substantially larger than for the case of $n = 1/3$. These fluctuations average out with increasing the system size N, as seen by comparing the curves for $N = 12$ and $N = 24$ systems. On average, the relations (2.97, 2.98) hold numerically despite the large fluctuations. This suggests that the system is at equilibrium during the type A stochastic dynamics, even though the freezing temperature $T_{1/2} = 0.20\,V(a)$ for $d = 2a$ is considerably lower than $T_{1/3}$. The singularities in temperature behavior of the quantities $\langle E \rangle$, C and $T\partial C/\partial T$ are less pronounced due to fluctuations, especially in the derivative of the heat capacity (lowest plot in the series). The transition features of a smaller system ($N = 12$) are sharper because it is possible to freeze it into a perfect ("flat") $n = 1/2$ ground state with a maximum average tilt $|\mathbf{t}|$, whereas the larger system ($N = 24$) always freezes into a state which has a domain structure with all three possible orientations of the tilt $\mathbf{t}$.

The behavior of the average energy and the heat capacity at $n = 1/2$ agrees with both the first and second order phase transition scenarios. Taking into account both the existence of a cubic invariant in the free energy expansion (2.84), and the double peaked distribution $p(E)$ in Fig. 2-9, we conclude that freezing into $n = 1/2$ ground state occurs via the first order phase transition. This transition is quite weak, which suggests that the coefficient B_3 in Eq. (2.84) is small.

Finally, let us compare the plots of the conductivity (Fig. 2-3) and average energy (Fig. 2-10) as functions of temperature for both $n = 1/2$ and $n = 1/3$ near the corresponding freezing transitions. There is an apparent similarity in the functional form

as well as excellent agreement in the transition temperatures between the two plots. This is in accord with the argument about the similarity of the critical behavior of average energy and kinetic coefficients [42]. Provided that conductivity is experimentally accessible in the quantum dots arrays, we suggest looking into singularities of the zero bias dc conductivity as a means of studying charge ordering in such systems.

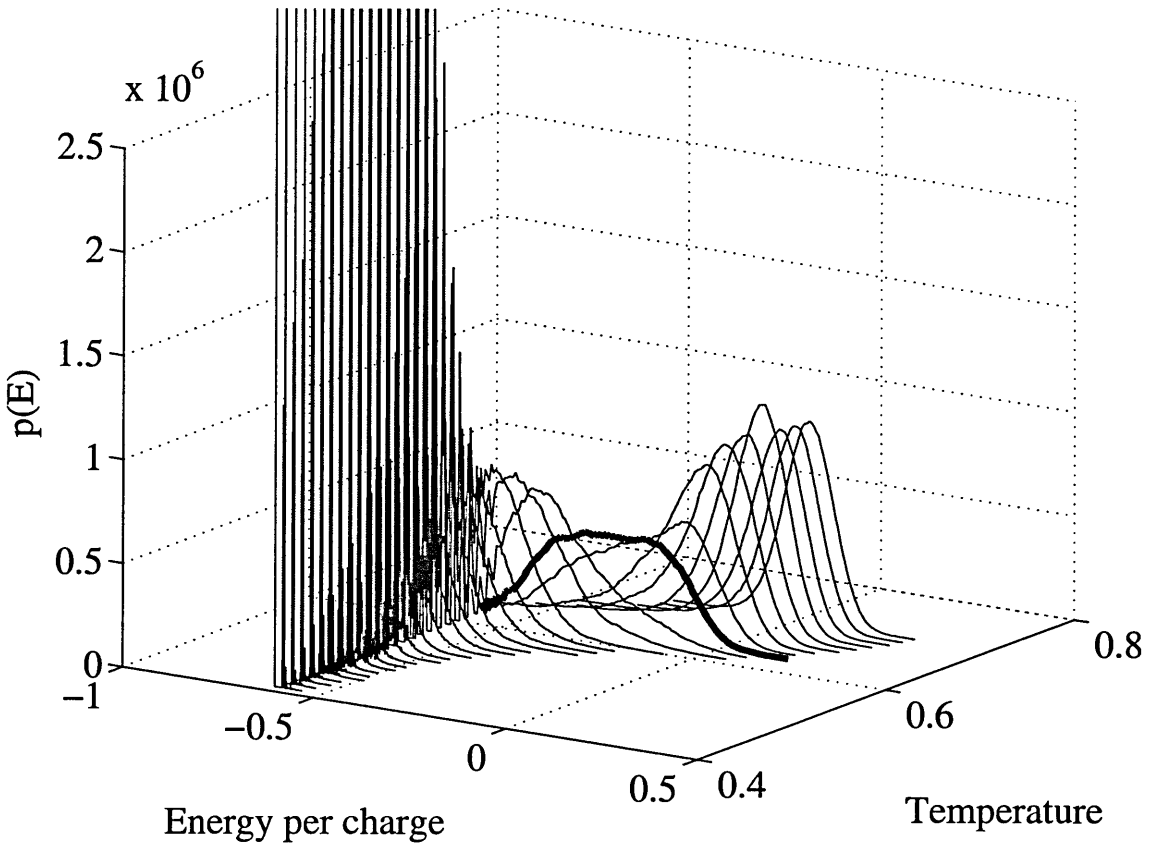

Figure 2-8: Energy histogram $p(E)$ for $n = 1/3$. The total number of trials $\mathcal{N} = 25{\cdot}10^6$ for each step in temperature. The type B dynamics was employed. Calculations were done for the screening length $d = 2a$. Histogram in bold corresponds to the phase transition at $T_{1/3} = 0.63\,V(a)$.

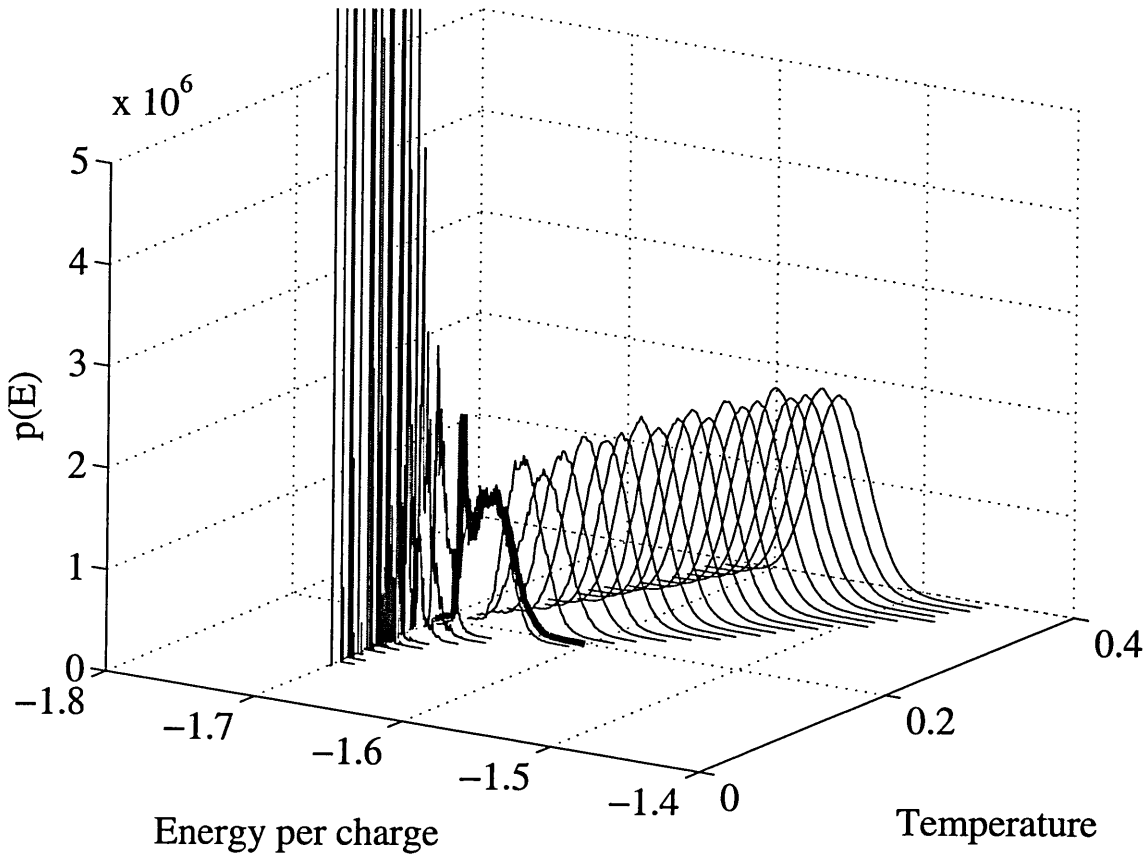

Figure 2-9: Energy histogram $p(E)$ for $n = 1/2$. The total number of trials $\mathcal{N} = 50 \cdot 10^6$ for each step in temperature. The nonconserving type A dynamics was used. Screening length was taken to be $d = 2a$. Histogram in bold corresponds to the phase transition at $T_{1/2} = 0.20\, V(a)$.

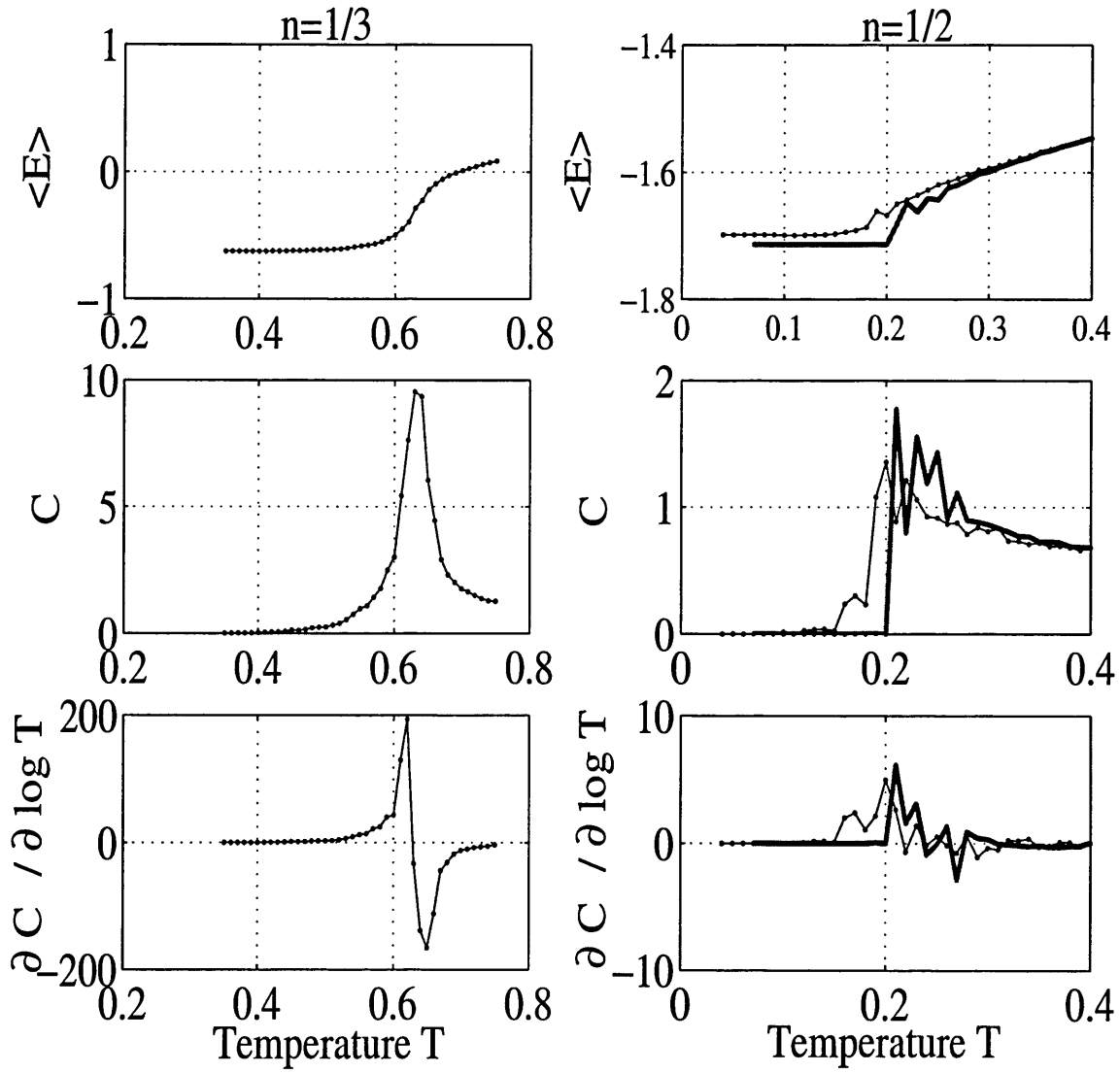

Figure 2-10: Phase transitions at $n = 1/3$ (left) and $n = 1/2$ (right). Given as a function of temperature: average energy $\langle E \rangle$ (above), heat capacity C (middle), and its derivative $\partial C / \partial \ln T$ (below), calculated as combinations of moments of the energy histograms $p(E)$ (Figs. 2-8, 2-9) according to Eqs. (2.94, 2.95, 2.96). For $n = 1/3$, the $N = 24$ patch is frozen into the ideal $\sqrt{3} \times \sqrt{3}$ ground state, Fig. 2-5 (A). The $n = 1/2$ $N = 24$ patch (fine curve in the right column of plots) is frozen into a polycrystalline state made of domains with different directions of the tilt $\mathbf{t}$, with $|\mathbf{t}| = \sqrt{2/3}$ in each domain. It has higher energy per electron and less pronounced transition features than the $N = 12$ patch (bold curve), which is frozen into the perfect ground state with the maximum tilt $|\mathbf{t}| = \sqrt{2/3}$. The curve corresponding to $N = 12$ patch has more noise due to the smaller system size.

2.4 Conclusions

To conclude, in this Chapter we considered charge ordering and dynamics of electrons on the triangular $2D$ array of quantum dots by mapping this system onto the triangular classical Ising spin model. The interactions between such "spins" are of the long range antiferromagnetic type due to the screened Coulomb repulsion between electrons on the dots. We have demonstrated that the long range nature of interaction yields the phase diagram which is more rich than that of the $\triangle$IAFM system. In particular, at electron density in the range $1/3 \leq n \leq 2/3$ there exists a temperature interval where the classical system of electrons exhibits collective behavior (correlated fluid phase).

The correlated fluid properties are described in terms of a height field order parameter. We have studied the height field dynamics by numerically calculating its effective rigidity. We have proven both numerically and by scaling arguments that the dislocation pairs binding phase transition does not take place in the correlated fluid. Scaling arguments show that the height order parameter is decoupled from the electron density at the large spatial scale, and that the corrections to the dynamics of the charged system due to fluctuations of the height field are local everywhere in the correlated fluid phase.

At low temperatures the correlated fluid freezes into the commensurate (solid) phase. Ordering in the ground states depends on the electron density n. We study the most pronounced phase transitions into the commensurate states at $n = 1/3,\ 2/3$ and at $n = 1/2$, and show that they are of the first order.

From the experimental standpoint, the novel feature of the charge ordering in the quantum dot array is the possibility for the conductivity measurements. We have shown that the zero bias dc conductivity singularities at the phase transitions are similar to those of the average energy of the system. This relates the system's dynamics with its charge ordering properties and suggests zero bias conductivity as an experimental probe of charge ordering.

Chapter 3

Transport

You do not know anything until you have practiced.

R. P. Feynman

In the previous Chapter we have found a phase diagram (Fig. 2-6) for an idealized lattice model of the nanocrystal arrays. We have also shown that conductivity measured at a low bias can be a probe of the system's properties in the ground state. In particular, we have related the singularities of conductivity to ordering phase transitions in Sec. 2.3.

In the present Chapter we study transport properties of the nanocrystal arrays in greater detail. As we have pointed out in Chapter 1 (Sec. 1.1.3), transport measurements are currently performed at a *high* bias, since the dot arrays appear to be very resistive. Such measurements always yield a power-law decaying current transient

$$I = I_0\, t^{-\alpha}\ , \quad 0 < \alpha < 1 \tag{3.1}$$

(Eq. (1.1), Sec. 1.1.3). This transient behavior has been previously explained by time-varying system's properties [17, 18, 19].

The aim of the present Chapter is to propose a novel model of transport in order to explain the behavior (3.1). Our phenomenological model of transport (described in Sec. 3.1 below) is based on a *stationary* Lévy process and therefore requires no time dependence of system's properties.

An important outcome of our model is a particular form of the *noise* in current. We calculate this noise in Sec. 3.2 below and show that it is given by a certain *power law* as a function of frequency. This power law is deterministically related to the power law (3.1) observed in current.

In Sec. 3.3 we analyze current and noise measurements performed on the nanocrystal arrays and show that they are consistent with the predicted non-Poissonian fluctuations in transport.

Finally, in Sec. 3.4 we discuss possible microscopic mechanisms that could result in the anomalous transport governed by the Lévy statistics.

3.1 Continuous time random walk model of transport

In the present Section we suggest an explanation for the transient response (3.1) without invoking any time dependence of the properties of the system. The key idea of the phenomenological model proposed below is that a non-stationary current (3.1) can arise in a system described by a *stationary* stochastic process.

Let us formulate our model of transport. We view the nanocrystal array as a host of $N \gg 1$ identical independent conducting channels switched in parallel. We assume that each channel is almost always closed (non-conducting). It opens up at random for a microscopically short interval τ_0 to conduct a current pulse that corresponds to a unit charge passing through, Fig. 3-1. Such a channel is completely characterized by the *waiting time distribution* (WTD) $p(\tau)$ of time intervals between successive pulses. We postulate this WTD to have a long power law tail:

$$p(\tau \gg \tau_0) \simeq \frac{a}{\tau^{1+\mu}} , \quad 0 < \mu < 1 . \tag{3.2}$$

The form of the distribution (3.2) is similar to the one given in Chapter 1 above in Eq. (1.14) for the dispersive transport. The short time behavior $p(\tau \sim \tau_0)$ does not affect the long time dynamics and will not be discussed here. The crucial observation

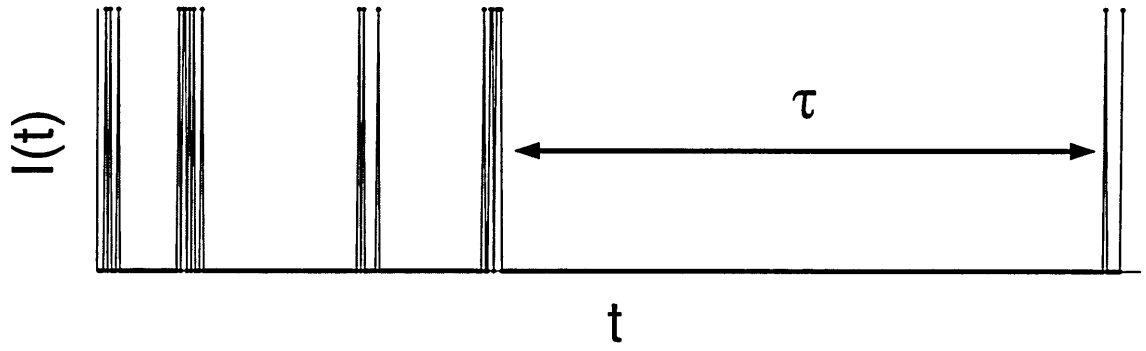

Figure 3-1: Current in a single conducting channel with a wide distribution of waiting times. Short current pulses are separated by very long waiting times $\tau \gg \tau_0$

is that *all* moments of $p(\tau)$ *diverge*,

$$\int_{\tau_0}^{\infty} d\tau\, \tau^n p(\tau) = \infty\ , \quad n = 1, 2, \ldots\ . \tag{3.3}$$

In Sec. 3.2 below we show that the WTD (3.2) yields a power law decay (3.1) with

$$\alpha = 1 - \mu \tag{3.4}$$

for the expected value of a current in a single channel. Qualitatively, the decrease in current with time can be undestood as follows: The expected value of the waiting time for a process (3.2) is *infinite* since it is given by the first moment of $p(\tau)$, $n = 1$ in Eq. (3.3). Thus if the stochastic process governed by the WTD (3.2) started infinitely early in the past, the expected value of the current is zero. Turning the bias on at $t = 0$ sets the clock for the process (3.2). Now for the measurement interval t waiting times $\tau \sim t$ can occur, as shown in Fig. 3-2 (note the double log scale). Observing the current over a longer time effectively increases the chances for a channel to be closed for larger time intervals, yielding the decay in current, the latter approaching zero in the infinite future. It is essential that in this transport picture *the system's properties are time independent*: the process (3.2) is *stationary*, i.e. $p(\tau)$ is independent of the measurement time t.

Continuous time random walks with long power law tails as in (3.2) (the so called

Lévy processes [35]) arise in various fields [36], from dispersive transport in amorphous semiconductors [28, 29, 30, 31] reviewed in Sec. 1.1.3 to the stock market fluctuations [59]. The main feature of such processes is that, as we show in the next section, due to divergent moments they violate the central limit theorem.

For a particular case of current in a conducting channel considered in the present Chapter, we will show that the Lévy statistics yields a large, non-Poissonian *noise* in current. In the next section we derive the noise spectrum that in this case is given by a power law of frequency, and find how the exponent of this law relates to the exponent α in the average current (3.1).

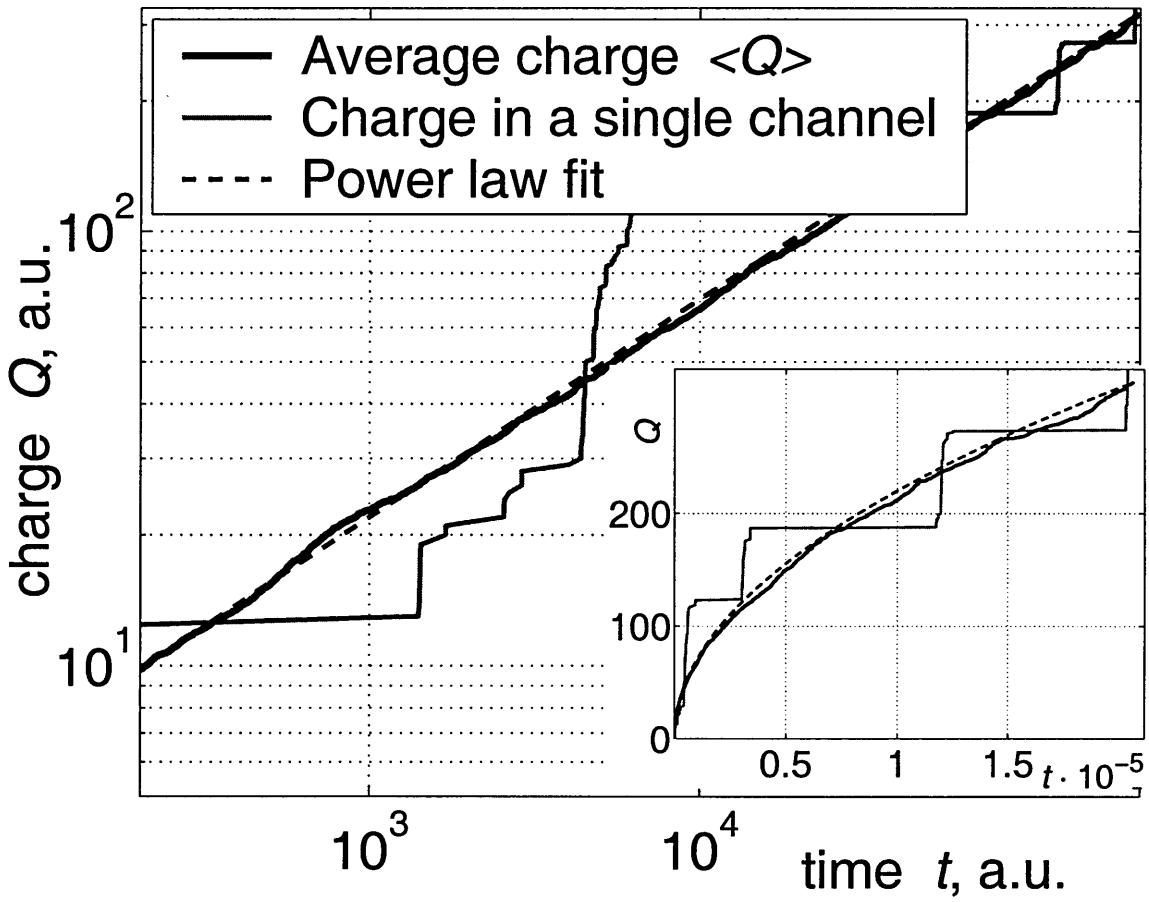

Figure 3-2: Net charge $Q(t)$ in a single channel and charge $\langle Q(t) \rangle$ averaged over $N = 100$ channels simulated according to the waiting time distribution (3.2) with μ=0.5 (plotted in the double log scale). Dashed line is a power law fit $Q \propto t^{\mu}$. *Inset:* Same plot in the linear scale. Charge in a single channel has extremely large noise and lacks self-averaging due to a wide WTD. It does not at all resemble the average $\langle Q \rangle$.

3.2 Calculation of current and noise

In the present Section we obtain expressions for average current and noise in a system of parallel conducting channels introduced in the previous Section. We first focus on the average current and noise in a single channel governed by an *arbitrary* waiting time distribution $p(\tau)$ between the current pulses. After that we study the case of a Lévy walk (3.2) and contrast it with the case of a conventional channel whose statistics is governed by the Poissonian process. Finally, we comment on the average current and noise in a system that consists of a number of identical independent parallel channels.

3.2.1 Single channel with an arbitrary WTD

Consider first the case of a *single channel* in which the probability for a waiting time τ between short current pulses to fall in the interval $[\tau,\ \tau + d\tau]$ is given by $p(\tau)d\tau$. The waiting time distribution $p(\tau)$ is assumed to be normalized,

$$\int_0^\infty p(\tau)d\tau = 1\ . \tag{3.5}$$

To derive current and noise in this channel, it is convenient to consider the current

$$I(t) = \sum_{i=1}^{\infty} \delta(t - t_i)\, e^{-\lambda t} \tag{3.6}$$

defined with a soft cutoff corresponding to a measurement time interval

$$\lambda^{-1} \gg \tau_0\ , \tag{3.7}$$

where τ_0 is the microscopic channel opening time introduced in the previous Section. Consider the Fourier component I_ω of the current (3.6):

$$I_\omega = \int dt\, I(t)\, e^{-i\omega t} = \sum_{n=1}^{\infty} e^{-zt_n}\ , \tag{3.8}$$

where

$$z = \lambda - i\omega \ , \tag{3.9}$$

and

$$t_n = \sum_{i=1}^{n} \tau_i \ . \tag{3.10}$$

We obtain the expected value of current in a single channel by averaging Eq. (3.8). Since waiting times τ_i are independent random variables distributed according to $p(\tau)$, this average is given by a geometric series:

$$\langle I_\omega \rangle = \frac{p_z}{1 - p_z} \ , \tag{3.11}$$

where the *characteristic function*

$$p_z \equiv \left\langle e^{-z\tau} \right\rangle = \int d\tau \, p(\tau) \, e^{-z\tau} \ . \tag{3.12}$$

The noise is defined as a reduced second moment,

$$\langle\langle I_{-\omega} I_\omega \rangle\rangle = \langle I_{-\omega} I_\omega \rangle - \langle I_{-\omega} \rangle \langle I_\omega \rangle \ . \tag{3.13}$$

The current correlator

$$\langle I_{-\omega} I_\omega \rangle = \sum_{n,n'=1}^{\infty} \left\langle e^{-\bar{z} t_{n'} - z t_n} \right\rangle \tag{3.14}$$

can be averaged using (3.10) and the fact that all the waiting times τ_i are independent random variables. This averaging yields

$$\langle I_{-\omega} I_\omega \rangle = \sum_{n=1}^{\infty} \left\langle e^{-2\lambda \tau_n} \right\rangle \left(1 + \sum_{m=1}^{\infty} \left\langle e^{-z\tau} \right\rangle^m + \text{c.c.} \right) . \tag{3.15}$$

The last formula is obtained by splitting summation into domains $n = n'$ and $n > n'$ with $m = n - n'$. After performing the geometric series summations in Eq. (3.15), for the noise (3.13) we obtain

$$\langle\langle I_{-\omega} I_\omega \rangle\rangle = \frac{p_{2\lambda} - p_z p_{\bar{z}}}{(1 - p_{2\lambda})(1 - p_z)(1 - p_{\bar{z}})} \ . \tag{3.16}$$

3.2.2 Current and noise in the case of a Lévy walk

Current average (3.11) and variance (3.16) obtained in the previous subsection are valid for any waiting time distribution. Consider now the power law WTD (3.2), whose characteristic function is

$$p_z = 1 - \frac{z^\mu}{A_\mu} , \quad |z|\tau_0 \ll 1 , \tag{3.17}$$

$$A_\mu = \frac{\mu}{a\Gamma(1-\mu)} . \tag{3.18}$$

Here τ_0 is a microscopic opening time for the WTD (3.2). In this case Eq. (3.11) yields average current

$$\langle I_\omega \rangle = A_\mu \, (\lambda - i\omega)^{-\mu} . \tag{3.19}$$

Fourier transforming Eq. (3.19) gives the average current as a function of time:

$$\langle I(t) \rangle = \mathcal{I}_0 \, t^{-\alpha} , \quad \lambda t \ll 1 , \tag{3.20}$$

where λ^{-1} is the measurement interval according to (3.6),

$$\alpha = 1 - \mu , \tag{3.21}$$

$$\mathcal{I}_0 = \frac{\mu \sin \pi\mu}{\pi a} . \tag{3.22}$$

Expression (3.20) is exactly the transient response (3.1) with the exponent (3.4).

For the noise, substituting the characteristic function (3.17) into Eq. (3.16) derived in the previous subsection, we obtain

$$\langle\langle I_{-\omega} I_\omega \rangle\rangle = A_\mu^2 \, \frac{z^\mu + \bar{z}^\mu - (2\lambda)^\mu - A_\mu^{-1}|z|^{2\mu}}{(2\lambda)^\mu \, |z|^{2\mu}} . \tag{3.23}$$

We are interested in the noise spectrum on the time scale much greater than the pulse width τ_0:

$$\lambda, \omega \ll \tau_0^{-1} . \tag{3.24}$$

Keeping only the leading terms in the numerator of (3.23), we obtain

$$\langle\langle I_{-\omega} I_{\omega} \rangle\rangle = A_{\mu}^{2} \, \frac{z^{\mu} + \bar{z}^{\mu} - (2\lambda)^{\mu}}{(2\lambda)^{\mu} \, |z|^{2\mu}} \; . \tag{3.25}$$

The limits of Eq. (3.25) are

$$\langle\langle I_{-\omega} I_{\omega} \rangle\rangle = \begin{cases} (2^{1-\mu} - 1) \, A_{\mu}^{2} \, \lambda^{-2\mu} \; , & \omega \ll \lambda \; , \\ 2^{1-\mu} A_{\mu}^{2} \cos \frac{\pi\mu}{2} \, (\lambda\omega)^{-\mu} \; , & \omega \gg \lambda \; . \end{cases} \tag{3.26}$$

Let us discuss our results (3.19), (3.20), and (3.26), contrasting them with the case of a conventional conducting channel governed by a Poissonian WTD

$$p^{\text{Poiss.}}(\tau) = \gamma e^{-\gamma\tau} \; . \tag{3.27}$$

For the average current in a single channel governed by the Lévy WTD (3.2) we have indeed obtained a *power law decay* (3.19) with a power $\alpha < 1$ given by (3.21), as it was anticipated in Sec. 3.1. The result (3.20) corresponds to the net charge

$$\langle Q(t) \rangle \sim t^{\mu} \; , \quad 0 < \mu < 1 \; , \tag{3.28}$$

increasing *sublinearly* with the measurement time t. We are going to show that this result is in sharp contrast with a conventional system. Consider a Poissonian WTD (3.27), whose characteristic function is given by

$$p_{z}^{\text{Poiss.}} = \frac{1}{1 + z\bar{\tau}^{\text{Poiss.}}} \; , \tag{3.29}$$

where

$$\bar{\tau}^{\text{Poiss.}} = \gamma^{-1} \tag{3.30}$$

is the *finite* expected value of the waiting time. Eq. (3.11) in this case yields average current

$$\langle I_{\omega} \rangle = \frac{1}{(\lambda - i\omega)\bar{\tau}} \; . \tag{3.31}$$

This current taken at zero frequency corresponds to the net charge that has passed through the channel between $t = 0$ and $t = \lambda^{-1}$. The latter grows *linearly* with time,

$$\langle Q \rangle^{\text{Poiss.}} = \frac{t}{\bar{\tau}^{\text{Poiss.}}} , \tag{3.32}$$

corresponding to a *constant* current

$$\langle I \rangle = \frac{d \langle Q \rangle}{dt} = \text{const} . \tag{3.33}$$

As for the noise, let us first consider the Poissonian channel. For the Poissonian WTD (3.27), Eq. (3.16) yields the *white noise* spectrum

$$\langle\langle I_{-\omega} I_{\omega} \rangle\rangle = \frac{1}{2} \langle I_{\omega=0} \rangle = \frac{1}{2\lambda\bar{\tau}} \tag{3.34}$$

for any frequency $\omega \ll \tau_0^{-1}$.

Let us first focus on the zero frequency limit of noise. In this limit the noise is just a variance of the charge that has passed through the channel during the time interval between $t = 0$ and $t = \lambda^{-1}$. The Poissonian result (3.34) means that this variance is proportional to the mean charge:

$$\left\langle\left\langle Q^2 \right\rangle\right\rangle^{\text{Poiss.}} = \frac{1}{2} \langle Q \rangle^{\text{Poiss.}} . \tag{3.35}$$

In other words, the *relative fluctuation*

$$\frac{\left(\left\langle\left\langle Q^2 \right\rangle\right\rangle^{\text{Poiss.}} \right)^{1/2}}{\langle Q \rangle^{\text{Poiss.}}} \propto t^{-1/2} \tag{3.36}$$

of the transported charge *decreases* with the measurement time. That is precisely what one obtains from the central limit theorem.

In the case of the WTD of the Lévy form (3.2), the $\omega \ll \lambda$ limit of (3.26) yields

that the dispersion in the charge Q transported through the channel

$$\Delta Q \equiv \left(\left\langle Q^2 \right\rangle - \langle Q \rangle^2\right)^{1/2} = \left(2^{1-\mu}-1\right)^{1/2} \langle Q \rangle \tag{3.37}$$

is proportional to the *net charge.* Hence the relative charge fluctuation $\Delta Q / \langle Q \rangle$ *does not decrease* with the measurement time t, violating the central limit theorem. In other words, the zero frequency noise in the net charge is extremely large when the channel is governed by the Lévy statistics. Fig. 3-2 shows that transport in a single channel is indeed dominated by large fluctuations.

It is possible to illustrate from a different perspective the fact that the noise in net charge in the case of the Lévy statistics is very large.

Consider a probability $\mathcal{P}_n(t)$ for exactly n current spikes occuring in a channel between 0 and t. For this quantity we may write an integral equation

$$\mathcal{P}_{n+1}(t) = \int_0^t dt'\, p(t-t')\, \mathcal{P}_n(t') \;, \tag{3.38}$$

where

$$\mathcal{P}_0(t) = \int_t^\infty d\tau p(\tau) \sim t^{-\mu} \;. \tag{3.39}$$

The integral in (3.38) is dominated by the singularity of the kernel (3.2). Thus

$$\mathcal{P}_{n+1}(t) \approx \mathcal{P}_n(t) \cdot \int_0^t dt'\, p(t-t') \equiv \mathcal{P}_n(t) \;, \quad 0 \le n < \mathcal{N} \;, \tag{3.40}$$

where the normalization $\int d\tau\, p(\tau) = 1$ has been employed. We obtain that configurations with

$$0 \le n < \mathcal{N} \tag{3.41}$$

current spikes are all approximately *equally probable* in the case of a WTD given by Eq. (3.2). The maximum number $\mathcal{N}$ of spikes for which this statement is valid can be found from the normalization $\sum \mathcal{P}_n = 1$:

$$\mathcal{N} \simeq \mathcal{P}_0^{-1} \sim t^\mu \ll t \;. \tag{3.42}$$

Finally, let us comment on the noise (3.26) in the case of a *finite frequency*. In the limit $\omega \gg \lambda$ the noise spectrum is proportional to the Fourier transform of the mean current, $\langle I_\omega \rangle$, and is given by a *power law* in frequency, in contrast to a white noise (3.34) for a Poissonian channel. This "colored" noise that is divergent at small frequencies once again underlines the difference of the Lévy statistics from the conventional Poissonian one.

3.2.3 The case of many channels

Having found the statistics of charge in a single channel, let us consider the case of a system with a large number $N \gg 1$ of independent parallel conducting channels. Although in our model any given channel lacks self-averaging, the current through a system with a large number of channels is a smooth power law. This is illustrated in Fig. 3-2, where the average charge is plotted as a function of time in the case of $N = 100$ independent channels. Fluctuations in the total current through a system with N parallel channels are reduced by a factor of $N^{-1/2}$. This noise reduction follows from the central limit theorem which is now applicable since we consider an *ensemble* of independent channels.

Furthermore, we have proven that the average current obtained from the model of independent channels is unchanged even if the channels are not completely identical, corresponding to spatially varying system properties. A simulated flat distribution of the exponent $0.45 < \mu < 0.55$ over a hundred channels yields average charge that is numerically very close to that in Fig. 1-3 for $\mu = 0.5$.

3.3 Comparison with experiment

In the previous Section we have shown that the current measured between time 0 and t in the model described in Sec. 3.1 leads to a non-Poissonian noise,

$$\langle\langle I_{-\omega} I_{\omega} \rangle\rangle \propto \begin{cases} t^{2\mu} , & \omega t \ll 1 \ , \\ t^{\mu} \omega^{-\mu} , & \omega t \gg 1 \ . \end{cases} \tag{3.43}$$

Here

$$I_{\omega} = \int_0^t dt' \, I(t') e^{i\omega t'} \tag{3.44}$$

is a Fourier transform of current. The noise (3.43) is proportional to $\langle I_{\omega} \rangle^2$ when $\omega \to 0$, and has a characteristic *power law spectrum* for large frequencies.

For the comparison with experiments that we consider in the present Section, it is crucial to note that the Lévy process (3.2) guarantees the *same* power law for the noise (3.43) and for the current (3.19),

$$\langle I_{\omega} \rangle \sim \omega^{-\mu} \ , \tag{3.45}$$

in the limit $\omega t \gg 1$. The exponent μ relates to the power law exponent in current (3.1) via Eq. (3.4).

Moreover, as we have pointed out in Sec. 3.2.3, averaging over $N \gg 1$ independent channels in our model simply reduces the noise by a factor of $N^{-1/2}$. It is important that the presence of many channels does not alter the power laws in current and noise, in particular preserving the relationship (3.4).

3.3.1 Current and noise

Let us now describe the current and noise measurements [2] performed on a single sample of a nanocrystal array.

We start from briefly describing the sample. The QDAs studied in Ref. [2] have been obtained by the procedures described in Chapter 1, Sec. 1.1.2 above, as well as in Refs. [17, 18]. This included self-assembly of an approximately 200nm thick film of

nearly identical CdSe nanocrystals, 3 nm in diameter, capped with trioctylphosphine oxide, an organic molecule about 1 nm long. The measurements have been performed in the field effect transistor geometry as described in Sec. 1.1.3. The sample has been annealed at 300C in vacuum inside of the cryostat prior to the electrical measurements. As discussed in Chapter 1, sample annealing reduces the distance between the nanocrystals and enhances electron tunneling [17].

The above sample parameters correspond to a QDA consisting of *ca.* 50 monolayers of quantum dots, with each layer $\approx 1.6 \cdot 10^5$ dots wide and 200 dots across. In this case one expects the effective number of effective conducting channels to be large, and observed fluctuations in current to be small, in accord with the discussion in Sec. 3.2.3.

To measure the noise, 200 current transients have been recorded, each $t = 100$ s long. Measurements have been made on a single sample continuously stored in vacuum, inside of a vacuum cryostat in the dark at 77K. Each current transient has been recorded for 100 s with a negative bias of -90 V. These periods of negative bias are separated from each other by a sequence of zero bias for 10 s, reverse pulse of $+90$ V for 100 s, and zero bias for 10 s, to eliminate the memory effects [17]. The current and noise measured for a substrate without the QDA yield that the typical current fluctuations are several orders of magnitude smaller than measured with the QDA.

Noise $\langle\langle I_{-\omega} I_{\omega} \rangle\rangle$ and average current $\langle I_{\omega} \rangle$ are found by performing an average over recorded current transients, treating them as independent experimental realizations.

Before analyzing the measurements performed in [2], it is important to note the following. An error in the average current $\langle I_{\omega} \rangle$ can yield an error proportional to $\langle I_{\omega} \rangle^2 \propto \omega^{-2\mu}$ in the noise spectrum. At the beginning of our measurement the current transients change from one to the next because of the memory effects described above in Sec. 1.1.3. For this reason we have discarded the first 150 transients. The noise (Fig. 3-3) has then been deduced from the remaining 50 transients, whose average current is nearly unchanged from one to the next. To further compensate for residual memory effects, we have normalized each transient by mutiplying it by a factor ≈ 1 to have the same net integrated charge.

Figure 3-3 shows the noise spectrum and the average current obtained in the way described above. The quantities have a similar power law behavior with $\mu \approx 0.72$ for $\omega t \gg 1$, $t = 100$ s. In Fig. 3-3 only finite frequency results are shown. The zero frequency noise that has been eliminated due to transients' normalization described above is not shown in this Figure. The measured power law spectrum differs from the $1/f$ noise usually found when conductivity is measured at these low frequencies [60]. We conclude that the results of Fig. 3-3 are consistent with the charge transport model based on the system's stationary properties proposed above in Sec. 3.1.

3.3.2 Memory effect

Based on our model the memory effect described in Sec. 1.1.3 can be explained as follows: Because of the very large typical waiting times $\tau \gg \tau_0$, any given channel is most likely non-conducting when the voltage is turned off at $t = t_1$. In addition, the very slow dynamics of a channel means that the channel's state may remain unchanged by the time the voltage is turned back on at $t = t_2$. In this case the channel conducts current as if the voltage had not been turned off. However, there is some chance that the channel changes its state (resets) while the voltage is turned off, with a probability $w_{12} \equiv w(t_2 - t_1)$. The function $w(t)$ monotonically grows between $w(\tau_0) = 0$ and $w(\infty) = 1$. The current at $t = t_2$ as a function of a *shifted time* $\tilde{t} = t - t_2$ is a sum over all channels:

$$I(\tilde{t}) = (1 - w_{12}) I_0 \, (\tilde{t} + t_2)^{-\alpha} + w_{12} I_0 \, \tilde{t}^{\,-\alpha} \, . \tag{3.46}$$

This has a singular part at $\tilde{t} = 0$ with amplitude

$$\tilde{I}_0 = w_{12} I_0 \tag{3.47}$$

determined by the reset probability $w_{12} < 1$. For $t_2 \gg \tau_0$, the first (regular) term in Eq. (3.46) is negligible compared to the second one. The current (3.46) is dominated by the second term, yielding an apparent suppression of the measured current

transient amplitude.

Experimentally it has been verified [61] that the reset probability defined as an amplitude ratio

$$w(t_2 - t_1) = \frac{\tilde{I}_0}{I_0} \tag{3.48}$$

is indeed a monotonic function of the time $t_2 - t_1$ with voltage off. Indeed, for waiting times from 10s to 10^4s between 100s long transients, we measure w_{12} in the range 0.65 to 0.85, as plotted in Fig. 3-4. The function w_{12} approaches unity when applying a reverse bias, exposing the dots to the bandgap light [18], or waiting for longer times.

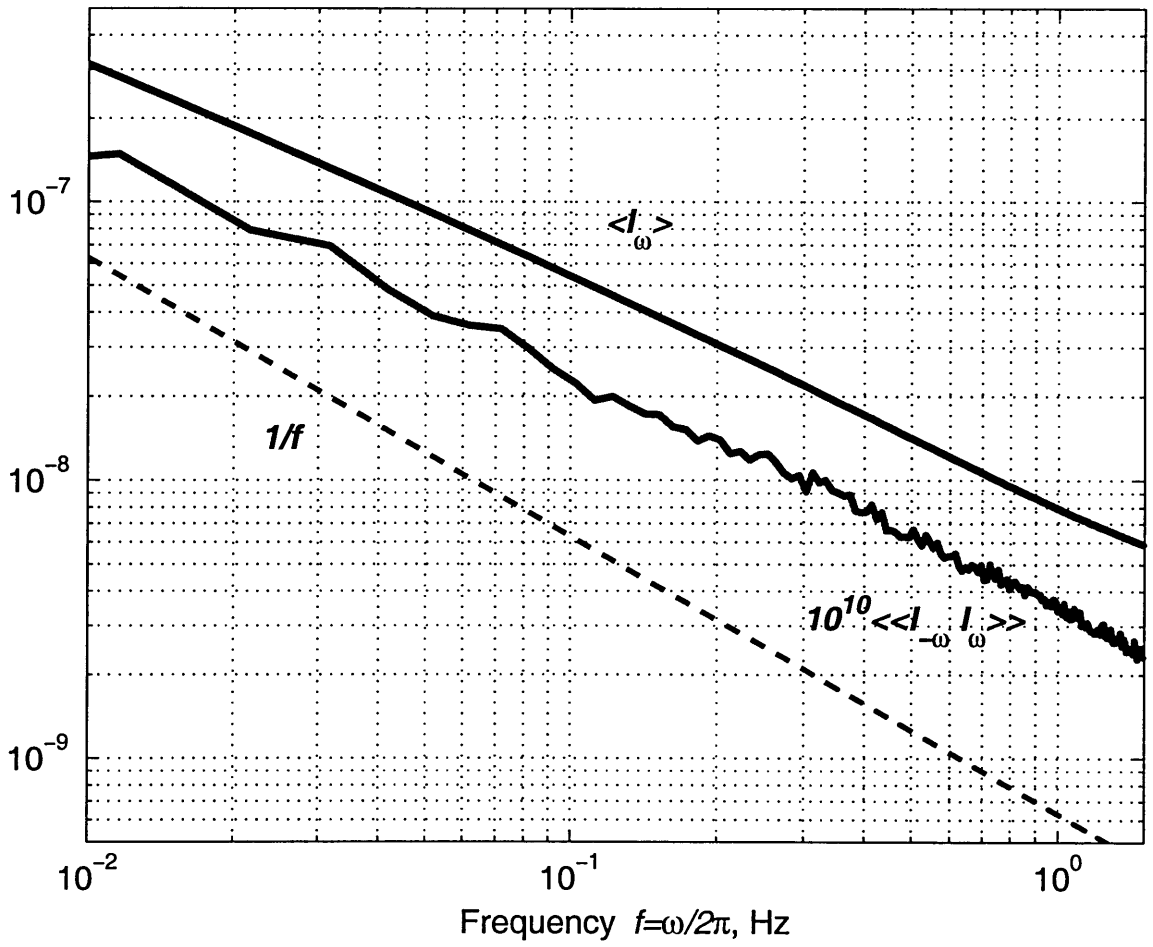

Figure 3-3: Current $\langle I_\omega \rangle$ and noise spectrum $\langle\langle I_{-\omega} I_\omega \rangle\rangle$. Averages are performed over 50 measurements on the same sample.

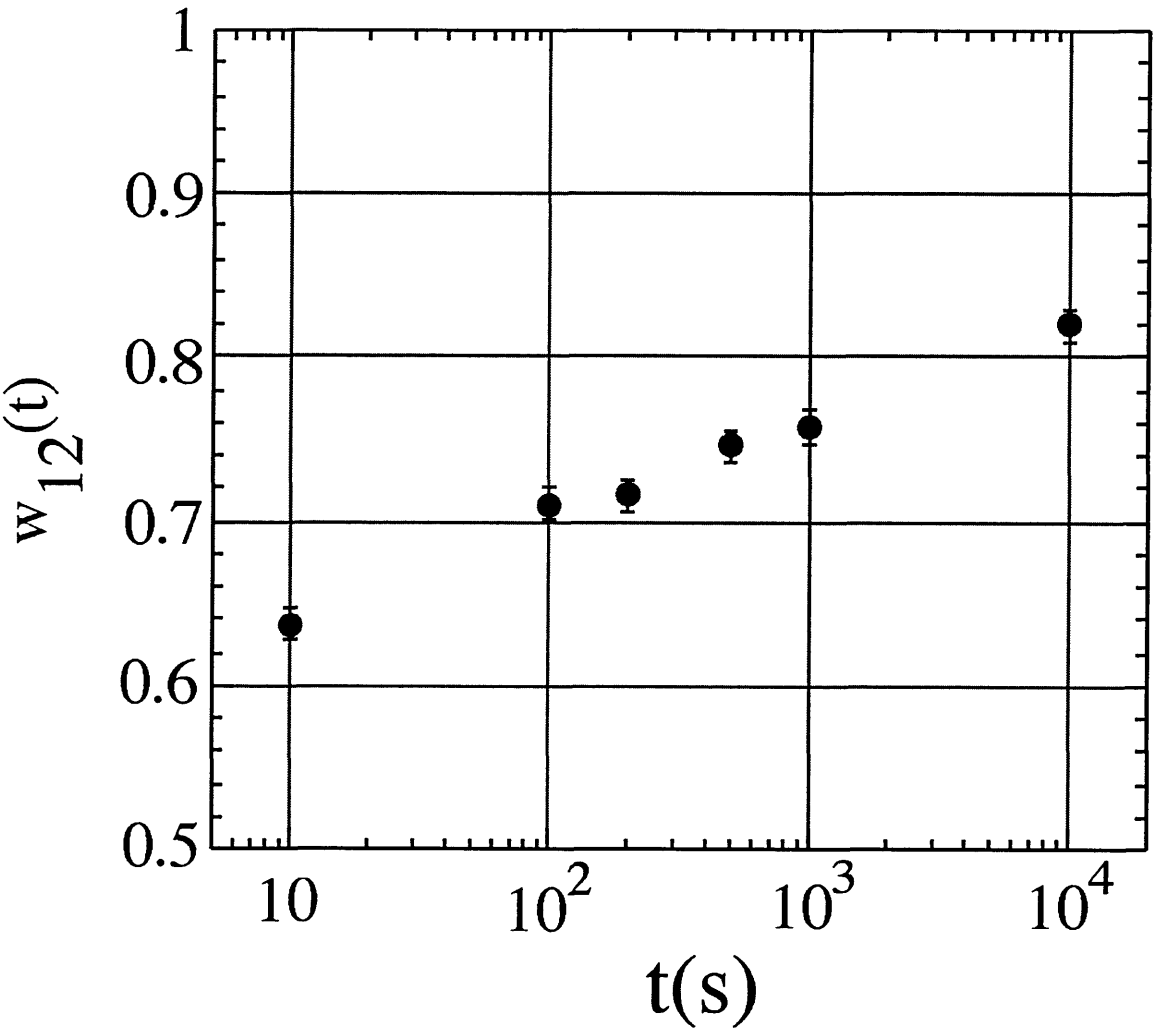

Figure 3-4: Reset probability $w(t)$ defined in Eq. (3.48) measured as a function of the "off" time $t = t_2 - t_1$

3.4 Discussion

In this Chapter we have suggested a novel phenomenological model of non-ohmic transport in the disordered system. This model, based on the Lévy statistics, yields a non-stationary transport in a *stationary* system.

We have shown that our model predicts a large non-Poissonian noise, and, in particular, a certain power law noise spectrum. In Sec. 3.3 we have used this prediction to test our model by analyzing current and noise measurements performed on the sample of semiconducting quantum dots.

We have found that the noise measurements on the QDA sample are consistent with our transport model. Based on that we suggest that the current transients that are observed in the QDAs [17] correspond to a *stationary* system of electrons on the array.

In the remaining part of this Chapter we discuss possible microscopic origins of the Lévy process governing conductivity of the dot arrays.

In Chapter 1 we have mentioned that the dot arrays are extremely resistive. This results in the failure of the standard picture of a (stationary) ohmic hopping conductivity based on the phonon relaxation mechanism.

It is reasonable to assume at this moment that the inobservably small ohmic conductivity in the dot arrays points at a possible phonon bottleneck for energy relaxation. Thus, we speculate that hops responsible for the observed current transients occur only between *aligned* energy levels of the neighboring dots. The assumption of having a WTD (3.2) requires that the energies of these levels fluctuate in time. We suggest two reasons for these fluctuations.

First, the energy ($\sim$ 0.1eV) dissipated per hop may provide the levels with the necessary energy reservoir for the fluctuations. Second, current-induced fluctuations in the electrostatic environment in the absense of screening may result in a random time-dependent chemical potential for each dot.

With dot energy levels strongly fluctuating, the waiting time for the electron to hop between the nearest neighbor dots is the time between successive alignments of

their levels. The level diffusion in energy itself can be governed by a continuous time random walk. If the latter is described by the WTD of the type (3.2),

$$\phi(\tau) \sim \frac{1}{\tau^{1+\nu}} , \tag{3.49}$$

and the distribution of hops in energy is

$$\psi(\epsilon) \sim \frac{1}{\epsilon^{1+\kappa}} , \tag{3.50}$$

it is possible to obtain (see Appendix) the corresponding power law exponent

$$\mu = \frac{\nu(\kappa - 1)}{\kappa} \tag{3.51}$$

for the nearest neighbor hopping WTD (3.2). The Gaussian diffusion in energy yields $\mu = 1/2$, as conjectured in Refs. [62, 63] to explain the Lévy statistics of a single dot fluorescence intermittency observed in [62, 64, 65, 66, 67].

So far in this Discussion we have found that a stationary energy level diffusion of the two neighboring nanocrystals can result in a waiting time distribution of the form (3.2) with the exponent (3.51) for the hops between them. Let us comment on what happens when a chain of such sites with fluctuating energy levels forms a conducting "channel". In this case the WTD for the channel has the same power law tail as the WTD for the nearest neighbor hops in the absense of Hubbard on-site correlations. The latter are believed to be unimportant since in experiments [17, 18] the estimated electron density per dot is small, of the order of $\sim 10^{-2} - 10^{-1}$.

To conclude, we have proposed a mechanism for a non-ohmic conductivity in a disordered system. In particular, we have showed that a non-stationary current response can arise in a stationary system governed by the Lévy statistics. The model is consistent with current and noise measurements in arrays of coated semiconducting nanocrystals. We believe that measurements of the fluorescence intermittency statistics and of the noise in current in *the same* nanocrystal array would help to understand the microscopic origin of the described effects.

Conclusions to Part I

In this Part of the Thesis I have considered charge ordering and transport in novel colloidal solids that are made of arrays of semiconductor nanocrystals. These arrays are shown to be a rich tunable system that can be used to study a variety of physical phenomena.

Charge ordering in triangular two-dimensional QDAs has been considered in Chapter 2 by mapping this system onto the triangular classical Ising spin model with antiferromagnetic couplings. An interplay of the geometrical lattice frustration with the long range nature of interaction yields a rich phase diagram (Fig. 2-6). A novel *correlated fluid phase* has been identified, in which hopping dynamics of classical electrons on a triangular lattice exhibits collective behavior. At low temperatures the correlated fluid freezes into the commensurate (solid) phase via the first order phase transition. System's dynamics have been related to its ordering types by relating the singularities of zero bias conductivity to freezing transitions.

Transport in QDAs has been considered in Chapter 3. There, a novel mechanism of non-ohmic transport in disordered systems has been suggested in order to explain current transients measured in recent experiments [17, 18]. Our transport model is based on the stationary stochastic process that is governed by the Lévy statistics. As a result it has been shown that a non-stationary current can arise in a stationary system. The proposed transport model predicts a power law noise spectrum that is consistent with recent measurements [2].

Bibliography

[1] D.S. Novikov, B. Kozinsky, L.S. Levitov, Ordered and disordered electron states in a quantum dot array, `cond-mat/0111345`

[2] D.S. Novikov, M. Drndic, M.A. Kastner, L.S. Levitov, M. Jarosz, M.G. Bawendi, Anomalous transport in quantum dot arrays, submitted

[3] M.A. Kastner, Artificial Atoms, Physic Today, **46**, 24 (January 1993)

[4] D. Rotman, Quantum Dot Com, Technology Review, p.51, Jan/Feb 2000

[5] C.B. Murray, D.J. Norris, and M.G. Bawendi, J. Am. Chem. Soc.**115**, 8706 (1993)

[6] C.B. Murray, C.R. Kagan, M.G. Bawendi, Self-Organization of CdSe Nanocrystallites into Three-Dimensional Quantum Dot Superlattices, Science **270**, 1335 (1995)

[7] C.B. Murray, C.R. Kagan, M.G. Bawendi, Synthesis and characterization of monodisperse nanocrystals and close-packed nanocrystal assemblies, Annu. Rev. Mater. Sci. **30**, 545 (2000)

[8] D. Heitmann, J.P. Kotthaus, Physics Today **46** (1), 56 (1993);
H.Z. Xu, W.H. Jiang, B.Xu, et al., J. Cryst. Growth **206** (4), 279-286 (1999), and *ibid.* J. Cryst. Growth **205** (4), 481-488 (1999)

[9] B. Meurer, D. Heitmann, and K. Ploog, Single electron charging of quantum dot atoms, Phys. Rev. Lett. **68**, 1371 (1992)

[10] G.Medeiros-Ribeiro, F.G.Pikus, P.M.Petroff, A.L.Efros, Single-electron charging and Coulomb interaction in InAs self- assembled quantum dot arrays, Phys. Rev. B **55**, 1568 (1997);

[11] A.I. Yakimov, A.V. Dvurechenskii, V.V. Kirienko, A.I. Nikiforov, C.J. Adkins, Oscillations of hopping conductance in an array of charge-tunable self-assembled quantum dots J.Phys. C **11** (48) 9715-9722 (1999)

[12] E. Ribeiro, E. Muller, T. Heinzel, H. Auderset, K. Ensslin, G. Medeiros-Ribeiro, P.M. Petroff, InAs self-assembled quantum dots as controllable scattering centers near a two-dimensional electron gas Phys. Rev. B**58**, 1506 (1998);
S. Cin, D.D. Arnone, H.P. Hughes, D. Whittaker, M. Pepper, and D.A. Ritchie, Novel effects produced on a two dimensional electron gas by introducing InAs dots in the plane of the quantum well, Physica E **6**, 276 (2000)

[13] A. Groshev, G. Schön, Physica B **189** (1-4), 157-164 (1993);
T. Takagahara, Optoelect. Dev. Tech. **8**, 545 (1993); Surf.Sci.**267**, 310 (1992);
O. Heller, P. Lelong, G. Bastard, Capacitance of InAs quantum dot arrays in a mean field approach Physica B **251**, 271-275 (1998)

[14] S. Teitel, C. Jayaprakash, Phys. Rev. Lett. **51**, 1999 (1983);
T.C. Halsey, J.Phys. C **18**, 2437 (1985);
S.E. Korshunov, G.V.Uimin, J. Stat. Phys. **43**, 1 (1986); S.E. Korshunov, *ibid.* **43**, 17 (1986);
E. Granato, J.M. Kosterlitz, J. Lee, and M.P. Nightingale, Phys. Rev. Lett. **66**, 1090 (1991);
J.-R. Lee, S. Teitel, Phys. Rev. Lett. **66**, 2100 (1991);

[15] J.E. Mooij, G. Schön, in *Single Charge Tunneling*, eds H. Grabert and M.H. Devoret, (Plenum, New York, 1992), Chapter 8 and references therein;
Proceedings of the NATO Advanced research Workshop on Coherence in Supercfonducting Networks, Delft, eds. J.E. Mooij, G. Schön, Physica **142**, 1-302 (1988);

H.S.J.van der Zant, et al., Phys. Rev. B **54**, 10081 (1996);
A.van Oudenaarden, J.E. Mooij, Phys. Rev. Lett.**76**, 4947 (1996)

[16] C.A. Leatherdale, C.R. Kagan, N.Y. Morgan, S.A. Empedocles, M.A. Kastner, M.G. Bawendi, Photoconductivity in CdSe quantum dot solids, Phys. Rev. B **62**, 2669 (2000)

[17] N.Y. Morgan, C.A. Leatherdale, M. Drndic, M. Vitasovic, M.A. Kastner, M.G. Bawendi, Electronic transport in films of colloidal CdSe nanocrystals, Phys. Rev. B **66**, 075339 (2002);
M. Drndic, M. Vitasovic, N.Y. Morgan, M.A. Kastner, M.G. Bawendi, Transport properties of annealed CdSe nanocrystal solids, J. Appl. Phys. **92**, 7498 (2002)

[18] N.Y. Morgan, *Electronic Transport in CdSe Quantum Dot Arrays*, Ph.D. dissertation, Massachusetts Institute of Technology, Departmnent of Physics, May 2001

[19] D.S. Ginger and N.C. Greenham, J. Appl. Phys. **87**, 1361 (2000)

[20] R.A.M. Hikmet, D.V. Talapin, and H. Weller, Study of conduction mechanism and electroluminescence in CdSe/ZnS quantum dot composites, J. Appl. Phys. **93**, 3509 (2003)

[21] V.K. La Mer, R.H. Dinegar, J. Amer. Chem. Soc. **72**, 4847 (1950)

[22] H. Reiss, J. Chem. Phys. **19**, 482 (1951)

[23] I.M. Lifshitz and V.V. Slyozov, J. Phys. Chem. Solids **19**, 35 (1961);
Y. De Smet, L. Deriemaeker, R. Finsy, Langmuir **13**, 6884 (1997);
H. Grätz, Scripta Materialia **37**, 9 (1997)

[24] M.V. Artemyev, V. Sperling, and U. Woggon, J. Appl. Phys. **81**, 6975 (1997)

[25] N.F. Mott and E.A. Davis, *Electronic Processes in Non-Crystalline Materials*, 2nd ed. Oxford University Press, Oxford (1979)

[26] B.I. Shklovskii, A.L. Efros, *Electronic Properties of Doped Semiconductors*, Springer-Verlag, New York (1984)

[27] Z. Ovadyahu, M. Pollak, Disorder and magnetic field dependence of slow electronic relaxation, Phys. Rev. Lett. **79**, 459 (1997)

[28] H. Scher, E.W. Montroll, Anomalous transit-time dispersion in amorphous solids, Phys. Rev. B **12**, 2455 (1975);

[29] F.W. Schmidlin, Phys. Rev. B **16**, 2362 (1977); J. Noolandi, Phys. Rev. B **16**, 4466 (1977); J. Noolandi, Phys. Rev. B **16**, 4474 (1977);

[30] S.D. Baranovskii, V.G. Karpov, Sov.Phys.: Semiconductors, **19**, 336 (1985)

[31] J. Orenstein, M.A. Kastner, Phys. Rev. Lett. **46**, 1421 (1981);
T. Tiedje, A. Rose Solid State Commun. **37**, 49 (1981);

[32] A. Miller and E. Abrahams, Impurity Conduction at Low Concentrations, Phys. Rev. 120, 745 (1960)

[33] M.E. Sharfe, Phys. Rev. B **2**, 5025 (1970)

[34] G. Pfister, Phys. Rev. Lett. **33**, 1474 (1974)

[35] P. Lévy, *Théorie de l'Addition des Variables Aléatoires*, Gauthier Villars, Paris (1954); B.V. Gnedenko and A.N. Kolmogorov, *Limit distributions for Sums of Independent Random Variables*, Addison Wesley, Reading, MA (1954); see also Ref. [36]

[36] For a review and references see J.-P. Bouchaud, A. Georges, Anomalous diffusion in disordered media – statistical mechanisms, models and physical applications, Phys. Rep. **195**, 127 (1990)

[37] R.A. Street, *Hydrogenated amorphous silicon*, Cambridge University Press, Cambridge, 1991

[38] R.A. Street, Solid State Communications 39, 263 (1981)

[39] M.J. Powell, Appl. Phys. Lett. **43**, 597 (1983); M.J. Powell, C. van Berkel, A.R. Franklin, S.C. Deane and W.I. Milne, Phys. Rev. B **45**, 4160 (1992)

[40] K.Kawasaki, Phys. Rev. **148**, 375 (1966); K. Kawasaki, in *Phase Transitions and Critical Phenomena*, C. Domb and M.S. Green, eds, Vol. 2 (Academic Press, London, 1972)

[41] R.J. Glauber, J. Math. Phys.**4**, 294 (1963)

[42] P.C. Hohenberg, B.I. Halperin, Rev. Mod. Phys. **49**, 435 (1977)

[43] G.H. Wannier, Phys.Rev. **79**, 357 (1950); J. Stephenson, J. Math. Phys. **5**, 1009 (1964); J. Math. Phys. **11**, 413 (1970)

[44] H.W.J. Blöte and H.J. Hilhorst, J. Phys. A**15**, L631 (1982);

[45] B. Nienhuis, H.J. Hilhorst, and H.W.J. Blöte, J. Phys. A**17**, 3559 (1984)

[46] L.D. Landau, E.M. Lifshits, *Statistical Physics, Part I*, Pergamon Press (1969)

[47] *M.C. Escher: The Graphic Work.* TASCHEN America (1996)

[48] For a review of roughening, see J.D. Weeks, in T. Riste (Ed.), *Ordering in Strongly Fluctuating Condensed Matter Systems*, Plenum Press, 1980

[49] V.L. Berezinskii, Sov. Phys. JETP **32** 493 (1971);
J.M. Kosterlitz and D.J. Thouless, J. Phys. C**6**, 1181 (1973); J.M. Kosterlitz, *ibid.***7**, 1046 (1974)

[50] B.I. Halperin and D.R. Nelson, Phys. Rev. Lett. **41** 121 (1978); A.P. Young, Phys. Rev. B **19** 1855 (1979)

[51] A.F. Andreev, Zh. Eksp. Teor. Fiz. **80**, 2042 (1981); Sov. Phys. JETP **53**, 1063 (1982)

[52] J. Stephenson, J. Math. Phys. A**11**, 413 (1970)

[53] C. Zeng and C.L. Henley, Phys. Rev. B**55**, 14935 (1997)

[54] H. Yin, B. Chakraborty, N. Gross, Phys. Rev E **61**, 6426 (2000)

[55] H.W.J. Blöte, M.P. Nightingale, X.N. Wu, A. Hoogland, Phys. Rev. B**43**, 8751 (1991)

[56] A.M. Tsvelik, *Quantum Field Theory in Condensed Matter Physics*, Cambridge University Press, Cambridge, 1996

[57] P. Chandra, P. Coleman, and L.B. Ioffe, Phys. Rev. B **49**, 12897 (1994)

[58] E. Domany, M. Schick, J.S. Walker, R.B. Griffiths, Phys. Rev. B **18**, 2209 (1978)

[59] J.-P. Bouchaud, An introduction to statistical finance, Physica A **313**, 238 (2002)

[60] P. Dutta and P.M. Horn, Low-frequency fluctuations in solids: $1/f$ noise, Rev. Mod. Phys. **53**, 497 (1981)

[61] M. Drndic, D.S. Novikov, unpublished

[62] K. T. Shimizu, R.G. Neuhauser, C.A. Leatherdale, S.A. Empedocles, W.K. Woo and M.G. Bawendi, Phys. Rev. B **63**, 205316 (2001)

[63] Y. Jung, E. Barkai, R.J. Silbey, Chemical Physics **284**, 181 (2002)

[64] Nirmal M, Dabbousi BO, Bawendi MG, *et al.*, Fluorescence intermittency in single cadmium selenide nanocrystals, Nature **383**, 802 (1996)

[65] Kuno M, Fromm DP, Hamann HF, Gallagher A, Nesbitt DJ J. Chem. Phys. **112**, 3117 (2000); J. Chem. Phys. **115**, 1028 (2001)

[66] G. Messin, J.P. Hermier, E. Giacobino, P. Desbiolles, M. Dahan, Opt. Lett. **26**, 1891 (2001)

[67] X. Brokmann, J.-P. Hermier, G. Messin, P. Desbiolles, J.-P. Bouchaud, M. Dahan, Phys. Rev. Lett. **90**, 120601 (2003)

[68] L.S. Levitov and A.V. Shytov, *Green's functions. Theory and practice*, Fizmatlit, Moscow, 2002 (in Russian)

Part II

Transport in Carbon Nanotubes

Chapter 4

Introduction

In the present Part of this Thesis I will focus on another promising class of artificial systems that can be building blocks of novel materials and devices, as well as be utilized to study new physical phenomena. *Carbon nanotubes* comprise a broad class of chemically similar molecules composed of a very large number of Carbon atoms. It is remarkable that the chemically similar structure of nanotubes gives rise to an extreme diversity of their properties. In fact, nanotubes whose cicumferences differ by a single Carbon atom can have opposite electronic properties, corresponding to those of a metal and of a semiconductor [10].

During a bit more than a decade since their discovery in 1991 [4], Carbon nanotubes have attracted a great deal of attention of researches in a variety of fields [10, 11]. Besides their potential technological applications [5, 6, 7, 14, 9], nanotubes are a testing ground for novel physical phenomena involving strong electron correlations [31, 28, 29, 32, 34].

In the present Part of the Thesis I will focus on a set of physical effects in nanotubes that can be manifest in electron transport. These effects will include the ones that appear already at the single electron level, as well as those specific to electron interactions.

I will start this Part by briefly reviewing selected experiments and outlining basic nanotube properties in Chapter 4. The main goal of the present Chapter will be to develop a single particle description of nanotubes in terms of the Dirac fermions.

In Chapter 5 I will demonstrate that interesting nanotube properties arise already at the level of noninteracting electrons due to the Dirac nature of the low energy spectrum. In particular, I will consider a theory [1] of a field effect and screening of the external electric field by nanotube electrons. This screening will be linked to the chiral anomaly that is inherent to the Dirac fermions.

In Chapter 6 I will describe a proposal to realize adiabatic charge pump based on the coupling of a semimetallic carbon nanotube to a slowly moving surface acoustic wave.

Finally, In Chapter 7 I will consider correlation effects in a nanotube in an external periodic potential. I will demonstrate that due to electron interactions, novel interaction-induced incompressible states exist when the electron density is commensurate with the potential period.

4.1 Basic properties of nanotubes

In this Thesis I will consider only single wall carbon nanotubes (NTs). Any such tube can be envisioned as a two-dimensional honeycomb lattice of Carbon atoms ("graphene sheet") rolled into a hollow cylinder [10, 11]. In this system all chemical bonds are satisfied and are very strong. This yields very high thermal, chemical and mechanical stability [14].

The purest nanotubes are currently grown using electric arc [42] and laser ablation [43] methods. High quality of the tubes obtained by these means is due to their creation at very high temperatures ($\sim$ 2000 C) [11]. Another method to grow NTs is based on the chemical vapor deposition techniques using catalyst particles and hydrocarbon precursors [44]. This method is very promising in terms of scalability of NT production.

The most remarkable feature of carbon nanotubes is their diversity. As it will be shown in the following Section, depending on a particular way of rolling the graphene sheet into a cylinder ("chirality"), a nanotube can be a semiconductor, a semimetal, or a metal [10]. This theoretically predicted property has been recently observed

experimentally using the STM techniques. Semiconductor energy gaps have been measured in Refs. [12, 13], and much smaller energy gaps in semi-metallic tubes have been observed in Refs. [19].

In addition to STM measurements, the information about the nanotube structure can be obtained by using the Raman spectroscopy [15]. This method, pioneered at MIT by the group of M.S. Dresselhaus and reviewed in Ref. [16], is capable of completely identifying the nanotube chirality.

Such a variability of NT properties stems from a semimetallic nature of the graphene sheet reviwed below in Section 4.2. A possibility of having nanotubes with drastically different properties is very attractive in many fields. However, this same feature can be vicious from the practical standpoint. Indeed, all the existing nanotube synthesis methods do not give any control on the resulting tube chirality and, therefore, produce all sorts of tubes at random.

Let us now briefly focus on transport properties of nanotubes. Transport in a nanotube is determined by the NT type.

The semiconducting nanotube properties have been demonstrated in the field effect geometry [41]. These experiments have shown that a semiconducting nanotube can be utilized as the thinnest field-effect transistor.

Metallic nanotubes are shown to be the purest one dimensional conductors [40, 35] with their conductance approaching the theoretical limit $4e^2/h$ [39]. These tubes also exhibit Luttinger liquid properties of a strongly interacting 1D metal [28, 29]. Luttinger effects in nanotubes have been observed in the tunneling measurements reviewed in Ref. [34].

Research efforts in the area of nanotubes are stimulated by a wide range of potential NT applications [5, 6, 7, 14, 9]. The latter range from prospects of using NTs in molecular electronics as the wires and logic gates in the smallest chips [5, 6, 14, 9] to making the strongest composite materials [7]. In the same range one can name usage of NTs as single molecule sensors and probes [17], as well as applications in flat panel displays using electron field emission [8].

4.2 Single electron description

The goal of the present Section is to develop a single particle treatment of the electronic NT spectrum. We will derive a low energy description of NT properties in terms of the Dirac fermions [10]. This will allow us to desrcibe qualitatively different classes of NTs, as well as will serve a basis for the rest of this Part.

In Sec. 4.2.1 we will review the basics of the theory of electron states of the 2D Carbon monolayer, making a connection with the 2D Dirac equation. This will provide a good starting point for the following discussion of nanotubes in external fields in the rest of the Thesis. We shall start with the tight-binding description of the Carbon π band (Sec. 4.2.1), following the approach of DiVincenzo and Mele [27], remind how the Dirac equation arises in this system and then consider electron coupling to external electro-magnetic fields.

After that, in Sec. 4.2.2 we will discuss the single electron NT spectrum obtained from the effective 1D Dirac equation. We will classify nanotubes with respect to the values of the gap at the band center, as well as study the effect of a parallel magnetic field on the NT properties.

4.2.1 Tight-binding model for a Carbon monolayer

The tight-binding Hamiltonian on a honeycomb lattice of Carbon atoms with hopping amplitude t between adjacent sites has the form

$$\epsilon\psi(r) = -t \sum_{|r'-r|=a_{cc}} \psi(r') \ , \tag{4.1}$$

where r' are the nearest neighbors of the site r, and a_{cc} is interatomic spacing. In Carbon, $t \approx 3\,\mathrm{eV}$, $a_{cc} = 0.143\,\mathrm{nm}$. For simplicity, and because the electron spectrum is $\epsilon \to -\epsilon$ symmetric, from now on we shall ignore the minus sign in (4.1).

Zero chemical potential in (4.1) describes the half-filled π band, i.e., the density of one electron per site. For an infinite system, the states of the problem (4.1) are

plane waves and the spectrum is given by

$$\epsilon(k) = \pm t \left| \sum_i e^{i\mathbf{k}\cdot\mathbf{r}_i} \right| , \tag{4.2}$$

where $\mathbf{r}_i$ are the nearest-neighbor bond vectors. This is a spectrum of a *semimetal* with the conduction ($\epsilon(k) > 0$) and valence ($\epsilon(k) < 0$) subbands touching each other at two points K and K' in the Brillouin zone (Fig. 4-1).

The tight-binding band width $6t \simeq 18\,\mathrm{eV}$ is much larger than the energies of the states close to the band center considered below. Because of that it is useful to project the problem (4.1) on the subspace of states with $|\epsilon| \ll t$ and derive an effective low energy Hamiltonian for such states. To carry out the projection, we note that there are only four independent states with $\epsilon = 0$. These states form two complex valued conjugate pairs which we denote as $u(r)$, $v(r)$, $\bar{u}(r)$, $\bar{v}(r)$. It is convenient to choose the states u and v to be zero on one of the two sublattices of the honeycomb lattice. On the other sublattice each state takes the values 1, $\omega = e^{\frac{2\pi}{3}i}$ and $\bar{\omega} = e^{-\frac{2\pi}{3}i}$ (see Fig. 4-2). The states $u(r)$ and $v(r)$ have the same quasimomentum of a value $4\pi/3\sqrt{3}a_{cc}$, opposite to that of the states $\bar{u}(r)$ and $\bar{v}(r)$. Each pair of states $u(r)$, $v(r)$ and $\bar{u}(r)$, $\bar{v}(r)$ forms a basis at the points K and K', respectively.

Projecting the wave function $\psi(r)$ on $u(r)$ and $v(r)$ and, respectively, on $\bar{u}(r)$ and $\bar{v}(r)$ defines *Dirac spinor components* for each of the two points K and K'. We focus on the u, v pair and write the states near the point K with small energies $|\epsilon| \ll t$ as linear combinations

$$\psi(r) = \psi_1(r)u(r) + \psi_2(r)v(r) \tag{4.3}$$

with the envelope functions $\psi_{1,2}(r)$ varying on the scale much larger than the interatomic spacing a_{cc}. By substituting the wave function (4.3) in the tight-binding Hamiltonian (4.1) we have

$$\epsilon\,\psi_1(r) = t\left\{\psi_2(r-a) + \bar{\omega}\psi_2(r-\omega a) + \omega\psi_2(r-\bar{\omega}a)\right\} \tag{4.4}$$

$$\epsilon\,\psi_2(r) = t\left\{\psi_1(r+a) + \omega\psi_1(r+\omega a) + \bar{\omega}\psi_1(r+\bar{\omega}a)\right\} \tag{4.5}$$

where a is a shorthand notation for a_{cc}. Here the products za with unimodular complex numbers $z = 1, \omega, \bar{\omega}$ in the arguments of $\psi_{1,2}$ are understood in terms of 2D rotations of the vector $a\hat{\mathbf{x}}$ by $\arg z$.

Expanding slowly varying $\psi_{1,2}(r)$, we obtain

$$\begin{aligned} \epsilon\psi_1(r) &= -\hbar v(\partial_x - i\partial_y)\psi_2(r) \\ \epsilon\psi_2(r) &= \hbar v(\partial_x + i\partial_y)\psi_1(r) \end{aligned} , \tag{4.6}$$

where

$$v = \frac{3t\, a_{cc}}{2\hbar} . \tag{4.7}$$

The Hamiltonian (4.6) defines massless Dirac fermions with the linear spectrum

$$\epsilon(k) = \pm\hbar v|\mathbf{k}| . \tag{4.8}$$

In Carbon, the velocity $v = 8 \cdot 10^7$cm/s. Similar relations hold for the point K'.

Eqs.(4.6) can be cast in the conventional Dirac form $\epsilon\psi = \mathcal{H}\psi$ with

$$\mathcal{H} = v\,\alpha \cdot \mathbf{p} = v\,(\alpha_1 p_1 + \alpha_2 p_2) \tag{4.9}$$

for the two-component wave function $\psi = (\psi_1, \psi_2)$, with $\alpha_{1,2}$ given by the Pauli matrices:

$$\alpha_1 = \sigma_2 , \quad \alpha_2 = -\sigma_1 . \tag{4.10}$$

The Hamiltonian near the K' point can be derived in a similar way. The result has the form (4.9) with a sign change in the second term:

$$\alpha_1 = \sigma_2 , \quad \alpha_2 = \sigma_1 . \tag{4.11}$$

In the present Thesis we shall consider electrons in the presence of external electromagnetic fields. The minimal form of the coupling to external fields follows from the

gauge invariance:

$$\mathcal{H} = v\,\alpha \cdot (\mathbf{p} - \tfrac{e}{c}\mathbf{A}) + e\varphi \ , \tag{4.12}$$

where φ and $\mathbf{A}$ are the scalar and vector electro-magnetic potentials. The effect of electron spin, ignored here for simplicity, can be included in (4.12) via a Zeeman term.

The equation (4.12) describes the lowest order approximation in the gradients of $\psi_{1,2}$ and the potentials φ and $\mathbf{A}$. Here we consider the exact tight-binding equations in the presence of external fields:

$$\epsilon\,\psi_1(r) = t\left(\sum_{z=1,\omega,\bar{\omega}} \bar{z}\, e^{i\gamma_{r,\,r-za}}\psi_2(r-za)\right) \tag{4.13}$$

$$\epsilon\,\psi_2(r) = t\left(\sum_{z=1,\omega,\bar{\omega}} z\, e^{i\gamma_{r,\,r+za}}\psi_1(r+za)\right) \tag{4.14}$$

where the phases $\gamma_{r,r'}$ are the integrals of the vector potential along the nearest-neighbor bonds,

$$\gamma_{r,r'} = \frac{2\pi}{\Phi_0}\int_{r'}^{r} \mathbf{A}(\mathbf{x}) \cdot d\mathbf{l} \ . \tag{4.15}$$

Eqs. (4.13, 4.14) can be used to obtain the gradient terms of higher order along with the coupling to external fields. One can check that expanding the exponents in Eqs. (4.13, 4.14) and keeping the lowest nonvanishing terms gives the Dirac Hamiltonian (4.12). Expanding Eqs. (4.13, 4.14) we could obtain higher order corrections to Eq. (4.12).

4.2.2 Electrons in a nanotube

To apply the above results to nanotubes, we consider electrons on a 2D Carbon sheet (also called a graphene sheet) rolled into a cylinder, as shown in Fig. 4-3. There are many ways to make such a cylinder. These ways correspond to different nanotube *chiralities*.

A nanotube chirality can be specified by the *chiral vector* connecting the sites of the graphene sheet that are identified with each other on a cylinder. According to the adopted notation [10], a (m, n) nanotube is defined in terms of the following

representation of the chiral vector

$$\mathbf{C} = m\mathbf{e}_1 + n\mathbf{e}_2 \ . \tag{4.16}$$

Here $\mathbf{e}_{1,2}$ are the basis vectors on a hexagonal lattice, as shown in Fig. 4-3. The angle Θ between the chiral vector and the zig-zag axis is called the *chiral angle.*

The transformation of the tight-binding problem (4.1) to the Dirac problem (4.6) based on the representation (4.3) is valid provided that the cylinder circumference $C = 2\pi R$ is much larger than the interatomic spacing a_{cc}. Since for typical NT radii the ratio

$$\frac{C}{a_{cc}} = \sqrt{3(m^2 + mn + n^2)} \tag{4.17}$$

can be between 10 and 20, the approximation (4.3) is entirely adequate.

The NT electron properties, depending on the nanotube structure, can be either metal like or dielectric like. Which of these situations takes place depends on the manner the cylinder is obtained from Carbon monolayer. In the Dirac approach, the condition for the metallic behavior can be formulated directly in terms of the functions $u(r)$ and $v(r)$: The nanotube is metallic *if and only if* one can define on the NT cylinder the two functions $u(r)$ and $v(r)$ according to Fig. 4-2 without running into a mismatch of the function values upon the cylinder closure.

To demonstrate this, let us suppose that the functions $u(r)$ and $v(r)$ on the cylinder exist. Without loss of generality we choose the x axis along the cylinder and the y axis along the circumference. The problem (4.6) has periodic boundary conditions in the y direction, and thus the wave functions can be factorized as

$$\psi_{1,2}(r) = \psi_{1,2}(x)e^{ik_n y} \ , \tag{4.18}$$

where

$$k_n = \frac{2\pi n}{C} = \frac{n}{R} \ . \tag{4.19}$$

Then the dispersion relation for the 1D problems describing motion along the x axis

with fixed k_n is

$$\epsilon_n(k_x) = \pm\hbar v(k_x^2 + k_n^2)^{1/2} \ . \tag{4.20}$$

In this case the subband with $n = 0$ has metallic properties and the subbands with $n \neq 0$ are dielectric.

Now let us consider the other possibility when the cylinder is constructed in such a way that the functions $u(r)$ and $v(r)$ cannot be defined without a value mismatch. In this case, upon rolling the Carbon sheet into the cylinder, the sites with different function values shown in Fig. 4-2 are glued together. However, since all values of the functions $u(r)$ and $v(r)$ are powers of $\omega = e^{\frac{2\pi}{3}i}$, one notes that Eqs. (4.6) can still be used here if they are augmented with *quasiperiodic* boundary conditions,

$$\psi_{1,2}(x, y + C) = \omega\psi_{1,2}(x, y) \tag{4.21}$$

or

$$\psi_{1,2}(x, y + C) = \bar{\omega}\psi_{1,2}(x, y) \ . \tag{4.22}$$

Factoring the wave function as above, one obtains 1D subbands with the dispersion of the form (4.20), in this case with

$$k_n = \frac{(n \pm \frac{1}{3})}{R} \ . \tag{4.23}$$

Note that in this case all spectral branches have dielectric character.

In the present Thesis we mainly focus on the NT properties in the vicinity of the band center. These properties are determined by the form of the electron dispersion $\epsilon(p)$ near half filling. The latter is given by the lowest spectral branch of Eq. (4.20),

$$\epsilon(p) = \pm\sqrt{p^2v^2 + \Delta_0^2} \ , \tag{4.24}$$

where the momentum p along the tube is measured with respect to the K or K' point. It is remarkable that depending on the tube chirality a wide range of values for the

Dirac "mass" Δ_0 is avaliable [10]. Let us now briefly classify the nanotubes according to the values of the gap term Δ_0 in Eq. (6.1). For a thorough treatment of this topic one can refer to the book [10].

As we have already seen above in Eq. (4.23), there exist *semiconducting nanotubes* that have a large gap

$$\Delta_0^{(\text{semic.})} = \frac{\hbar v}{3R} \simeq 0.18 \text{ eV}/R_{[\text{nm}]} \tag{4.25}$$

due to the value mismatch of the basis functions u and v. It is possible to show [10] that these are all (m, n) tubes for which $m - n$ is not a multiple of 3. The semiconducting gap (4.25) is inversely proportional to the NT radius R.

Metallic NTs are the ones [10] for which $m - n \bmod 3 = 0$. They can be of two kinds. The (n, n) tubes are "truly" metallic, having a zero gap at half-filling, $\Delta_0 = 0$, as follows from Eq. (4.19). These tubes are sometimes called *armchair* NTs. Any other nominally metallic tube has a small gap that appears due to the *curvature* of the graphene sheet [18, 19]. This gap is inversely proportional to the square of the NT radius, and is numerically given by

$$\Delta_0 \approx 10 \text{ meV} \cdot |\cos 3\Theta| / R^2_{[\text{nm}]} \tag{4.26}$$

for a nanotube with a chiral angle Θ [18, 19]. The maximum value of the gap (4.26) is achieved for the *zig-zag* tube $(3l, 0)$, for which $\Theta = 0$ (see Fig. 4-3). The curvature induced gap (4.26) is much smaller than the 1D bandwidth

$$D = \frac{\hbar v}{R} = 0.53 \text{ eV}/R_{[\text{nm}]} \, . \tag{4.27}$$

Finally, consider a nanotube in the presence of a parallel external magnetic field. In this case, electron properties are described by the Dirac equation (4.12) with $\varphi = 0$ and the vector potential $\mathbf{A}$ with just the y component,

$$A_y = \frac{\Phi}{C} \, , \tag{4.28}$$

where

$$\Phi = \pi R^2 B \tag{4.29}$$

is the magnetic flux. The boundary conditions in the y direction are periodic for the metallic case and quasiperiodic for the dielectric case. In the presence of parallel magnetic field the problem remains separable and thus the wave function can be factorized in just the same way as above. One again finds 1D subbands with the spectrum (4.20), where

$$k_n R = \begin{cases} n + \phi_{\|} \,, & \text{metallic} \\ n \pm \frac{1}{3} + \phi_{\|} & \text{semicond.} \end{cases} \tag{4.30}$$

for the metallic and semiconducting NT, respectively, with

$$\phi_{\|} = \frac{\Phi}{\Phi_0} \tag{4.31}$$

and

$$\Phi_0 = \frac{hc}{e} \,. \tag{4.32}$$

Thus in the presence of a parallel field the gapless $n = 0$ branch of the metallic nanotube spectrum (4.20) acquires a gap [20, 21, 23]. Interestingly, there is no threshold for this effect, since the gap forms at arbitrarily weak field. The gap size is $2\Delta_\phi$, where

$$\Delta_\phi = |\phi_{\|}| \frac{\hbar v}{R} \,. \tag{4.33}$$

One notes that the field-induced gap appears not at the Fermi level but at the center of the electron band. Thus it affects the metallic NT properties only for electron density sufficiently close to half-filling.

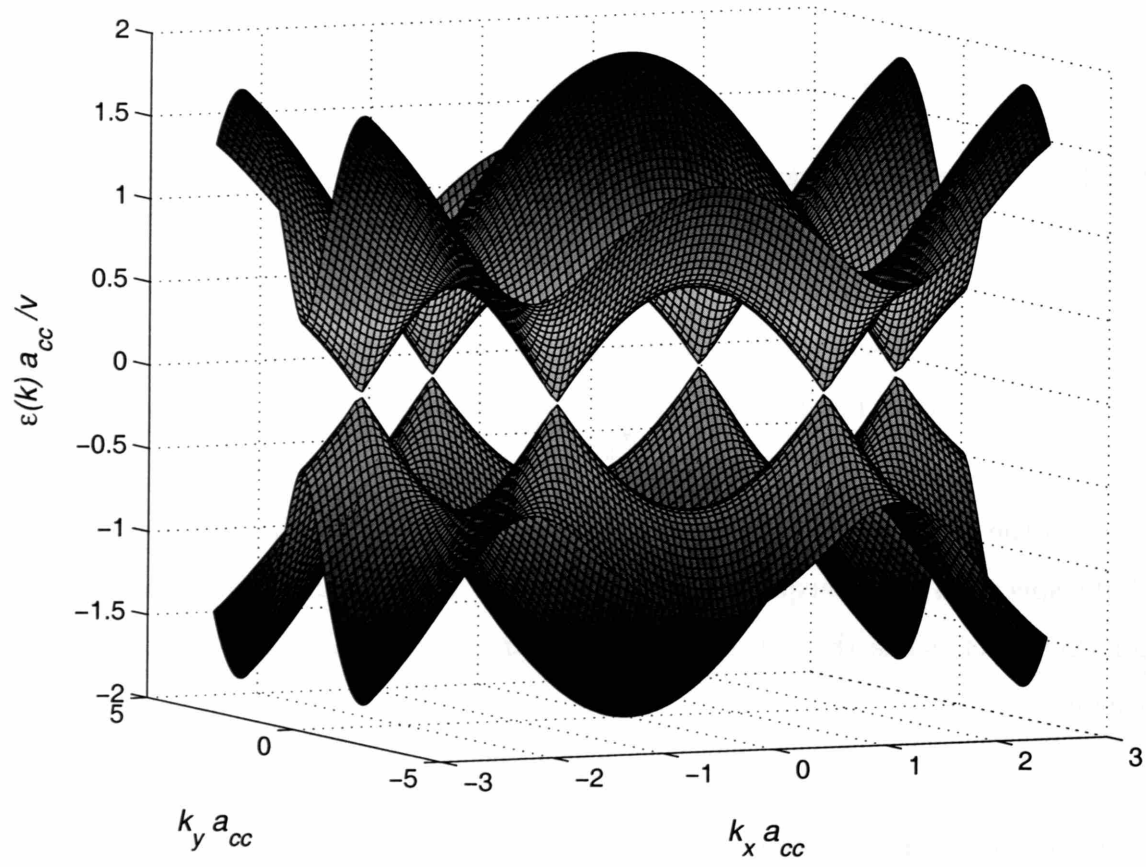

Figure 4-1: Energy dispersion for a 2D Carbon monolayer obtained in a tight-binding approximation. Hexagonal symmetry of the Brilloin zone reflects the underlying symmetry of the graphite honeycomb lattice. Graphite is a semimetal with the pairs of opposite Fermi points (K and K') corresponding to the band center. Near each of the Fermi points the linearized dispersion follows from a 2D massless Dirac Equation

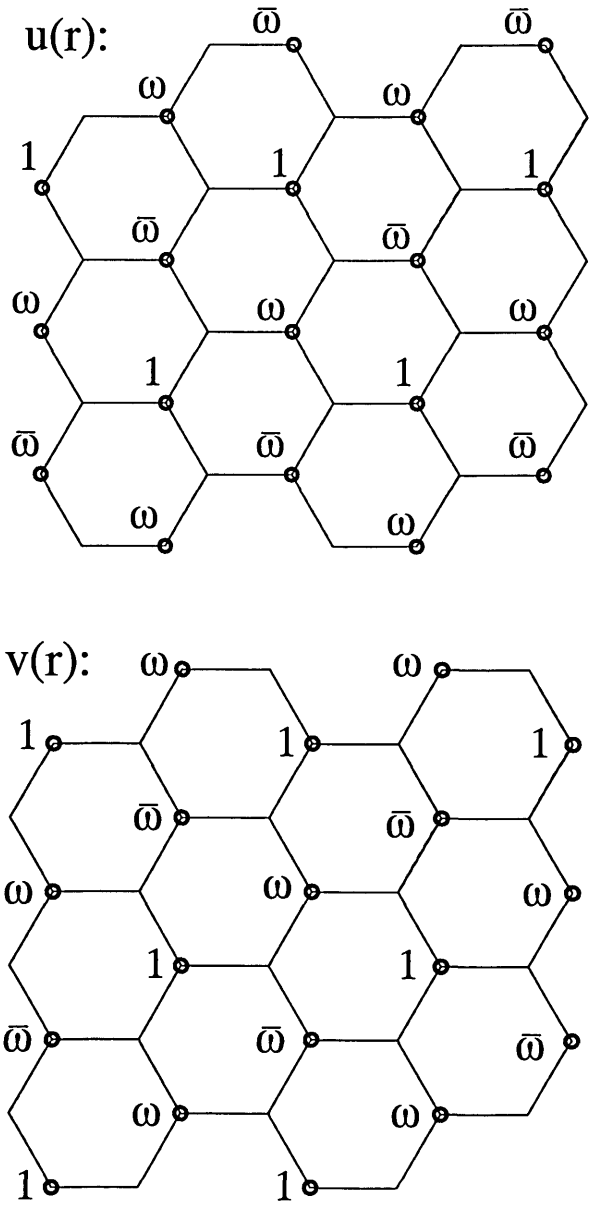

Figure 4-2: Shown are two plane wave basis states $u(r)$ and $v(r)$ of the problem (4.1) with $\epsilon = 0$. Both $u(r)$ and $v(r)$ take the values 1, $\omega = e^{\frac{2\pi}{3}i}$ and $\bar{\omega} = e^{-\frac{2\pi}{3}i}$ on one sublattice and vanish on the other sublattice of the honeycomb lattice. The states $u(r)$ and $v(r)$ have the same quasimomentum and form a basis of the Dirac problem (4.10) at the point K. The independent basis states at the point K' are $\bar{u}(r)$ and $\bar{v}(r)$.

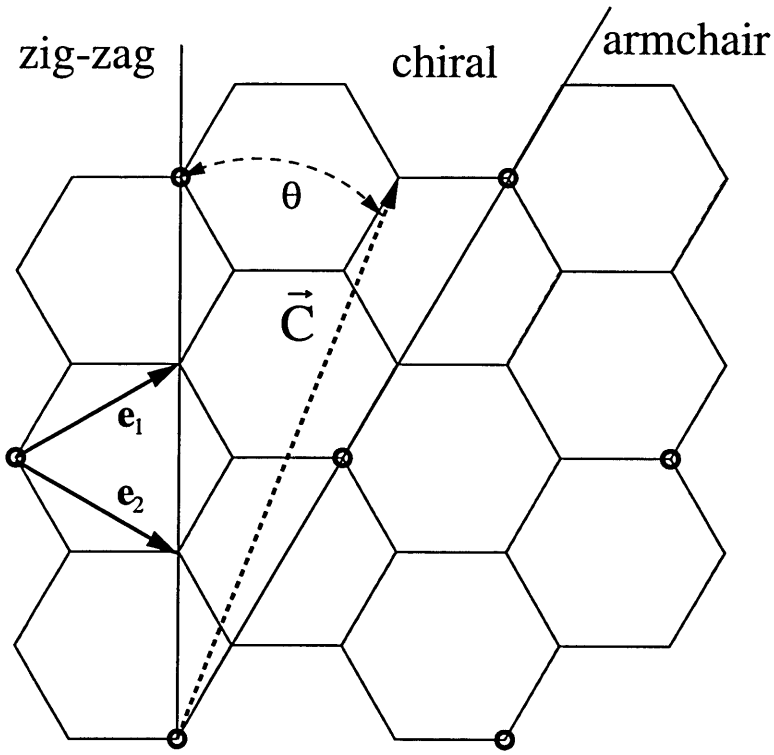

Figure 4-3: (m, n) nanotube as a graphene sheet rolled into a cylinder by identifying the points connected by a *chiral vector* $\mathbf{C} = m\mathbf{e}_1 + n\mathbf{e}_2$. Angle Θ between $\mathbf{C}$ and the zig-zag axis is called *chiral angle*. Chiral vectors that connect cites in bold correspond to *metallic* nanotubes, for which $n - m = 3l$, l integer. Armchair NTs are truly metallic, whereas other nominally metallic NTs have a small curvature-induced gap (4.26) at the band center

Chapter 5

Field effect, polarizability and chiral anomaly

In the present Chapter we will show that single electron properties of Carbon nanotubes described in Section 4.2.2 can change qualitatively in a strong electric field applied perpendicularly to the tube axis. In particular, in Section 5.2 we find that in metallic tubes the sign of Fermi velocity can be reversed in a sufficiently strong field, while in semiconducting tubes the effective mass can change sign. These changes in the spectrum manifest themselves in a breakup of the Fermi surface and in the energy gap suppression, respectively. The effect is controlled by the field inside the tube which is screened due to the polarization induced on the tube. The theory of screening developed in Sec. 5.3 below links it with the chiral anomaly for 1D fermions and obtains a universal screening function determined solely by the Carbon π–electrons conduction band [1]. In Sec. 5.4 we consider the connection between anomaly and universality of screening in detail.

5.1 Introduction

The possibility to change electron spectrum of Carbon nanotubes by external field is of interest for basic research as well as for nanoscale device engineering. As we have seen above in Sec. 4.2.2, a Carbon nanotube (NT) can be either a metal or

a semiconductor depending on the chiral angle [10]. We have also shown that the metallic behavior of a NT can be suppressed by both the intrinsic curvature of a graphene sheet [18, 19], as well as by a parallel magnetic field [22]. Both effects can induce a minigap at the band crossing.

In the present Chapter we examine the changes induced in the NT electron spectrum by the perpendicular electric field $\mathcal{E}$ strong enough to mix different NT subbands:

$$e\mathcal{E}R \simeq D \equiv \frac{\hbar v}{R}, \quad \mathcal{E}\,[\mathrm{MV/cm}] \simeq 5.26/R^2\,[\mathrm{nm}^2], \tag{5.1}$$

where R is the tube radius and v is electron velocity. In such a field the effect on electron spectrum is dramatic: in metallic tubes the electron velocity $v = d\epsilon/dp$ can be reduced and even reverse the sign, causing Fermi surface breakup, while in semiconducting tubes the effective mass sign can change, which is accompanied by strong suppression of the excitation gap (Fig. 5-1).

The NT electron system in this regime can be a host of intriguing many-body phenomena. In the absence of the field, the dimensionless electron interaction in a nanotube is

$$\frac{e^2}{\hbar v} \simeq 2.7\ . \tag{5.2}$$

The reduction of electron velocity in metallic tubes leads to an increase of the interaction (5.2) that controls the Luttinger liquid properties [28, 29, 30, 31]. One expects this to enhance the intrinsic, interaction-induced energy gap predicted to be small in pristine NTs [28, 29, 30, 31].

Even more peculiar is the negative v state with intertwining electron and hole Fermi surfaces (Fig. 5-1 top). This system provides a realization of a metallic state unstable with respect to electron-hole pairing into excitons. Such an instability, long-envisioned [24] by Mott, Keldysh and Kopaev, and others, is especially interesting for the mirror symmetric electron and hole bands, described by an analog of the BCS theory. The chiral gauge symmetry (5.6) of the NT electron Hamiltonian discussed below eliminates the interband matrix elements of particle density. This makes the phase of the excitonic order parameter a gapless Goldstone field, similar to the BCS

order parameter. Despite its simplicity, no system with such properties has been unambiguously identified so far, and it is thus possible that nanotubes in a transverse field present a unique opportunity to study this phenomenon.

The field (5.1) required to create this state is to be achieved within the tube where the external field is partially screened [25]. However, because of the discrete bands with relatively large interband separation (4.27), the transverse field penetrates in the NT fairly well. In Sec. 5.3 we will find the screening factor to be R-independent and close to 5 (in accord with [25]), for both metallic and semiconducting tubes. With the screening taken into account the numbers for the required field remain feasible.

Unexpectedly, the problem of transverse field screening has a relation with the chiral anomaly. A significant part of electron energy in an external field, in the effective Dirac model considered in Sec. 4.2.2, arises from the effects at the *Fermi sea bottom*, where a regularization of this model is required. However, the anomaly links the regularized energy with the properties near the Fermi level (the number of fermion species and their velocity), and thereby generates a *universal screening function* determined only by the Carbon π-electron band.

5.2 Field effect

We consider the nanotube at half-filling subject to a homogeneous electric field that is perpendicular to its axis. Below we ignore charge accumulation due to gating. Gating in itself will not modify the transverse field within the tube, since a uniformly charged cylinder is equipotential. Charging may affect the inner NT field indirectly via changing screening, but this effect should not be significant at moderate gating.

As it has been shown in the previous Chapter, the NT states with small energies $|\epsilon| \ll t$ calculated from the band center are described, separately at each of the K and K' points, by a massless Dirac Hamiltonian

$$\mathcal{H}_0 = -i\hbar v(\sigma_y \partial_x - \sigma_x \partial_y) \ , \tag{5.3}$$

where the velocity v is given in Eq. (4.7) in terms of the tight-binding integral t. For a NT in the presence of a transverse electric field $\mathcal{E}$,

$$\mathcal{H}_0 = \hbar v \left(i\sigma_x \partial_y + \sigma_y k\right) - e\mathcal{E}R\cos(y/R) \tag{5.4}$$

with k the (conserved) longitudinal momentum and R the NT radius. The boundary conditions are quasiperiodic:

$$\psi(y + 2\pi R) = e^{2\pi i\delta}\psi(y) \ , \quad \delta = \begin{cases} 0 \ , & \text{metallic} \\ \pm\frac{1}{3} \ , & \text{semicond.} \end{cases} \tag{5.5}$$

The effects of NT curvature [18] as well as of a parallel magnetic field [22] described above in Sec. 4.2.2 can in be included by slightly shifting δ away from the ideal values (5.5).

We employ a chiral gauge transformation

$$\psi(y) = e^{-i\sigma_x\phi(y)}\tilde{\psi}(y) \ , \quad \phi(y) = \frac{e\mathcal{E}R^2}{\hbar v}\sin(y/R) \tag{5.6}$$

which preserves the condition (5.5) and turns Eq. (5.4) into

$$\widetilde{\mathcal{H}}_0 = \hbar v \left(i\sigma_x\partial_y + ke^{2i\sigma_x\phi(y)}\sigma_y\right) \ . \tag{5.7}$$

The transformed Hamiltonian reveals that, in particular, the spectrum at $k = 0$ is totally independent of the transverse field (Fig. 5-1).

The spectrum of a metallic NT near the band crossing at $kR \ll 1$ can be found by employing the degenerate perturbation theory. We project the Hamiltonian (5.7) on the two states $|\uparrow\rangle$, $|\downarrow\rangle$ degenerate at $k = 0$, and obtain

$$\epsilon(k) = \pm\left[\hbar v J_0(2u)\right] k \ , \quad u \equiv \frac{e\mathcal{E}R}{D} = \frac{e\mathcal{E}R^2}{\hbar v} \ . \tag{5.8}$$

Electron velocity changes sign at the roots of the Bessel function J_0, first at $2u = \mu_1 \approx 2.405$ (Fig. 5-1). At u above critical the Fermi surface fractures: an additional

small pocket appears for each spectral branch.

The level shifts in semiconducting NT at small k are given by the second order perturbation theory in the k-term of the transformed Hamiltonian (5.7):

$$\epsilon_n^{\pm}(k) = \pm D\left((n+\delta) + A_n(kR)^2\right) , \tag{5.9}$$

$$A_n = \sum_{m=-\infty}^{\infty} J_m^2(2u)\frac{2(n+\delta)}{4(n+\delta)^2 - m^2} . \tag{5.10}$$

For $\delta = 1/3$ the curvature of the lowest band A_0 changes sign at $u_c \approx 0.6215$ (Fig. 5-1). This leads to a singular behavior of the excitation gap which is constant at $u < u_c$ and sharply decreases at $u > u_c$ (Fig. 5-1 inset). This occurs because of the lowest excitation energy shifting from $k = 0$ at $u < u_c$ to $k \neq 0$ at $u > u_c$. The threshold-like suppression of the gap can be detected by a transport measurement in a thermally activated regime.

The chiral gauge symmetry (5.6) that protects the spectrum at $k = 0$ is a distinct feature of the Dirac model (5.3), (5.4). The π–electron tight-binding problem, in the next-lowest gradient order, generates a correction to the Hamiltonian (5.3) violating the symmetry (5.6):

$$\mathcal{H} = \mathcal{H}_0 + \lambda e^{-\frac{3i}{2}\Theta\sigma_z}\left[\sigma_x\left(\partial_x^2 - \partial_y^2\right) - 2\sigma_y\partial_x\partial_y\right]e^{\frac{3i}{2}\Theta\sigma_z} \tag{5.11}$$

with $\lambda = \frac{1}{4}a_{cc}\hbar v$ and Θ the NT chiral angle [10]. The transformation (5.6) applied to (5.11) gives a minigap [26]

$$\Delta_{\mathcal{E}} = |\sin 3\Theta|\,(a_{cc}/8\hbar v)\,(e\mathcal{E}R)^2 \tag{5.12}$$

Since $8R \gg a_{cc}$, the minigap (5.12) is too small to alter the behavior at the energies of interest, $\epsilon \simeq D$.

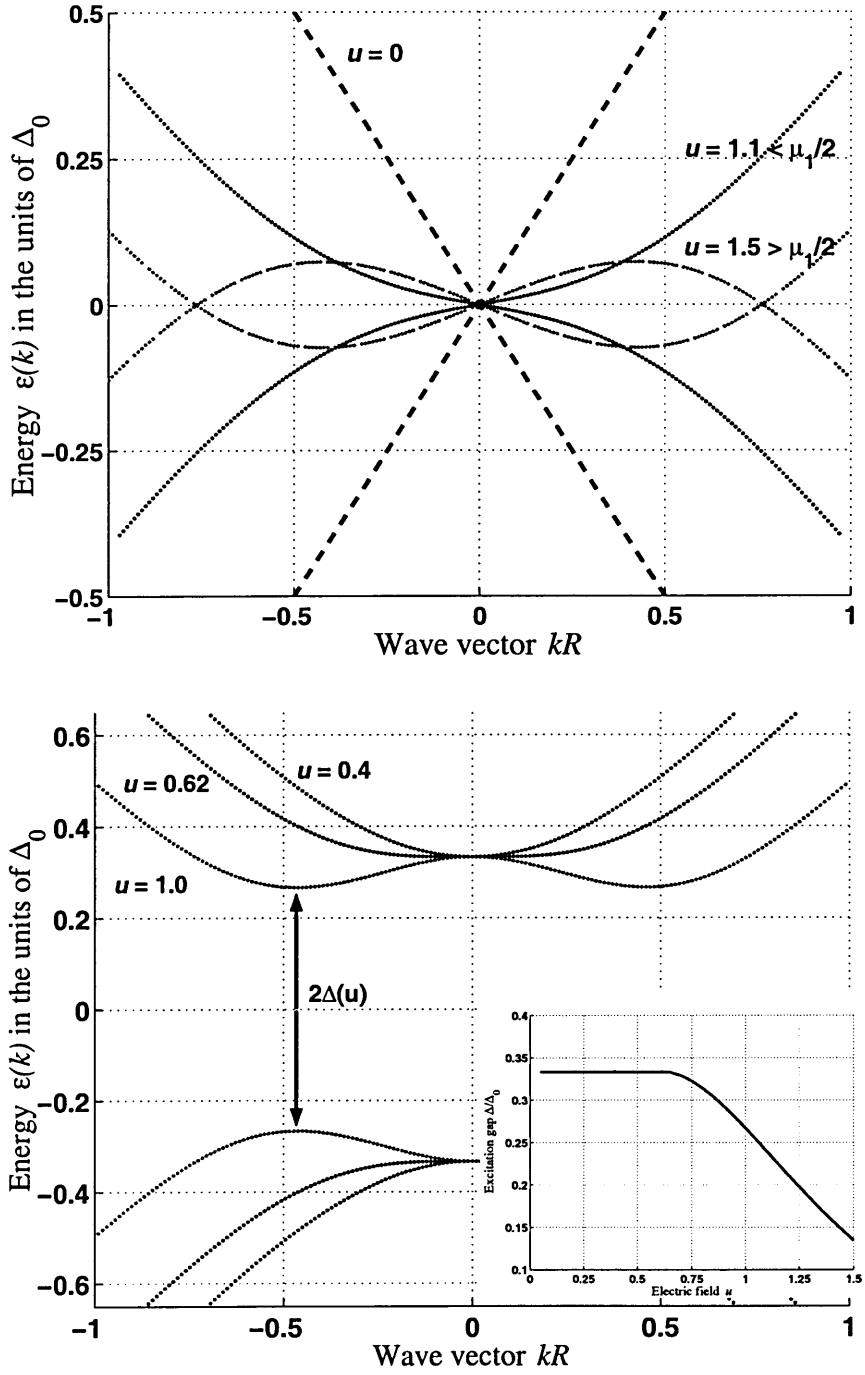

Figure 5-1: Electron bands transformation: velocity reversal in metallic NT (top); effective mass sign change in semiconducting NT (bottom). The bands are shown for the dimensionless transverse field $u = e\mathcal{E}R/D$. *Inset:* Energy gap suppression in a semiconducting NT in a perpendicular electric field

5.3 Screening and chiral anomaly

The main effect of electron interaction is screening of the inner field that couples to the electron motion. Here we derive the relation between the inner and outer fields. We first show how the screening problem is reduced to the calculation of the NT electron energy in the presence of an external field. Hereafter we measure all energies in the units of $D = \hbar v/R$ and use dimensionless field $u = e\mathcal{E}R/D$. From Gauss' law, the fields inside and outside the tube are related with the induced surface charge density per one fermion species (spin and valley) by

$$\mathcal{E}_{\rm ext} = \mathcal{E} + \tfrac{1}{2} \cdot 4\pi \cdot 4\sigma \ , \tag{5.13}$$

where the factor 1/2 accounts for depolarization in the cylindrical geometry. In Eq. (5.13) we projected the actual charge density on the $\cos\varphi$ harmonic as $\sigma(\varphi) \to 4\sigma\cos\varphi$, ignoring the higher order harmonics. (Here $\varphi \equiv y/R$.)

To obtain the $\cos\varphi$ harmonic of the induced charge, we evaluate the dipole moment per unit length as

$$P = -\frac{dW(\mathcal{E})}{d\mathcal{E}} \ , \tag{5.14}$$

where $W(\mathcal{E})$ is the energy of one fermion species as a function of the inner field. Combining this with the relation

$$\sigma = \frac{P}{\pi R^2} \tag{5.15}$$

and with the Gauss' law (5.13), and passing to dimensionless $u_{\rm ext}$, u, we obtain

$$u_{\rm ext} = u + 8\frac{e^2}{\hbar v}P(u) \ . \tag{5.16}$$

After the dipole moment $P(u)$ is known Eq. (5.16) can be solved for the inner field u in terms of the outer field $u_{\rm ext}$.

We consider the general problem of electron energy in a transverse field in a free particle model. The electron levels $\epsilon_{n,k}$ perturbed by the field can be easily found numerically at each value of the longitudinal momentum k by using a transfer matrix

for Eq. (5.7). The level shifts $\delta\epsilon_{n,k} = \epsilon_{n,k}(u) - \epsilon^{(0)}_{n,k}$ decrease at large $|n|$, and the series the total change of the occupied states energy

$$E_0(k) = \sum_{n=-\infty}^{+\infty} \delta\epsilon_{n,k} \quad (\text{such that } \epsilon_{n,k}(u) < 0) \tag{5.17}$$

rapidly converge at $n \to \pm\infty$.

There are two basic problems with Eq. (5.17): (i) Due to an upward shift of the filled levels (Fig. 5-1), E_0 is positive and also has positive derivative dE_0/du. Hence Eq. (5.17) leads to the dipole moment $P_0 = -dE_0/du$ opposite to the field, i.e. to an unphysical "diamagnetic" polarization sign instead of the expected "paramagnetic" effect. (ii) The dependence of the energy E_0 on the longitudinal wavevector k leads to an ultraviolet divergence in the integral

$$P = \int \frac{dk}{2\pi} P(k) \ , \tag{5.18}$$

because $E_0(k)$ increases with $|k|$, saturating at $|k|R \gg 1$ at an asymptotic value $\frac{1}{2}u^2$.

Both difficulties are resolved by taking into account a fundamentally important contribution to the energy that arises due to the effects at the *Fermi sea bottom.* Physically, the finite electron band width invalidates the massless Dirac approximation at large negative energies. This contribution, however, depends solely on the number of Dirac fermion species and their velocity v, and is totally insensitive to any other details including the longitudinal momentum k value. We find that

$$E_{\text{anom}} = -\tfrac{1}{2}u^2 \tag{5.19}$$

for each fermion species. Remarkably, Eq. (5.19) can be obtained without detailed discussion of the behavior at the interatomic length scales — the universality of Eq. (5.19) is rooted in the physics of *the chiral anomaly* in the $1+1$ dimensional Dirac fermion problem. The resulting total energy integral

$$W = \int_{-\infty}^{\infty} (E_0(k) + E_{\text{anom}}) \, \tfrac{dk}{2\pi} \tag{5.20}$$

converges after $E_0(k)$ is offset by $E_{\rm anom}$ (Fig. 5-2).

A general proof of the formula (5.19) for the energy anomaly will be given in Sec. 5.4, where it will be seen that this result is regularization-independent and holds for arbitrary external field. In this section, to gain intuition in the origin of this surprising effect, we focus on a relatively more simple case of weak field $u \ll 1$.

Let us evaluate the energy (5.17) and derive the anomaly (5.19) using perturbation theory in weak field. The NT bands at $u = 0$ are

$$\epsilon_n^{\pm}(k) = \pm\sqrt{(n+\delta)^2 + k^2}\,, \quad -\infty < n < +\infty \tag{5.21}$$

In a half-filled system with just the $\epsilon_n^-(k)$<0 bands filled, the external field u changes the Fermi sea energy by

$$W = \int \sum_n{}' \delta\epsilon_n^-(k) \frac{dk}{2\pi} \tag{5.22}$$

Here the superscript in $\sum'$ indicates regularization by truncating the interaction with the external field at a certain large negative energy. We check that this contribution to the energy is independent of the details of truncation and obtain the anomaly (5.19) by choosing a convenient truncation scheme.

The level shifts $\delta\epsilon_n^-(k)$, in the second order of the perturbation theory in the external field $\hat{V}$=$-e\mathcal{E}R\cos\varphi$, are

$$\delta\epsilon_n^- = \sum_m \frac{|\langle m^+|\hat{V}|n^-\rangle|^2}{\epsilon_n^- - \epsilon_m^+} + \sum_m \frac{|\langle m^-|\hat{V}|n^-\rangle|^2}{\epsilon_n^- - \epsilon_m^-} \tag{5.23}$$

where the superscript $\pm$ indicates the electron and hole branches and the k dependence is suppressed. Due to the integration over φ with $\hat{V} \propto \cos\varphi$ in the matrix elements the only nonzero terms in (5.23) are those with $m = n \pm 1$.

We now show that the sums over ϵ_m^+ and ϵ_m^- in (5.23), respectively, give the regular and the anomalous contributions to the total energy $W = \sum_n' \delta\epsilon_n^-$. Different behavior of the two sums under regularization stems from their different convergence type. Individual terms in the sum over ϵ_m^+ decrease rapidly at large m, so that the series for W is absolutely convergent. On the other hand, in the sum over ϵ_m^- the terms do not

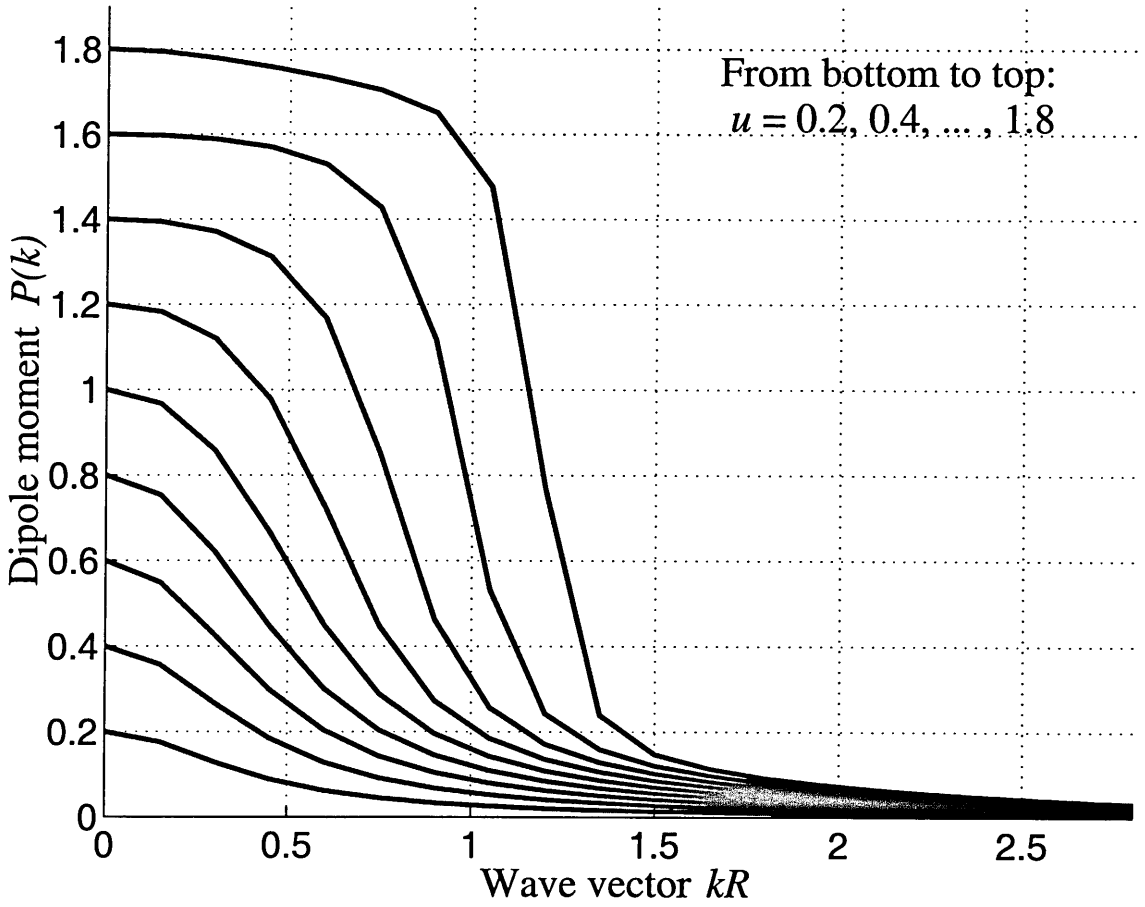

Figure 5-2: Dipole moment $P(k) = -d(E_0(k) + E_{\text{anom}})/du$ per one fermion species in a semiconducting NT as a function of k. Note that the energy anomaly (5.19) cancels with $E_0(k)$ at $kR \gg 1$, assuring convergence of $P_{\text{total}} = \int P(k)dk/2\pi$. Note also that $P(k \to 0)$ is dominated by the anomaly, since $E_0 = 0$ at $k = 0$ due to the chiral gauge invariance (5.6).

change at large m and thus the corresponding contribution to W is given by poorly convergent and regularization-sensitive series.

Taking from (5.23) just the terms with ϵ_m^+, evaluating the matrix elements $\langle m^+|\hat{V}|n^-\rangle$ and summing over n yields

$$E_0(k) = \frac{u^2}{4}\sum_n \frac{\epsilon_n^+(k)\epsilon_{n'}^+(k) - (n+\delta)(n'+\delta) - k^2}{\epsilon_n^+(k)\epsilon_{n'}^+(k)(\epsilon_n^-(k) - \epsilon_{n'}^+(k))} \tag{5.24}$$

with $n' = n+1$. The sum (5.24) rapidly converges at large $n \to \pm\infty$ and can be easily evaluated numerically.

Now we consider the sum of the level shifts $W = \sum_n' \delta\epsilon_n^-$ taking into account only the second term in (5.23). At the first sight this sum is identically zero. Indeed, due to the symmetry $\langle m^-|\hat{V}|n^-\rangle = \langle n^-|\hat{V}|m^-\rangle$, in the sum over n with $m = n \pm 1$ all the terms cancel in pairs. However, truncation of the interaction at a large negative energy compromises the cancellation and yields a finite result. If one sets $\langle m^-|\hat{V}|n^-\rangle = 0$ for all $|m|$ or $|n|$ exceeding a large number N, there will be just two terms in the sum over n that do not cancel:

$$E_{\text{anom}} = \frac{|\langle N'^-|\hat{V}|N^-\rangle|^2}{\epsilon_N^- - \epsilon_{N'}^-} + \frac{|\langle -N'^-|\hat{V}|-N^-\rangle|^2}{\epsilon_{-N}^- - \epsilon_{-N'}^-} \tag{5.25}$$

with $N' = N-1$. Evaluating the matrix elements and energy levels is straightforward because at large $N \gg |k|$ one can set $k = 0$. The result, coinciding with (5.19), is robust under a change of the regularization.

The expression (5.19) for the energy anomaly, derived above for the weak field, is in fact more general. To illustrate this we consider a special case of zero longitudinal momentum $k = 0$ and derive (5.19) from bosonization, without using perturbation theory in $u \ll 1$. After the problem (5.4) is bosonized in the standard way [64], as described in Appendix B using $\psi_{L,R} \propto e^{i\phi_L}, e^{-i\phi_R}$, we obtain a quadratic Hamiltonian

$$\mathcal{H} = \int_0^{2\pi R} \sum_{j=L,R} \left[\tfrac{\hbar v}{4\pi}(\partial_x\phi_j)^2 + \tfrac{e}{2\pi}\partial_x\phi_j U(y)\right] dy\ . \tag{5.26}$$

The second term in (5.26) representing interaction with the external field $U(y)$ can

be decoupled by a shift

$$\phi_j \to \phi'_j - \frac{1}{\hbar v}\int_0^y U(y')dy' \ . \tag{5.27}$$

The Hamiltonian for ϕ'_j takes the form (5.26) with $U = 0$, while the ground state energy

$$\delta E = -\frac{e^2}{2\pi\hbar v_F}\int_0^{2\pi R} U^2(y)dy \tag{5.28}$$

is nothing but the anomaly (5.19) scaled by $D = \hbar v/R$.

After adding the energies (5.24) and (5.19) we obtain a contribution to the dipole moment of states with specific longitudinal momentum k (see Fig. 5-3). Integrating in (5.20) over k numerically, we have

$$W = -\frac{\alpha}{2}u^2, \quad \alpha = \begin{cases} 0.196... & \text{for } \delta = 1/3 \\ 0.179... & \text{for } \delta = 0 \end{cases} \tag{5.29}$$

Eq. (5.13) with the dipole moment (5.14) and the charge density (5.15) yield the screening function

$$\mathcal{E}_{\text{ext}} = \left(1 + 8\alpha\,\tfrac{e^2}{\hbar v}\right)\mathcal{E} \ . \tag{5.30}$$

With $e^2/\hbar v = 2.7$ this gives $\mathcal{E}_{\text{ext}}/\mathcal{E} = 5.24$ for $\delta = 1/3$, and $\mathcal{E}_{\text{ext}}/\mathcal{E} = 4.87$ for $\delta = 0$. The outer-to-inner field ratio $\simeq 5$ (see Ref. [25] for another derivation using *ab-initio* calculations) renders the required fields (5.1) feasible. Interestingly, the screening (5.30) is independent of the tube radius R and is almost the same in the metallic and semiconducting NTs. The latter is not surprising, since the screening is absent in a single 1D mode approximation: the polarizability is related with dipolar transitions between *different* subbands.

The radius-independence of (5.30) resembles an effect of a dielectric constant. We note, however, that the change of the inner field due to individual Carbon atoms polarizability is small in $a_{\text{cc}}/2\pi R \ll 1$. The result (5.30) reflects the semimetallic character of the Carbon π–electron band with the density of states vanishing at the band center.

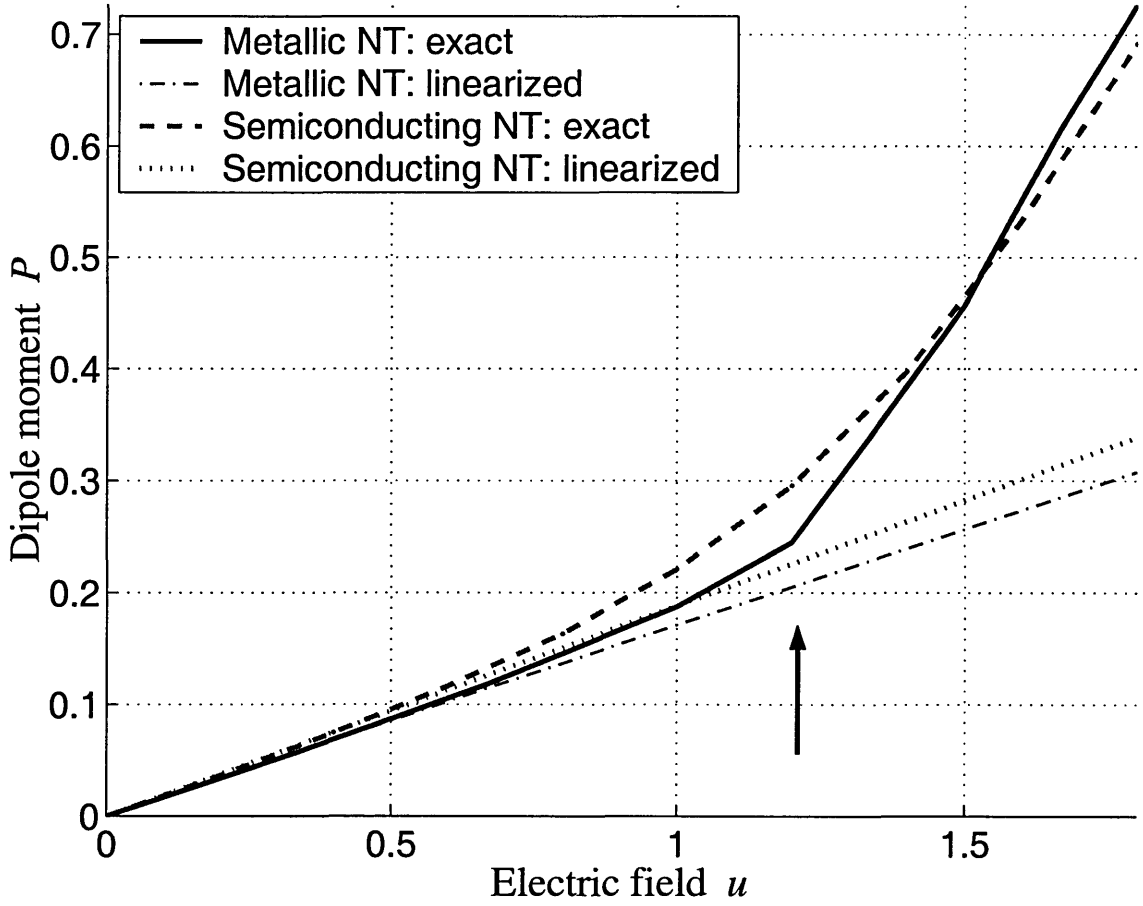

Figure 5-3: Dipole moment P per one fermion species versus the field $u = e\mathcal{E}R^2/\hbar v$, obtained as $P = -dW/du$ with W given by (5.20). The weak field result obtained from (5.29) is also shown. The cusp (marked) occurs at the field where velocity changes sign in metallic NT.

5.4 Energy anomaly for 1D Dirac fermions

In the present Section we consider an *energy anomaly*, a counterpart of a chiral anomaly, for a general infinite three-diagonal matrix of the form

$$\mathcal{H} = \begin{pmatrix} \dots & \dots & \dots & \dots & \dots & \dots & \dots & \dots \\ \dots & -2 & a_{-1} & 0 & 0 & \dots & \dots & \dots \\ \dots & a_{-1} & -1 & a_0 & 0 & 0 & \dots & \dots \\ \dots & 0 & a_0 & 0 & a_1 & 0 & 0 & \dots \\ \dots & 0 & 0 & a_1 & 1 & a_2 & 0 & \dots \\ \dots & \dots & 0 & 0 & a_2 & 2 & a_3 & \dots \\ \dots & \dots & \dots & 0 & 0 & a_3 & 3 & \dots \\ \dots & \dots & \dots & \dots & \dots & \dots & \dots & \dots \end{pmatrix} \tag{5.31}$$

and then comment on the relation with the NT problem.

We start with the case of constant off-diagonal elements $a_m = a$. In the Fourier representation $|m\rangle = e^{im\theta}$ the operator $\mathcal{H}$ has the form

$$\mathcal{H} = -i\partial_\theta + 2a\cos\theta \ . \tag{5.32}$$

Eliminating the term $2a\cos\theta$ by a gauge transformation

$$\psi(\theta) = e^{-2ia\sin\theta}\widetilde{\psi}(\theta) \ , \quad \widetilde{\mathcal{H}} = -i\partial_\theta \tag{5.33}$$

brings us back to the problem with $a = 0$ and proves that in this case the eigenvalues of the operator $\mathcal{H}$ are integers independent of a. [We point to the similarity with the above discussion of the chiral gauge transformation and robustness of the NT electron spectrum with $k = 0$. Note that $a = 2u$.]

What we are really interested in is the problem (5.31) with a_m asymptotically zero at large negative m and non-zero at large positive m, for example

$$a_m = \begin{cases} 0, & m \leq 0 \\ a, & m > 0 \end{cases} \tag{5.34}$$

Although in this case the energy levels depend on a, only a relatively small cluster of levels with $|m| \sim 1$ depends on a strongly, while the level shifts at large $|m|$ are exponentially small in $|m|$. This is the case because far away from $m = 1$, where switching from 0 to a occurs, the sequence a_m is constant, which allows one to use the above argument of integer eigenvalues robustness.

We are interested in the sum of all level shifts

$$\delta \operatorname{tr} \mathcal{H} = \sum_m \delta \epsilon_m \ . \tag{5.35}$$

One can make a general argument for the insensitivity of this quantity to the character of switching from $a_m = a$ to $a_m = 0$ as follows. To show this let us truncate the matrix (5.31) at some large negative and positive row and column $m = \pm M$ and consider the spectrum of this *finite size* matrix. The truncation may shift the levels only near the top and the bottom of the spectrum, $m \simeq \pm M$. However, the lower levels with $m \simeq -M$ are not affected by truncation since the matrix is diagonal at $m \to -\infty$. Only the upper levels with $m \simeq M$ will be sensitive to the value of a. This group of levels is far away in m from the group near $m \simeq 1$ contributing to $\delta \operatorname{tr} \mathcal{H}$ in Eq. (5.35). One notes that the sum of all the upper levels shifts $\delta \operatorname{tr} \mathcal{H}_{\text{upper}}$ satisfies an identity

$$\delta \operatorname{tr} \mathcal{H} + \delta \operatorname{tr} \mathcal{H}_{\text{upper}} = 0 \ . \tag{5.36}$$

This is true because the sum (5.36) is nothing but variation of the trace of the finite $(2M + 1) \times (2M + 1)$ matrix upon a change of a_m. However, the trace of a *finite* matrix does not depend on the off-diagonal matrix elements.

The relation (5.36) of the sum of the shifts of the levels with $m \simeq 1$ and $m \simeq M$ demonstrates that each of them is a universal number insensitive to the exact rule for switching from a to 0 is the sequence a_m. Indeed, the group of the upper levels is so far from the place where the switching occurs that $\delta \operatorname{tr} \mathcal{H}_{\text{upper}}$ cannot possibly depend on a_m with $m \simeq 1$. But then the identity (5.36) guarantees that the value $\delta \operatorname{tr} \mathcal{H}$ is also completely universal. This result can be used to compute $\delta \operatorname{tr} \mathcal{H}$ by choosing a convenient sequence a_m for which individual level shifts can be evaluated explicitly.

Since the levels are unperturbed by constant $a_m = a$, the level shifts will be small for any slowly varying a_m such that $|da_m/dm| \ll |a_m|$. This enables one to obtain the shifts by a perturbation theory in small da_m/dm. Performing a gradient expansion for a_m in the vicinity of $m = m_0$ one finds

$$a_m = \bar{a} + b(m - m_0), \quad \bar{a} = a_{m_0}, \quad b = \tfrac{da_m}{dm}|_{m=m_0} . \tag{5.37}$$

The Hamiltonian is

$$\mathcal{H} = -i\partial_\theta + 2(\bar{a} - b)\cos\theta + b\left(-i\partial_\theta e^{-i\theta} + \text{h.c.}\right) . \tag{5.38}$$

The gauge transformation $\psi(\theta) = e^{-2i(\bar{a}-b)\sin\theta}\widetilde{\psi}(\theta)$ brings the Hamiltonian to the form

$$\widetilde{\mathcal{H}} = -i\partial_\theta + b\left[(-i\partial_\theta - 2(\bar{a} - b)\cos\theta)e^{-i\theta} + \text{h.c.}\right] . \tag{5.39}$$

The energies ϵ_m with m near m_0 obtained in the lowest order of perturbation theory are

$$\epsilon_m = \langle m|\widetilde{\mathcal{H}}|m\rangle = m - 2b(\bar{a} - b) . \tag{5.40}$$

The sum of level shifts (5.40) is

$$\delta \operatorname{tr}\mathcal{H} = \sum_m -2b(\bar{a} - b) = \int \left(\left(\tfrac{da_m}{dm}\right)^2 - 2a_m \tfrac{da_m}{dm}\right) dm = -a_m^2|_{-\infty}^{+\infty} = a^2 . \tag{5.41}$$

The first term in the integral is quadractic in da/dm and thus can be ignored for slowly varying a_m, while the second term, being a full derivative, gives a result that depends only on the asymptotic behavior of a_m.

To relate the above calculation with the fermionic anomaly we note three things. First, the transverse electric field $\mathcal{E}$ does make the Hamiltonian (5.4) a three-diagonal matrix with $a_m = -\frac{1}{2}u$ in the plane wave basis $\psi_{n,\alpha}(y) = e^{iny/R}\chi_\alpha$. Second, the electron levels $\epsilon_{n,k}$ grow infinitely negative at both $n \to +\infty$ and $n \to -\infty$. Thus the regularization of the interaction performed by altering the sequence a_m as described above will yield *two identical contributions* to the anomaly. Third, the electron levels

have an asymptotic form

$$\epsilon_{n,k} \simeq -|n+\delta| - \frac{k^2}{2|n+\delta|} \tag{5.42}$$

with the correction due to finite longitudinal k becoming small at large $|n|$. This proves that the contribution of regularization $E_{\text{anom}} = -2(-\frac{1}{2}u)^2$ per one fermion species is identical to Eq. (5.19) independent of k.

5.5 Conclusions

In summary, in the present Chapter we have shown that nanotube electron states undergo interesting transformations in the field effect regime, leading to novel phenomena in both the single particle and many-body properties. The relation of the applied field with the screened field within the tube, that controls electron properties, is found. In the framework of 1D Dirac fermions, the screening arises mainly due to the effect of the field on the states at the bottom of 1D band. However, due to an energy anomaly, which is a counterpart of the chiral anomaly, this contribution is expressed in terms of the properties of the states at the middle of the band, near Fermi level. This makes screening properties of nanotubes universal and robust. We find that screening properties depend on nanotube type, with a few percent difference between metallic and semiconducting tubes, and practically do not depend on nanotube radius. The analysis of screening, performed using the theory of chiral anomaly, indicates that the fields required for the observation of the proposed effects are in the experimentally feasible range for nanutubes of sufficiently large radius.

Chapter 6

Adiabatic Charge Transport

In the present Chapter we describe the proposal [2] for an adiabatic charge pump based on a coupling of a semi-metallic Carbon nanotube to a surface acoustic wave (SAW). In Sec. 6.2 below we demonstrate that electron backscattering by a periodic SAW potential, which results in miniband formation, can be achieved at energies near the Fermi level. Quantized SAW induced current is a function of chemical potential (or gate voltage) and can be positive or negative, depending on the sign of doping. The sign reversal is illustrated within a theory of the acoustoelectric effect when the SAW potential is weak. In Sec. 6.5 we discuss the feasibility of the pumping experiment.

6.1 Introduction

The mechanism of quantized adiabatic transport, as first conceived by Thouless [45], involves a one-dimensional (1D) electron system in a periodic potential that, via backscattering, opens a gap in the electron spectrum. If the potential varies slowly and periodically in time in such a way that the Fermi level lies within a gap of the instantaneous Hamiltonian, then an integer charge me is transported across the system during a single period. This results in a quantized current $j = mef$, where f is the frequency of the external field. If realized experimentally, such a device would present an important application as a current standard.

Although the quantized adiabatic transport mechanism is compelling in its simplicity, is has proven difficult to realize experimentally: the goal is to find such a combination of a host 1D system and a sliding external perturbation to engineer a miniband spectrum with minigaps sufficiently large that disorder, thermal excitations, and finite size effects do not compromise the integrity of the quantization. Recently, a surface acoustic wave (SAW) has been used to achieve quantized current in a split gate point contact [49]. The SAW field can be strong enough to induce a bulk gap, and the SAW wavenumber can be chosen to match $2p_F$ to pin electrons. Among the existing 1D systems, one possibility is to use quantum wires which can be coupled easily to the SAW. However, since the densities for which adiabatic transport is most pronounced correspond to a few electrons per SAW spatial period (realistically, ca. a few microns), one would need wires with low electron 1D density of around 10^4cm^{-1}. The densities currently available in such systems are at least an order of magnitude higher [51].

In this Chapter we argue that a surface acoustic wave (SAW) coupled to a semimetallic carbon nanotube presents an ideal system in which quantized transport can be realized. The experimental arrangement is illustrated in Fig 6-1. A nanotube is placed between two metallic contacts on the surface of a piezoelectric crystal, with a gate electrode nearby to allow adjustment of the Fermi level in the tube. In a piezoelectric substrate the SAW is accompanied by a wave of electrostatic potential that can have an amplitude up to a few Volts [50]. The potential decays both into the free space and into the substrate to a depth comparable to the wavelength λ_{SAW}. We assume that the tube is suspended at a height $\ll \lambda_{\text{SAW}}$ above the substrate, so that there is no direct mechanical coupling and only the free space component of a SAW potential matters. When a SAW is launched from a transducer (such as an interdigitated electrode array) its electric field penetrates the tube and electron diffraction on the sliding SAW potential results in miniband formation. By positioning the Fermi level within the energy gap, the conditions for current quantization are fulfilled.

High electron velocity in nanotubes, $v \approx 8 \times 10^7\text{cm/s}$, makes it possible to create large minigaps. The expected minigap size can be estimated in view of the obser-

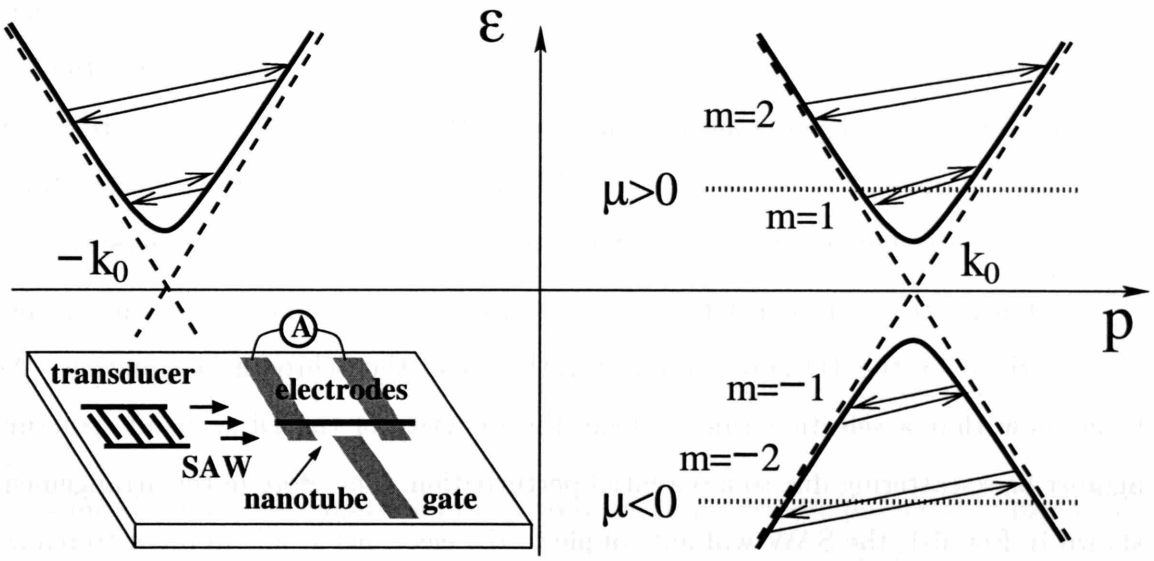

Figure 6-1: The low energy spectrum of a metallic Carbon nanotube (broken line) acquires a minigap (solid line) in the presence of a symmetry breaking perturbation. The backscattering transitions (6.23) induced by the SAW potential are shown. *Inset:* proposed experimental arrangement consisting of a nanotube suspended between contacts, with a gate on the side, and a SAW source.

vation [40, 35] of resonant states formed as standing waves in a finite sample. The resonances were found to be spaced by hv/L, where L the sample length. This gives $E_{\rm gap} = 0.6$meV for $L = 3\mu$m, which implies that a periodic SAW potential with $\lambda_{\rm SAW}$ of several microns is sufficient to form large minigaps. A period of the SAW-induced grating down to $200 - 300$nm can be realized, so that minigaps as large as 10 meV are expected. For comparison, the same periodic perturbation acting on a GaAs 1D channel will induce minigaps of an order of magnitude smaller because of a smaller $v_F \approx 10^7$ cm/s. A further advantage of metallic nanotube system results from its semi-metallic spectrum in which two pairs of oppositely moving spin degenerate states intersect exactly at the Fermi level (at half-filling). Thus despite the fact that the SAW wavelength is always much larger than the lattice constant, principal minigaps will open close to the Fermi level (Fig. 6-1) and moreover a minute doping or gating is sufficient to align the chemical potential with one of the minigaps.

As it has been shown in Chapter 4, electron states in semi-metallic nanotubes are described by the 1D Dirac equation rather than the Schrodinger equation. We shall show that a selection rule protects the integrity of the Dirac band structure against backscattering due to a potential perturbation. Therefore in the arrangement shown in Fig. 6-1, the SAW will not couple to the electrons at all. In order to realize adiabatic charge transport, backscattering must be restored by applying an external perturbation that lowers the symmetry of the Dirac system (by mixing left and right states). In Sec. 4.2.2 we have shown that this can be achieved by applying a magnetic field [22] along the nanotube axis. Also, as it has been pointed out there, in a number of nominally metallic nanotubes such as the so-called "zig-zag" nanotubes, a matrix element mixing the left and right states appears [18] due to the curvature of the 2D Carbon sheet rolled into a tube. Both effects open a minigap at the band center, as confirmed experimentally [23, 19].

To simplify our analysis, in this Section we consider adiabatic charge transport in the non-interacting system. The effects of electron interactions on the electron spectrum will be accounted for in Chapter 7 below. There we will demonstrate that the electron interaction *enhances* the minigaps thus making adiabatic current

quantization more pronounced.

6.2 Single particle spectrum

As it has been shown in Sec. 4.2.2, the single-particle NT spectrum near half-filling in the vicinity of either K or K' points can be obtained from the massive 1D Dirac system,

$$\mathcal{H}_D = -i\hbar v\,\sigma_3\partial_x + \Delta_0\,\sigma_1\ . \tag{6.1}$$

The Hamiltonian (6.1) is written in the Weyl basis where the components of the wave function $\psi = (\psi_R\ \psi_L)^T$ represent the right and left moving particles. $\sigma_{1,3}$ are the Pauli matrices and $v \approx 8\cdot 10^7$ cm/s is the NT Fermi velocity. The Hamiltonian (6.1) yields the Dirac dispersion

$$\epsilon(p) = \pm\sqrt{p^2v^2 + \Delta_0^2} \tag{6.2}$$

where the momentum p is measured with respect to the NT Dirac points $\pm k_0$, see Fig. 6-1.

Consider now the nanotube in the presence of a periodic potential induced by a SAW that propagates in the piezoelectric substrate as described above. We assume a monochromatic SAW with a wavenumber $k_{\rm SAW}$ and velocity s. This wave produces harmonically varying potential which decays exponentially in the direction z perpendicular to the surface: $\mathcal{U} \propto e^{-k_{\rm SAW}z}\cos k_{\rm SAW}(x-st)$. In principle, this requires adding an extra dimension to the Hamiltonian (6.1). Practically, the SAW wavelength

$$\lambda_{\rm SAW} = \frac{2\pi}{k_{\rm SAW}} \tag{6.3}$$

is much greater than the tube radius R, and thus one can ignore the SAW-induced potential variation over the tube cross-section. For example, for $\lambda_{\rm SAW} = 1\,\mu$m and $R = 0.5\,$nm, from the exponential factor $e^{-k_{\rm SAW}z}$ one expects that the potential is uniform over the nanotube circumference to within 0.5%.

The realization that the factor $e^{-k_{\rm SAW}z}$ can be dropped amounts to a significant

simplification since the problem with

$$\mathcal{U}(x,t) = A\cos k_{\mathrm{SAW}}(x - st) \tag{6.4}$$

is separable. Focussing on the lowest (metallic) sub-band, the wave function satisfies the following non-stationary Dirac equation in the Hamiltonian form:

$$i\hbar\partial_t\psi = \{\mathcal{H}_D + \mathcal{U}(x,t)\}\,\psi\ . \tag{6.5}$$

So far we have neglected the effects of the electron spin. In the present Chapter we do not consider effects of a magnetic field. The SAW-induced potential (6.4) couples to the total charge density and therefore does not distinguish between spin polarizations. Also since we are focussing on the low energy phenomena near half-filling, we discard interactions between the K and K' points in the Brilloin zone since these processes involve a momentum transfer $\sim 1/a_{\mathrm{cc}} \gg k_{\mathrm{SAW}}$. As a result we effectively have four $(2_{\mathrm{spin}} \times 2_{\mathrm{valley}})$ decoupled fermion types, which we call "flavors", each described by the same Dirac equation (6.5). The resulting spin and valley degeneracy will be taken into account in Sec. 6.3 by quadrupling the amount of carriers contributing to the quantized current.

A further simplification to a problem (6.5) arizes when one utilizes adiabaticity due to a small sound velocity:

$$s \ll v\ . \tag{6.6}$$

In this case one may study the spectrum of a *stationary* problem

$$\{\mathcal{H}_D + U(x)\}\ \psi = \epsilon\psi\ , \tag{6.7}$$

where

$$U(x) = A\cos k_{\mathrm{SAW}}x\ . \tag{6.8}$$

Below we analyze the energy spectrum of the problem (6.7). It is convenient to

perform a gauge transformation

$$\psi'(x) = e^{-i\bar{A}\sigma_3 \sin k_{\rm SAW} x}\, \psi(x) \ , \tag{6.9}$$

where we introduced the dimensionless SAW coupling

$$\bar{A} = \frac{A}{\epsilon_0} \ . \tag{6.10}$$

The energy scale

$$\epsilon_0 \equiv \hbar k_{\rm SAW} v = 3.3 \text{ meV}/\lambda_{\rm SAW\,[\mu m]} \tag{6.11}$$

is a natural measure of the relevant energies and it will be utilized throughout this work. After the gauge transformation (6.9) the Hamiltonian $\mathcal{H}_D + U(x)$ becomes

$$\mathcal{H}' = -i\hbar v\, \partial_x \sigma_3 + \Delta_0 \sigma_1 e^{-2i\bar{A}\sigma_3 \sin k_{\rm SAW} x} \ . \tag{6.12}$$

One can readily see from Eq. (6.12) that in the absence of electron backscattering ($\Delta_0 = 0$) the external potential is gauged away and does not affect the spectrum. In the presence of backscattering, the periodic system (6.12) is characterized by the Bloch states $\psi_p(x) = u_p(x) e^{ipx}$ with a quasimomentum p taking values in the effective Brillouin zone defined by the SAW period, $-k_{\rm SAW}/2 < p < k_{\rm SAW}/2$. The corresponding energy spectrum $\epsilon(p)$ can be obtained analytically [2] in the *weak coupling limit*,

$$\Delta_0 \ll \epsilon_0 \ , \tag{6.13}$$

by treating the last term in (6.12) as a perturbation. This perturbation mixes right and left moving spectral branches at the momenta values

$$p_m = \pm \frac{m}{2} k_{\rm SAW} \ , \quad m = \pm 1, \pm 2, \ \ldots \ . \tag{6.14}$$

Using the decomposition

$$e^{-iz\sin x} = \sum_{n=-\infty}^{\infty} J_n(z)\, e^{-inx} \,, \tag{6.15}$$

we obtain the minigaps $2\Delta_m^{(0)}(\bar{A})$, where

$$\Delta_m^{(0)}(\bar{A}) = \Delta_0 \, |J_m(2\bar{A})| \tag{6.16}$$

are oscillatory functions of the SAW amplitude A, with zeros at the nodes of Bessel functions J_m. In particular, for $A \ll \epsilon_0$,

$$\Delta_m \simeq \frac{\Delta_0}{|m|!} \left(\frac{A}{\epsilon_0}\right)^{|m|} \,. \tag{6.17}$$

Minigaps (6.16) open at the energy values $\epsilon_m = m\epsilon_0/2$. We use the superscript (0) in Eq. (6.16) to underline that the minigaps (6.16) are obtained in the single particle model. In Chapter 7 we will find out how the result (6.16) is modified in the presence of electron interactions.

As long as $\Delta_0 \ll \epsilon_0$, the gaps (6.16) occupy only a tiny fraction of the energy domain. The *strong coupling regime* is reached at $\Delta_0 \geq \epsilon_0$, when the gaps become wider than the sub-bands. With Δ_0 arbitrary, the spectrum can be studied numerically [2]. This amounts to integrating the system of two first-order differential equations

$$\mathcal{H}'\psi' = \epsilon\psi' \tag{6.18}$$

over the SAW period, which gives rise to a transfer matrix relating the wavefunction values on the ends of the interval $0 < x < \lambda_{\mathrm{SAW}}$. The transfer matrix is unimodular, with two eigenvalues $e^{\pm i\gamma}$. The parameter γ can be real or imaginary, depending on the value of ϵ. The former case corresponds to a Bloch state with a quasimomentum $p = \gamma k_{\mathrm{SAW}}/2\pi$, whereas the latter case corresponds to ϵ in the spectral gap. Examples of the energy spectrum obtained in this way are shown in Fig 6-2 for the case $\Delta_0 = 0.4\epsilon_0$ and in Fig. 6-3 for the case $\Delta_0 = \epsilon_0$. We note the persistence of qualitative

features of the spectrum derived above from the perturbation theory. Energy gaps oscillate as a function of $2\bar{A}$ taking zero values at particular $\bar{A}$'s. Gaps become wider than the subbands already in the cae $\Delta_0 = \epsilon_0$. The spectrum also possesses an electron-hole symmetry, $\epsilon \to -\epsilon$, characteristic of a Dirac system.

6.3 Adiabatic current

Having solved the electron spectrum problem, we now proceed with discussing adiabatic transport. When electron density matches the SAW periodicity, the chemical potential falls in one of the energy gaps separating filled and empty states. In this case, moving SAW carries electrons as a conveyer, and so the current is integer in the units of electron charge per cycle. Let us derive the condition for electron density corresponding to full occupancy of minibands. The number of filled minibands, counted from the middle of the spectrum shown in Fig. 6-3, should be approximately proportional to doping (or to gating potential).

We denote ρ to be the electron density measured from the half-filling. Its contribution to electric current is $j = e\rho s$, where s is the SAW velocity. Integer filling of m minibands corresponds to the density

$$\rho = 4\int_{-mk_{\rm SAW}/2}^{mk_{\rm SAW}/2} \frac{dk}{2\pi} = \frac{4m}{\lambda_{\rm SAW}} \tag{6.19}$$

of $4m$ electrons per SAW period $\lambda_{\rm SAW}$, where the factor of four takes care of the spin and valley degeneracy described above. The resultant adiabatic current is

$$j = 4em\,\frac{s}{\lambda_{\rm SAW}}\ . \tag{6.20}$$

Introducing the SAW frequency

$$f = \frac{s}{\lambda_{\rm SAW}}\ , \tag{6.21}$$

we obtain for the quantized current.

$$j = 4mef \ , \quad m = \pm 1, \pm 2, \ldots \ . \tag{6.22}$$

The consequence of our result (6.22) is that there is no current in a nanotube doped exactly to half-filling. Only the excess charge density ρ contributes to electric current when the SAW is applied. This is because electrons in the half-filled (undoped) system represent a solid state analogue of the Dirac vacuum: under the SAW perturbation, the many-body state carries neither charge nor current. For a weak SAW potential this follows from adiabatic continuity: quantized transport takes place when the chemical potential μ falls in one of the minigaps. The value of the quantized current will remain the same [45] within a whole range of values of μ and A that stay within a gap. Since the spectral gap at the band center is adiabatically connected to the minigap at $A = 0$ (induced by the symmetry breaking perturbation Δ_0), it is evident that at half-filling the current is zero. The dependence of the energy gaps on A, shown in Figs. 6-2 and 6-3, describes the width of the plateaus of quantized current.

6.4 Current in the weak perturbation limit

Below we show that, in fact, the sign reversal of the current at $\rho < 0$, as well as its vanishing at half-filling, $\rho = 0$, are generic features unrelated to adiabaticity. To illustrate this point, an alternative scheme can be developed to evaluate the current when the SAW amplitude is small and the temperature is high, i.e. $T \gg \Delta_1 \sim A$. In this limit, the left to right backscattering (depicted in Fig. 6-1) is incoherent, and transition rates are given by the Fermi Golden rule:

$$dw_{p \to p'} = \frac{2\pi}{\hbar} \sum_{m \neq 0} \delta_{\epsilon' - \epsilon - mhf} n_\epsilon (1 - n_{\epsilon'}) |\mathcal{M}_m(p, p')|^2 \frac{dp}{2\pi} \frac{dp'}{2\pi}$$

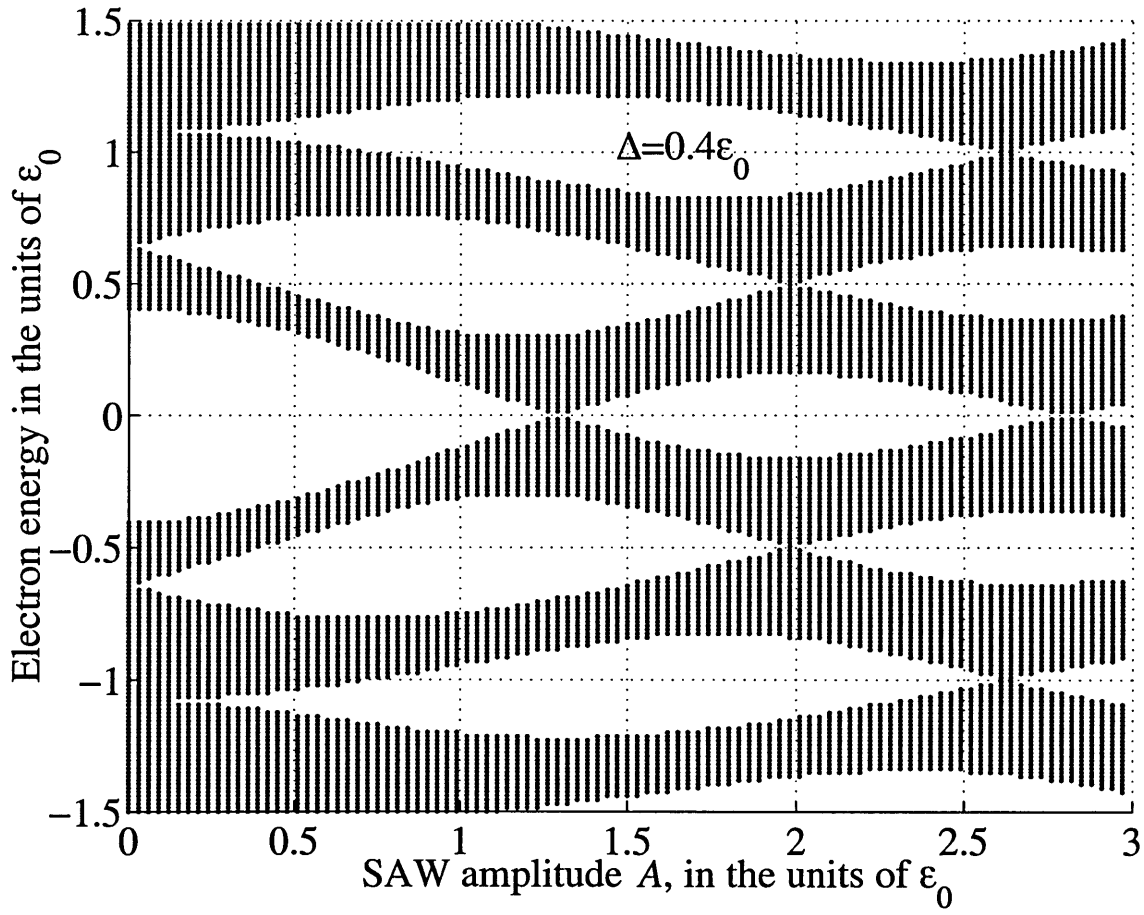

Figure 6-2: Electron energy spectrum of Eq. (6.5) *vs.* the SAW field strength A, scaled by $\epsilon_0 = \hbar k v$. Qualitative features of the perturbation theory (6.16) persist. In particular, the energy gaps oscillate as a function of A vanishing at values close, but generally not equal, to the roots of Bessel functions.

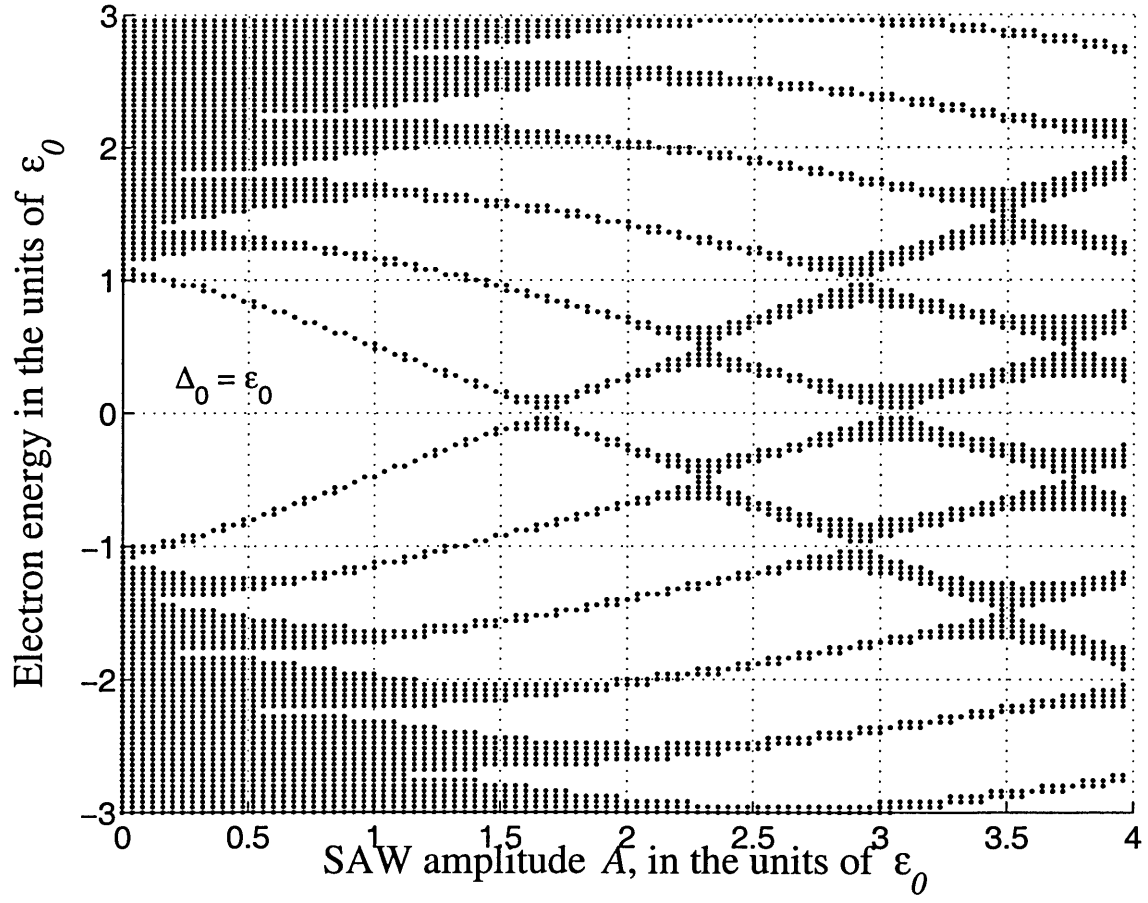

Figure 6-3: Electron energy spectrum of Eq. (6.5) *vs.* the SAW field strength A/ϵ_0, for $\Delta_0 = \epsilon_0$. In the region $A \sim \epsilon_0$ the minibands become exponentially narrow

where $n_\epsilon = (e^{\beta(\epsilon-\mu)}+1)^{-1}$. For spatially periodic SAW the conditions of momentum and energy conservation,

$$p' - p = mk, \qquad \epsilon_r(p') - \epsilon_l(p) = mhf \ , \tag{6.23}$$

must be fulfilled. As a simple model of momentum relaxation, we consider the SAW potential confined to an interval $|x| < \ell/2$ smearing the resonance condition (6.23) on momentum conservation. Physically, $\ell = v\tau$ is associated with the scattering mean-free path of the electron. Also, the transitions take place only for $m = \pm 1$ to lowest order in the SAW strength. This gives

$$\mathcal{M}_{m=\pm 1}(p,p') = \frac{1}{2}\langle l|r\rangle A_{p'-p-mk} \ , \tag{6.24}$$

where

$$A_q = \frac{2A}{q}\sin\frac{q\ell}{2} \ , \tag{6.25}$$

and, for $\Delta_0 \ll \epsilon_0$,

$$\langle l|r\rangle = \frac{2\Delta}{\epsilon_0} \ . \tag{6.26}$$

At temperatures $T \geq \hbar/\tau, hf$, the smearing of Fermi step n_ϵ exceeds the smearing of momenta, which allows the replacement

$$|A_q|^2 \to 2\pi\ell\,|A|^2\,\delta(q) \ . \tag{6.27}$$

In this approximation, by evaluating the total induced current,

$$I = e\sum_{p,p'}(dw_{p\to p'} - dw_{p'\to p}) \ , \tag{6.28}$$

one obtains

$$I = \frac{e|A|^2\ell}{2\hbar^2 v}\left(\frac{\Delta_0}{\epsilon_0}\right)^2 \frac{hf}{T}\,\frac{\sinh(\epsilon_0/2T)\,\sinh(\mu/T)}{\left(\cosh(\epsilon_0/2T)+\cosh(\mu/T)\right)^2} \ . \tag{6.29}$$

The current (6.29) is an odd function of μ: indeed, the sign reversal at $\mu = 0$ can be inferred directly from Fig. 6-1 since the transitions induced by SAW are left $\to$

right at $\mu > 0$, and right $\rightarrow$ left at $\mu < 0$. The dependence I vs. μ in the weak SAW regime is shown in Fig. 6-4. As the temperature is decreased (or the SAW amplitude increased) the system moves out of the range of validity of the Golden rule estimate and enters the regime of adiabatic transport $A \gg \max(\hbar/\tau, T)$.

6.5 Discussion

In this Chapter we have shown that a SAW-induced periodic potential opens minigaps (6.16) in the NT single particle spectrum. With the chemical potential inside the minigap, adiabatically moving SAW generates a quantized current (6.22) that changes sign at half-filling.

The picture described in the present Chapter does not take into account electron interactions that are important in one dimension. In the following Chapter we develop a bosonized description of interacting electrons in a nanotube. This framework will allow us to renormalize the noninteracting minigaps (6.16) in Sec. 7.3.1. There we will see that the renormalized minigap values (7.78) are strongly enhanced by electron interactions.

To complete our discussion, let us comment on the feasibility of the experiment (Fig. 6-1 inset). Maximal values of the SAW induced minigaps in Fig. 6-3 are close to Δ_0, one half of the value of the central gap. If a longitudinal magnetic field is used to open the central gap, then for a single-walled nanotube with a diameter 1.6 nm (such as that grown by Ref. [52]), and a field $B = 16\,\mathrm{T}$, one finds $\Delta_0 \simeq 5\,\mathrm{meV}$. Applied to the spectra in Fig. 6-2 where $\Delta_0 = 0.4\epsilon_0$ (i.e. $\epsilon_0 = 12\,\mathrm{meV}$), it corresponds to a SAW wavelength of $\lambda_{\mathrm{SAW}} \simeq 0.25\,\mu\mathrm{m}$, frequency $f = 13\,\mathrm{GHz}$, and quantized current of around 8 nA. In order to reach a maximum value of the principal SAW induced minigap shown in Fig. 6-2 the SAW potential should be around $A = 10\,\mathrm{meV}$. This value obtained in the single electron approximation should be corrected by the factor $K \sim 10$ to account for the screening in the 1D system (Chapter 7, Eqs. (7.78) and (7.23)). Thus a SAW potential of around several hundred meV may be required. These values do not present a problem even when a weak piezoelectric such as GaAs

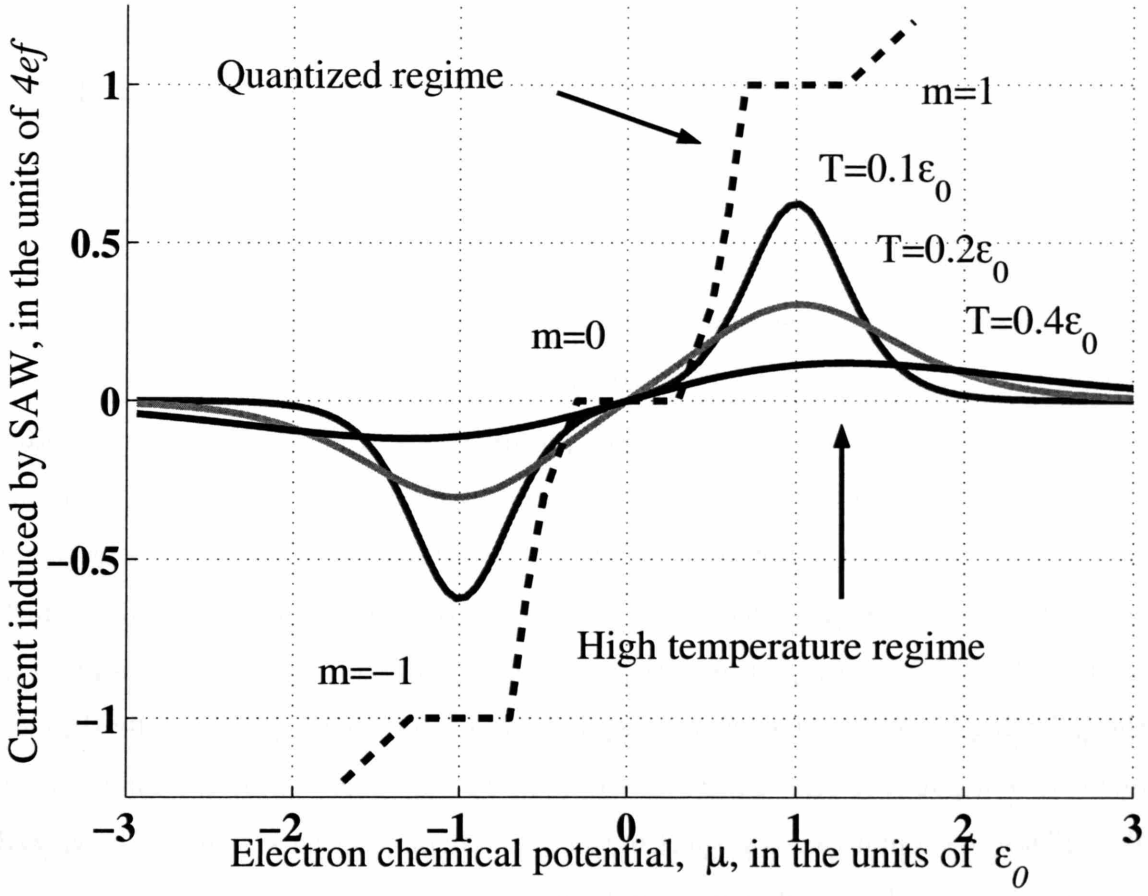

Figure 6-4: Current *vs.* electron chemical potential μ (with $\epsilon_0 = \hbar k v$) as predicted by the Golden rule (6.29) valid in the range $A \ll \hbar/\tau \ll T$, where $\Delta_1 \simeq A$. The peaks positions, $\mu = \pm\epsilon_0$, are defined by the resonance condition (6.23) for $m = \pm 1$. Negative current at $\mu < 0$ is due to the charge reversal of the carriers: $e \to h$. A schematic plot of the quantized current plateaus in the adiabatic regime $A \gg \max(\hbar/\tau, T)$ is shown as a broken line. Here, since $\Delta \ll \epsilon_0$, the quantized plateaus are centered at the values of μ corresponding to the resonances (6.23).

is used.[49] Moreover, for the experiments with nanotubes one can use a much stronger piezoelectric such as $LiNbO_3$ as a substrate, which will make SAW potential in the eV range available. A strong piezoelectricity of the substrate will also facilitate generation of the high frequency SAW required for the proposed experiment (in $LiNbO_3$ the SAW frequencies of ca. 17 GHz have been reported [53]). One could also use the "zig-zag" nanotubes in which the central gap opens [18] due to the curvature of the carbon sheet, Eq. (4.26). In this case the gap is predicted to be in a range up to 20 meV for a tube diameter of 1.6 nm, and the magnetic field is not necessary. Thus a SAW induced minigap as large as 10 meV could be obtained in this case.

To summarize, we have considered a metallic carbon nanotube in the field of a slowly moving periodic potential. If the nanotube is subjected to a further perturbation that mixes right and left moving states, the coupling between the electrons and the SAW potential acts as a charge pump conveying electrons along the tube. An estimate of the miniband spectrum induced by electron diffraction on the sliding potential revealed that minigaps of ca. 10 meV are viable. We therefore conclude that the carbon nanotube combined with the SAW provides a promising system in which quantized adiabatic charge transport can be observed. As it will be demonstrated in the following Chapter, the energy gaps, that can be detected experimentally through quantization plateaux widths, are sensitive to the character of electron interactions. We will see that quantized transport in this strongly interacting system can be viewed as a novel probe of the Luttinger liquid physics.

Chapter 7

Interaction Induced Ordering

In the present Chapter we consider a nanotube in an external periodic potential. We show that such a potential can change NT electronic properties. Minigaps in the spectrum open up at electron density commensurate with potential period, giving rise to incompressible electron states.

As it has been shown in Chapter 6, in the single electron model such incompressible states appear only at integer density. In contrast, in the presence of electron interactions, incompressible states with *fractional* densities exist. This problem is analyzed below in the Luttinger liquid framework. We use the phase soliton approach to estimate the minigaps at integer and fractional densities. The sensitivity of minigaps to density and interaction strength opens new possibilities for controlling transport properties [3].

7.1 Introduction

In the present Chapter we consider electron properties of Carbon nanotubes in an external periodic potential with period λ_{ext} much greater than the NT radius a, $\lambda_{\text{ext}} \gg a$. Such a potential can be realized using optical methods, by gating, or by an acoustic field. In all three cases, realistic period λ_{ext} is of a micron scale. In the previous Chapter we have studied an acoustoelectric effect in a NT in the presence of a surface acoustic wave. This effect has been proposed as a vehicle to realize

adiabatic charge transport [2]. In the latter proposal, a surface acoustic wave (SAW) propagating in the piezoelectric substrate is accompanied by a wave of charge density that results in the electric coupling between the SAW and the NT electrons. We have shown that a number of incompressible electron states appear due to the SAW-induced periodic potential. With a chemical potential inside the minigap corresponding to such an incompressible state, a slowly moving SAW induces a *quantized current* (6.22) in the nanotube.

In this Chapter we show that the coupling of an external periodic potential to electronic NT system can be used to alter electrolic properties and as a probe of electron correlations and interactions. In the absence of interactions, electron diffraction on the periodic potential results in minigaps opening at certain values of electron energy. In the previous Chapter we have only considered incompressible states in the single electron picture. In such states, the total electron density (counted from half-filling) is

$$\rho = \frac{4m}{\lambda_{\text{ext}}} \tag{7.1}$$

with an integer m (cf. Eq. (6.19)). Here the factor of four corresponds to a number of fermion flavors in a nanotube near half-filling due to spin and valley degeneracy, and m is the number of fermions of each flavor per potential period λ_{ext}. Below we show that in the presence of electron interactions, additional incompressible states arise at any *rational* $m = p/q$.

In this Chapter we treat interactions in the Luttinger liquid framework. In the bosonized picture, an incompressible state corresponds to a lattice of sine-Gordon solitons of bose-fields that is commensurate with the external potential. Such a state is characterized by an average number m of solitons of each flavor per potential period λ_{ext}. In the noninteracting case, the Bloch theorem allows only *integer* m, while in the interacting case m can be any simple fraction. Excitation gaps for such fractional states depend on interaction strength and vanish in the noninteracting limit. We estimate excitation gaps over commensurate states using a *phase soliton* approach that describes a distortion of a soliton lattice over a length scale much greater than

the potential period.

The method of treating an excitation in a commensurate state as a phase soliton that we use below has been formulated in the works of Dzyaloshinskii [46] and Pokrovsky and Talapov [47]. A novel feature of the NT electrons is the $SU(4)$ symmetry [31, 29, 28] of the NT Dirac Hamiltonian [10]. In the bosonized language this results in two different phase soliton lengths, $l_{\rm ch}$ and $l_{\rm fl}$, with the first one corresponding to the stiff charge mode, and another to three neutral flavor modes [33]. When the interactions are strong, $l_{\rm ch} \gg l_{\rm fl}$. Depending on the relation between $l_{\rm ch}$, $l_{\rm fl}$, and the external potential period $\lambda_{\rm ext}$, in the presence of interactions we will consider *three* qualitatively different regimes of coupling of the NT fermions to the external potential:

(i) Weak coupling limit, when

$$\lambda_{\rm ext} \ll l_{\rm fl} \ll l_{\rm ch} \ . \tag{7.2}$$

In this limit we will show that the minigaps are strongly *enhanced* by the electron interactions [2]. We will also consider a novel interaction-induced incompressible state with a fractional filling $m = 1/2$ in the limit (7.2). We will find its ground state and the corresponding renormalized excitation gap, as well as briefly discuss other fractions.

(ii) Strong coupling limit, when

$$l_{\rm fl} \ll \lambda_{\rm ext} \ll l_{\rm ch} \ . \tag{7.3}$$

In this limit we will find that due to the large Coulomb repulsion, the four-flavor NT electron system behaves as a system of single flavor fermions with a *quadrupled density*. We will use this observation to estimate the interaction-induced minigaps in this limit. We will show that the $SU(4)$ symmetry of NT electrons manifests itself in a universal scaling power $4/5$ of renormalized minigaps in the limit of large electron interaction.

(iii) Weak tunneling, or *quasiclassical limit*

$$l_{\rm fl} \ll l_{\rm ch} \ll \lambda_{\rm ext} \tag{7.4}$$

corresponds to semi-classical electrons localized in the potential minima. In this case the NT properties will be determined by a *classical* Coulomb energy of a chain of localized electrons and holes.

The outline of the present Chapter is as follows.

In Section 7.2 we introduce and bosonize an effective $SU(4)$ Dirac Hamiltonian for *interacting* NT electrons. We identify a stiff charge mode and fluctuating flavor modes.

Weak coupling limit (7.2) is considered in In Section 7.3. First we renormalize the minigaps (6.16) corresponding to the integer m incompressible states that we have identified in the previous Chapter for a noninteracting system. We next focus on the simplest interaction-induced incompressible state with a fractional filling $m = 1/2$.

The *strong coupling limit* (7.3) of interacting fermions localized in the potential minima is described in Section 7.4.

In Section 7.5 we consider the weak tunneling limit (7.4) of classical electrons and holes localized in the potential minima and plot a charge filling diagram.

In Section 7.6 we briefly discuss a possibility to measure interaction-induced minigaps in the adiabatic current setup described in Chapter 6 and summarize the main results of the present Chapter.

7.2 Bosonization

In the present Section we develop a many-body description of the nanotube close to half-filling taking into account the Coulomb repulsion between electrons. This treatment will be used later in Sections 7.3 and 7.4 to study the role of interactions on the energy spectrum.

In the Appendix B we have outlined the key steps for bosonizing 1D spinless

electrons. In the present Section we will bosonize the effective $SU(4)$ invariant Dirac Hamiltonian that describes the NT properties close to half-filling.

Assuming spin and valley degeneracy discussed in Sec. 6.2, we introduce the Hamiltonian

$$\mathcal{H} = \mathcal{H}_0 + \mathcal{H}_{\rm bs} + \mathcal{H}_{\rm ext} \tag{7.5}$$

for the NT electrons. In Eq. (7.5), the first term is a massless Dirac Hamiltonian

$$\mathcal{H}_0 = -i\hbar v \int \sum_{\alpha=1}^{4} \psi_\alpha^+ \sigma_3 \partial_x \psi_\alpha dx + \frac{1}{2} \sum_k \rho_k V(k) \rho_{-k} \ . \tag{7.6}$$

Here

$$\psi_\alpha = \begin{pmatrix} \psi_\alpha^R \\ \psi_\alpha^L \end{pmatrix} \ , \quad 1 \leq \alpha \leq 4 \tag{7.7}$$

is a two component Weyl spinor of a flavor α, and

$$\rho(x) = \sum_{\alpha=1}^{4} \psi_\alpha^+(x) \psi_\alpha(x) \tag{7.8}$$

is the total charge density.

The Hamiltonian (7.6) is written in the forward scattering approximation for nanotubes [28, 29]. Under this approximation we have discarded the backscattering and Umklapp processes between different Dirac points of the graphene Brilloin zone. Since the ratio $N = 2\pi R/a_{\rm cc}$ of the NT circumference to the inter-atomic distance $a_{\rm cc}$ is large (ca. 10), backscattering and the Umklapp interactions are small scaling as $1/N$ [28]. The Umklapp amplitude is also shown to be small numerically [32]. The long-range electron interaction in the spin- and valley-degenerate modes is symmetric with respect to the four 'flavors'. In the Luttinger liquid theory of nanotubes [28, 29] this interaction is described by the forward scattering amplitude $V(k)$ with a form that depends on the electrostatic environment. In the absence of screening,

$$V_0(k) = \int \frac{e^2}{|x|} \, e^{ikx} dx = e^2 \ln \left[1 + (kR)^{-2} \right] \ . \tag{7.9}$$

The substrate dielectric constant ε changes $V_0(k)$ to

$$V(k) = \tfrac{2}{\varepsilon+1} V_0(k) \ . \tag{7.10}$$

Backscattering in the model (7.5) is described by the term

$$\mathcal{H}_{\rm bs} = \Delta_0 \int \textstyle\sum_{\alpha=1}^{4} \psi_\alpha^+ \sigma_1 \psi_\alpha dx \ . \tag{7.11}$$

As discussed above in Sec. 4.2.2, such a term is present in semiconducting nanotubes, and it can also originate in metallic tubes due to curvature of the graphene sheet or due the external magnetic field.

Finally, the interaction with the external periodic potential is described by

$$\mathcal{H}_{\rm ext} = \int dx \, \rho U(x) \ , \tag{7.12}$$

where the potential U is defined similarly to the one in Eq. (6.8):

$$U = A \cos k_{\rm ext} x \ , \quad k_{\rm ext} = \frac{2\pi}{\lambda_{\rm ext}} \ . \tag{7.13}$$

The Hamiltonian $\mathcal{H}_0 + \mathcal{H}_{\rm bs} + \mathcal{H}_A$ is bosonized in a standard way [64, 28, 29]. We represent the fermionic operators (7.7) as nonlocal combinations of bose fields

$$\psi_\alpha = \frac{1}{\sqrt{2\pi R}} \begin{pmatrix} e^{i(\Phi_\alpha - \Theta_\alpha)} \\ e^{i(\Phi_\alpha + \Theta_\alpha)} \end{pmatrix} \ , \tag{7.14}$$

similarly to the single flavor case discussed in the Appendix B. Here the conjugate bose fields obey the commutation algebra

$$[\Phi_\alpha(x), \, \Theta_\beta(y)] = \delta_{\alpha\beta} \frac{i\pi}{2} \, {\rm sign}(x-y) \ . \tag{7.15}$$

As a result we obtain the Lagrangian

$$\mathcal{L} = \frac{v}{2\pi}\int dx \sum_{\alpha=1}^{4} (\partial_\mu \Theta_\alpha)^2 - \frac{1}{2}\sum_q \rho_{-q} V_q \rho_q - \int dx \left(\frac{\Delta_0}{\pi a} \sum_{\alpha=1}^{4} \cos 2\Theta_\alpha + \rho(x) U(x) \right) \quad (7.16)$$

where the total particle density in terms of the bosonic variables is given by

$$\rho(x) = \sum_{\alpha=1}^{4} \rho_\alpha = \sum_{\alpha=1}^{4} \tfrac{1}{\pi}\, \partial_x \Theta_\alpha \ . \quad (7.17)$$

The Lagrangian (7.16) corresponds to the classical sine-Gordon Hamiltonian for the four interacting bosonic fields Θ_α,

$$\begin{aligned} \mathcal{H}_{\rm cl}[\Theta_\alpha] = \tfrac{\hbar v}{\pi} \int dx \, \Big\{ \tfrac{1}{2} \textstyle\sum (\partial_x \Theta_\alpha)^2 + \tfrac{K-1}{8} \left(\textstyle\sum \partial_x \Theta_\alpha \right)^2 + \\ + g_0 \textstyle\sum \cos 2\Theta_\alpha + \tfrac{1}{\hbar v} \textstyle\sum \partial_x \Theta_\alpha \cdot \big(U(x) - \mu \big) \Big\} \ . \end{aligned} \quad (7.18)$$

Here the coupling

$$g_0 = \frac{\Delta_0}{\hbar v R} \ , \quad (7.19)$$

μ is the chemical potential calculated from the half filling, and the charge stiffness

$$K_q = 1 + \frac{4}{\pi \hbar v} V(q) \ . \quad (7.20)$$

Below we drop the (irrelevant) logarithmic dependence of the stiffness K_q on the momentum, assuming a constant value $K \equiv K_{k_{\rm ext}}$.

As a next step we shift the displacement fields

$$\Theta_\alpha(x) \to \Theta_\alpha(x) - \tfrac{1}{\hbar v} \textstyle\int^x K^{-1} (U - \mu)\, dx' \ . \quad (7.21)$$

This procedure is analogous to gauge transforming fermion operators (6.9). The transformed Hamiltonian (7.18) is

$$\begin{aligned} \mathcal{H}'_{\rm cl}[\Theta_\alpha] = \tfrac{\hbar v}{\pi} \int dx \, \Big\{ \tfrac{1}{2} \textstyle\sum (\partial_x \Theta_\alpha)^2 + \tfrac{K-1}{8} \left(\textstyle\sum \partial_x \Theta_\alpha \right)^2 \\ + g_0 \textstyle\sum_{\alpha=1}^{4} \cos \big(2\Theta_\alpha + 2\tilde{\mu}\, k_{\rm ext} x - 2\tilde{A} \sin k_{\rm ext} x \big) \Big\} \ , \end{aligned} \quad (7.22)$$

where the dimensionless quantities

$$\tilde{A} = \frac{A}{K\epsilon_0} , \quad \tilde{\mu} = \frac{\mu}{K\epsilon_0} , \quad \epsilon_0 = \hbar k_{\rm ext} v \tag{7.23}$$

are introduced in a way similar to Eq. (6.10). The difference between Eqs. (7.23) and (6.10) is in additional *screening* (by a factor of $1/K$) of external fields $U(x)$ and μ by the interacting NT system.

Finally, we diagonalize the Gaussian parts of the Lagrangian (7.16) and Hamiltonians (7.18,7.22) by the unitary transformation

$$\begin{pmatrix} \Theta_1 \\ \Theta_2 \\ \Theta_3 \\ \Theta_4 \end{pmatrix} = \frac{1}{2} \begin{pmatrix} 1 & 1 & 1 & 1 \\ 1 & -1 & 1 & -1 \\ 1 & -1 & -1 & 1 \\ 1 & 1 & -1 & -1 \end{pmatrix} \begin{pmatrix} \theta^0 \\ \theta^1 \\ \theta^2 \\ \theta^3 \end{pmatrix} . \tag{7.24}$$

In the new variables the total charge density (7.17) reads

$$\rho(x) = \tfrac{2}{\pi}\, \partial_x \theta^0 . \tag{7.25}$$

Transformation (7.21) leaves θ^a intact, and shifts

$$\theta^0 \to \theta^0 - \tfrac{2}{\hbar v} \textstyle\int^x K^{-1}(U-\mu)\, dx' . \tag{7.26}$$

As a result we obtain the Lagrangian

$$\mathcal{L}' = \mathcal{L}_0 + \mathcal{L}_{\mathcal{F}} \tag{7.27}$$

describing one stiff charge mode and three soft flavor modes, where ($\hbar = v = 1$)

$$\mathcal{L}_0 = \frac{1}{2\pi} \int dx \left\{ (\partial_t \theta^0)^2 - K\, (\partial_x \theta^0)^2 + \textstyle\sum_{a=1}^{3} (\partial_\mu \theta^a)^2 \right\} , \tag{7.28}$$

$$\mathcal{L}_{\mathcal{F}} = -\frac{4 g_0}{\pi} \int dx\, \mathcal{F}\left(\theta^a,\ \theta^0 + 2\tilde{\mu} k_{\rm ext} x - 2\tilde{A} \sin k_{\rm ext} x \right) , \tag{7.29}$$

$$\mathcal{F}\left(\theta^a,\,\theta^0\right) = \cos\theta^0 \cdot \prod_{a=1}^{3} \cos\theta^a + \sin\theta^0 \cdot \prod_{a=1}^{3} \sin\theta^a. \tag{7.30}$$

The Gaussian Lagrangian $\mathcal{L}_0$ describes three flavor modes that move with a velocity v, and one charge mode that has a strongly enhanced velocity

$$\bar{v} = K^{1/2} v\ . \tag{7.31}$$

This is a manifestation of a separation between charge and flavor in an excitation in a strongly interacting system described by the Hamiltonian $\mathcal{H}_0$.

We also note here that the Lagrangians (7.16) and (7.27) are $SU(4)$ invariant, as is the original Hamiltonian $\mathcal{H}$. This invariance is not explicit in the adapted notation and arises at a level of renormalization.

7.3 Weak coupling limit

As shown in Section 6.2 above, in the case of noninteracting electrons in the nanotube an external periodic potential opens minigaps in the electron spectrum. Such minigaps correspond to an integer number m of electrons of each flavor per potential period. The goal of the present Section is to consider the role of electron interactions on the minigaps in the case of a small backscattering.

Below we treat the bosonized interacting problem (7.16) and (7.27) perturbatively in small backscattering amplitude g_0 defined in Eq. (7.19). As we will show below, small backscattering corresponds to a *weak coupling limit* (7.2) for an interacting system. This limit is defined in terms of the flavor soliton length that will be estimated below. For now we assume that this is the limit when the perturbative treatment in backscattering g_0 is valid.

In the absence of backscattering ($g_0 = 0$), the Lagrangian (7.16) describes a *compressible* (i.e. gapless) Tomonaga - Luttinger liquid. Thus, similarly to the noninteracting case considered in Sec. 6.2, the external potential can be gauged away and thus it does not affect the spectrum when the backscattering is absent. The total

density (7.1) corresponds to the chemical potential

$$\tilde{\mu} = \frac{m}{2} \, . \tag{7.32}$$

Here the screened value $\tilde{\mu}$ of the chemical potential is defined in Eq. (7.23) above. The density (7.1) corresponding to a *filling* of m fermions of each flavor per potential period varies continuously with $\tilde{\mu}$ when $g_0 = 0$.

Backscattering qualitatively changes the spectrum. As shown above in Sec. 6.2, in the noninteracting system (corresponding to charge stiffness $K = 1$) a periodic potential (7.13) opens energy gaps in electron spectrum $\epsilon(p)$ near the momentum values $p_m = \pm m k_{\rm ext}/2$. In the case of a small backscattering $\Delta_0 \ll \epsilon_0$ the minigaps are given by Eq. (6.16).

In Sec. 7.3.1 we will prove that electron interactions ($K \gg 1$) strongly *enhance* the minigaps (6.16).

In Sec. 7.3.2 we will show that interactions result in existence of incompressible states with a *fractional* number m of electrons of each flavor per potential period. We will illustrate this point by considering the simplest case of the filling $m = 1/2$ in the limit (7.2).

7.3.1 Integer filling m

In the present subsection we renormalize the noninteracting minigaps (6.16) for incompressible states with integer m due to the presence of interactions. For that we utilize the bosonization picture developed in Section 7.2 above.

Our course of action will be a generalization of the phase soliton approach suggested by Pokrovsky and Talapov and others [47] to the case of four boson modes. First we will find a classical ground state of the Hamiltonian $\mathcal{H}'_{\rm cl}$ given by Eq. (7.22) by decomposing the fields $\Theta_\alpha(x)$ in a series in the coupling g_0,

$$\Theta_\alpha = \bar{\Theta}_\alpha + \Theta_\alpha^{(1)} + \ldots \, , \quad \Theta_\alpha^{(n)} = \mathcal{O}(g_0^n) \, . \tag{7.33}$$

We will obtain the effective potential for the "slow" phase modes $\bar{\Theta}_\alpha$ that are constant in the commensurate state. Next we will renormalize this effective potential by applying the canonical transformation (7.24) and integrating out the fluctuations of the soft flavor fields $\bar{\theta}^a$. Finally, we will estimate the excitation energy as that of a classical phase soliton of a stiff charge mode governed by the renormalized effective potential.

Below we find a classical ground state of the Hamiltonian (7.22) with the chemical potential $\tilde{\mu}$ given by Eq. (7.32) with an integer m. For that we need to solve the Euler-Lagrange equations

$$\frac{\delta \mathcal{H}'_{\rm cl}}{\delta \Theta_\alpha} = 0 \tag{7.34}$$

perturbatively in g_0. Using the decomposition (7.33), in the lowest order in g_0 we find the effective potential for the "slow" components

$$\bar{V}_m[\bar{\Theta}_\alpha] = \frac{\hbar v}{\pi} \int dx \; g_{\tilde{A}} \sum_\alpha \cos 2\bar{\Theta}_\alpha \; , \tag{7.35}$$

$$g_{\tilde{A}} \equiv g_0 J_m(2\tilde{A}) \; . \tag{7.36}$$

In the ground state the fields $\bar{\Theta}_\alpha$ are all *equal* and *constant*, their value being $\pi/2$ or 0 depending on the sign of $J_m(2\tilde{A})$.

An excitation over the ground state is a soliton configuration

$$\bar{\Theta}_\alpha \to \bar{\Theta}_\alpha + \pi \; , \quad 1 \le \alpha \le 4 \; , \tag{7.37}$$

in which the components $\bar{\Theta}_\alpha$ acquire a coordinate dependence that is slow on the scale of $\lambda_{\rm ext}$. Such a configuration corresponds to adding fermions of each flavor *simultaneously*. The minigap Δ_m is by definition an energy cost to add a *single* fermion and thus it is given by a quarter of the energy of this configuration.

To find Δ_m we change the basis according to (7.24). In the new basis the excitation energy $4\Delta_m$ is an energy of a charge soliton $\bar{\theta}^0 \to \bar{\theta}^0 + 2\pi$ with the flavor modes fluctuating around $\bar{\theta}^a = 0$. Such a soliton adds the total charge of $4e$ and is a flavor

singlet. Its energy can be estimated from a Lagrangian

$$\mathcal{L}_0[\bar{\theta}^0\ ,\bar{\theta}^a] + \bar{\mathcal{L}}_m \tag{7.38}$$

for the "slow" modes $\bar{\theta}^0\ ,\bar{\theta}^a$. Here the Gaussian part $\mathcal{L}_0$ is given by Eq. (7.28), and

$$\bar{\mathcal{L}}_m = -\frac{\hbar v}{\pi}\int dx\ 4g_{\tilde{A}}\cos\bar{\theta}^0 \cdot \prod_a \cos\bar{\theta}^a\ . \tag{7.39}$$

Integrating over the Gaussian fluctuations of $\bar{\theta}^a$ we obtain the scaling law

$$g_{\tilde{A}}(l) = g_{\tilde{A}}\left(\frac{l}{a}\right)^{-3/4} \tag{7.40}$$

for the coupling (7.36) when $K \gg 1$. Quantum fluctuations of each of the three flavor modes θ^a contribute by $-1/4$ to the scaling dimension of $g_{\tilde{A}}$. In deriving Eq. (7.40) we neglected fluctuations of the stiff charge mode $\bar{\theta}^0$, contributing via $K^{-1/2} \ll 1$ in the power laws.

Quantum fluctuations of flavor modes around $\bar{\theta}^a = 0$ are important on the length scales $a < l < l_{\rm fl}$ smaller than the flavor soliton size $l_{\rm fl}$. The latter can be estimated self-consistently from the balance of kinetic and potential terms for the flavor modes in the Lagrangian (7.38),

$$g_{\tilde{A}}(l_{\rm fl}) \sim \frac{1}{l_{\rm fl}^2}\ . \tag{7.41}$$

From Eq. (7.41) we obtain the flavor soliton size

$$l_{{\rm fl}m} \sim a\left(\frac{D}{\Delta_m^{(0)}(\tilde{A})}\right)^{4/5}\ . \tag{7.42}$$

Here the 1D bandwidth D is defined in Eq. (4.27), and "bare" minigaps

$$\Delta_m^{(0)}(\tilde{A}) = \Delta_0\,|J_m(2\tilde{A})| \tag{7.43}$$

are given by their noninteracting values (6.16) with the screened potential amplitude $\tilde{A}$ defined in Eq. (7.23). Finally, we estimate the renormalized minigap Δ_m as an

energy of a *classical* charge soliton from the Hamiltonian

$$\bar{\mathcal{H}}_m[\bar{\theta}^0] = \frac{\hbar v}{\pi}\int dx \left\{ \frac{K}{2}(\partial_x \bar{\theta}^0)^2 + 4g_{\tilde{A}}(l_{\mathrm{fl}m})\cos\bar{\theta}^0 \right\} \tag{7.44}$$

that follows from the Lagrangian (7.38) with the flavor degrees of freedom integrated out. From Eq. (7.44) we find the charge soliton size

$$l_{\mathrm{ch}} \sim K^{1/2}\, l_{\mathrm{fl}} \ , \tag{7.45}$$

and the corresponding charge soliton energy

$$E_{\mathrm{sol}} = \tfrac{8}{\pi}\hbar v \left[K g_{\tilde{A}}(l_{\mathrm{fl}})\right]^{1/2} \ . \tag{7.46}$$

Using (7.42) and (7.41), this gives an estimate for a renormalized minigap value

$$\Delta_m \simeq K^{1/2} D^{1/5} \left(\Delta_m^{(0)}(\tilde{A})\right)^{4/5} \ . \tag{7.47}$$

Let us briefly discuss the result (7.47). We notice that the qualitative features of the noninteracting minigaps (6.16) persist in the interacting case. Namely, as a function of a *screened* potential amplitude (7.23), the minigaps (7.47) oscillate, collapsing to zero at particular values of $\tilde{A}$. However, minigaps (7.47) are strongly *enhanced* in magnitude compared to (6.16) due to electron interactions. Also the dependence of the minigaps on both the bare backscattering Δ_0 and the periodic potential amplitude A has a characteristic power law behavior which, in the limit of strong interactions $K \gg 1$, is given by a universal power law 4/5. This power law is a manifestation of the $SU(4)$ flavor symmetry in the nanotube near half filling.

Finally, let us define the applicability range of the result (7.47). The perturbative renormalization group treatment of the flavor modes' fluctuations that has led to Eq. (7.40) is valid provided the *renormalized* coupling $g_{\tilde{A}}(l_{\mathrm{fl}})$ stays small,

$$\hbar v \lambda_{\mathrm{ext}} g_{\tilde{A}}(l_{\mathrm{fl}}) \ll \epsilon_0 \ . \tag{7.48}$$

The above condition requires a renormalized potential energy of the flavor modes to be smaller than their typical kinetic energy over the potential period λ_{ext}. In other words, the weak coupling limit described above holds provided that the soliton scale l_{fl} obtained in (7.42) is greater than the period of the potential, yielding the condition (7.2). The opposite case $l_{\text{fl}} < \lambda_{\text{ext}}$ of a strong coupling between the potential and interacting NT electrons is studied in Section 7.4 below.

7.3.2 Fractional filling, $m = 1/2$

So far we have been studying incompressible states with an integer filling of m fermions per potential period. Such states arise due to a single electron diffraction on the periodic potential and their spectrum is qualitatively similar in the interacting and non-interacting systems. However, as we will show in the present subsection, in the interacting system ($K > 1$) additional incompressible states appear. This happens since in this case the restrictions due to the Bloch theorem are lifted, which leads to incompressible states with fractional fermion density.

Existence of incompressible states with rational densities $m = p/q$ follows from the theory of commensurate states [47]. In this Thesis we generalize the approach [47] to the case of four bosonic modes that correspond to four fermion flavors. Qualitatively, each bosonic mode Θ_α can be viewed as classical for a large stiffness K. In this case a ground state with a rational filling $m = p/q$ corresponds to a commensurate state where the density of every flavor $\frac{1}{\pi}\partial_x\Theta_\alpha$ is $q\lambda_{\text{ext}}$-periodic. An excitation in this language is a configuration where this periodicity is distorted on the scale that is much greater than the potential period λ_{ext}. Following the approach [47], for a general rational fraction $m = p/q$ the excitation gap

$$\Delta_{p/q} \propto {\Delta_0}^q \tag{7.49}$$

in the classical system. In the case of electrons in the nanotube, additional renormalization of this classical energy due to flavor fluctuations will be required.

Below we consider the simplest case of an interaction-induced state with a frac-

tional filling $m = 1/2$. Our course of action will be similar to the one adopted in Sec. 7.3.1 above. We first find a classical ground state of the Hamiltonian (7.22) for the commensurate state which is characterized by the chemical potential

$$\tilde{\mu} = \frac{1}{4} \tag{7.50}$$

in accord with Eq. (7.32). For that we solve the Euler-Lagrange equations for the Hamiltonian (7.22) perturbatively in backscattering and identify the constant ground state values of the "slow" components $\bar{\Theta}_\alpha$ introduced in Eq. (7.33). Next we describe an excitation over the commensurate state by allowing the phase fields $\bar{\Theta}_\alpha$ to acquire a slow coordinate dependence. We estimate the excitation gap in terms of the energy of a phase soliton $\bar{\theta}^0$ by utilizing the canonical transformation (7.24) and integrating out fluctuations of flavor modes.

Below we find the classical $m = 1/2$ soliton configuration perturbatively in backscattering g_0 by minimizing the energy (7.22). In analogy to Sec. 7.3.1 above, we look for an effective potential $\bar{V}_{1/2}[\bar{\Theta}_\alpha]$ for the "slow" fields $\bar{\Theta}_\alpha$ defined in Eq. (7.33). The Euler - Lagrange equations for the Hamiltonian (7.22) are

$$\Theta^{(1)}_{\alpha\, xx} + \frac{K-1}{4} S^{(1)}_{xx} = -\frac{g_0}{2} \sin\left(2\bar{\Theta}_\alpha + \tfrac{1}{2} k_{\rm ext} x - 2\tilde{A} \sin k_{\rm ext} x\right) , \tag{7.51}$$

where $S = \sum \Theta_\alpha$. Integrating (7.51) we obtain

$$\Theta^{(1)}_{\alpha\, x} = \frac{1-K}{4} S^{(1)}_x + \frac{g_0}{k_{\rm ext}} \tilde{\Theta}_\alpha , \tag{7.52}$$

$$S^{(1)}_x = \frac{g_0}{K k_{\rm ext}} \sum \tilde{\Theta}_\alpha , \tag{7.53}$$

$$\tilde{\Theta}_\alpha = \sum_m \frac{J_m(2\tilde{A})}{1-2m} \cos\left(2\bar{\Theta}_\alpha + (\tfrac{1}{2} - m) k_{\rm ext} x\right) . \tag{7.54}$$

Substituting (7.52) and (7.54) into (7.22), after somewhat lengthy but straightforward algebra the slow mode potential follows:

$$\bar{V}_{1/2} = \frac{\hbar v g_{1/2}}{16\pi} \int dx \left\{ (4-\kappa)\, v_{1/2}(2\tilde{A}) \sum_\alpha \cos 4\bar{\Theta}_\alpha \right.$$

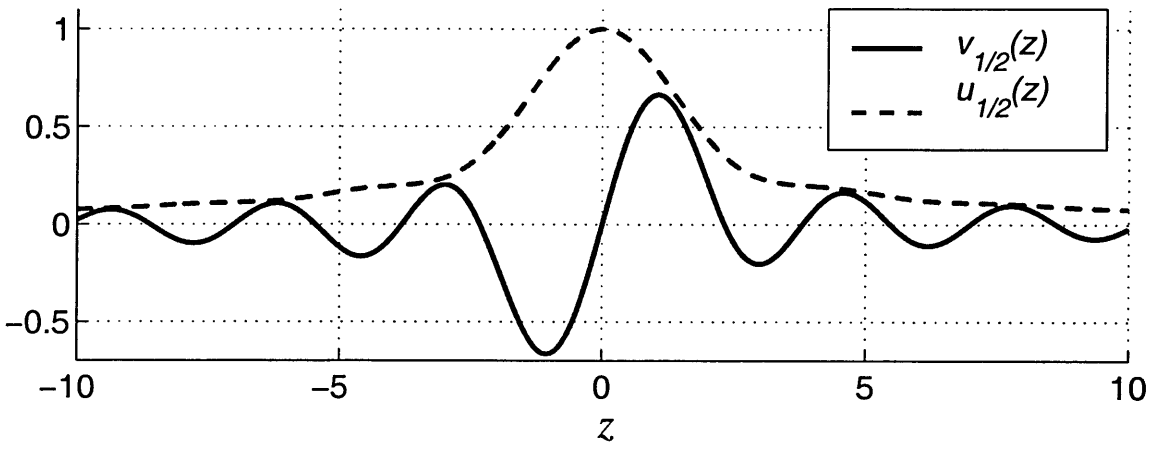

Figure 7-1: The functions $v_{1/2}$ and $u_{1/2}$ defined in Eqs. (7.58) and (7.59). We find that $v_{1/2}(z) > u_{1/2}(z)$ holds for all z. Zeroes of $v_{1/2}$: $z = 0,\ \pm 2.33,\ \pm 3.80,\ \pm 5.47\ , \ldots$.

$$+\kappa \sum_{\alpha \neq \alpha'} \left(u_{1/2}(2\tilde{A}) \cos(2\bar{\Theta}_\alpha - 2\bar{\Theta}_{\alpha'}) - v_{1/2}(2\tilde{A}) \cos(2\bar{\Theta}_\alpha + 2\bar{\Theta}_{\alpha'}) \right) \Bigg\} \ . \tag{7.55}$$

Here

$$g_{1/2} = \left(\frac{g_0}{k_{\text{ext}}} \right)^2 , \tag{7.56}$$

$$\kappa = \frac{K-1}{K} , \tag{7.57}$$

and the functions $v_{1/2}$ and $u_{1/2}$ are defined as

$$v_{1/2}(z) = \sum_{m=-\infty}^{\infty} \frac{J_m(z) J_{1-m}(z)}{(2m-1)^2} , \tag{7.58}$$

$$u_{1/2}(z) = \sum_{m=-\infty}^{\infty} \left(\frac{J_m(z)}{1-2m} \right)^2 . \tag{7.59}$$

Here z is a shorthand notation for $2\tilde{A}$. The functions $v_{1/2}(z)$ and $u_{1/2}(z)$ are plotted in Fig. 7-1.

In the commensurate state we find that the minimum value

$$\min \bar{V}_{1/2}[\bar{\Theta}_\alpha] = -\frac{\hbar v g_{1/2}}{4\pi} \int dx \left\{ 4|v_{1/2}(2\tilde{A})| + \kappa u_{1/2}(2\tilde{A}) \right\} \tag{7.60}$$

of the potential (7.55) corresponds to $\{\bar{\Theta}_\alpha\}$ being an arbitrary permutation of a set of constant values $\{\phi_1\ \phi_1\ \phi_2\ \phi_2\}$, with $\phi_{1,2} = \pm\pi/4$ for $v_{1/2}(2\tilde{A}) > 0$ and $\phi_1 = 0,\ \phi_2 = \pi/2$ for $v_{1/2}(2\tilde{A}) < 0$.

Let us now discuss the symmetry of the obtained commensurate classical state. The ground state degeneracy in the noninteracting case ($\kappa = 0$) is equal to 2^4. This follows from the potential (7.55) in which only the first term is non-zero. We find that in the presence of interactions ($\kappa > 0$), the other terms in (7.55) reduce this degeneracy from 16 to six. This result could have been foreseen without any calculation since it is just a number of configurations where any two *different* fields Θ_α are placed in the same minimum of the external potential. In other words, effect of fermion *exchange* manifests itself in the bosonized treatment by a stronger repulsion between the solitons of the same flavor.

An excitation over the $m = 1/2$ state is described by allowing the components $\bar{\Theta}_\alpha$ to acquire a coordinate dependence that is slow on the scale of λ_{ext}, similarly to our previous treatment in Sec. 7.3.1. To find an excitation gap we change the basis according to the canonical transformation (7.24). The excitation gap $\Delta_{1/2}$ is half an energy of a soliton

$$\bar{\theta}^0 \to \bar{\theta}^0 + \pi\ , \quad \bar{\theta}^a \to \bar{\theta}^a\ , \tag{7.61}$$

that carries two fermions. From the Gaussian Lagrangian (7.28) and the effective potential (7.55) we obtain the effective Lagrangian

$$\mathcal{L}_0[\bar{\theta}^0, \bar{\theta}^a] + \bar{\mathcal{L}}_{1/2}[\bar{\theta}^0, \bar{\theta}^a] \tag{7.62}$$

for the slow modes, where $\mathcal{L}_0$ is given by Eq. (7.28), and

$$\bar{\mathcal{L}}_{1/2} = -g_{1/2} v_{1/2}(2\tilde{A}) \frac{\hbar v}{\pi} \int dx\ \left\{ \frac{4-\kappa}{4} \mathcal{F}(2\bar{\theta}^0,\, 2\bar{\theta}^a) - \frac{\kappa}{4} \sum_a \cos 2\bar{\theta}^a \cos 2\bar{\theta}^0 \right\}\ . \tag{7.63}$$

Here the function $\mathcal{F}$ is defined in Eq. (7.30). The Lagrangian $\bar{\mathcal{L}}_{1/2}$ is obtained from the potential (7.55) by applying the canonical transformation (7.24) and dropping the terms that are independent of $\bar{\theta}^0$.

Quantum fluctuations of the flavor fields $\bar{\theta}^a$ in the problem (7.62) are treated in a way similar to that described in Sec. 7.3.1. The first term in the Lagrangian (7.63) is less relevant than the second one. We obtain the scaling dimension -1 for the second term in $\bar{\mathcal{L}}_{1/2}$, the flavor soliton scale

$$l_{\mathrm{fl},1/2} \simeq a \frac{K}{K-1} \frac{1}{|v_{1/2}(2\tilde{A})|} \left(\frac{\epsilon_0}{\Delta_0}\right)^2 , \tag{7.64}$$

and the renormalized minigap

$$\Delta_{1/2} \simeq \frac{K-1}{\sqrt{K}} D\,|v_{1/2}(2\tilde{A})| \left(\frac{\Delta_0}{\epsilon_0}\right)^2 . \tag{7.65}$$

Here the 1D band width D is defined in Eq. (4.27).

Let us discuss the result (7.65). The excitation energy $\Delta_{1/2}$ is quadratic in the backscattering amplitude Δ_0 in accord with Eq. (7.49). It is strongly *enhanced* by the band width due to fluctuations of the flavor modes. We also note that the $m = 1/2$ excitation is interaction-induced, since its gap (7.65) vanishes in the non-interacting limit $K \to 1$, as required by the Bloch theorem.

The perturbation theory developed here is valid when the flavor soliton size (7.64) is large,

$$l_{\mathrm{fl},1/2} \gg \lambda_{\mathrm{ext}} , \tag{7.66}$$

in agreement to the condition (7.2) above. Practically, Eq. (7.66) requires a very small bare gap Δ_0. For typical values of parameters, $\lambda_{\mathrm{ext}} \sim 1$ μm and $\Delta_0 \sim 10$ meV, the soliton scale $l_{\mathrm{fl},1/2}$ defined in Eq. (7.64) is small compared to the potential period λ_{ext} and the condition (7.66) does not hold. Physically this suggests that there is a more energy efficient way to excite the system with $m = 1/2$ when the backscattering Δ_0 is not very small. This situation will be considered below in Section 7.4.

However, even for the above mentioned parameter values there are cases when the result (7.65) is applicable. This happens when the flavor soliton size $l_{\mathrm{fl},1/2}$ becomes large due to either small interaction strength $K - 1 \ll 1$, or for the certain potential amplitude values that correspond to vanishing of the function $v_{1/2}(2\tilde{A})$, see Fig. 7-1.

Later we will compare the result (7.65) with a strong coupling limit of the same filling $m = 1/2$ considered below in Section 7.4.

7.4 Strong coupling limit

In the previous Section we have considered interacting NT electrons in a periodic potential in the limit of a small backscattering that corresponds to the condition (7.2). In this limit we have shown in Sec. 7.3.1 that minigaps (7.47) are obtained from their noninteracting values (6.16) by rescaling both their magnitude and the external potential amplitude. In this regard the limit of a small backscattering is qualitatively similar to the noninteracting case of nearly free electrons whose spectrum is altered by minigaps that open at certain energy values. Accordingly, we have called this regime as a "weak coupling limit".

We have also seen in Sec. 7.3.2 that electron interactions lead to a qualitative change in the NT spectrum. Namely, we have found novel interaction-induced minigaps that correspond to a fractional amount m of electrons of each flavor per potential period $\lambda_{\rm ext}$. In discussion after the result (7.65) for the filling $m = 1/2$ we have mentioned that our perturbative treatment is generally valid only for very small backscattering. Indeed, the corresponding flavor soliton length $l_{{\rm fl},1/2}$ defined in (7.64) is *smaller* than $\lambda_{\rm ext}$ for realistic parameter values. Due to this fact the corresponding minigap $\Delta_{1/2}$ obtained in (7.65) appears to be very large (proportional to the bandwidth).

The above arguments suggest that a lowest energy charged excitation in the case $l_{\rm fl} < \lambda_{\rm ext}$ should be qualitatively different from the ones we considered above. Indeed, in Section 7.3 we have dealt with charged excitations that carry more than one electron. For instance, the soliton of the field $\bar{\theta}^0$ whose energy we have used to estimate the renormalized gaps (7.47) for the case of an integer filling m carries *four electrons* of different flavors whose wave functions completely overlap. Clearly, such an excitation becomes too costly in the case when electrons are not delocalized and their repulsion is sufficiently strong.

The latter point can be best seen if one considers the extreme opposite limit (7.4) in which the charge excitation is strongly localized, with a *charge* soliton length being smaller than the potential period. In this limit, discussed in Section 7.5 below, the

Coulomb energy determines ordering of essentially classical electrons in the ground state. The corresponding incompressible charge states depend on the *total* charge density (7.1) with the exchange effects being negligible. An excitation in this limit corresponds to adding a single electron into a particular potential minimum without significantly altering the charge configuration in the other minima. Such an excitation cannot carry a multiple electron charge due to a very strong Coulomb repulsion.

In the present Section we consider an intermediate case (7.3) of a moderate backscattering g_0 and strong interactions $K \gg 1$, for which a flavor soliton scale defined in Eq. (7.47) is small, but the charged excitation is delocalized over many λ_{ext}. Below we will show that in this limit, the system of four flavors Θ_α each of a filling m behaves as a system of a *single* flavor θ^0 with a filling $4m$. Such an effective density quadrupling is expected since, when the repulsion between the particles is strong, fermions both of the same and of different flavors avoid each other in a similar way.

We illustrate this point by first reviewing the case [33] of the same system without an external potential. We discuss the nature of a charged excitation over the Dirac vacuum ($\mu = 0$) as well as compressible multisoliton configurations at finite chemical potential μ. Then we add the potential (7.13) and find the corresponding incompressible charge states from the effective Hamiltonian for the charge mode θ^0. Next we estimate the (renormalized) energy gaps as an energy of a phase soliton of the charge mode. We obtain that these gaps (given in Eq. (7.78) below) are a function of a *total* filling $4m$.

Before discussing the nature of charge excitations of the full problem (7.27), it is instructive to first consider interacting NT electrons in the case of no external potential, $U(x) = 0$ at half filling ($\mu = 0$). In this case the system is described by a Lagrangian

$$\tfrac{1}{2\pi}\left\{(\partial_t\theta^0)^2 - K\,(\partial_x\theta^0)^2 + \textstyle\sum_a(\partial_\mu\theta^a)^2\right\} - \tfrac{4g_0}{\pi}\mathcal{F}\,(\theta^a,\ \theta^0) \qquad (7.67)$$

with the function $\mathcal{F}$ given in (7.30). In writing (7.67) we dropped the x-integration

for brevity.

Below we describe the lowest energy charge excitation of the system (7.67). As it has been shown in Ref. [33], such an excitation is a combination of solitons of a charge and flavor modes characterized by a presence of two length scales: flavor $l_{\rm fl}$ and charge $l_{\rm ch} \sim K^{1/2} l_{\rm fl}$. To illustrate this point let us consider adding an electron of the flavor 1. This corresponds to a configuration where the field Θ_1 is changed by π and the other fields $\Theta_{2,3,4}$ are unchanged. According to the transformation (7.24), in such a configuration all the fields θ^0, θ^a change by $\pi/2$. Since $l_{\rm ch} \gg l_{\rm fl}$ in the limit of a large stiffness $K \gg 1$, solitons of the flavor modes θ^a can be viewed as infinitely sharp steps on the scale of $l_{\rm ch}$. From the Lagrangian (7.67) it follows that such a sharp "switching" of the flavor modes can optimize the potential energy $\mathcal{F}$ in Eq. (7.67) if it happens at a point when θ^0 is changed by $\pi/4$, i.e. right in the middle of a slow soliton of the charged mode. In other words, the lowest energy charge excitation corresponds to a composite soliton configuration in which the flavor solitons adjust themselves to provide an effective potential

$$\bar{\mathcal{F}}(\theta^0) = \min_{\{\theta^a\}} \mathcal{F}(\theta^a,\ \theta^0) \tag{7.68}$$

for a soliton of the stiff charge mode.

The function $\bar{\mathcal{F}}(\theta^0)$ is shown in Fig. 7-2 (bold). One can see that the period of $\bar{\mathcal{F}}(\theta^0)$ is *four times smaller* than that of the original potential $\mathcal{F}(\theta^a,\ \theta^0)$ with fixed θ^a. Let us illustrate the meaning of this period reduction by considering an example of a charge excitation.

First consider the noninteracting case $K = 1$, when the four Fermi systems that correspond to different flavors are decoupled. Such a decoupling means that in the rotated basis (7.24) the flavor modes θ^a stay fixed with the potential $\mathcal{F}(\theta^a,\ \theta^0)$ being 2π-periodic in θ^0. In this case an excitation is a soliton $\theta^0 \to \theta^0 + 2\pi$ that is a flavor singlet and carries four (noninteracting) fermions according to (7.25).

When the Coulomb repulsion is strong, $K \gg 1$, it becomes favorable to split such a '2π' excitation into four successive charge solitons $\theta^0 \to \theta^0 + \pi/2$ each corresponding

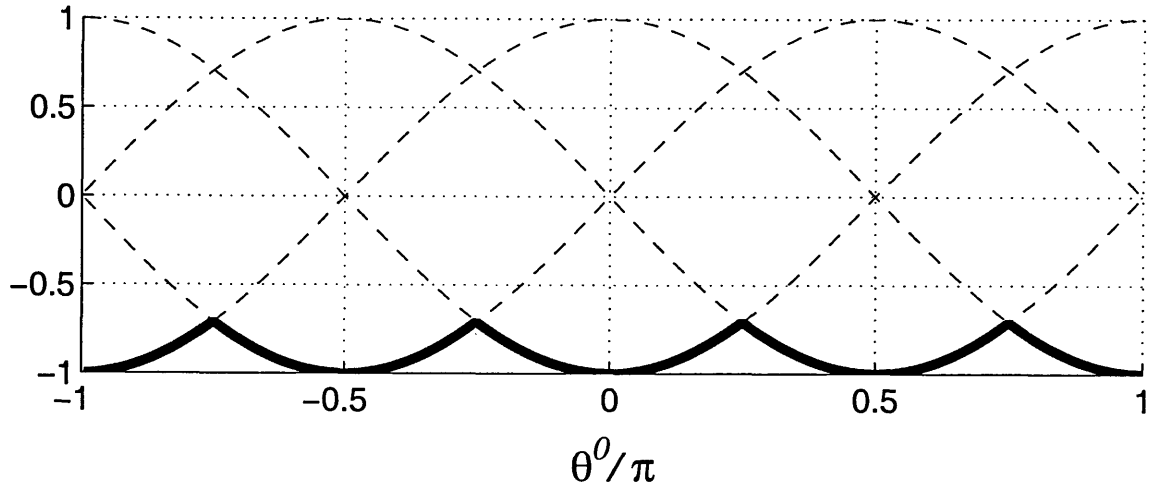

Figure 7-2: Effective potential $\tilde{\mathcal{F}}(\theta^0)$ (bold) for the charge mode in the case of $K \gg 1$, Eq. (7.68)

to an electron of a particular flavor. Let us see how such a splitting occurs. Suppose in the ground state $\theta^a = 0$ and $\theta^0 = -\pi$, Fig. 7-2. Excitation corresponding to say, flavor 1, is a composite soliton in which the charge mode slowly changes as $\theta^0 = -\pi \to -\pi/2$ while the flavor modes rapidly switch as $\theta^a \to \theta^a + \pi/2$ according to the tranformation (7.24). Such a switching occurs at a point where $\theta^0 = -3\pi/4$ in a fashion described above. Since the problem is $SU(4)$ symmetric, one can provide a soliton of any type Θ_α by choosing an appropriate switching combination of the fields $\theta^a \to \theta^a \pm \pi/2$ according to the canonical transformation (7.24) at the points when $\theta^0 = \{\pm 3\pi/4,\ \pm\pi/4\}$, Fig. 7-2. The flavor of a resulting composite soliton Θ_α is confined to the region of size $l_{\rm fl}$ inside the charge soliton width $l_{\rm ch} \gg l_{\rm fl}$.

Consider now the case of a finite fermion density corresponding to nonzero chemical potential $\mu \neq 0$. Its ground state is a lattice of composite solitons described above [33]. We assume a low density case, in which charge solitons overlap but flavor solitons practically do not. In such a configuration all the charge states are compressible, with the density following the chemical potential in a continuous fashion. If we adopt the parametrization of the density (7.1) in terms of a filling of $4m$ fermions (or charged solitons) per length $\lambda_{\rm ext}$, the filling m is proportional to the chemical potential $\tilde{\mu}$ in accord with Eq. (7.32).

Now let us add the external periodic potential (7.13). In this case there appear incompressible multisoliton configurations that are commensurate with the potential period λ_{ext}. If the total filling $4m$ is integer, the charge density in the corresponding configuration has a period equal to that of the external potential. If $4m = p/q$ is a fraction, the density is $q\lambda_{\text{ext}}$-periodic [47].

Let us illustrate the latter point by a following example. Consider a classical ground state for the simplest fractional case of $m = 1/2$. This is a configuration where solitons of the fields Θ_α occupy every other potential minimum, as shown in Fig. 7-3. This Figure is a result of a numerical minimization of the classical Hamiltonian (7.18) with respect to the fields Θ_α. For any rational filling $m = p/q$ the period of each field Θ_α is $q\lambda_{\text{ext}}$, with $q = 2$ in Fig. 7-3. The *total* density $4m = 2$ is integer, its period coinsiding with that of $U(x)$ in accord with the above discussion. In the absence of $U(x)$, all the Θ_α solitons would be equally separated from each other due to mutual repulsion. The finite U configuration shown in Fig. 7-3 is a result of an interplay between the mutually repelling solitons and a confining periodic potential. Fermionic exchange of the original problem (7.5) is manifest in the fact that solitons of the same flavor are located in different potential minima, similarly to the weak coupling case $m = 1/2$ considered in Sec. 7.3.2.

A charge excitation over such a classical state would be a soliton of one of the fields Θ_α that is added to the configuration in Fig. 7-3. To minimize the system's Coulomb energy, this soliton of a size smaller than λ_{ext} ("flavor scale") would push the other solitons apart. This would result in a deformation of a soliton lattice on a scale of many λ_{ext} ("charge scale").

Let us now turn from a particular example to the problem (7.27) with any given filling m. We assume that the flavor solitons switch as described above on the scale l_{fl} smaller than the potential period in agreement with the condition (7.3). The flavor scale l_{fl} will be estimated below in Eq. (7.75) self-consistently. In this case minimization (7.68) yields the following Hamiltonian

$$\frac{\hbar v}{\pi}\left\{\frac{K}{2}\left(\partial_x\theta^0\right)^2 + 4g_0\bar{\mathcal{F}}(\theta^0 + mk_{\text{ext}}x - 2\tilde{A}\sin k_{\text{ext}}x)\right\} \tag{7.69}$$

for the charge mode, where the function $\bar{\mathcal{F}}$ is plotted in Fig. 7-2, and the flavor modes θ^a are adjusted to optimize (7.68).

Below we find the commensurate charge ground state of the Hamiltonian (7.69) and estimate the corresponding minigap by finding an energy of a phase soliton of the charge mode $\bar{\theta}^0$.

The commensurate charge ground state follows from minimizing the energy (7.69). For simplicity, let us first assume *integer* m. We minimize (7.69) perturbatively in the coupling g_0 similarly to our treatment in Section 7.3. Expanding the charge mode in the powers of coupling similarly to Eq. (7.33),

$$\theta^0 = \bar{\theta}^0 + \theta^{0(1)} + \dots , \quad \theta^{0(n)} = \mathcal{O}(g_0^n) , \tag{7.70}$$

we find in the lowest order the potential energy

$$\bar{V}^*[\bar{\theta}^0] = \frac{4\hbar v}{\pi} \int dx \sum_{n=1}^{\infty} g_n^* \cos(4n\bar{\theta}^0) \tag{7.71}$$

for the "slow" charge mode in terms of the renormalized couplings g_n^* defined below in Eq. (7.74). Their bare values

$$g_n = g_0 f_n J_{4mn}(8n\tilde{A}) \tag{7.72}$$

are given in terms of the Fourier coefficients of the charge mode potential $\bar{\mathcal{F}}$ plotted in Fig. 7-2:

$$\bar{\mathcal{F}}(\theta^0) = \sum_{n=0}^{\infty} f_n \cos(4n\theta^0) . \tag{7.73}$$

The quadrupling of the harmonics in the decomposition (7.73) is a manifestation of the effective density quadrupling discussed above.

We integrate over Gaussian fluctuations of the flavor modes in analogy to our treatment in Sec. 7.3.1. As a result we estimate the renormalized couplings g_n^* from

the following scaling law:

$$g_n^* = g_n \left(\frac{l_{\mathrm{fl},n}}{a} \right)^{-3/4} \sim \frac{1}{\left(l_{\mathrm{fl},n} \right)^2} \, . \tag{7.74}$$

The couplings g_n are renormalized by the fluctuations of $\bar{\theta}^a$ on the scale $a < l < l_{\mathrm{fl},n}$, where the flavor scale for each term in the sum (7.71) is estimated self-consistently from Eq. (7.74). The flavor soliton scale l_{fl} is determined by the largest term in the series (7.71):

$$l_{\mathrm{fl}} = \min \{ l_{\mathrm{fl},n} \} \, , \tag{7.75}$$

with $l_{\mathrm{fl},n}$ from (7.74).

Minimizing the potential (7.69) we find that in the commensurate state, the phase mode $\bar{\theta}^0$ is constant.

An excitation over the ground state is an energy of a combination of the phase solitons for the charge and flavor modes, in analogy to the $U(x) \equiv 0$ case described above. In the limit $K \gg 1$ this energy is dominated by that of the charge mode soliton. The latter is described by the phase field $\bar{\theta}^0$ acquiring a slow coordinate dependence on the scale much greater than λ_{ext}. We estimate the excitation energy from the effective charge mode Hamiltonian

$$\bar{\mathcal{H}}^*[\bar{\theta}^0] = \frac{\hbar v}{\pi} \int dx \, \frac{K}{2} \, (\partial_x \bar{\theta}^0)^2 + \bar{V}^*[\bar{\theta}^0] \, , \tag{7.76}$$

with the potential $\bar{V}^*$ given by Eq. (7.71). In analogy to our previous treatment in Sec. 7.3.1, Eqs. (7.44) and (7.45), the charge phase soliton size

$$l_{\mathrm{ch}} \sim K^{1/2} \, l_{\mathrm{fl}} \, . \tag{7.77}$$

In the case when the coupling g_1 defined in Eq. (7.72) is nonzero, the corresponding renormalized gaps are given by

$$\Delta_m^*(\tilde{A}) \simeq 4 |f_1|^{4/5} \Delta_{4m}(4\tilde{A}) \, . \tag{7.78}$$

Here $\Delta_m(\tilde{A})$ are the weak coupling minigaps (7.47). The coefficient $f_1 = -4\sqrt{2}/15\pi \approx -0.120$. In general, the lowest non-vanishing harmonic would contribute to the gap Δ_m^*, since the relevance of the successive terms in the sum (7.71) decreases.

Let us pause here to analyze the result (7.78). The $4m$ dependence in Eq. (7.78) suggests that, in the limit of a strong coupling to the external potential and large Coulomb repulsion between the NT electrons, the system behaves as if it had a quadrupled density. This fact has a simple physical explanation. In the noninteracting case, fermions of the same flavor avoid each other due to the Pauli principle. The ground state wave function is then given by a product of four Slater determinants, one for each flavor. However, when the repulsion between the fermions is infinitely strong, fermions of *all* flavors avoid each other in a similar way, and the ground state wave function is a Slater determinant of a four-fold size. The original $SU(4)$ flavor symmetry of the problem reappears at the level of renormalization. It is manifest in a particular scaling law of 4/5 of the renormalized minigaps (7.78).

It is notable that although the gaps in the strong coupling limit oscillate with varying the potential amplitude, they never collapse to zero contrarily to the cases (6.16) and (7.47) considered above. Indeed, if the coupling $g_1 = 0$ for a particular value of A, the corresponding energy gap would be determined by the next harmonic in the expansion (7.71). The latter harmonic would *not* be zero at that very value of A since the zeroes of the Bessel functions never coincide. Let us underline that nonvanishing energy gaps are solely an effect of electron interactions. We shall see a qualitatively similar effect of nonvanishing gaps due to interactions in the classical limit of localized electrons in Section 7.5 below.

Finally, let us comment on the case of *fractional* fillings m. When the *total* filling $4m$ is integer, the excitation gap in the strong coupling limit is given by the result (7.78). For example, in the case of $m = 1/2$ studied in detail in Sec. 7.3.2 above, the weak coupling result (7.65) holds only for a very small bare backscattering $\Delta_0 \ll \epsilon$. For the realistic parameter values $\Delta_0 \sim 10$ meV away from zeroes of $v_{1/2}(2\tilde{A})$ the excitation gap in the state with $m = 1/2$ is given by the strong coupling result $\Delta_{1/2}^*$,

Eq. (7.78) with $4m = 2$. Switching between the two regimes happens when

$$\Delta_{1/2}(\tilde{A}) = \Delta^*_{1/2}(\tilde{A}) \propto \Delta_2(4\tilde{A}) \ . \tag{7.79}$$

When the *total* filling $4m = p/q$ is fractional, one needs to perform the Pokrovsky-Talapov analysis as in Sec. 7.3.2 for a single charge mode described by the Lagrangian (7.76). Namely, one would need to perform an expansion (7.70) to the order g_0^q, solve the corresponding Euler-Lagrange equations, and find the effective potential for the "slow" charge mode $\bar{\theta}^0$. The corresponding minigap can be estimated as an energy of a $\bar{\theta}^0$ soliton and will be proportional to $(\Delta_0)^q$. For a simplest case of $4m = 1/2$, the classical commensurate configuration has a total charge density with a period $2\lambda_{\text{ext}}$. An excitation over such a state is proportional to Δ_0^2. We will not proceed with a renormalization of this excitation.

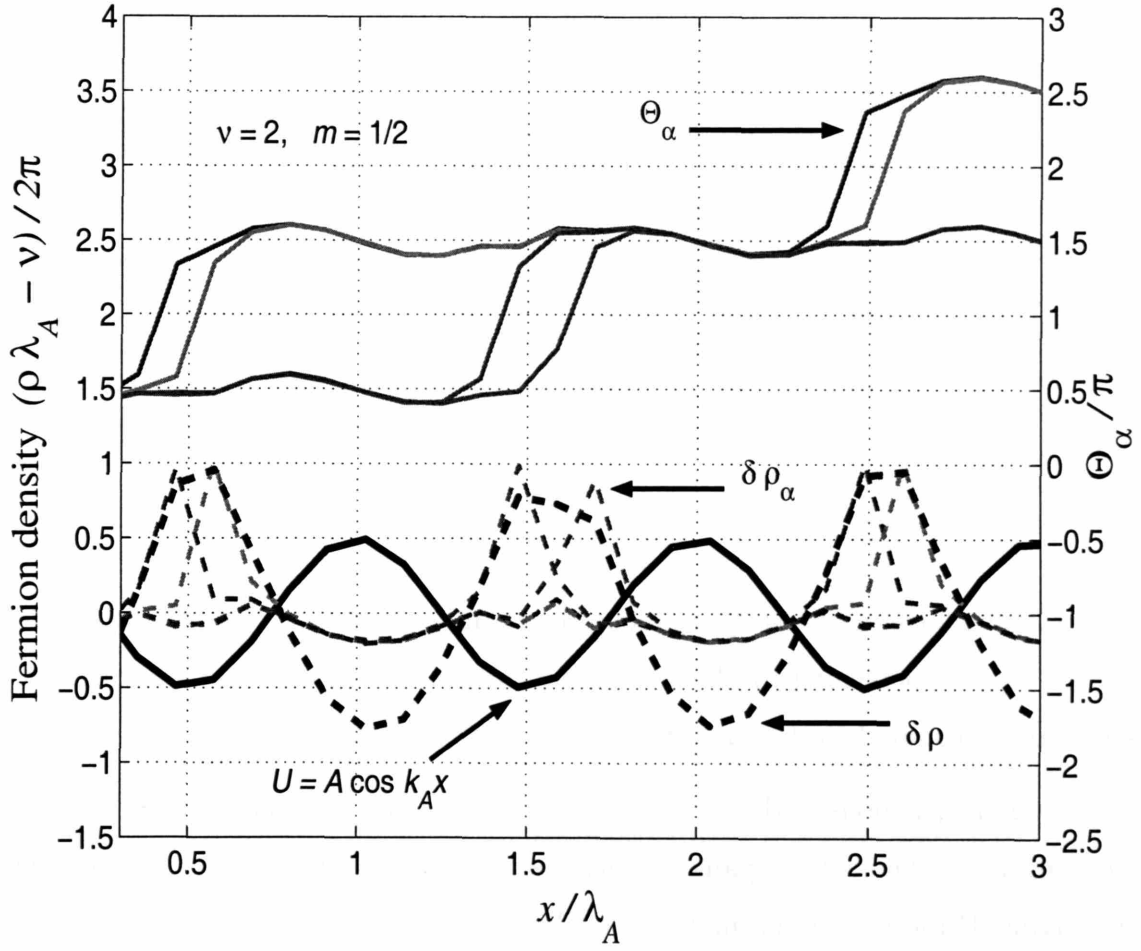

Figure 7-3: Classical ground state of the Hamiltonian (7.18) for the fractional filling $m = 1/2$. Solitons of the fields Θ_α (solid lines) as a result of numerical minimization of Eq. (7.18) for $\tilde{\mu} = 1/4$, $K = 10$, $g_0 = 12k_A^2$, $A = 10\epsilon_0$. Dashed lines are the corresponding charge densities $\delta\rho_\alpha = \rho_\alpha - m/\lambda_{\text{ext}}$ calculated with respect to the average. Bold dashed line is the total charge density calculated with respect to the average $4m/\lambda_{\text{ext}}$. Note the period doubling for the fields $\Theta_\alpha(x)$.

7.5 Weak tunneling limit

In the present Section we consider the regime (7.4) of fermions strongly localized in the potential minima of $U(x)$. Such a regime is characterized by exponentially small overlap of both the charge and flavor soliton tails and negligible quantum effects. This leads to the following classical treatment of the charge states in this limit.

The charge states (Fig. 7-4) are obtained by minimizing the *classical* energy functional

$$\frac{E_{\rm cl}}{N} - \mu(n_e - n_h) \tag{7.80}$$

with respect to positions x_i and y_i of electron and holes. Here

$$\begin{aligned} E_{\rm cl} = &\sum_{i=1..N_e} (\Delta_0 + U(x_i)) \; + \sum_{j=1..N_h} (\Delta_0 - U(y_j)) \\ &+ \sum_{\substack{i,j=1 \\ i>j}}^{N_e} \frac{e^2}{|x_i - x_j|} + \sum_{\substack{i,j=1 \\ i>j}}^{N_h} \frac{e^2}{|y_i - y_j|} - \sum_{\substack{i,j=1 \\ i>j}}^{N_e,N_h} \frac{e^2}{|x_i - y_j|} \end{aligned} \tag{7.81}$$

is the Coulomb energy of electrons along the chain with $N = L/\lambda_{\rm ext}$ sites, where L is the NT length. Screening by the underlying substrate with the dielectric constant ε is trivially accounted for by substituting $e^2 \to 2e^2/(\varepsilon + 1)$.

In Fig. 7-4, regions with $n_e = N_e/N$ electrons and $n_h = N_h/N$ holes per SAW wavelength are labeled by pairs (n_e, n_h), with total filling $4m = n_e - n_h$. The underlying Dirac symmetry makes the filling diagram symmetric with respect to $\mu \leftrightarrow -\mu$, $n_e \leftrightarrow n_h$. Each border separating regions with different (n_e, n_h) is itself comprised of incompressible states with larger fractions m, as shown by the domain $(1/2, 0)$ between $(0, 0)$ and $(1, 0)$. The state $(1/2, 0)$ is characterized by a fractional total filling $4m = 1/2$ and has a charge in every other SAW minimum, similarly to the strong coupling case of a fractional filling discussed above in the end of Sec. 7.4.

The results of numerical energy minimization (color in Fig. 7-4) can be fairly accurately reproduced by plotting the minima of $E_{n_e,n_h}(A) - \mu(n_e - n_h)$, where

$$E_{n_e,n_h} = (n_e + n_h)(\Delta_0 - A) + \frac{(n_e - n_h)^2 e^2}{2C} + V_{n_e} + V_{n_h} \; . \tag{7.82}$$

The first term in (7.82) is an energy of n_e electrons placed into each minimum and n_h holes into each maximum of $U(x)$. It corresponds to the first two terms of (7.81). The second term in (7.82) is the interaction energy of positive and negative charges located in the extrema of $U(x)$. Here

$$C = \frac{\lambda_{\text{ext}}}{2\ln(L/\lambda_{\text{ext}})} \tag{7.83}$$

is a capacitance corresponding to the length λ_{ext} of a nanotube. The logarithm of the system size enters since the overlap of charge solitons is negligible and thus the Coulomb interaction is unscreened. Finally, V_n in (7.82) is the interaction energy of n electrons (or n holes) minimized with respect to their positions inside the corresponding potential well of the periodic potential (7.13). The Dirac symmetry yields $E_{n,m} = E_{m,n}$.

In the case when the Coulomb interaction is small,

$$\frac{e^2}{\lambda_{\text{ext}}} \ll A\,, \tag{7.84}$$

the energy $V_n(A)$ can be found by approximating each potential well of (7.13) by a quadratic polynomial:

$$U(x) \approx -A + \min_n \frac{M\Omega^2}{2}\left(x - (n+\tfrac{1}{2})\lambda_{\text{ext}}\right)^2\,. \tag{7.85}$$

Here M is the "relativistic Dirac mass"

$$M = \frac{\Delta_0}{v^2} \tag{7.86}$$

and

$$\Omega^2 = \frac{Ak_{\text{ext}}^2}{M}\,. \tag{7.87}$$

Minimizing the Coulomb energy of n charges in a parabolic potential (7.85), we obtain

first several values of V_n:

$$V_0 = V_1 = 0 \ , \tag{7.88}$$

$$V_2 = 3\,(\pi/2)^{2/3} \left(\frac{e^2}{\lambda_{\rm ext}}\right)^{2/3} A^{1/3} \ , \tag{7.89}$$

$$V_3 = 5^{2/3} V_2(A), \ \ldots \ . \tag{7.90}$$

The characteristic power law $\sim A^{1/3}$ due to the above expressions is illustrated in Fig. 7-4 for small values of A.

Eq. (7.82) gives the width $\delta\mu_{n_e,n_h}$ of the incompressible state corresponding to filling (n_e, n_h):

$$\delta\mu_{n_e,n_h}(A) = \chi_0^{-1} + \chi_n^{-1} \ , \tag{7.91}$$

where

$$n = \max\{n_e, \ n_h\} \ , \tag{7.92}$$

$$\chi_0^{-1} = \frac{e^2}{C\lambda_{\rm ext}} \ , \tag{7.93}$$

$$\chi_n^{-1} = V_{n+1} + V_{n-1} - 2V_n \ . \tag{7.94}$$

Here the "bare" compressibility χ_0 is proportional to the NT capacitance. The regions (n_e, n_h) and $(n_e + 1, n_h + 1)$ of the filling diagram are separated by the vertical lines of fixed A, with its value implicitly defined by

$$A = \Delta_0 + \frac{1}{2}\left(V_{n_e+1}(A) - V_{n_e}(A) + V_{n_h+1}(A) - V_{n_h}(A)\right) \ . \tag{7.95}$$

Let us discuss the main results of this Section. We have considered a limit of strongly localized electrons. In this limit the system is classical and its filling diagram can be obtained by minimizing the energy functional (7.81).

We have obtained a charge filling diagram that consists of the domains corresponding to the incompressible states with n_e electrons and n_h holes with the total filling $4m = n_e - n_h$. Only the most pronounced states are shown in Fig. 7-4. Their boundaries consist of the states with fractional fillings $4m = p/q$ and the correspond-

ing energy gaps rapidly decay with increasing the fraction denominator q. Since we discarded the kinetic energy, there are strictly speaking no compressible energy states in the filling diagram Fig. 7-4.

We also note that energy gaps for the fixed fillings $4m = n_e - n_h$ oscillate as a function of the potential amplitude A (as, for instance, regions $(1,0)$ and $(2,1)$ that correspond to the same filling of $4m = 1$). Such oscillations are similar to the ones observed in the quantum-mechanical cases for both noninteracting electrons (Sec. 6.2 and Figs. 6-2,6-3) and weakly coupled interacting electrons (Sec. 7.3) described above. However, the energy gaps in Fig. 7-4 never collapse to zero, with their width determined by the strength of interactions. This is similar to the situation in strong coupling limit considered above in Sec. 7.4. Conversely, in the noninteracting case considered in detail in Section 6.2, minigaps are equal to zero for certain values of A. We again see that the non-vanishing minigaps arise in the system due to electron interactions.

7.6 Discussion

In the present Chapter we have considered different regimes of coupling of interacting NT electrons to the periodic potential. We have found novel interaction-induced incompressible states that correspond to minigaps in the NT spectrum. We showed that minigaps in an interacting system oscillate as a function of the amplitude of the external potential but they never vanish. The value of these minigaps is a direct measure of electron interaction strength in a nanotube.

We suggest that novel incompressible states with *fractional* m can be revealed in a SAW-NT setup described in the previous Chapter with the adiabatic current (6.22) quantized in *fractions* of $4ef$. For that, the adiabaticity of transport should be fulfilled:

$$hf \ll \Delta_m \ , \tag{7.96}$$

where Δ_m is a corresponding (renormalized) minigap for the fractional m, and f is the SAW frequency. This condition can be achieved since the substrate sound velocity is

much smaller than the Fermi velocity in the nanotube. For $f = 10$ GHz corresponding to the SAW wavelength of the order of 1 μm, the phonon energy $hf \approx 40$ μeV. Given typical minigap values Δ_m in the meV range, the adiabaticity condition (7.96) can be fulfulled.

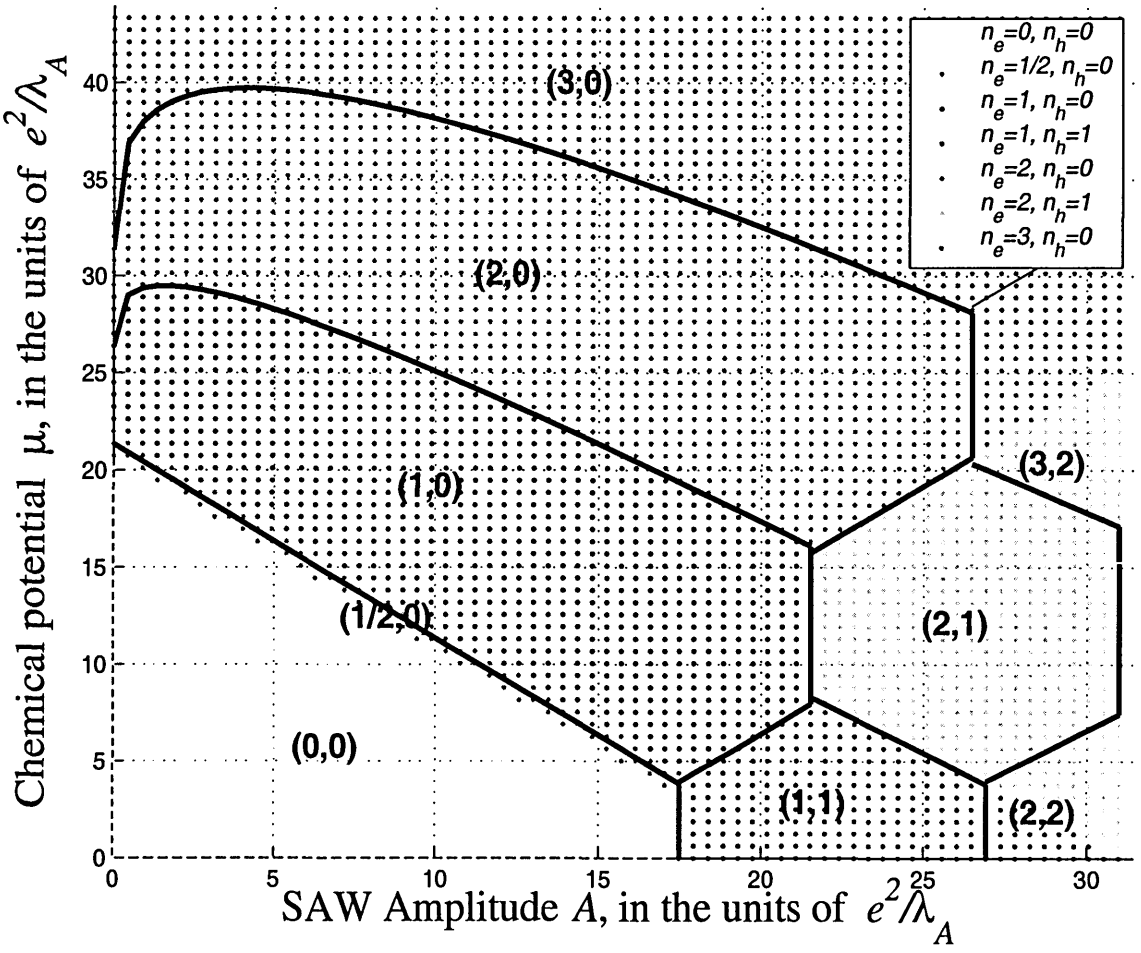

Figure 7-4: Charge filling diagram for the nanotube, $\Delta_0 = 6\pi e^2/\lambda_{\text{ext}}$, $\ln(L/\lambda_{\text{ext}}) = 2.5$, $e^2/\lambda_{\text{ext}} = 1.44$ meV for $\lambda_{\text{ext}} = 1\mu$m. Color regions are the result of numerical minimization, black lines are approximations obtained from Eq. (7.82).

Conclusions to Part II

In the present Part of the Thesis we have considered a set of physical effects in nanotubes that can be manifest in transport measurements.

In Chapter 5 we have developed a theory of a nanotube field effect. We have shown that at sufficiently large electric field, single electron NT properties can change drastically. In particular, the Fermi surface of a metallic tube can fracture, whereas the gap of a semiconducting NT can be strongly reduced. These effects, although require extremely strong fields, can prove useful in applications as well as in studying strongly correlated phenomena.

From the theoretical standpoint, the depolarization problem considered in Chapter 5 has been connected to the chiral anomaly of 1+1D Dirac fermions. We have found a universal screening function that depends solely on the low energy NT properties.

In Chapter 6 we have proposed an experimental setup to realize adiabatic charge pump of Thouless. For that, we suggest to use a semi-metallic nanotube coupled electrically to a surface acoustic wave (SAW). We have identified incompressible single electron states and found the corresponding minigaps. With a chemical potential inside a minigap, a slowly moving surface acoustic wave can induce adiabatic current quantized in the units of $4ef$, where e is electron charge and f is the SAW frequency.

Finally, in Chapter 7 we have considered in detail the electron NT properties in the presence of an external periodic potential. We have found novel interaction-induced incompressible states that appear when the electron density is commensurate with the potential period. We have treated interactions in the Luttinger liquid framework, and used the phase soliton approach to estimate the spectral gaps. We have suggested

to use the SAW-NT setup proposed in Chapter 6 to probe NT electron interactions.

Bibliography

[1] D. S. Novikov, L. S. Levitov, Electron properties of Carbon nanotubes in the field effect regime, cond-mat/0204499.

[2] V.I. Talyanskii, D.S. Novikov, B.D. Simons, L.S. Levitov, Quantized adiabatic charge transport in Carbon nanotubes, Phys. Rev. Lett. **87**, 276802 (2001); `cond-mat/0105220`

[3] D.S. Novikov and L.S. Levitov, Electron properties of Carbon nanotubes in a periodic potential, in preparation

[4] S. Iijima, Helical Microtubules of Graphitic Carbon, Nature **354**, 56-58 (1991)

[5] P.L. McEuen, Nanotechnology: Carbon-based electronics, Nature **393**, 15 (1998)

[6] C. Dekker, Carbon nanotubes as molecular quantum wires, Physics Today, May 1999, p. 22

[7] P.M. Ajayan and O.Z. Zhou, Applications of Carbon nanotubes, in the book [11]

[8] A.G. Rinzler *et al.* , Science **269**, 1550 (1995)

[9] D. Rotman, The nanotube computer, Technology Review **105**, 37 (March 2002)

[10] R. Saito, G. Dresselhaus and M. S. Dresselhaus, *Physical Properties of Carbon Nanotubes*, Imperial College Press, London, 1998.

[11] M.S. Dresselhaus, G. Dresselhaus, Ph. Avouris, *Carbon Nanotubes: Synthesis, Structure, Properties and Applications*, Springer Verlag, New York, 2001

[12] J.W.G. Wildoer *et al.*, Nature **391**, 59 (1998)

[13] T.W. Odom *et al.*, Nature **391**, 62 (1998)

[14] P. Avouris, Molecular electronics with Carbon nanotubes, Acc. Chem. Res. **35**, 1026 (2002)

[15] A. M. Rao, E. Richter, Shunji Bandow, Bruce Chase, P. C. Eklund, K. A. Williams, S. Fang, K. R. Subbaswamy, M. Menon, A. Thess, R. E. Smalley, G. Dresselhaus, and M. S. Dresselhaus, Diameter-Selective Raman Scattering from Vibrational Modes in Carbon Nanotubes, Science **275** 187 (1997)

[16] R. Saito and H. Kataura, Optical properties and Raman spectroscopy of Carbon nanotubes, in the book [11]

[17] S.S. Wong *et al.* , Nature **394**, 52 (1998)

[18] C. L. Kane and E. J. Mele, Phys. Rev. Lett. **78**, 1932 (1997).

[19] C. Zhou, J. Kong, and H. Dai, Phys. Rev. Lett. **84**, 5604 (2000);
M. Ouyang, J.L. Huang, C.L. Cheung, C.M. Lieber, Science **292**, 5517 (2001)

[20] H. Ajiki and T. Ando, J. Phys. Soc. Jpn. **62**, 1255 (1993)

[21] H. Ajiki and T. Ando, Energy Bands of Carbon Nanotubes in Magnetic Fields, J. Phys. Soc. Jpn. **65**, 505 (1996)

[22] H. Ajiki and T. Ando, J. Phys. Soc. Jpn. **65**, 505 (1996)

[23] J. -O. Lee, J. R. Kim, J. J. Kim, J. Kim, N. Kim, J. W. Park, and K. H. Yoo, Observation of magnetic-field-modulated energy gap in Carbon nanotubes, Sol. Stat. Comm. **115**, 467 (2000)

[24] N. F. Mott, Phil. Mag. 6, 287 (1961);
L. V. Keldysh, Yu. V. Kopaev, Fiz. Tverd. Tela 6, 2791 (1964); [Soviet Phys.-Solid State 6, 2219 (1965)];

J. J. des Cloizeaux, Phys. Chem. Solids 26, 259-266 (1965);
B. I. Halperin, T. M. Rice, in Solid State Physics 21, 115-192 (1968).

[25] L. X. Benedict, S. G. Louie, and M. L. Cohen, Static polarizabilities of single-wall carbon nanotubes, Phys. Rev. B**52**, 8541 (1995)

[26] X. Zhou *et al.*, Hu Chen, Ou-Yang Zhong-can, Electric Field-Induced Energy Gaps In Carbon Nanotubes: Prediction Of Controllable Nanoscale Switching Devices cond-mat/0010124;
The Polarizability and Electric Field-Induced Energy Gaps In Carbon Nanotubes, `cond-mat/0102094`

[27] D. P. DiVincenzo and E. J. Mele, Phys. Rev. B **29**, 1685 (1984).

[28] C. Kane, L. Balents, M. P. A. Fisher, Phys. Rev. Lett. **79**, 5086 (1997)

[29] R. Egger, A. O. Gogolin, Phys. Rev. Lett. **79**, 5082 (1997)

[30] L. Balents, M.P.A. Fisher, Phys. Rev. B **55**, R11973 (1997)

[31] Y.A. Krotov, D.-H. Lee, S.G. Louie, Phys. Rev. Lett. **78**, 4245 (1997)

[32] H. Yoshioka and A. Odintsov, Phys. Rev. Lett. **82**, 374 (1999)

[33] L. S. Levitov, A. M. Tsvelik, Phys. Rev. Lett. **90**, 016401 (2003); `cond-mat/0205344`

[34] J. Nygard, D.H. Cobden, M. Bockrath, P.L. McEuen, P.E. Lindelof, Electrical transport measurements on single-walled carbon nanotubes, Applied Physics A **69**, 297 (1999)

[35] M. Bockrath, D. H. Cobden, P. L. McEuen, N. G. Chopra, A. Zettl, A. Thess, R. E. Smalley, Single-electron transport in ropes of carbon nanotubes, Science **275**, 1922 (1997)

[36] M. Bockrath, D. H. Cobden, Jia Lu, A. G. Rinzler, R. E. Smalley, L. Balents, P. L. McEuen, Luttinger-liquid behaviour in carbon nanotubes, Nature **397**, 598 (1999)

[37] Z. Yao, H. W. Ch. Postma, L. Balents, C. Dekker, Nature **402**, 273 (1999)

[38] P. L. McEuen, M. Bockrath, D. H. Cobden, Y.-G. Yoon, and S. G. Louie, Disorder, Pseudospins, and Backscattering in Carbon Nanotubes, Phys. Rev. Lett. **83**, 5098 (1999)

[39] Liang WJ, Bockrath M, Bozovic D, Hafner JH, Tinkham M, Park H, Fabry-Perot interference in a nanotube electron waveguide, Nature **411**, 665 (2001)

[40] S. J. Tans, M. H. Devoret, H. Dai, A. Thess, R. E. Smalley, L. J. Geerligs, and C. Dekker, Individual single-wall carbon nanotubes as quantum wires, Nature, **386** 474 (1997)

[41] S.J. Tans, A.R.M. Verschueren, and C. Dekker, Room-temperature transistor based on a single carbon nanotube, Nature **393**, 49 (1998)

[42] T.W. Ebbesen, P.M. Ajayan, Nature **358**, 220 (1992);
C. Journet *et al.* , Nature **388**, 756 (1997)

[43] A. Thess *et al.* , Science **273**, 483 (1996)

[44] W.Z. Li *et al.* , Science **274**, 1701 (1996);
M. Terrones *et al.* , Nature **388**, 52 (1997);
Z.F. Ren *et al.* , Science **282**, 1105 (1998);
J. Kong *et al.* , Nature **395**, 878 (1998)

[45] D. J. Thouless, Phys. Rev. B **27**, 6083 (1983)

[46] I.E. Dzyaloshinsky, Zh.E.T.F. **47**, 1420 (1964);

[47] V.L. Pokrovsky, A.L. Talapov, Sov. Phys. JETP **75**, 1151 (1978)

[48] Q. Niu and D. J. Thouless, Quantised adiabatic charge transport in the presence of substrate disorder and many-body interaction, J. Phys. A: Math. Gen. **17** 2453 (1984).

[49] J. M. Shilton, V. I. Talyanskii, M. Pepper, D. A. Ritchie, J. E. F. Frost, C. J. B. Ford, C. G. Smith, and G. A. C. Jones, High-frequency single-electron transport in a quasi-one-dimensional GaAs channel induced by surface acoustic waves, J. Phys.: Cond. Matt. **8**, L531 (1996);
V. I. Talyanskii, J. M. Shilton, M. Pepper, C. G. Smith, C. J. B. Ford, E. H. Linfield, D. A. Ritchie, and G. A. C. Jones, Single-electron transport in a one-dimensional channel by high-frequency surface acoustic waves, Phys. Rev. B **56**, 15180 (1997).

[50] R. L. Miller, C. E. Nothnick, and D.S. Bailey, *Acoustic charge transport: Device technology and Applications*, Artech House, Boston, 1992

[51] L. Pfeiffer, K. W. West, H. L. Stormer, J. P. Eisenstein, K. W. Baldwin, D. Gershoni, and J. Spector, Formation of a high quality 2D electron gas on cleaved GaAs, Appl. Phys. Lett. **56** (17), 1697 (1990);
L. Pfeiffer, A. Yacoby, H. L. Stormer, K. L. Baldwin, J. Hasen, A. Pinczuk, W. Wegscheider, and K. W. West, Transport and optics in quantum wires fabricated by MBE overgrowth on the (110) cleaved edge, Microelectronics Jour. **28**, 817 (1997).

[52] S. Iijima and T. Ichihashi, Nature, **363**, 603 (1993).

[53] K. Yamanouchi *et al.*, Jpn. J. Appl. Phys. **33**, 3018, (1994).

[54] A.A. Abrikosov, L.P. Gorkov, I.E. Dzyaloshinskii, *Methods of Quantum Field Theory in Statistical Physics*, Dover Publishers, 1977

[55] S. Tomonaga, Progr. Theor. Phys. (Kyoto) **5**, 544 (1950)

[56] K.D. Schotte, U. Schotte, Tomonaga's model and the threshold singularity of X-ray spectra of metals, Physical Review A **182**, 479-82 (1969)

[57] I.E. Dzyaloshinskii and A.I. Larkin, Zh.E.T.P. **65**, 411 (1973)

[58] A. Luther and V.J. Emery, Phys. Rev. Lett. **33**, 589 (1974); A. Luther and I. Peschel, Phys. Rev. B **9**, 2911 (1974)

[59] S. Coleman, Quantum sine-Gordon equation as the massive Thirring model, Phys. Rev. D **11**, 2088 (1975)

[60] S. Mandelstam, Phys. Rev. D **11**, 3026 (1975)

[61] F.D.M. Haldane, J.Phys. C **14**, 2585 (1981)

[62] D. Sénéchal, An introduction to bosonization, `cond-mat/9908262`

[63] L.S. Levitov, A.V. Shytov, *Zadachi po teoreticheskoi fizike* (in Russian), `http://mit.edu/levitov/www/book/`

[64] M. Stone (Ed.), *Bosonization*, World Scientific, Singapore (1994)

[65] M.P.A. Fisher, L.I. Glazman, Transport in a one - dimensional Luttinger liquid, `cond-mat/9610037`

Appendix A

Calculation of the distribution of return times in anomalous diffusion

Below we consider the following problem:

What is the distribution of the intervals between successive returns to the origin of a random walker whose dynamics is governed by a generic continuous time random walk?

Consider a random walker whose probability distribution function $\mathcal{P}(x,t)$ to be at position x at time t is governed by the following master equation:

$$\mathcal{P}(x,t) = \int_0^t dt'\, \phi(t') \int dx'\, \psi(x')\, \mathcal{P}(x-x', t-t') + \delta(x) \left[\theta(t) - \int_0^t \phi(t')dt'\right] . \quad \text{(A.1)}$$

Eq. (A.1) defines a diffusion propagator $\mathcal{P}(x,t)$ in a most general case when the hops in time are distributed according to the continuous time random walk $\phi(t)$ and hops in parameter space x (that can be a coordinate, energy, etc) by the probability distribution function $\psi(x)$. A similar equation has been already considered in Sec. 1.2.2 while reviewing the dispersive transport. In analogy to the discussion after Eq. (1.15), from Eq. (A.1) we obtain the Fourier transform of the diffusion propagator:

$$\mathcal{P}_{k,\omega} = \frac{i}{\omega + i0} \cdot \frac{1-\phi(\omega)}{1-\psi(k)\phi(\omega)} . \quad \text{(A.2)}$$

To find a distribution of return times[1] it is convenient to find a probability distribution function $\bar{\mathcal{P}}(x,t)$ of the particle that *never comes back to the origin.* For that we need to modify the conditions of the random walk, demanding that the particle disappears after it comes back to the point $x = 0$:

$$\bar{\mathcal{P}}(x = 0, t) = 0 \quad \text{after the first hop} . \tag{A.3}$$

The condition (A.3) is equivalent to subtracting the term

$$\int_0^t dt' \, \phi(t') \int dx' \, \psi(x') \, \bar{\mathcal{P}}(-x', t - t') \tag{A.4}$$

that describes returns to the origin, from the master equation (A.1) written for the function $\bar{\mathcal{P}}(x,t)$. This results in the integral equation for the diffusion propagator $\bar{\mathcal{P}}(x,t)$, that in the Fourier space reads

$$\bar{\mathcal{P}}_{k,\omega} = \phi(\omega)\psi(k)\bar{\mathcal{P}}_{k,\omega} - \phi(\omega) \int \frac{dq}{2\pi} \, \psi(q)\bar{\mathcal{P}}_{q,\omega} + \frac{i}{\omega + i0}(1 - \phi(\omega)) . \tag{A.5}$$

The latter equation can be rewritten in the form

$$\bar{\mathcal{P}}_{k,\omega} = \mathcal{P}_{k,\omega} + \mathcal{P}_{k,\omega} \int \frac{dq}{2\pi} \, V(\omega, q)\bar{\mathcal{P}}_{q,\omega} , \tag{A.6}$$

where

$$V(\omega, q) = \frac{i\omega\phi(\omega)\psi(q)}{1 - \phi(\omega)} . \tag{A.7}$$

Eq. (A.6) is the analog of the Dyson Equation for the Green's function in quantum theory.

We are looking for a solution of Eq. (A.6) in the following form:

$$\bar{\mathcal{P}}_{k,\omega} = \lambda(\omega)\mathcal{P}_{k,\omega} . \tag{A.8}$$

[1] In our treatment we are generalizing the case of the Gaussian diffusion on a lattice considered in the book [68].

Substituting (A.8) into (A.6), obtain

$$\frac{1}{\lambda(\omega)} = \int \frac{dq}{2\pi} \frac{1}{1 - \psi(q)\phi(\omega)} \ . \tag{A.9}$$

Having found the propagator $\bar{\mathcal{P}}(x,t)$ for the particle that never returns to the origin, we now consider the probability distribution of times $p(\tau)$ between successive returns. The probability P_t that a random walker never returns to the origin during the time interval $(0,t)$ is given by

$$P_t = \int_t^\infty p(\tau) d\tau \ . \tag{A.10}$$

The latter quantity can be obtained from the propagator $\bar{\mathcal{P}}(x,t)$ as

$$P_t = \int dx \, \bar{\mathcal{P}}(x,t) \equiv \bar{\mathcal{P}}(q=0;t) \ . \tag{A.11}$$

From the solution (A.8),(A.9) for the propagator $\bar{\mathcal{P}}(x,t)$ we find that the Fourier transform of P_t is given by

$$P_\omega = \frac{i}{\omega + i0} \lambda(\omega) \ . \tag{A.12}$$

On the other hand, from the definition (A.10),

$$P_\omega = \frac{i}{\omega + i0} (1 - p(\omega)) \ , \tag{A.13}$$

where

$$p(\omega) = \int_0^\infty e^{i\omega\tau} p(\tau) d\tau \ . \tag{A.14}$$

Therefore, the characteristic function $p(\omega)$ of the waiting time distribution $p(\tau)$ between successive returns to the origin is given by

$$p(\omega) = 1 - \lambda(\omega) \tag{A.15}$$

with $\lambda(\omega)$ defined in Eq. (A.9).

In the case considered in Sec. 3.4, when $\phi(\tau)$ is given by the Lévy walk (3.49), and $\psi(x)$ is given by Eq. (3.50) with $x = \epsilon$, the corresponding asymptotic behavior

of the characteristic functions is

$$\phi(\omega) = 1 - B(-i\omega)^{\nu} , \tag{A.16}$$

$$\psi(k) = 1 - Dk^{\kappa} , \tag{A.17}$$

where B and D are some coefficients. Plugging the latter into Eq. (A.9), for small k and ω we obtain

$$\frac{1}{\lambda(\omega)} \simeq \int \frac{dk}{2\pi} \frac{1}{Dk^{\kappa} + B(-i\omega)^{\nu}} \sim (-i\omega)^{-\mu} , \tag{A.18}$$

where μ is given by Eq. (3.51). Therefore from the inverse Fourier transform of Eq. (A.15) we obtain the asymptotic behavior of the resulting waiting time distribution

$$p(\tau) \sim \frac{1}{\tau^{1+\mu}} . \tag{A.19}$$

The case of a Gaussian diffusion in energy with a Poissonian waiting time distribution $\phi(t)$ corresponds to $\kappa = 2$, $\nu = 1$, $\mu = 1/2$, yielding the WTD

$$p(\tau) \sim \frac{1}{\tau^{3/2}} . \tag{A.20}$$

Appendix B

Bosonization (single flavor)

Below we briefly review bosonization for the spinless fermions. We consider the Tomonaga model, develop its Lagrangian formulation, as well as renormalize the mass term for the interacting fermions.

A role of electron interaction strongly depends on the spatial dimensionality of the system. Electron interactions in two or three dimensions lead to the Landau Fermi liquid (for a detailed treatment and references, see the book [54], Chapter 4). The main outcome of the Fermi liquid theory is that in 2D or 3D repulsively interacting electrons behave qualitatively in the same way as an ideal Fermi gas, albeit with renormalized parameters. Interactions do not qualitatively change the properties of an electron system due to a restricted phase space for scattering in high dimensionality [54].

The case of one dimension is very different. Even an arbitrarily small electron interaction drastically changes the spectrum. This happens because energy and momentum conservation laws mean essentially the same for 1D electrons. In this case an excited electron and a hole are propagating coherently in the same direction with the same velocity, and thus even a small interaction between them has a large effect. This leads to a special excitation spectrum for 1D fermions. It turns out that the neutral electron-hole excitations exhaust all of the low energy spectrum of the 1D

metallic system, turning it into a so-called *Luttinger liquid.*

Since even small interactions change the properties of the system, one needs a non-perturbative treatment of the interacting problem in one dimension. It is remarkable that such a treatment (called bosonization) exists, allowing one to describe a strongly interacting 1D metal. Its main outcome is that in 1D low energy excitations of interacting spinless electrons can be parametrized in terms of a scalar *boson* field with a linear dispersion

$$\epsilon = \hbar \bar{v} k \ , \tag{B.1}$$

similar to that of acoustic phonons. The role of interactions is in renormalizing of the plasmon velocity $\bar{v}$.

Historically, the question of whether the low lying excitations of Fermi systems can be approximated by the bosonic degrees of freedom has been first raised by Felix Bloch in 1934. The bosonic algebra of density operators for 1D fermions was first obtained by Pascual Jordan in 1935-1937 in a somewhat different context. A pivotal point for bosonization was the work by S.-I. Tomonaga [55] in 1950 who applied the Jordan formalism to 1D electrons and expressed their properties in terms of bosonic density operators with simple commutation relations. A remarkable application of this technique to finding the singularity in the X-ray emission spectra in metals was demonstrated by K.D. Schotte and U. Schotte [56] in 1969. A perturbative treatment starting from the ideal 1D Fermi gas by summing all logarithmically divergent diagrams has been carried out by Dzyaloshinskii and Larkin [57] in 1973. They were the first to realize that the Green's function of the 1D interacting electrons has a power law singularity instead of a simple pole in a noninteracting case. They also found that the step in the Fermi distribution disappears at arbitrary small interaction strength.

So far we have been discussing *gapless* electron systems. One dimensional electron systems with an energy gap at a Fermi level can also be treated within the Luttinger liquid framework. A major progress in this field occured when in 1974 simultaneously A. Luther and coworkers [58] and S. Coleman [59] noticed the equivalence of the 1D massive Dirac fermions to the sine-Gordon bosons. This equivalence suggested that a

lump of a 1D fermion density corresponds to a quantum soliton of a sine-Gordon field, and lead to the development of the renormalization group treatment of the electron backscattering in the Luttinger liquid framework. The picture was completed by S. Mandelstam [60] in 1975 who expressed fermion creation and annihilation operators through an exponential of bose operators, obtaining relations now known as inverse bosonization transformations. The full self-consistent treatment of Luttinger liquids with a non-linear electron dispersion was outlined by F.D.M. Haldane [61] in 1981.

There are many excellent reviews of bosonization, with that by D. Sénéchal [62], by L.S. Levitov and A.V. Shytov (Chapter 12 of the book [63]), a collection of reprints by M. Stone [64], to name a few. Due to recent advances in a low-dimensional physics there appeared numerous applications of the Luttinger liquid theory, some of which are reviewed in Ref. [65].

B.1 Tomonaga Model

Below we bosonize gapless spinless fermions and find the dispersion relation (B.1). The Hamiltonian for 1D interacting fermions is $\mathcal{H} = \mathcal{H}_0 + \mathcal{H}_{\rm int}$, where

$$\mathcal{H}_0 = \sum_q \xi_q \, c_q^\dagger c_q \ , \tag{B.2}$$

$$\mathcal{H}_{\rm int} = \frac{1}{2L} \sum_q \rho_{-q} V_q \rho_q \ . \tag{B.3}$$

Here $\xi_q = \hbar v(|q| - k_F)$ is the electron dispersion relation linearized in the vicinity of the Fermi points $\pm k_F$, and ρ is the total electron density. Below it is always implied that the sum is dimensionless, $\sum_p \equiv L \int \frac{dp}{2\pi}$, L is the system size. The fermion creation and annihilation operators $c_q^\dagger, c_q$ are also dimensionless in the momentum representation, with their anticommutator

$$\left\{ c_p^\dagger, c_q \right\} = \delta_{p,q} \ , \tag{B.4}$$

where

$$\delta_{p,q} \equiv \frac{2\pi\delta(p-q)}{L} \ . \tag{B.5}$$

Following the pioneering work of Tomonaga [55], we represent the total density ρ as

$$\rho = \rho^R + \rho^L \ , \tag{B.6}$$

$$\rho^R(k) = \sum_{q>0} c^\dagger_{q-k/2}\, c_{q+k/2} \ , \tag{B.7}$$

$$\rho^L(k) = \sum_{q<0} c^\dagger_{q-k/2}\, c_{q+k/2} \ , \tag{B.8}$$

where the indices R, L correspond to the right and left fermion chiralities. The key to bosonization are the following density commutation relations, which are obtained by neglecting excitations with $k \sim k_F$:

$$\left[\rho^R(k), \rho^R(-k')\right] = k\,\delta(k-k') \ , \tag{B.9}$$

$$\left[\rho^L(k), \rho^L(-k')\right] = -k\,\delta(k-k') \ , \tag{B.10}$$

$$\left[\rho^R, \rho^L\right] = 0 \ . \tag{B.11}$$

Below we verify Eq. (B.9):

$$\left[\rho^R(k), \rho^R(-k')\right] \tag{B.12}$$

$$= \sum_{p>0} \left(c^\dagger_{p-k/2} c_{p+k/2-k'} - c^\dagger_{p-k/2+k'} c_{p+k/2} \right) \tag{B.13}$$

$$\approx \delta_{kk'} L \int_{-k/2}^{k/2} \frac{dp}{2\pi} = k\delta(k-k') \ . \tag{B.14}$$

In (B.14) we approximated the commuatator of fermion operators by its ground state average. In coordinate space commutation relations (B.9,B.10) look as

$$\left[\rho^R(x), \rho^R(y)\right] = \frac{1}{2\pi i}\,\partial_x \delta(x-y) \ , \tag{B.15}$$

$$\left[\rho^L(x), \rho^L(y)\right] = -\frac{1}{2\pi i}\,\partial_x \delta(x-y) \ . \tag{B.16}$$

The idea of bosonization is that in one dimension all the low energy excitations are

exhausted by the (bosonic) density fluctuations represented by the operators ρ^R, ρ^L. Indeed, it is possible to show that the kinetic energy $\mathcal{H}_0$ is quadratic in $\rho^{R,L}$:

$$\mathcal{H}_0 = \frac{\pi\hbar v}{L} \sum_p \left(\rho^R_{-p}\, \rho^R_p + \rho^L_{-p}\, \rho^L_p \right) . \tag{B.17}$$

The interaction part is trivially quadratic in densities:

$$\begin{aligned} \mathcal{H}_{\text{int}} = \frac{\pi\hbar v}{L} \sum_q \Big(& \rho^R_{-q}\, g_{1,q}\, \rho^R_q + \rho^L_{-q}\, g_{1,q}\, \rho^L_q \\ & + \rho^R_{-q}\, g_{2,q}\, \rho^L_q + \rho^L_{-q}\, g_{2,q}\, \rho^R_q \Big) , \end{aligned} \tag{B.18}$$

where dimensionless scattering amplitudes

$$g_1 = \tfrac{1}{2}\nu V^{(1)}(q) , \quad g_2 = \tfrac{1}{2}\nu V^{(2)}(q) , \tag{B.19}$$

and

$$\nu = \frac{1}{\pi\hbar v} \tag{B.20}$$

is the 1D density of states. The forward scattering amplitude $V^{(1)}$ describes interaction between fermions of the same chirality, whereas the dispersion amplitude $V^{(2)}$ represents scattering of fermions of different chiralities. Both $V^{(1)}$ and $V^{(2)}$ result in a small momentum transfer, and in most cases can be regarded as constants, $V^{(1,2)} = V^{(1,2)}(q = 0)$. Below we will give the general bosonization summary assuming that $V^{(1)} \neq V^{(2)}$. In the present Thesis, for the case of electrons in a nanotube, these amplitudes are set equal, $V^{(1)} = V^{(2)} = V$, where $V(q)$ is the interaction potential introduced in Eq. (B.3), as the difference between them is irrelevant [28, 29]. In writing the interaction part we omitted the large ($\sim 2k_F$) momentum transfer processes, such as backscattering and Umklapp. Backscatering will be considered in a greater detail later, whereath Umklapp is irrelevant away from half-filling and will be neglected in what follows. Extensive treatment of all scattering processes is given in the review by D. Sénéchal, Ref. [62].

It is convenient to represent the bosonic densities $\rho^{R,L}$ in terms of canonical di-

mensionless bosonic creation $b^\dagger$ and annihilation b operators:

$$\begin{aligned} \rho_k^R &= \lambda_k(b_k\theta_k + b_{-k}^\dagger\theta_{-k}) \ , \\ \rho_k^L &= \lambda_k(b_k\theta_{-k} + b_{-k}^\dagger\theta_k) \ , \end{aligned} \tag{B.21}$$

$$\lambda_k^2 = \frac{|k|L}{2\pi} \ , \quad \left[b_p, b_q^\dagger\right] = \delta_{p,q} \ . \tag{B.22}$$

The operator ρ^R annihilates and creates right-handed fermions, i.e. particles with $k > 0$. Similarly, ρ^L only deals with particles with $k < 0$. To diagonalize the total Hamiltonian $\mathcal{H} = \mathcal{H}_0 + \mathcal{H}_{\rm int}$ we use the Bogoliubov transformation

$$\begin{aligned} b_k &= \cosh\theta_k \, a_k - \sinh\theta_k \, a_{-k}^\dagger \ , \\ b_{-k}^\dagger &= \cosh\theta_k \, a_{-k}^\dagger - \sinh\theta_k \, a_k \ , \end{aligned} \tag{B.23}$$

with

$$\tanh 2\theta_k = \frac{g_{2,k}}{1 + g_{1,k}} \ . \tag{B.24}$$

The transformation (B.23) is canonical, with operators a_p and $a_p^\dagger$ obeying the bosonic commutation relation

$$\left[a_p, a_q^\dagger\right] = \delta_{p,q} \ . \tag{B.25}$$

The result of diagonalization is a *bosonic* Tomonaga - Luttinger Hamiltonian with an approximately linear dispersion relation:

$$\mathcal{H}_{\rm TL} = \sum_k |k| \bar{v}_k \, a_k^\dagger \, a_k \ . \tag{B.26}$$

Electron interactions renormalize the plasmon velocity,

$$\bar{v}_k = v\sqrt{(1 + g_{1,k})^2 - g_{2,k}^2} \ . \tag{B.27}$$

Note that Eqs. (B.26,B.27) are exact for *arbitrary* interaction strength in the limit of $|k| \ll k_F$.

B.2 Lagrangian Formulation

The goal of the present section is to derive a Lagrangian for the Tomonaga model. The action for the bosonized system is conventionally written in terms of the bosonic *displacement fields* $\varphi^{R,L}$, introduced as

$$\rho^R = \frac{1}{2\pi}\,\partial_x\varphi^R\ , \quad \rho^L = \frac{1}{2\pi}\,\partial_x\varphi^L\ . \tag{B.28}$$

From (B.9,B.10,B.11) the commutation algebra of the displacement fields follows:

$$\begin{aligned}
\left[\varphi^R(x),\varphi^R(y)\right] &= i\pi\,\mathrm{sign}(x-y)\ ,\\
\left[\varphi^L(x),\varphi^L(y)\right] &= -i\pi\,\mathrm{sign}(x-y)\ ,\\
\left[\varphi^L(x),\varphi^R(y)\right] &= 0\ .
\end{aligned} \tag{B.29}$$

From now on we discard the (irrelevant) momentum dependence of scattering amplitudes $g_{1,2}$ defined in Eq. (B.19), treating them as constants. The total Hamiltonian

$$\mathcal{H} = \mathcal{H}_0 + \mathcal{H}_{\rm int}\ , \tag{B.30}$$

where $\mathcal{H}_0$ and $\mathcal{H}_{\rm int}$ given by Eqs. (B.17) and (B.18), can be written in terms of the displacement fields (B.28) as

$$\mathcal{H} = \frac{v}{4\pi}\int dx\,\left\{(1+g_1)\left((\partial_x\varphi^R)^2+(\partial_x\varphi^L)^2\right)+2g_2\,\partial_x\varphi^R\partial_x\varphi^L\right\}\ . \tag{B.31}$$

It is convenient to introduce the mutually conjugate density and phase fields

$$\theta = \frac{\varphi^R+\varphi^L}{2}\ , \quad \phi = \frac{\varphi^R-\varphi^L}{2}\ . \tag{B.32}$$

The field θ is a displacement field for a total density,

$$\rho = \frac{1}{\pi}\,\partial_x\theta\ , \tag{B.33}$$

whereas the field ϕ describes the phase of the wave function. Their commutation

relations follow from (B.29):

$$\begin{aligned} &[\theta,\theta] = [\phi,\phi] = 0 \ , \\ &[\phi(x),\theta(y)] = \tfrac{i\pi}{2}\,\mathrm{sign}(x-y) \ . \end{aligned} \tag{B.34}$$

Therefore the canonically conjugate momentum for the θ field is

$$\hat{\Pi}_\theta = -\frac{1}{\pi}\,\partial_x\phi \ , \tag{B.35}$$

and that for the ϕ field is

$$\hat{\Pi}_\phi = -\frac{1}{\pi}\,\partial_x\theta \ . \tag{B.36}$$

Using (B.35), the Lagrangian (in the Euclidean space-time) for the gapless spinless fermions in terms of the density field θ is

$$\mathcal{L}_0[\theta] = \frac{1}{2\pi v(1+g_1-g_2)} \int dx \left\{ (\partial_\tau\theta)^2 + \bar{v}^2(\partial_x\theta)^2 \right\} \ , \tag{B.37}$$

where $\bar{v}$ is given by (B.27). Similarly, the (Euclidean) Lagrangian in terms of the phase field ϕ reads

$$\mathcal{L}_0[\phi] = \frac{1}{2\pi v(1+g_1+g_2)} \int dx \left\{ (\partial_\tau\phi)^2 + \bar{v}^2(\partial_x\phi)^2 \right\} \ . \tag{B.38}$$

The descriptions (B.37) and (B.38) are dual.

Finally, the Euclidean pairwise correlators of the fields θ and ϕ can be read out from the Lagrangians (B.37) and (B.38):

$$\langle \theta_{-k,-\omega}\theta_{k,\omega} \rangle = \frac{\pi v(1+g_1-g_2)}{\omega^2 + k^2\bar{v}^2} \ , \tag{B.39}$$

$$\langle \phi_{-k,-\omega}\phi_{k,\omega} \rangle = \frac{\pi v(1+g_1+g_2)}{\omega^2 + k^2\bar{v}^2} \ . \tag{B.40}$$

B.3 Inverse Bosonization Transformations

In the previous section B.2 we introduced the bosonic displacement fields $\varphi^{R,L}$ and expressed them through the densities of right and left moving fermions. It is possible to invert this procedure by representing the *fermion* operators through $\varphi^{R,L}$. For that, we introduce the *slow* chiral components $\psi^{R,L}$ of fermion operators c and $c^\dagger$:

$$\begin{aligned} \sqrt{L}\, c(x) &= e^{ik_F x}\psi^R(x) + e^{-ik_F x}\psi^L(x) \ , \\ \sqrt{L}\, c^\dagger(x) &= e^{-ik_F x}\psi^{R\dagger}(x) + e^{ik_F x}\psi^{L\dagger}(x) \ . \end{aligned} \tag{B.41}$$

Following (B.4), the commutation relations for the chiral components are

$$\begin{aligned} \left\{\psi^R(x), \psi^{R\dagger}(y)\right\} &= \delta(x-y) \ , \\ \left\{\psi^L(x), \psi^{L\dagger}(y)\right\} &= \delta(x-y) \ , \end{aligned} \tag{B.42}$$

with all other anticommutators being zero. The inverse bosonization transformations are then defined as [60]

$$\psi^R(x) = A^R\, e^{i\varphi^R} \ , \quad \psi^L(x) = A^L\, e^{-i\varphi^L} \ . \tag{B.43}$$

Eqs. (B.43) are a highly non-local way of representing a 1D fermion via the bosonic fields. These relations suggest that in one dimension the notions of the Fermi and Bose statistics are in some sense relative, and one can go from one to another interchangeably to describe the same system. The factors

$$A^R = A^L = \frac{1}{\sqrt{2\pi a}} \tag{B.44}$$

are related to the lattice cutoff a. Below we verify the expression for A^R by computing the equal time average $\left\langle \psi^{R\dagger}(x)\psi^R(0)\right\rangle$ for a non-interacting case $g_1 = g_2 = 0$ directly and using the bosonization representation (B.43). A direct calculation using the causal 1D Green's function $G^R(x,t) = -i\left\langle T\psi^R(x,t)\psi^{R\dagger}(0,0)\right\rangle$ yields

$$\left\langle \psi^{R\dagger}(x)\psi^R(0)\right\rangle = iG^R(x; t=-0)$$

$$= i \int \frac{d\omega}{2\pi} \frac{dk}{2\pi} \frac{e^{i\omega 0} e^{ikx}}{\omega - kv + i0 \operatorname{sign} k} = -\int_{-\infty}^{0} \frac{dk}{2\pi} e^{ikx} = \frac{i}{2\pi x} \,. \tag{B.45}$$

Same quantity using the bosonization formulae (B.43) and (B.29) is given by

$$\left\langle \psi^{R\dagger}(x)\psi^{R}(0) \right\rangle = |A^R|^2 \left\langle e^{-i(\varphi_x^R - \varphi_0^R) + \frac{1}{2}\left[\varphi_x^R, \varphi_0^R\right]} \right\rangle$$

$$= |A^R|^2 e^{-\frac{1}{2}\left\langle (\varphi_x^R - \varphi_0^R)^2 \right\rangle} e^{\frac{i\pi}{2}\operatorname{sign} x} = |A^R|^2 \cdot (i \operatorname{sign} x) \cdot \frac{a}{|x|} \tag{B.46}$$

$$= |A^R|^2 \cdot \frac{ia}{x} \,. \tag{B.47}$$

Here we used the value of the equal time correlator of bosonic fields,

$$\left\langle (\varphi_x^R - \varphi_0^R)^2 \right\rangle = \int \frac{d\omega}{2\pi} \frac{dk}{2\pi} |1 - e^{ikx}|^2 \left\langle \phi_{-k,-\omega} \phi_{k,\omega} \right\rangle$$

$$= 2 \int_{1/|x|}^{1/a} \frac{dk}{k} (1 - \cos kx) = 2 \ln \frac{|x|}{a} \,. \tag{B.48}$$

In calculating it we utilized the correlator (B.40). The coefficient A^L can be found in a similar way. One may check in a similar way that operators (B.43) obey the (anti)commutation relations (B.42). A more rigorous derivation of the above statements can be found in Refs. [62, 63].

B.4 Massive Dirac Fermions

In the present Section we develop a renormalization group (RG) treatment of spinless fermions in the presence of backscattering. We will show that the energy gap due to backscattering is *enhanced* by repulsive electron interactions.

Consider massive interacting Dirac fermions described by the Hamiltonian

$$\mathcal{H} = \mathcal{H}_{0D} + \mathcal{H}_{\text{int}} + \mathcal{H}_{\text{bs}} \,. \tag{B.49}$$

Here the free Dirac Hamiltonian is

$$\mathcal{H}_{0D} = -i\hbar v \int dx \, \psi^\dagger \sigma_3 \partial_x \psi \,, \tag{B.50}$$

and the backscattering term

$$\mathcal{H}_{\rm bs} = \Delta_0 \int dx\, \psi^\dagger \sigma_1 \partial_x \psi \ , \tag{B.51}$$

with Δ_0 being a bare gap giving mass to Dirac fermions. The wave function

$$\psi(x) = \begin{pmatrix} \psi^R \\ \psi^L \end{pmatrix} \tag{B.52}$$

is a two-component Weyl spinor in the basis of right- and left-movers, and σ_i are the Pauli matrices. The Hamiltonian $\mathcal{H}_{\rm int}$ describing electron interactions is given by Eq. (B.3) with the Dirac fermion density $\rho = \psi^\dagger \psi$.

In the absence of interactions the Hamiltonian $\mathcal{H}_{0\,D} + \mathcal{H}_{\rm bs}$ describes free relativistic fermions with a Dirac spectrum

$$\epsilon_k^2 = (\hbar k v)^2 + \Delta_0^2 \ . \tag{B.53}$$

Interactions can be taken into account by bosonizing the full Hamiltonian (B.49) using the technique developed above. This yields [58, 59] the (Euclidean) sine-Gordon Lagrangian

$$\mathcal{L} = \mathcal{L}_0[\theta] + \mathcal{L}_{\rm bs} \ , \tag{B.54}$$

where $\mathcal{L}_0$ is given by Eq. (B.37) and the backscattering term

$$\mathcal{L}_{\rm bs} = \frac{\Delta_0}{\pi a} \int dx\, \cos 2\theta \ . \tag{B.55}$$

The sine-Gordon problem (B.54) can be studied using the renormalization group methods. Below we calculate the scaling dimension of the backscattering term Δ_0 at one loop. Performing the average of the cosine term $\langle \cos 2\theta \rangle = e^{-2\langle \theta^2 \rangle}$ we obtain the RG flow for the backscattering (l is the length scale):

$$\Delta(l) = \Delta_0 \left(\frac{l}{a} \right)^{-\alpha} \ . \tag{B.56}$$

Here the exponent

$$\alpha = \sqrt{\frac{1+g_1-g_2}{1+g_1+g_2}}\,, \tag{B.57}$$

and the correlator $\langle\theta^2\rangle$ is found analogously to Eq. (B.48),

$$\left\langle\theta^2\right\rangle = \int \frac{d\omega}{2\pi}\frac{dk}{2\pi}\,\langle\phi_{-k,-\omega}\phi_{k,\omega}\rangle = \frac{\alpha}{2}\ln\frac{l}{a}\,. \tag{B.58}$$

From the scaling behavior (B.56) we find that backscattering term is *relevant* when

$$\alpha < 2\,. \tag{B.59}$$

In particular, this is the case for the free fermions, $\alpha = 1$.

Finally, let us estimate the value of the renormalized charge gap due to backscattering. Adding a fermion above the gap corresponds to a sine-Gordon soliton of the bosonized model $\mathcal{L}_0[\theta] + \mathcal{L}_{\rm bs}$. The excitation gap is given by an energy of such a soliton. The corresponding classical sine-Gordon Hamiltonian for the θ field reads

$$\mathcal{H}_{s-G} = \frac{\hbar v}{\pi}\int dx\,\left\{\frac{K}{2}(\partial_x\theta)^2 + \lambda_0\cos 2\theta\right\}\,. \tag{B.60}$$

Here the coupling

$$\lambda_0 = \frac{\Delta_0}{\hbar v a}\,, \tag{B.61}$$

and a charge stiffness

$$K = 1+g_1+g_2 = 1+\frac{\nu}{2}\left(V^{(1)}+V^{(2)}\right)\,. \tag{B.62}$$

Quantum fluctuations renormalize the coupling,

$$\lambda(l) = \lambda_0\left(\frac{l}{a}\right)^{-\alpha} \tag{B.63}$$

according to Eq. (B.56). These fluctuations are important at all length scales l between the lattice cutoff and the sine-Gordon soliton size l^*, $a < l < l^*$. At a scale $l > l^*$ beyond the soliton size the kinetic term in the Hamiltonian (B.60) is less im-

portant than the potential one and the RG flow stops yielding the renormalized value of the coupling

$$\lambda^* = \lambda_0 \left(\frac{l^*}{a}\right)^{-\alpha} . \tag{B.64}$$

The soliton size l^* is determined self-consistently from the Hamiltonian (B.60) with a renormalized coupling, λ^*:

$$\frac{K}{(l^*)^2} \sim \lambda^* , \tag{B.65}$$

obtaining

$$l^* \sim a \left(\frac{KD}{\Delta_0}\right)^{\frac{1}{2-\alpha}} , \tag{B.66}$$

where

$$D \equiv \frac{\hbar v}{a} \tag{B.67}$$

is the cutoff energy (1D bandwidth). The excitation gap is the energy of a classical sine-Gordon soliton with a renormalized size l^*,

$$\Delta \sim K \frac{\hbar v}{l^*} \sim (KD)^{\frac{1-\alpha}{2-\alpha}} \Delta_0^{\frac{1}{2-\alpha}} . \tag{B.68}$$

The excitation gap (B.68) is *enhanced* by a factor

$$\left(\frac{KD}{\Delta_0}\right)^{\frac{1-\alpha}{2-\alpha}} \gg 1 \tag{B.69}$$

in the case of an electron *repulsion*, $0 < \alpha < 1$. In the limit of an infinitely strong repulsion $\alpha \to 0$, the charge mode fluctuations are suppressed, and the gap (B.68) is given by the energy of a classical sine-Gordon soliton with rigidity $K \to \infty$. Finally, in the noninteracting case $\alpha = 1$ the gap (B.68) is not renormalized, $\Delta = \Delta_0$.